UNIVERSIDAD POLITÉCNICA DE MADRID

Escuela Técnica Superior de Ingenieros de Caminos,
Canales y Puertos

Microstructure sensitive simulation framework for additively manufactured Hastelloy-X

TESIS DOCTORAL

Chandrashekhar Machhindra Pilgar
Ingeniero Industrial

2022

Departamento de Ciencia de Materiales

Escuela Técnica Superior de Ingenieros de Caminos, Canales y Puertos

---

Microstructure sensitive simulation framework for additively manufactured Hastelloy-X

Autor:

Chandrashekhar Machhindra Pilgar
Ingeniero Industrial

Director de Tesis:

Javier Segurado
Doctor en Ingeniería

2022

"Ultimately, education in its real sense is the pursuit of truth. It is an endless journey through knowledge and enlightenment."

Dr.APJ Abdul Kalam, Former Indian President

Resumen

La fabricación aditiva de aleaciones metálicas se ha convertido en una técnica disruptiva que permite diseñar y fabricar componentes muy complejos con una forma casi final. Esto es especialmente relevante para la industria aeroespacial que tiene un gran alto en producir componentes de formas complejas, construidos por Selective Laser Meling (SLM), en superaleaciones de alto rendimiento como Hastelloy-X. Sin embargo, en la fabricación SLM las piezas resultantes presentan una fuerte anisotropía y con gran dispersión de propiedades. Estas características se deben a las microestructuras especiales desarrolladas como resultado del calentamiento y enfriamiento rápidos durante el proceso SLM. Este comportamiento mecánico es consecuencia por las microestructuras desarrolladas durante SLM (es decir, tamaños, relación de aspecto y orientaciones de los granos) y defectos como la rugosidad de superficial. Para parámetros de fabricación similares, estas microestructuras varían según la orientación de fabricación y grosor de la muestra. La caracterización experimental de la respuesta cuasiestática y de fatiga de probetas fabricados por SLM requiere una campaña experimental completa para cada microestructura.

De forma complementaria, la modelización computacional tiene como objetivo predecir la respuesta mecánica de las aleaciones SLM en función de la microestructura real, reduciendo así la cantidad de experimentos necesarios para la caracterización del

material. Sin embargo, los métodos computacionales existentes y su aplicación para predecir el análisis cuasiestático y de fatiga tienen ciertas limitaciones. a) Respecto a los modelos de comportamiento mecánico, la mayoria son emprpíricos y ajustables con datos experientales para cada microestructura. b) No existe ningún estudio que analice (y sea capaz de predecir cuantitativamente) la respuesta mecánica anisotrópa de los componentes en función de la microestructura, el espesor de la muestra y la rugosidad superficial. c) No existen modelos de fatiga que tengan en cuenta los efectos de la microestructura, la dirección de construcción y la rugosidad de la superficie en la predicción de la vida.

En este trabajo, se presenta un marco para ensayos virtuales de probetas de Hastelloy-X fabricadas por SLM sensible a la microestructura para superar las limitaciones antes mencionadas. Con respecto a a), se ha desarrollado modelos numéricos dependientes de la microestructura para la predicción de la respuesta cuasiestática y de fatiga, lo que reduce la necesidad de experimentos repetidos para la caracterización del material. Estos modelos se basan en homogeneización computacional que determina la respuesta macroscópica de una pieza SLM a partir de su microestructura policristalina. La respuesta de cristal se ha modelado con un modelo de plasticidad cristalina (CP), calibrado con un número limitado de datos macroscópicos. Finalmente, el comportamiento se obtiene simulando la deformación de los Elementos de Volumen Representativos (RVE) de la microestructura real mediante un solver FFT eficiente, que permite la resolución de grandes RVE sintéticos con microestructura compleja y detallada, construidos a partir de datos obtenidos por EBSD. Además, el efecto de la geometría de la muestra (grosor de la muestra) y la rugosidad de la superficie también se han considerado en las simulaciones.

Con respecto a b) la primera aplicación del modelo propuesto es predecir la respuesta cuasiestática de Hastelloy-X en función de la microestructura resultante de SLM (para diferentes direcciones de fabricación) y también considerando el efecto de la temperatura y el espesor de la muestra. El modelo de CP se ajustó utilizando la respuesta a tracción de uno de los especímenes ensayados. La dependencia de la temperatura se agregó al modelo de CP a través de la tension critica resuelta en cortante inicial y de saturación. El marco propuesto predijo correctamente (con un error de 4%) el módulo de Young y la respuesta de tensión-deformación plástica de todos los especímenes en un amplio rango de temperatura. El trabajo demuestra que la respuesta mecánica anisotropa que se encuentra en las piezas fabricadas por SLM puede atribuirse completamente a lan microestructura policristalina.

Con respecto al estudio de fatiga, el marco CP-FFT propuesto se ha empleado para

predecir el comportamiento en fatiga de Hastelloy-X fabricado con SLM a 750 °C, teniendo en cuenta la influencia de las microestructuras producidas durante el proceso SLM. En este modelo, se ha empleado un modelo CP fenomenológico con un término de "back-stress", calibrado mediante un ajuste inverso a la curva de histéresis experimental de un experimento ciclico controlado en deformación. La técnica se basa en la extracción de parámetros indicadores de fatiga (FIP) de las simulaciones y su uso en leyes de predicción de la vida a fatiga tanto para control de deformación como de tensión, que se basan en el trabajo cíclico y total disipado, respectivamente. La vida de fatiga se calcula para cada caso usando la distribución FIP obtenida de la ley de potencia propuesta que se calibra usando dos experimentos de fatiga. El modelo es capaz de predecir de forma bastante precisa la vida en fatiga para las diversas microestructuras SLM y condiciones de carga consideradas.

Finalmente, el modelo se ha extendido para predecir la vida de fatiga de muestras planas en función de la microestructura y rugosidad superficial. La capa de rugosidad superficial, que se genera en base a la rugosidad superficial media experimental R_a, se ha añadido como una superficie libre al RVE. La inclusión en la simulación de una superficie libre con rugosidad permite predecir con precisión la vida de fatiga de las muestras planas, que es considerablemente menor que la de probetas gruesas pulidas.

Abstract

Additive manufacturing of metallic alloys have become a disruptive technique allowing to design and fabricate very complex components with a near neat shape. This is specially relevant for the aerospace industry with high interest in producing complex shape components using Selective Laser Meling (SLM), in high performance superalloys as Hastelloy-X. However, in SLM fabrication the resulting parts present strong anisotropy and their response have large dispersion. These features are due to the special microstructures developed as a result of rapid heating and cooling during the SLM process. The mechanical behavior of these alloys is determined by the microstructures developed during SLM (namely grain size, aspect ratio, and orientations) and defects such as surface roughness. For similar fabrication parameters, these microstructures also vary depending on build orientation and sample thickness. The experimental characterization of the quasi-static and fatigue response of SLM-fabricated specimens necessitates a large experimental campaign for a wide variety of microstructures.

Complementary, computational modelling approaches aims to predict the mechanical response of SLM alloys as a function of the actual microstructure thus reducing

the number of experiments required for material characterization. However, the existing computational methods and their application to predict the quasi-static and fatigue response have certain limitations. a) Regarding the models for mechanical behavior, the majority are empirical and based on large experimental datasets. b) There is no study which analyzes (and quantitatively predicts) the anisotropic mechanical response of SLM components that results from microstructure, sample thickness, and surface roughness defect. c) There is a lack of fatigue models that takes into account the effects of microstructure, build direction, and surface roughness in the life prediction.

In this work, a microstructure sensitive virtual testing framework for SLM-fabricated Hastelloy-X is presented, which overcomes the aforementioned limitations. Regarding a) numerical models that take microstructural details into account have been developed to predict the quasistatic and cyclic response, reducing the number of experiments for material characterization. These models are based on a computational homogenization approach that links the macroscopic response of an SLM part with its polycrystalline microstructure. A crystal plasticity (CP) model is used to represent the single crystal response which is fitted using limited macroscopic data. Finally, the behavior is obtained by simulating the deformation of Representative Volume Elements (RVE) of the actual microstructure using an efficient FFT solver, which allows for the resolution of large synthetic RVEs, with complex and detailed microstructure, built from data obtained using EBSD. Furthermore, the effect of sample geometry (sample thickness) and surface roughness has also been considered in the simulations.

Regarding b) the proposed model is used to predict the quasi-static response of SLM-fabricated Hastelloy-X as a function of the SLM resulting microstructure (for different building directions) and also considering the effect of temperature and sample thickness. The CP model was fitted using the tensile response of one of the specimens considered. The temperature dependency was added into the CP model via the initial and saturation critical resolved shear stresses. The proposed framework correctly predicted (within error 4%) the Young's modulus and plastic stress-strain response of various specimens across a wide temperature range. The work demonstrates that the anisotropic mechanical response found in SLM parts can be entirely attributable to the polycrystalline microstructure.

With respect to the study of fatigue, the proposed CP-FFT framework is utilized to forecast the fatigue performance of SLM-fabricated Hastelloy-X at 750°C while taking into account the influence of the microstructures produced during the SLM process. A phenomenological CP model with a back stress term is utilized, and it is calibrated using inverse fitting to the experimental hysteresis curve of one experiment under

strain-controlled loading. The technique is based on extracting fatigue indicator parameters (FIP) from simulations, and different fatigue life prediction laws are utilized for both strain- and stress-controlled, which are based on cyclic and total dissipated work, respectively. The fatigue life is calculated for each case using the FIP distribution obtained from proposed power law which is calibrated using two fatigue experiments. For the different SLM microstructures and loading conditions considered, there is a very good agreement with the experimental data on fatigue life. Furthermore, the model can capture the effect of fabrication direction on anisotropic fatigue performance, highlighting the importance of microstructure on the fatigue performance of Hastelloy-X manufactured using SLM.

Finally, the fatigue model is extended to predict the fatigue life of flat samples as a function of microstructure and surface roughness. The surface roughness layer, which is generated based on the experimental mean surface roughness R_a, is added to the RVE that imposed by free boundary conditions. It is shown that including in the simulation free surface with roughness allows to accurately predict the fatigue life of flat un-machined specimens which is considerable lower than polished bulk specimens.

Acknowledgements

I would like to acknowledge my supervisor, Dr. Javier Segurado, for his excellent counsel, encouragement, and good guidance, as well as the faith he placed in me and giving me a chance to work with him. His assistance has been invaluable both academically and personally. This Ph.D. would not be possible without his support.

I’d want to thank all of the team members of the ’Multiscale Materials Modelling’ group, as well as all of the members of IMDEA materials, for maintaining the institute’s research atmosphere pleasant and joyful. I’d like to thank Venkata Sai, Maumita, Akshya, Wahaj, Shruti, Rodrigo, Mohib, Lucia, Mohammad and Venktesh for their friendship and encouragement over the last three and a half years. I’d like to thank Dr. Sergio Lucarini and Dr. Marco Magri in particular for being my mentors and friends in the early stages of my Ph.D.

Thank you to Dr. Ana Fernandez for all of her academic assistance and personal support, as well as Dr. Jon Molina and Dr. Iñaki Madariaga for the productive discussions on a variety of topics during the project.

I would also want to thank Dr. Alankar Alankar for putting me on the path of research and encouraging me to complete this Ph.D.

My family members Mr. Machhindra Pilgar, Manisha Pilgar, and Saurabh Pilgar, and my wife Pratiksha Pilgar, deserve special recognition for their emotional and personal support during this course.

Finally, I'd like to express my gratitude to ITP Aero, community of Madrid, and the Spanish Ministry of Science, Innovation, and Universities for their project "Entorno Virtual de Diseo y Fabricación de Turbinas Aeronáuticas (ENVIDIA)" - RTC-2017-6150-4.

Chandrashekhar Machhindra Pilgar

To the four cornerstones of my
family—my father, mother, brother,
and wife—for helping me blossom
into a more moral and wise person.
This thesis is also dedicated to all
people throughout the globe who have
been impacted directly or indirectly
by the COVID19 pandemic.

Contents

List of Figures

List of Tables

List of abbreviations

AM	Additive Manufacturing
SLM	Selective Laser Melting
SR	Surface Roughness
FFT	Fast Fourier Transform
EBSD	Electronic Backscatter Diffraction
SEM	Scanning Electron Microscope
PF	Pole Figure
FEM	Finite Elements Method
CP	Crystal Plasticity
RVE	Representative Volume Element
LCF	Low Cycle Fatigue
HCF	High Cycle Fatigue
LEFM	Linear Elastic Fracture Mechanics

BVP	Boundary Value Problem
FIP	Fatigue Indicator Parameter
SVE	Statistical Volume Element
CRSS	Critical Resolved Shear Stress
FCC	Face Centered Cubic

1 INTRODUCTION

1.1 Motivation

Additive manufacturing is an emerging technology to manufacture complex 3D objects by building consecutive layers on top of each previous layer. During the first years of AM development, these techniques were mainly used by designers and architects to create tiny, sophisticated designs and prototypes. However, in the last decade, additive manufacturing has emerged as a viable replacement for conventional subtractive manufacturing processes. Due to its benefits over traditional manufacturing methods, additive manufacturing (AM) was soon embraced in a variety of areas including biomedical, aerospace, military, architectural, sports, chemical, and infrastructure. These benefits include the ability to produce complicated geometries with extreme precision, design freedom, cost savings, and compatibility with a wide range of materials. Metals, polymers, composites, concrete, and ceramics are just a few of the materials that can be used in additive manufacturing. According to a HUBS report (HUB, 2021), the global market for 3D printing is expected to exceed 17.4 billion US dollars by 2022, with a CAGR of 21%. Figure 1.1 highlights the historical and projected market size of 3D printing as stated by nine standard market analytic industries. According to them, the average projection for 3D printing in 2026 is approximately 37.2 billion US dollars.

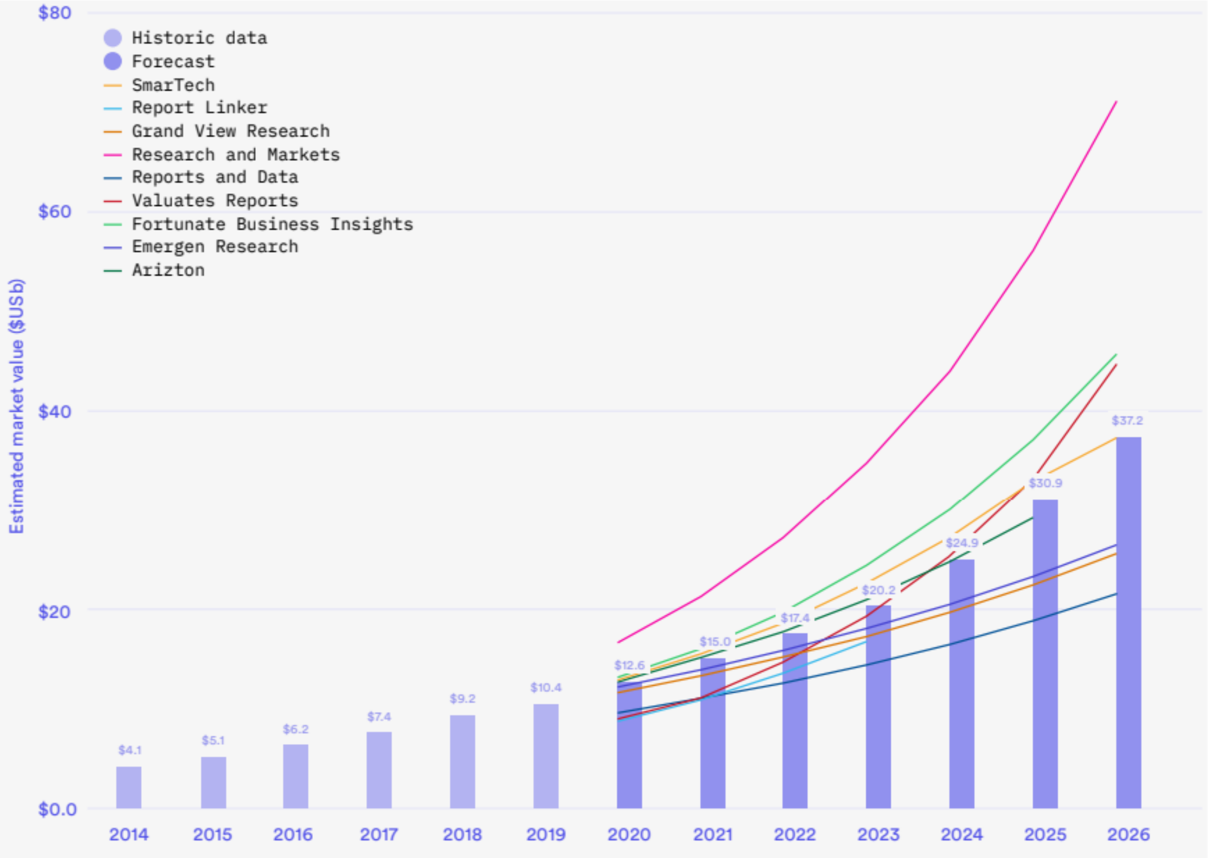

Figure 1.1: The histogram displays the upward trend in the exposure of the worldwide market to additive manufacturing and provides a forecast through 2026.HUB (2021)

AM is quickly being adopted in the metal manufacturing and research communities in the drive to make increasingly complex components with a high degree of flexibility, a low machining cost, and little material waste using tailor-made microstructures. AM has a high development potential, particularly in the defense, aerospace, and healthcare industries, where costly metals or alloys are used to create complicated geometries. Despite the fact that various AM processes for metals have been developed, selective laser melting (SLM) is the most widely used technology to date. SLM is a powder-based additive manufacturing technology in which the powder is evenly spread on a platform and a laser beam traverses a preset 2D route. The platform is lowered by the predetermined layer thickness after one laser beam passage. This technique is continued until the 3D structure is completed. SLM also allows for the customization of microstructures by modifying process parameters, laser energy, scanning method, build/sample geometries, and powder composition.

Metallic alloys such as stainless steel, titanium alloys, nickel alloys, manganese alloys, and cobalt-based alloys are some of the alloys which are being studied to fabricate parts using AM processes. In the case of aerospace industry, interest is specially focused on the SLM fabrication of nickel-based superalloys, because of their high mechanical strength at high temperatures (540-1000 °C). These alloys are resistant to oxidation, corrosion, and thermal fatigue, making them perfect for gas turbine and jet engine components such as turbine blades, nozzle vanes, etc. As a result, the AM fabricability and mechanical performance of alloys such as CM247LC, Hastelloy-X, IN625, Rene41, and Waspalloy is a very hot research topic in this industry. Figure 1.2 shows the pie chart for the various Ni-based superalloys studied for the aerospace application for selective laser melting until 2021 out of a total of 290 studies (Sanchez et al., 2021). It is apparent that members of the Inconel family, such as IN718, and IN625, are extensively examined, while other alloys are not thoroughly investigated, despite the fact that they are employed for specialized applications in the aerospace sector.

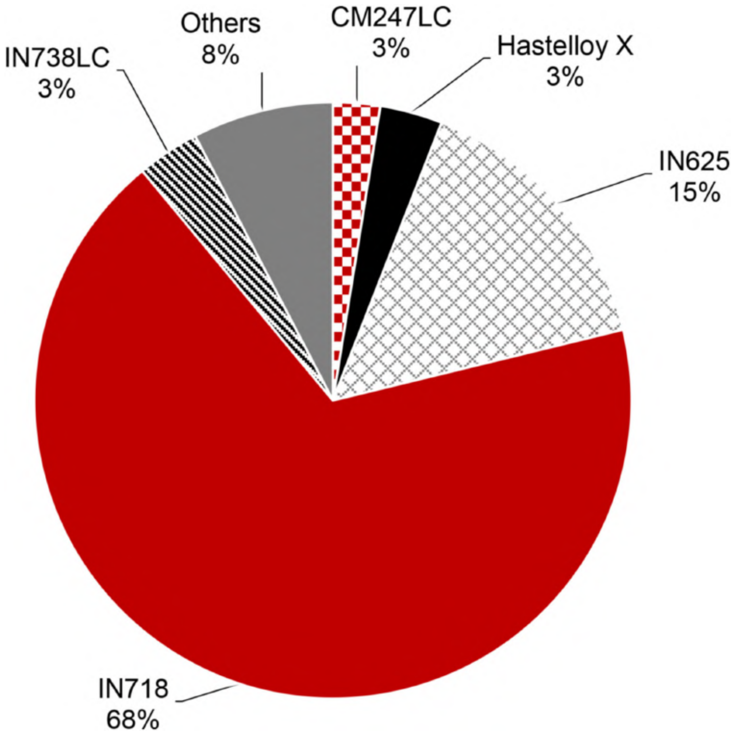

Figure 1.2: The pie chart depicts the various Ni-based superalloys researched for aerospace application for selective laser melting until 2021, out of a total of 290 studies (Sanchez et al., 2021).

An example of a superalloy with a great interest for the aerospace industry and which performance related to AM fabrication not yet been fully explored is Hastelloy-X, the material studied in this PhD thesis. Hastelloy-X is a nickel-based FCC superalloy strengthened by solid solution with the addition of Mo, Cr and W (M.A.Rowley and E.A.Thornton, 1996; Attallah et al., 2016). The alloy is extremely resistant to oxidation, corrosion, and grain coarsening (M.A.Rowley and E.A.Thornton, 1996; Sakthivel et al., 2012). Furthermore, despite the fact that Hastelloy-X does not contain precipitates, it retains most of its strength up to 1000 K as a result of the influence of the solute, making this alloy a good option for jet engine parts that operate at high temperatures. Moreover, the alloy has exceptional formability and weldability, making it a perfect option for additive manufacturing production, primarily through a selective laser melting (SLM) technique (Montero-Sistiaga et al., 2019b).

During the SLM process, the material experiences complex thermal cycles that induce large temperature gradients with very rapid cooling rates, generally in the range of 10^6 K / s (Yan et al., 2018; Zhonggang et al., 2020; Attallah et al., 2016; Tang et al., 2021; Sanchez et al., 2021; Yu et al., 2020b). Layer-wise addition, coupled with this rapid cooling, leads to the development of residual stresses, porosity and microstructural changes. As a result, the macroscopic response of SLM fabricated parts becomes strongly anisotropic (Montero-Sistiaga et al., 2019b; Yan et al., 2018; Barba Cancho et al., 2019; Tomus et al., 2013; Esmaeilzadeh et al., 2017; Etter et al., 2015) and vary greatly depending on the process parameters and part shape (Pei et al., 2019; Lewandowski and Seifi, 2016; Wilson-Heid et al., 2017; Kok et al., 2018). The origin of this process-dependent response is, on the one hand, at the macroscale with the development of residual stresses or solidification cracks (Kapoor et al., 2018; Attallah et al., 2016) and, on the other hand, at the microscale by changes at the subgrain level (e.g., accumulation of GNDs (Witzen et al., 2020; Wang et al., 2019), or changes in the cellular dislocation structure (Li et al., 2020)) or the development of a very characteristic polycrystalline microstructure in terms of grain shapes, sizes, and orientation distributions. Generally, SLM generates columnar grain structures (Attallah et al., 2016; Barba Cancho et al., 2019; Rodgers et al., 2017; Charmi et al., 2021; Azhari et al., 2022) with marked crystallographic orientation. In most studies of AM on cubic materials, the grains are elongated in the building direction and show a fiber texture of <100> which is the preferred growth direction for cubic crystals (Attallah et al., 2016; Niendorf et al., 2013; Riemer et al., 2014; Rodgers et al., 2017; Zhao et al., 2022; Yadroitsev et al., 2013).

Multiple experimental studies can be found with the objective of estimating the mechanical behavior as function of the processing parameters, which control the development of a particular microstructure. Special emphasis has been paid in the monotonic elasto-plastic response and fatigue performance due to their implications in the design of structural components. Han et al. (Han et al., 2020) reported that changing alloying elements could reduce the likelihood of hot cracking in Hastelloy-X, and many authors investigated the effects of processing parameters such as laser power (Esmaeilizadeh et al., 2021; Montero-Sistiaga et al., 2019b), scanning speed (Esmaeilizadeh et al., 2021), hatch distance (Yadroitsev et al., 2013), layer thickness and volumetric energy density(Wang et al., 2011) on static and fatigue performance in a variety of metallic alloys. As a summary, the most important fabrication parameters influencing mechanical performance are build orientation, specimen shape, and scanning method (Sanchez et al., 2021; Attallah et al., 2016; Zhonggang et al., 2020; Wang et al., 2011; Barba Cancho et al., 2019). In the particular case of fatigue performance, several studies (Edwards and Ramulu, 2014a; Gribbin et al., 2016; Leuders et al., 2013; Kanagarajah et al., 2013; Kirka et al., 2017; Johnson et al., 2017; Konecna et al., 2016; Li et al., 2020) have investigated the cyclic deformation and fatigue characteristics of SLMed components. Most of these investigations showed comparable results for a wide range of SLM alloys, including IN718 or Ti-6Al-4V (Agius et al., 2017; Lewandowski and Seifi, 2016), indicating that the SLMed component had lower fatigue performance compared to the wrought and cast components. The reduction in fatigue life can be more than an order of magnitude in some circumstances (Pei et al., 2019; Agius et al., 2017; Johnson et al., 2017). This worse fatigue performance of SLM components has been associated with porosity (Li et al., 2021), surface roughness (Konečná et al., 2016), or residual stresses(Yadollahi et al., 2017), as well as part anisotropy and orientation in relation to the direction of the cyclical load (Agius et al., 2017; Yadollahi et al., 2017). When loaded under stress control, vertically oriented specimens have a fatigue life shorter than that of horizontally oriented components. Some recent research that examines the fatigue analysis of AM Hastelloy-X can be found in the literature. Han et al. (Han et al., 2020) investigated the impact of hot isostatic pressing (HIP) on the fatigue life of AM Hastelloy-X and found that closing internal pores and reducing residual stresses can greatly increase the fatigue life. Esmaeilizadeh et al. (Esmaeilizadeh et al., 2021) investigated the fatigue life of AM Hastelloy-X as a function of the laser scanning speed at room temperature and determined that the fatigue lifetimes could be extended by optimizing the processing parameters.

The main limitation of a pure experimental approach, is the time and resources needed to establish a quantitative relationship between the process parameters, defects (e.g., surface roughness, porosity, residual stresses), and other influences (build orientation and heat treatments) on the microstructure and macroscopic mechanical performance. Due to this constraint, it is difficult to calibrate the mechanical performance of additive manufacturing parts, especially in the case of fatigue, where several experiments are required for each configuration.

For this reason, there is a high technological interest in developing models which account for both the interaction between the SLM process parameters and the microstructure (virtual processing) and the relationship between this microstructure and mechanical behavior (virtual testing). Moreover, the coupling of both strategies would allow to close the loop material-processing-properties and virtually estimate the performance of SLM fabricated parts. Regarding *process-microstructure* relationship, several studies can be found in the literature which apply different techniques to simulate microstructure evolution in SLM process. These techniques include statistics-based machine learning algorithms, the Monte Carlo Algorithm (Rodgers et al., 2017), cellular automata (Lopez-Botello et al., 2017; Rai et al., 2016; Elahi et al., 2022, 2023), and phase field models (Fallah et al., 2012; Acharya et al., 2017; Keller et al., 2013; Elahi et al., 2023). However, current simulations of SLM process still have limitations in accurately predicting the resulting 3D microstructures as function of the process conditions. The requirement for a large-fitting experimental data set for each alloy and the high computational costs are major challenges. Furthermore, even some characteristics of the polycrystalline microstructure can be predicted (Elahi et al., 2022) , very few models assess the formation of porosity, phase formation, and precipitation during microstructural evolution(Zhang et al., 2022). In the case of *microstructure-property* relationship, polycrystalline homogenization approaches (Segurado et al., 2018; Lebensohn and Tomé, 1993; Lebensohn et al., 2013; Lebensohn and Cazacu, 2012) have been widely used in the past decade to model the effect of polycrystalline microstructure (grain size, shape and orientation distributions) on the macroscopic response of metals. Polycrystalline homogenization is a complicated non-linear problem that is tackled using two different approximations, mean-field and full-field homogenization. Both mean field (Taylor, 1938; Lebensohn and Tomé, 1993; Sachs, 1928) and full field (Lebensohn, 2001; Segurado et al., 2018; Raabe et al., 2001; Bhattacharyya et al., 2001) approaches provide the effective macroscopic responses with relative accuracy. However, the simplification of the microstructure and the consideration of constant microfields over the grain in mean field approaches limit their use for fatigue and damage(Segurado et al., 2018). These limitations are overcome by full-field computational homogenization approaches which rely on simulating the deformation of a realistic synthetic representation of microstructure, representative volume element or RVE, resolving the local microfields such as stress and strain. In computational polycrystalline homogenization, the RVE comprises a statistical description of the size, shape, and orientation of the grains (Gitman et al., 2007; Terada et al., 2000; Segurado et al., 2018). The crystal plasticity (CP) model is used to represent the constitutive relationship of a single crystal (Peirce et al., 1983) and accounts for deformation by slip and twinning considering both isotropic and kinematic hardening. To solve the boundary problem in the polycrytalline RVE, the Finite Element Method (FEM) is the most common approach, leading to the commonly named CPFE models. Computational homogenization have been widely used to model the monotonic response of different polycrystalline superalloys fabricated using standard routes, including Inconel 718 (Cruzado et al., 2017), René 88DT (Soare et al., 2020), MD2 and CMSX-4 (Gupta and Bronkhorst, 2021; Bronkhorst et al., 2019), or generic FCC superalloys (Farooq et al., 2020). Polycrystalline computational homogenization techniques have also been applied for micromechanics-based fatigue in order to estimate the number of cycles for crack nucleation and enable statistical analysis of crack nucleation as a function of microstructure. These models rely on obtaining fatigue indicator(FIP) parameter from the polycrystalline simulations of the cyclic response which are further correlated with the number of cycles for crack nucleation. These micromechanics-based fatigue-life prediction models have been successfully applied to a wide range of alloys manufactured using typical fabrication processes, such as Ni-based wrought superalloys (Manonukul and Dunne, 2004; Cruzado et al., 2018; Shenoy et al., 2008).

Computational homogenization of polycrystals has been gradually introduced to study the effect of the particular microstructural features of SLM fabricated parts, such as surface roughness, residual stresses, porosity, and texture, on their mechanical performance. These simulation techniques have been applied to additively manufactured Ti alloys (Kapoor et al., 2018; Gorji et al., 2018; Barba Cancho et al., 2019; Azhari et al., 2022) , FCC metals (Liu et al., 2017; Ahmadi et al., 2016; Taheri Andani et al., 2018; Charmi et al., 2021; Muhammad et al., 2021; Bronkhorst et al., 2019) or several superalloys (Ghorbanpour et al., 2017, 2020; Prithivirajan and Sangid, 2018; GaoLe et al., 2020). Although CPFE is the most common approach for polycrystalline homogenization, developing geometrically conform meshes of polycrystals is a complex and expensive operation, becoming a limiting factor when tens of models are required for statistical purposes (Manonukul and Dunne, 2004; Cruzado et al., 2018). Alternatively, the use of FEM regular meshes allow automatization, but require very fine grids, which might result into computationally unaffordable models, specially when large-size RVEs are necessary to accommodate an accurate depiction of microstructural characteristics (Cruzado et al., 2017). Fast Fourier Transform (FFT)-based solvers have become very popular in the last two decades as an alternative to FEM for addressing full-field homogenization problems. These methods were initiated by the seminal work of Moulinec and Suquet (Moulinec and Suquet, 1994) in 1994 and present superior numerical performance with respect FEM (providing computing performance on the $O(n \log n)$ scale) preserving the accuracy of FEM approaches (Segurado et al., 2018; Roters et al., 2010; Lucarini and Segurado, 2018). These solvers are specially interesting for polycrystalline homogenization, due to the limited phase property contrast of a polycrystal which result in fast convergence (Lebensohn, 2001) and allow the resolution of large representative volume elements (RVEs) containing statistically representative microstructures with realistic grain shapes and orientation distributions (Segurado et al., 2018).

The application of polycrystalline homogenization to study the microstruture- behavior relation in SLM fabricated polycrystals is quite limited yet, and most works have been published the last 5 years. Regarding stress-strain behavior, some works have studied SLM superalloys such as Ti-6Al-4V(Azhari et al., 2022), AlSi10Mg(Kim et al., 2017), 316L-SS (Andani et al., 2018), IN718(Prithivirajan and Sangid, 2018), Hastelloy -X(Keshavarzkermani et al., 2019) etc., with fully periodic RVEs (Rodgers et al., 2020; Charmi et al., 2021; Liu et al., 2021) or plain strain with columnar grains (Ahmadi et al., 2016). These studies provided the effect of texture or grain morphology on the monotonic response, but neglect the strong effect that the thickness of the AM specimen has on the actual sample mechanical response (Yu et al., 2020a). Moreover, the use of CPFE limited the complexity of the RVEs used, not allowing to include the microstructure variations in the same model.

In the case of microstructure sensitive fatigue life prediction approaches for SLMed parts, the works available provide valuable information of the effect of the microstructure on the fatigue performance. Despite these interesting conclusions, these studies still present some limitations. In some cases real microstructures are not considered and simplified random textures are assumed (Cao et al., 2022; Ozturk and Rollett, 2017). In other cases, complex experimental microstructure information obtained by Electron Backsacatter Diffraction(EBSD) is directly included in the model (Ou et al., 2020; Eghtesad and Knezevic, 2021; Prithivirajan and Sangid, 2018; Ye et al., 2021), but studies are limited to a particular fatigue regime, either LCF (Eghtesad and Knezevic, 2021; Ou et al., 2020; Ye et al., 2021) or HCF (Zhang et al., 2022; Han et al., 2020), and a particular loading control, either strain or stress control.

When focusing the attention on models for the mechanical behavior SLMed Hastelloy -X very few works can be found up to date. In the case of monotonic response, the work by Lindstrom et.al. (Lindström et al., 2020; Lindström et al., 2020) develop a macroscopic elasto-plasticity which accurately considers the anisotropic response of the SLM samples. However, this approach is macroscopic and therefore does not allow to include directly the effect of variations in texture or grain sizes. Regarding cyclic response and fatigue performance, a model for the fatigue response of SLM Hastelloy-X was proposed by Esmaelizadeh et al.(Esmaeilizadeh et al., 2021, 2022). The model accurately reproduced the effect of laser scan speed on microstructure and surface roughness, as well as their influence on the S-N curve. Furthermore, by incorporating ratcheting phenomenon, these models captured the cyclic hardening/softening behaviour and accurately predicted the half-life hysteresis loops. Nevertheless, the fatigue model was empirical and fitted on the basis of the experimental data, so was not able to consider complex microstructural aspects such as texture or grain shape developed during SLM process.

In summary, most of the studies proposed to obtain the effect of the microstructures resulting from SLM process in the mechanical response present some of these limitations, (1) use of approximated and non-fully representative microstructures due to the cost of the CPFE framework, (2) limitation of the applicability to an specific regime such as monotonic response, LCF, HCF (3) do not consider the influence that the building direction, surface roughness, and sample thickness have on the performance of the SLM alloys.

In the particular case of additively manufactured Hastelloy-X, the only approaches published are macroscopic and do not explicitly consider the microstructure.

The objectives of this thesis are to overcome these shortcomings, as described in the following sections.

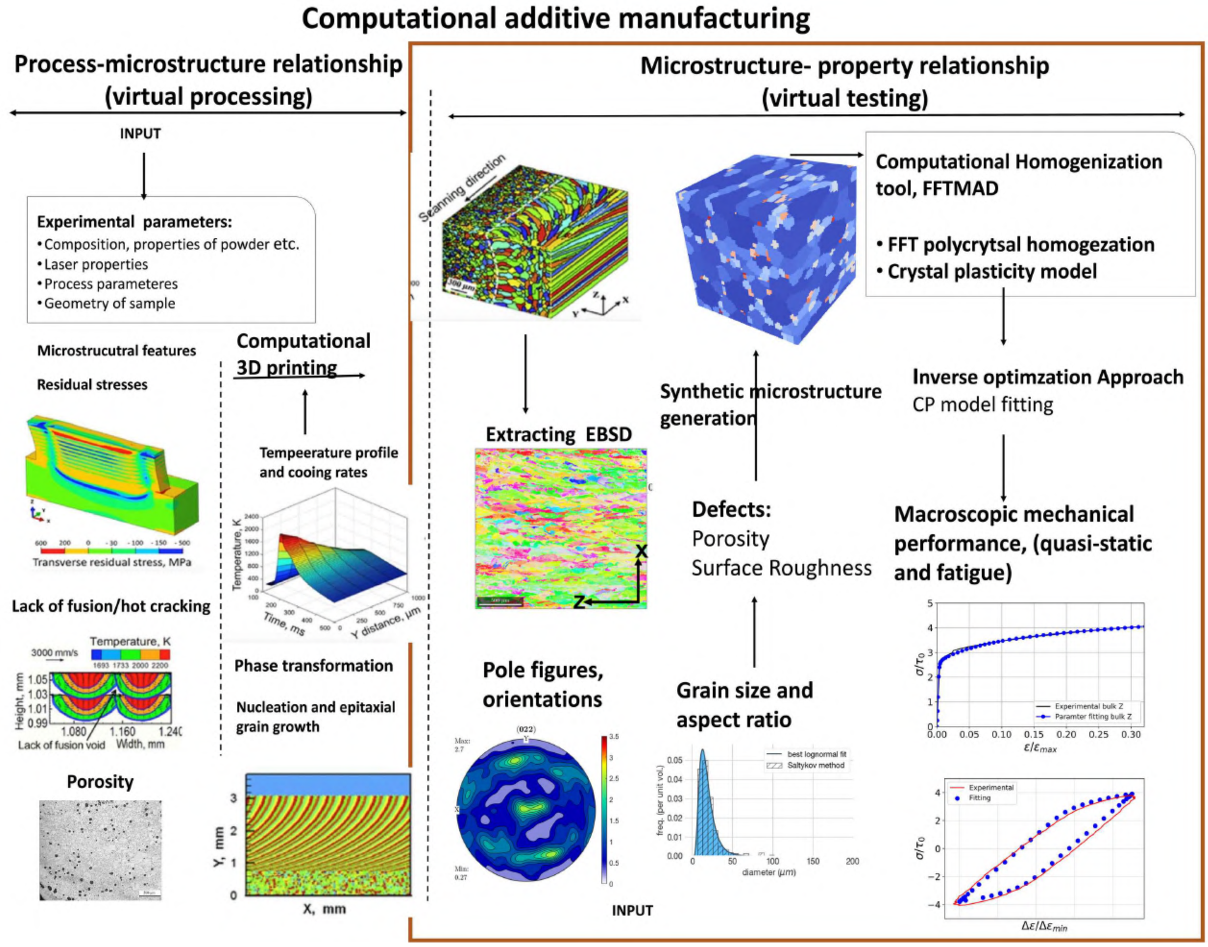

Figure 1.3: The graphical display of the computational framework for additive manufacturing while emphasizing the objective of the thesis (virtual testing).(Images of virtual processing section are taken from (Yan et al., 2018))

1.2 Objectives

The overall objective of this thesis is to provide a microstructure-sensitive virtual testing platform to predict the monotonic and fatigue response of the SLM Hastelloy-X superalloy (see figure 1.3). In addition to microstructure, the model will consider the geometry of the sample, the surface roughness, and the build direction. The thesis has three main objectives.

The **first objective** is **to develop and validate a computational model for the monotonic response Hastelloy-X fabricated using SLM** which considers both microstructure and temperature dependencies. The model will be based on Crystal Plasticity-Fast Fourier Transform (CP-FFT). The following sub-objectives are included in this study:

- Generation of statistically representative RVEs of the typical microstructures resulting from the SLM process, including grain size, aspect ratio and orientation distribution, as well as free external surfaces and porosity for thin samples.

- Development and implementation of a phenomenological crystal plasticity model accounting for the effect of temperature.
- Identification of the crystal plasticity parameters using the Levenberg-Marquardt algorithm with respect to experimental stress-strain curve for a single fabrication condition.
- Validate the computational tool by comparing the stress-strain curves in different directions predicted by model with experimental data for different thickness and fabrication conditions not used in the calibration of the model.

The second objective is to develop a robust **microstructure-sensitive fatigue life prediction model**, based on CP-FFT, of Hastelloy-X fabricated from SLM at elevated temperatures. The model should be valid for both strain- and stress-controlled loading. The following sub-objectives are included in this study:

- Calibration, using strain controlled experimental data, of a crystal plasticity model for cyclic elasto-plastic response including back-stress to predict of the hysteresis curve in general loading situations.
- Development of a new approach to predict fatigue life under stress-controlled loading while taking into account the elastic shakedown.
- Analysis, using the model developed, of the origin in the observed dependence of the fatigue performance with the SLM fabrication direction.

Finally, the microstructure-sensitive fatigue life prediction model is extended to **analyze the effect in the fatigue performance of the surface roughness** on Hastelloy-X flat specimen at elevated temperatures.

2 STATE OF THE ART

2.1 Additive Manufacturing

Additive manufacturing (3D printing) is defined as per ASTM as *'The process of joining materials to make objects from 3D model data, usually layer upon layer, as opposed to subtractive manufacturing methodologies, such as traditional machining (AST).'*

AM is a layerwise process to build a component. Fundamentally, AM can manufacture an object with any geometric complexity. The subtractive manufacturing techniques (cutting, grinding, milling) always have a constrained degree of freedom in manufacturing complex objects due to the need for different tools or tool palettes, jogs, and fixtures, difficulty to reach the cutter in invisible zones, and the possibility of collision. Other traditional techniques such as casting and forming also need patterns and tools which impose difficulties in manufacturing complex objects. In contrast, AM can manufacture complex geometries such as lattices, medical implants, and complex aerospace components without needing any further tooling(Shipley et al., 2018; Attallah et al., 2016; Yap et al., 2015). AM is a process of layer-wise manufacturing of an object. The final intended item is digitally scanned, cut and sent to the AM machine as a computer-generated CAD model. Finally, the part is created by layering the material and fusing it with the assistance of heat sources such as a laser. Based on the application, heat source, and materials, various AM techniques has been developed. A detail review on variety of AM processes and its applications can be found in Bhushan et al. (Bhushan B., 2017). Among the different AM techniques, selective laser melting (SLM) is probably the most common one for metallic alloys and has shown excellent ability to produce complex parts with minimal material waste.

2.1.1 Selective Laser Melting(SLM)

SLM (Selective Laser Melting) is a powder-based fusion method developed by Dr. M. Fockele and Dr. D.Schwarze in 1995 (Yap et al., 2015). It has since become the most widely used AM method for metallic components. SLM is a step-by-step procedure to produce a component. As in other AM techniques, the procedure begins with the creation of a CAD model and the transmission of the CAD data to the SLM machine in STL files, which then generates the CAD data in sections for the thickness of the individual layer. In the build chamber, a thin layer of powder is deposited on a substrate. A high-powered laser or electron is employed to melt the powder and fuse the material locally. The building platform is then lowered by a layer thickness. After one laser scan, a new layer of powder is placed on a substrate, and the laser scans the new layer again. This procedure is repeated until the last section is completed (Zhang et al., 2022; Chua and Leong, 2014; Yap et al., 2015). After the final laser scan, any loose or residual powder is removed and the completed part is recovered from the substrate either manually or with an electrical discharge machine (Shipley et al., 2018). Figure 2.1 shows the philosophy of the SLM process (Yap et al., 2015). The most recent research demonstrates that SLM can produce highly dense, almost net-shaped components without the need for post-processing procedures. However, to prevent oxidation, SLM requires an inert environment in a building chamber. Typically, the build chamber is filled with argon or nitrogen gas (Attallah et al., 2016).

2.1.2 SLM fabricated Nickel based superalloys

This section aims to review the studies about the microstructure and mechanical characteristics of nickel-based superalloys manufactured using SLM. Special attention will be paid to the research on Hastelloy-X, since this material will be the focus of this thesis. Some review papers about the applicability of SLM process on Ni-based superalloys have been published in the last years, and will be recalled in this chapter, including the papers by Attallah et al. (Attallah et al., 2016), Zhang et al.(Zhang et al., 2022), and Sanchez et al.(Sanchez et al., 2021).

Nickel-based superalloys are commonly utilized in high-temperature applications such as aircraft engine components, gas turbine blades, combustion chambers, and

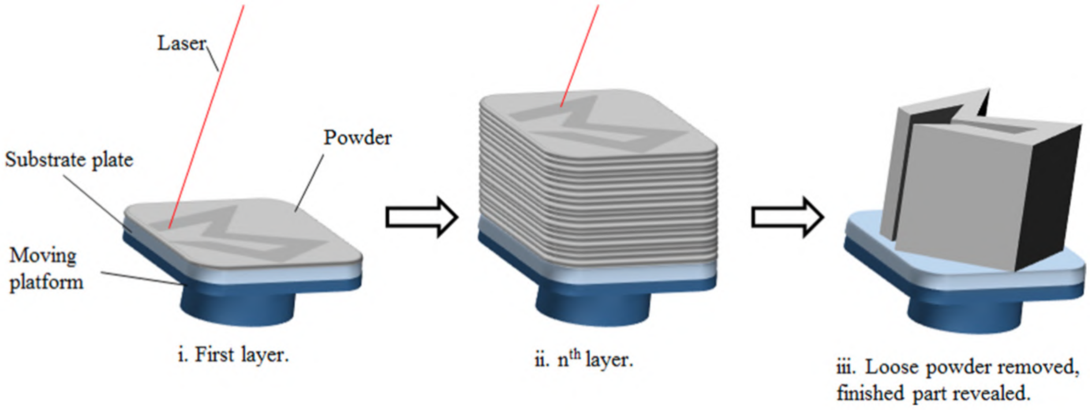

Figure 2.1: Shows the conceptual ideology of SLM process. (i) High power laser locally melts and fuses the metal powder layer on the substrate. (ii) Process is repeated till n^{th} layer (iii) The final part is recovered by removing loose powder (Yap et al., 2015).

many more because of their increased strength at elevated temperatures, good corrosion, fatigue, and wear resistance (Attallah et al., 2016; Sanchez et al., 2021). These alloys offer excellent mechanical (quasi-static, fatigue, and creep) and physical properties up to 1000 °C. In the aerospace sector, extremely complicated geometry components are required and Ni-based superalloys are difficult to manufacture using conventional manufacturing processes (Yap et al., 2017; Sanchez et al., 2021) due to poor workability, high machining costs, long lead times and segregation. SLM is capable of producing these complicated geometric components with minimal material waste. Weldable Ni-based superalloys such as Inconel 718 (Deng, 2018; Wang et al., 2012), Inconel 625 (Anam et al., 2013; Witkin et al., 2015; Lee et al., 2020), Hastelloy-X (Tomus et al., 2013, 2016; Montero-Sistiaga et al., 2019b,a; Wang et al., 2011), and Nimonic 263 (Vilaro et al., 2012) have been widely used for SLM. The research was also extended to investigate the use of SLM in poorer weldability alloys such as Inconel 100 (Bi et al., 2014), Inconel 939(Kanagarajah et al., 2013), Rene 142 (Murr et al., 2013), Inconel 738LC (Kunze et al., 2015; Geiger et al., 2016; Cloots et al., 2016), and MAR-M247(Divya et al., 2016; Muñoz-Moreno et al., 2016).

Ni-based superalloys

The chemistry of nickel-based superalloys is complex since several alloying elements are used while nickel remains the main component. These alloying elements allow these alloys to obtain the above-mentioned properties at high temperatures. Each element contributes significantly and specifically by affecting different crystallographic phases, which results in a wide range of mechanical behavior. Based on the alloying elements, Ni-based superalloys are classified into four types: commercially pure, solid-solution strengthened, precipitation strengthened, and other speciality alloys (Lippold et al., 2009; Reed, 2006). Figure 2.2 shows details on alloys made of nickel and their alloying elements. This section provides a brief overview of solid solution strengthened alloys. The review of other types of nickel-based alloys is beyond the scope of this thesis. However, interested readers are referred to the review published by Lippold et al.(Lippold et al., 2009)

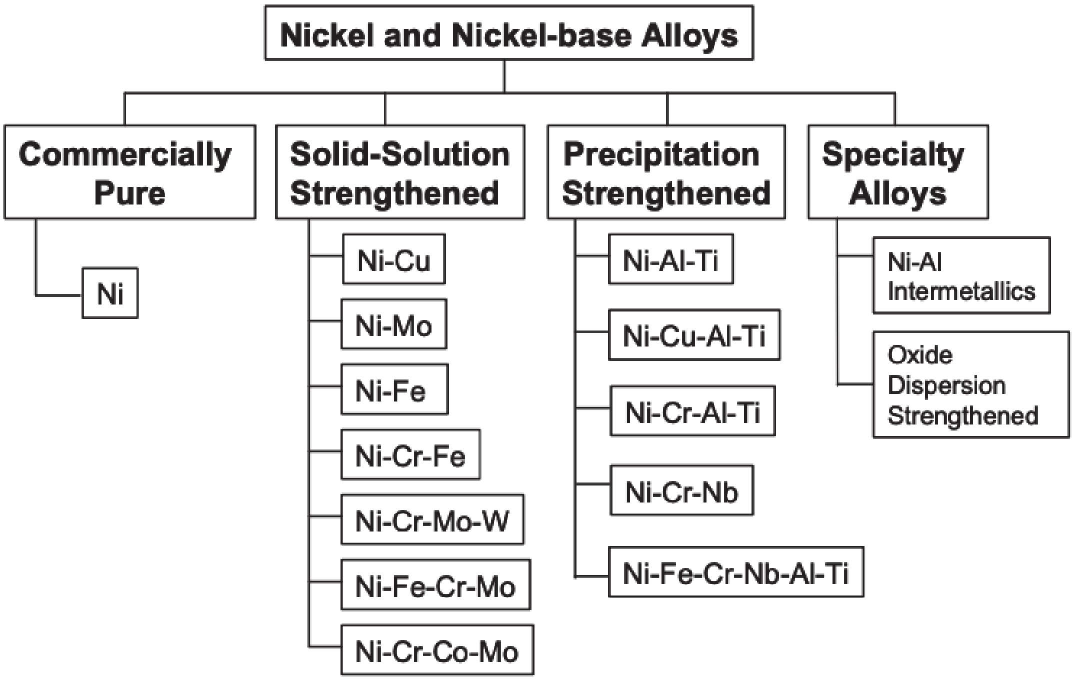

Figure 2.2: Classification of Ni-based superalloys based on the alloying elements. (Lippold et al., 2009)

Solid solution Ni-based alloys are generally formed by a single phase and the hardening mechanism is the reduction of mobility of dislocations due to the lattice friction. Although their strength do not reach the values of solid-solution alloys, they are thermally stable and have significant performance in corrosion. Nickel is significantly isomorphous with copper, making single-phase alloys containing both elements possible across a wide range of concentrations. These Ni-Cu alloys are corrosion resistant and so utilized in corrosive environments. They are highly weldable, however they require protective shielding or a regulated environment to reduce porosity problems. Ni-Fe alloys have also demonstrated reasonable weldability, but are best recognized for their lower coefficient of expansion (Lippold et al., 2009). Other elements, including chromium, tungsten, and molybdenum, form a strong solid solution strengthening alloy with nickel; nevertheless, it also affects weldability and mechanical properties.

Table 2.1: *Review of chemical composition Hastelloy-X used by multiple authors.*

Reference	Ni	Cr	Fe	Mo	Co	W	Mn	Si	C
(Wang et al., 2012)	Bal.	20.6	18.4	8.8	1.3	0.62	0.69	0.78	0.009
(Harrison et al., 2015)	Bal.	21.8	18.6	9.4	1.8	1.05	0.22	0.31	0.054
(Tomus et al., 2013)	Bal.	21.4	18.4	8.8	1.8	0.86	<0.01	0.11	0.01
(Montero-Sistiaga et al., 2019b)	Bal.	22.7	18.9	9	2.02	0.71	0.02	0.14	0.057
(Yin et al., 2021)	Bal.	21.9	18.6	9	2.0	0.8	—	0.5	0.03
(Marchese et al., 2018)	Bal.	21.7	18.6	9.2	1.8	0.9	—	0.36	0.056

Ni-based solid solution strengthened alloys have yield strengths of up to 480MPa and ultimate tensile strengths of up to 830MPa at room temperature. Inconel 625 (Anam et al., 2013; Witkin et al., 2015; Lee et al., 2020) and Hastelloy-X (Montero-Sistiaga et al., 2020; Tomus et al., 2013, 2016), the alloy studied in this thesis, are the most common Ni-based solid solution strengthened alloys.

2.2 SLM Hastelloy-X: fabrication and resulting microstructures

Hastelloy-X is a solid solution strengthening alloy that is strengthened with Mo, Cr, and W (M.A.Rowley and E.A.Thornton, 1996; Attallah et al., 2016) and is commonly used in gas turbine combustors, jet engine tailpipes, turbine blades, and nozzle vanes. The alloy has strong oxidation and corrosion resistance as well as good cold processing capabilities due to solute strengthening (Montero-Sistiaga et al., 2019b; Cheng et al., 2022b; Marchese et al., 2018; Zhang et al., 2022). Furthermore, Hastelloy-X has good creep and fatigue strength in high-temperature applications. Casting and forging have traditionally been used to make Hastelloy-X components. The biggest restriction, however, is excessive time-consuming manufacturing with difficulties producing complex shapes. Hastelloy-X is one of the Ni-based superalloys that exhibits good weldability and formability, making it the perfect alloy to create intricate parts using SLM.

Regarding its weldability, Hastelloy-X was clasiffied as a *readily weldable* alloy in the work of (Attallah et al., 2016), with similar response than IN625 or IN718. Nevertheless, although weldable, these alloys might present susceptibility to cracking during the SLM process (Montero-Sistiaga et al., 2019b).

Tomus et al.(Tomus et al., 2013) proposed that crack tendency can be minimized by reducing the percentage of alloying elements (Mn, Si, C) located near grain boundaries, which is a likely crack initiation site. Harrison et al.(Harrison et al., 2015) found that hot cracking problems occur owing to the alloy's weaker thermal shock resistance;

thus, they proposed that increasing solid solution strengthening components in the alloy can reduce 57% crack density.

2.2.1 Effect of process parameters

SLM is a complex process with numerous affecting parameters. Figure 2.3 depicts all possible parameters that influence the SLM process, from powder manufacture to final part fabrication. All these parameters have to be controlled in order to generate high-quality final parts.

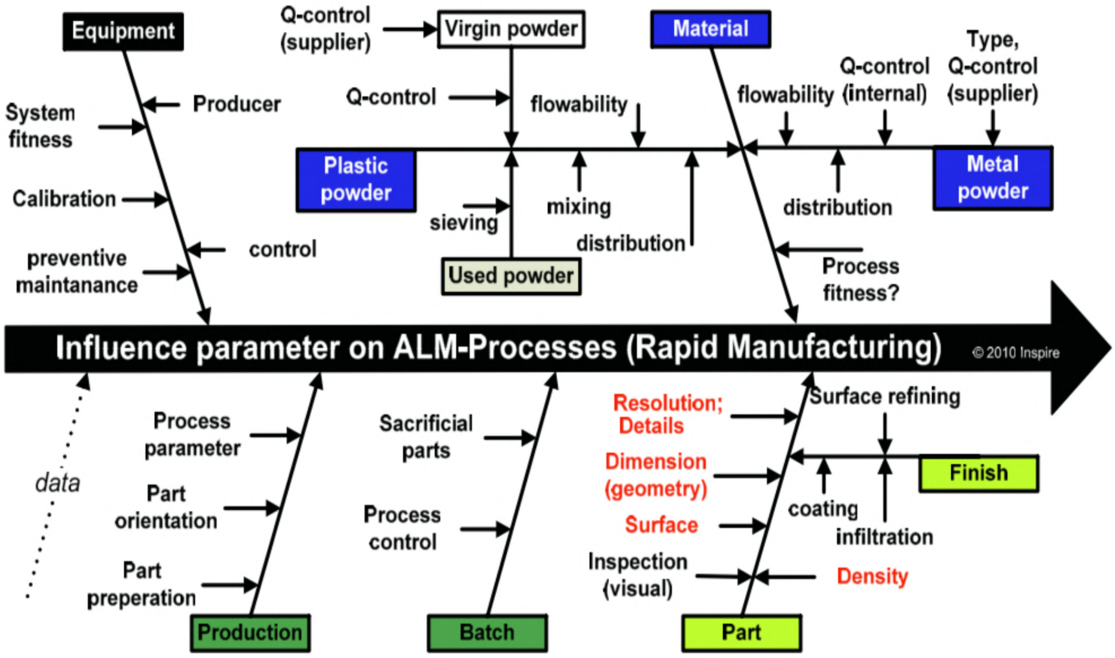

Figure **2.3:** Major factors that affect the selective laser melting(SLM) process. (AST)

The final qualities of the SLM part are strongly influenced by the **powder quality**. The powder is produced by gas or water atomization, rotary atomizer and plasma rotating electrode process (PERP), and might differ in size distribution, surface roughness, shape, and chemical composition. It has been shown that ensuring high-quality powder results in a highly dense component with good mechanical properties (Sutton et al., 2016; Tan et al., 2015).

Commercial Hastelloy-X powder is generally produced by argon-gas atomization which result in particle sizes ranging from 15-53μm (Tomus et al., 2013; Montero-Sistiaga et al., 2019b; Ni et al., 2019; Tomus et al., 2016), with an average particle size varied from 32-43 μm(Zhonggang et al., 2020; Ni et al., 2019; Tomus et al., 2013). SEM analysis of the powder exhibits a spherical particle shape with few satellites. Figure

2.4 depicts the SEM image, shows the size, spherical morphology, and small satellites in Hastelloy-X powder particles.

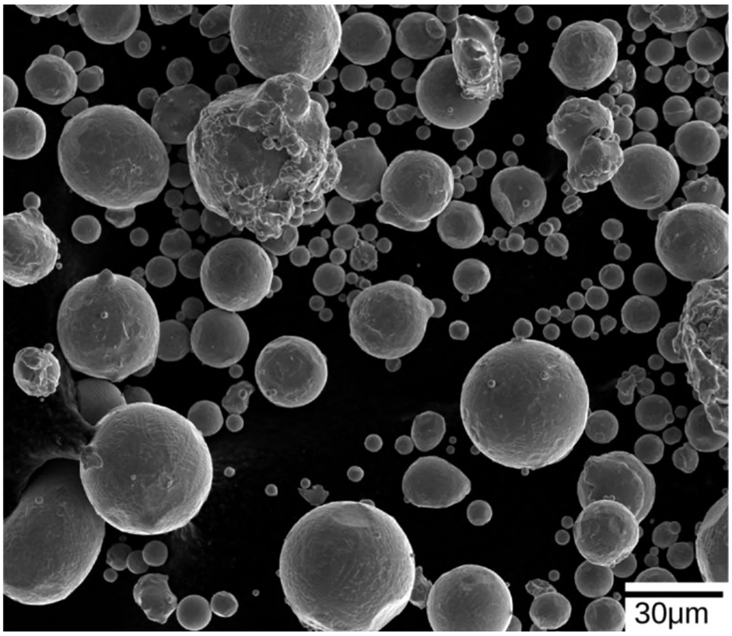

Figure 2.4: SEM image showing argon gas atomized pre-alloyed Hastelloy-X particle size and spherical morphology. (Tomus et al., 2013)

There is a strong effect of some **SLM process parameters** (laser speed, hatch distance, laser power, and layer thickness) on the final density of SLMed Hastelloy-X. Among them, several authors (Yin et al., 2021; Montero-Sistiaga et al., 2019b; Ni et al., 2019; Kasperovich et al., 2016; Xu et al., 2015; Qiu et al., 2015; Kang, 2019) have shown that the most influential parameters on final part density are laser speed and energy.

Laser energy has a strong effect on the resulting porosity (Carter et al., 2016; Montero-Sistiaga et al., 2019b), and many times a critical energy density is defined for a material in order to have a highly dense region (Carter et al., 2016). Moreover, an optimal window is many times needed since excess energy density will result in key-hole pores, and too little energy density will attract unmolten areas.

Montero-Sistiaga et al. (Montero-Sistiaga et al., 2019b) proposed a laser energy between (40-80 J/mm^3) window for Haselloy-X within which highly dense parts with a density of 99.3$\%$ could be achieved. Ni et al. (Ni et al., 2019) also reported a process window for fabrication Hastelloy-X that reached almost 99$\%$ relative density. The process window found in this case was between 140 and 170 J/mm^3.

Regarding **laser speed** also an optimal window can be defined for each material. If speed is too high for a constant laser power, the balling effect of molten powder is observed (Yadroitsev et al., 2007; Wang et al., 2011). The primary causes of this balling phenomenon, which causes Plateau-Rayleigh instability, are surface tension and increased melt viscosity due to a drop in temperature. At low scan speeds, there is more melt volume and a larger heat-affected zone, which involves more subsequent powder in the region of the melt track. This increase in melt volume and decrease in melt viscosity (at higher temperatures) causes the Marangoni effect (Mercelis and Kruth, 2006; Wang et al., 2011), which leads to an uneven build structure due to dominant melt hydrodynamics. Therefore, high power lasers and intermediate scan speeds can be used to produce highly dense parts with steady-state builds.

A relationship between laser power, scan speed, and final part density for Hastelloy-X was proposed by (Ni et al., 2019), and is graphically represented in the figure 2.5.

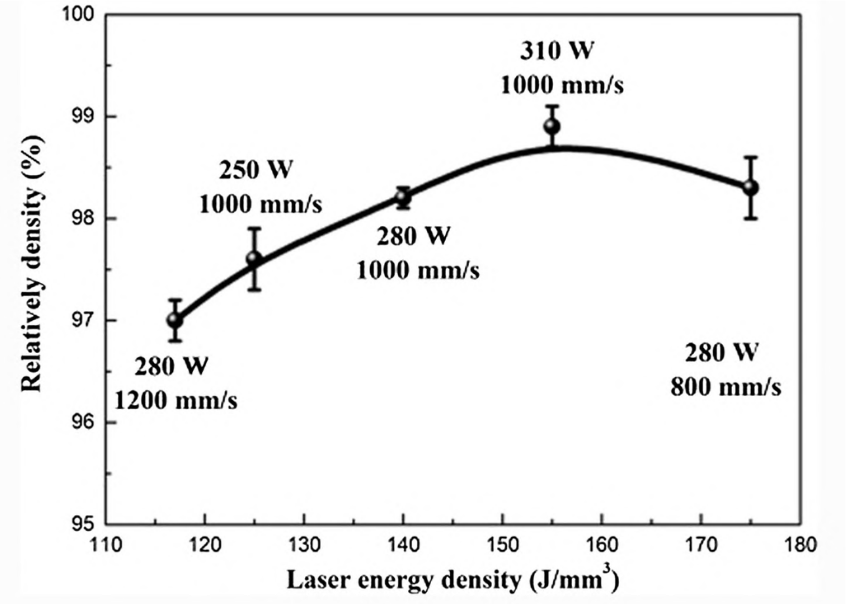

Figure 2.5: Relationship between the final part density and processing parameters(laser power, scan speed and, laser energy density). (Ni et al., 2019)

According to the current research on SLMed Hastelloy-X, processing parameters play a substantial effect on final part density and should be carefully optimised. In Hastelloy-X the established values for processing parameters including laser scan speed, laser power, and processing window (volumetric energy density) are 1000mm/s, 150-300W, and 145-165J/mm^3, respectively (Ni et al., 2019; Keshavarzkermani et al., 2019) With regards to other parameter with weaker influence, as the hatch distance,120μm has been proposed as an optimal hatch distance for Hastelloy-X as a compromise between geometry accuracy and fabrication time(Ni et al., 2019).

2.2.2 Microstructure of SLM fabricated Hastelloy-X

SLM is a multi-pass welding process which uses a highly focused energy beam to melt the deposited powder layer. SLM produces a unique microstructure due to its high cooling rates ($10^6 K/s$) and complex thermal history. This peculiar microstructure results in highly anisotropic mechanical response (quasi-static and fatigue) of the final part. Therefore, it is crucial to understand the solidification process which determines the resulting microstructure.

Grain Growth Mechanism in SLM

The performance of any polycrystalline material is determined by its microstructure. The grain growth mechanism is fundamental for the evolution of microstructure, especially for grain size, shape, and orientation(Wei et al., 2015).

For SLM fabricated metals and alloys, Zhang et al.(Zhang et al., 2019), Wei et al. (Wei et al., 2015), Oliveira et.al (Oliveira et al., 2020), and Sistiga et al. (Montero-Sistiaga et al., 2019b) have well documented the grain growth phenomenon, and some key highlights from these studies are documented here.

The SLM process is similar to welding in that grain growth is observed as a result of the localised rapid solidification process, which leads to epitaxial grain growth towards the centre of the melt pool (Zhang et al., 2019). The localised temperature gradient influences solidification. When the laser interacts with the deposited powder of material, a melt pool is formed. When the laser exits the melt pool, grain growth from partially melted grain from the previous layer leads to solidification. The temperature gradient, G_L, solid growth rate at the solid-liquid interface(travel velocity), R, and solute diffusion coefficient, D_L, control the grain morphology and substructure and it is well known that are strongly influenced by the SLM process parameters. Depending on theses parameters, solid-liquid interface can have a)planar, b)cellular, c)columnar dendritic, and d) equiaxed dendritic fronts.

The product, $G_L.R$, is characterized as the cooling rate, and this factor will determine the grain size (from fine to coarse). The ratio G_L/R, on the other hand, determines the grain morphology based on solidification, which encompasses grain morphologies such as planar, cellular, columnar, and equiaxed (Oliveira et al., 2020; Akbari and Kovacevic, 2019).

At the bottom of the melt pool, ($R \approx 0$) an infinite G_L/R ratio exist resulting in a planar grain structure. At low to moderate G_L/R ratios ($G_L/R < \Delta T/L$), the cellular structure is visible near the planar structure. Further lowering the G_L/R ratio results in the formation of a columnar dendritic structure(Oliveira et al., 2020; Zhang et al., 2019). The equiaxed dendritic structure is only seen near the surface of the melt pool, where the temperature gradient is relatively low. Figure 2.6 depicts the effect of thermal gradient and solidification rate on the type of microstructure produced.

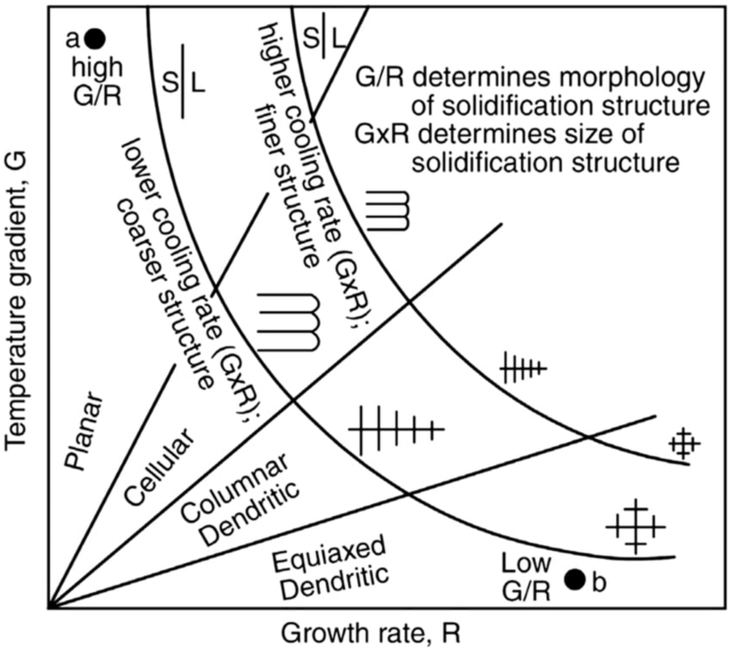

Figure 2.6: Variations in temperature gradient, G, and solid growth rate, R, result in a variety of microstructures. (Akbari and Kovacevic, 2019)

In the SLM process, the columnar grain structure is typical, resulting in a highly textured microstructure. The columnar grain growth direction becomes highly aligned with the thermal gradient direction as solidification progresses. As shown in figure 2.7, epitaxial grains have multiple orientations during the initial solidification phase. However, grains grow in a specific direction due to crystallographic effects being <100> direction an energetically preferred one for growth direction in face-centered cubic crystals (Oliveira et al., 2020). As a result, grains aligned in a direction similar to the thermal gradient grow faster than grains aligned in other crystallographic directions. Grains initially grow in other directions, but their growth is suppressed by the faster competitive growth of other grains.

When the degree of undercooling at the solidification interface exceeds the degree of undercooling for nucleation, the transition from columnar to equiaxed grains occurs (Yang et al., 2021). If the volume proportion of nucleated equiaxed grains is greater, the development of columnar grains is restricted. For fully equiaxed grain growth, the volume fraction of equiaxed grains should be more than 49% (Hunt, 1984). Furthermore, micro-segregation of solute atoms (observed in Ni-based superalloys), increased undercooling(Yang et al., 2021), added impurities, and different scanning strategies(Thijs et al., 2013) lead to the equiaxed grain structure due to the abundance of multi- orientation sites (Zhang et al., 2019; Oliveira et al., 2020).

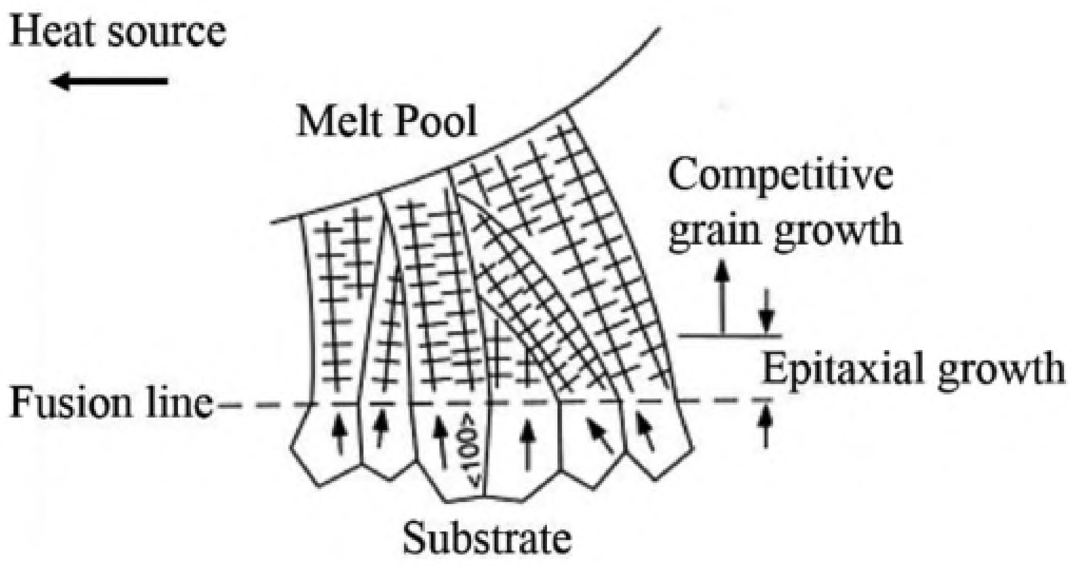

Figure 2.7: Grain growth in SLM, includes early epitaxial growth and following competitive growth (Zhang et al., 2019)

There are several numerical studies that characterize the resulting grain structure by simulating the solidification of the melt pool using either a phase field model or cellular automata (Acharya et al., 2017; Lopez-Botello et al., 2017; Rai et al., 2016; Fallah et al., 2012; Elahi et al., 2022, 2023; Cao and Choi, 2006). These investigations are capable of determining columnar or more equiaxed grain structures as a function of temperature gradient, which is obtained from process parameters via a macro-scale FE themal simulation. Furthermore, the microstructure and its grain orientation maps can be predicted by accounting for a variety of physical phenomena such as fluid flow, the Marangoni effect (Rai et al., 2016), and temperature dependent variables such as heat capacity, density, and thermal conductivity (Elahi et al., 2023). Figure 2.8 shows an example of cellular automation and phase field approach for the prediction of columnar microstructure, including grain orientation maps and melt pool.

Microstructural observations

This section reviews the microstructures observed in SLM-fabricated Hastelloy-X, both at the polycrystalline and subgrain levels, as well as typical microstructural defects and mitigating strategies. Sanchez et al. (Sanchez et al., 2021), and Zhang et al.(Zhang et al., 2019, 2022) provided a concise review of the effect of defects and process parameters on the SLM microstructure of SLM Hastelloy-X.

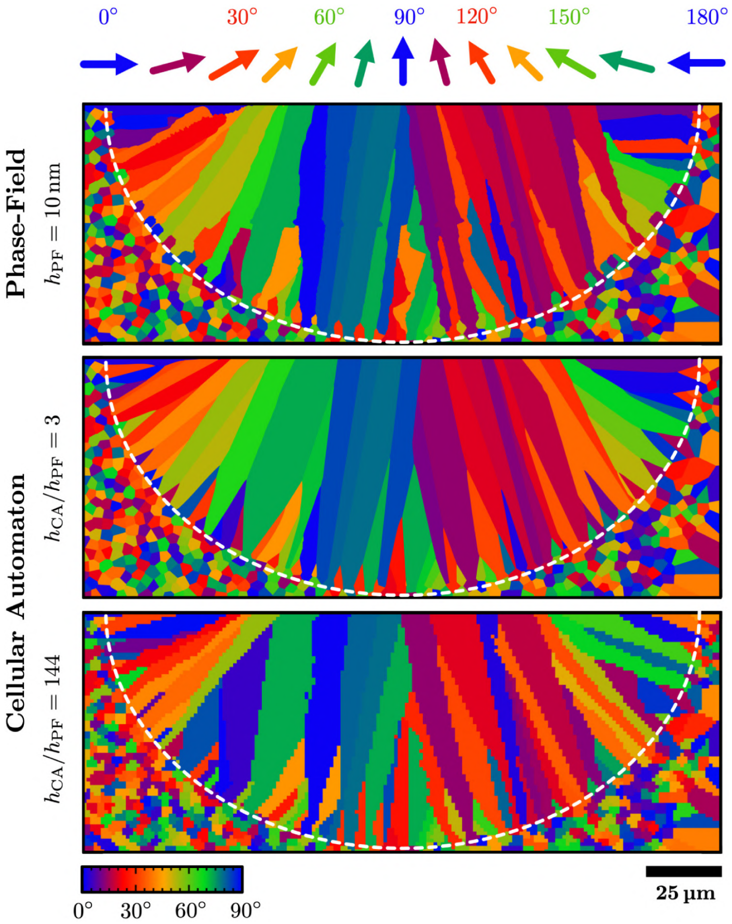

Figure 2.8: The numerical prediction of microstructure, melt pool and grain orientation maps obtained from phase-field(PF) and cellular automata(CA) simulations. (Elahi et al., 2023)

The microstructure generated in SLM-fabricated Hastelloy-X exhibits the typical SLM characteristics decribed in previous subsection, including fine grain size due to rapid thermal cycle, stacked molten pool, and epitaxial grain growth in the <100> direction leading to columnar grain structure (Tomus et al., 2013, 2016; Sanchez et al., 2021; Esmaeilizadeh et al., 2022). A graphical representation of this microstructure can be found in figure 2.9, where the Electron Backscatter Diffraction (EBSD) maps of SLM-fabricated Hastelloy-X in three perpendicular directions is represented (Esmaeilizadeh et al., 2022). The colours in the EBSD maps represent the orientation of build direction(BD) in relation to the crystal reference frame that follows the IPF triangle. According to the grain growth theory discussed in section 2.2.2, the EBSD scan reveals columnar grain structure along the build direction as a result of epitaxial grain growth and direction heat flow. Furthermore, as result of rapid cooling and epitaxial grain growth leads to columnar grains has been demonstrated by Keshavarzkermani et al.(Keshavarzkermani et al., 2019).

The consequence of having very different microstructures in different directions is a highly anisotropic mechanical behavior. As a result, understanding the *microstructure-property* relationship is critical when developing the final part, and is one of the main objectives of this work.

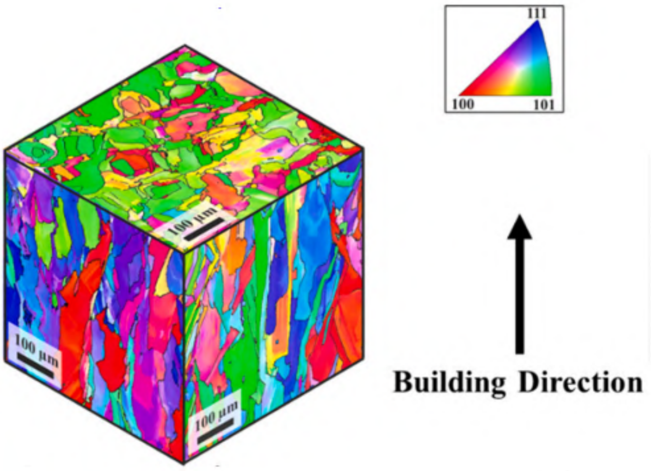

Figure 2.9: 3D representation of the microstructure of a bulk Hastelloy-X specimen manufactured by the SLM technique. (Esmaeilizadeh et al., 2022)

Post-processing heat treatments

Post-processing heat treatments are techniques for improving mechanical properties by removing residual stresses, which might eventually affect to the microstructure by inducing recrystalization or nucleation of metallic carbides.

Montero-Sistiaga et al.(Montero-Sistiaga et al., 2019b) confirmed that an increase in heat treatment temperature produced a decrease in the dislocation density was decreased. Regarding side effects of the heat treatment, Montero-Sistiaga et al.(Montero-Sistiaga et al., 2019b) found that for heat treatment conditions 800°C/2h the presence of molten pool boundaries but these boundaries vanished when the heat treatment temperature was elevated to 1177°C/2h. Furthermore, they found no difference in grain size and shape before and after heat treatment, implying that no recrystallization occurs in the microstructure. Moreover, identical to the as-built condition, the texture was aligned to the <100> crystallgraphic axis following heat treatment.

More recently, Cheng et al.(Cheng et al., 2022b) used the low angle and high angle grain boundary ratio in the grain boundary map to assess the decrease in dislocation density, closely related with residual stresses, with an increase in heat treatment temperature.

The ratio of high angle grain boundaries (HAGB) to low angle grain boundaries (LAGB) varies for the as-built, 1050°C/2h(HT1), and 1150°C/2h(HT2) conditions, as shown in figure 2.10. Low angle grain boundaries, or LAGBs, are the subgrain boundaries that result from the dislocation rearrangement that is seen within the grains. The high angle grain boundaries(HAGBs) have a misorientation angle greater than 15°. Figure 2.10 demonstrates that the proportion of LAGB greatly decreased at HT1 in comparison to the AB condition, and that it drastically decreased at HT2 condition, with HAGB constituting the predominant grain boundaries. In contrast to Montero-Sistiaga et al.(Montero-Sistiaga et al., 2019b), Chen et al.(Cheng et al., 2022b) show that grain recrystallization is responsible for the decrease in dislocation density with an increase in heat treatment temperature.

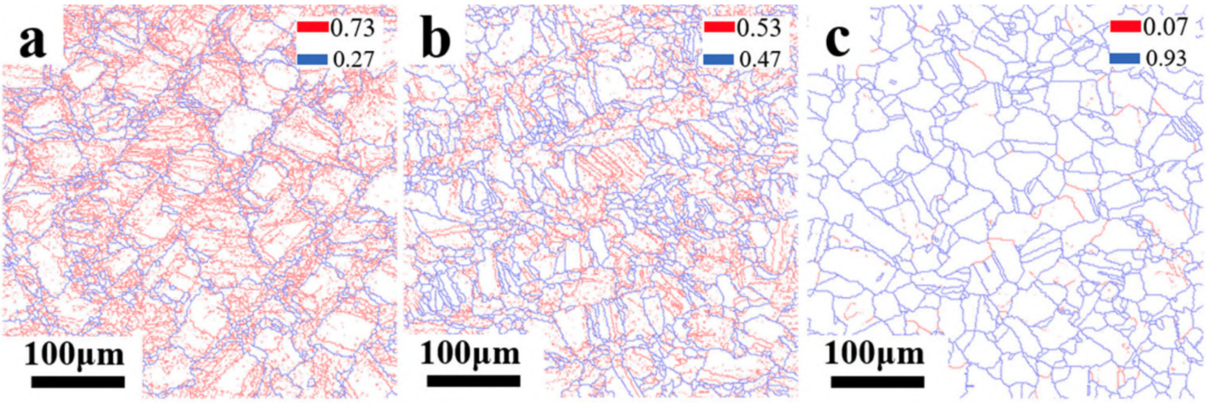

Figure 2.10: The micrograph shows the variation in the ratio of high angle grain boundaries(HAGB) and low angle grain boundaries(LAGB) for a)as built, b)HT1, and c)HT2 conditions. (Cheng et al., 2022b)

Finally, regarding metal carbides (MC), it is well known that the mechanical response of metallic alloys might be significantly influenced by their presence in case they are formed at higher temperatures (Zhang et al., 2022). The results are contradictory in this case. TEM analysis in (Cheng et al., 2022b) reveals precipitation of metal carbides (Mo-rich M_6C, Cr-rich $M_{23}C$), and a needle-shaped Mo-rich μ phase in intergranular and intragranular regions, as shown in Figure 2.11(a-d). On the contrary, Tomus et al.(Tomus et al., 2016) did not report any MC after HT treatment and provided a justification that too little carbon in the alloy reduced MC formation. Therefore, the origin of variation in the formation of metal carbides in Hastelloy-X is dependent on the heat treatment temperature and the amount of carbon in the powder.

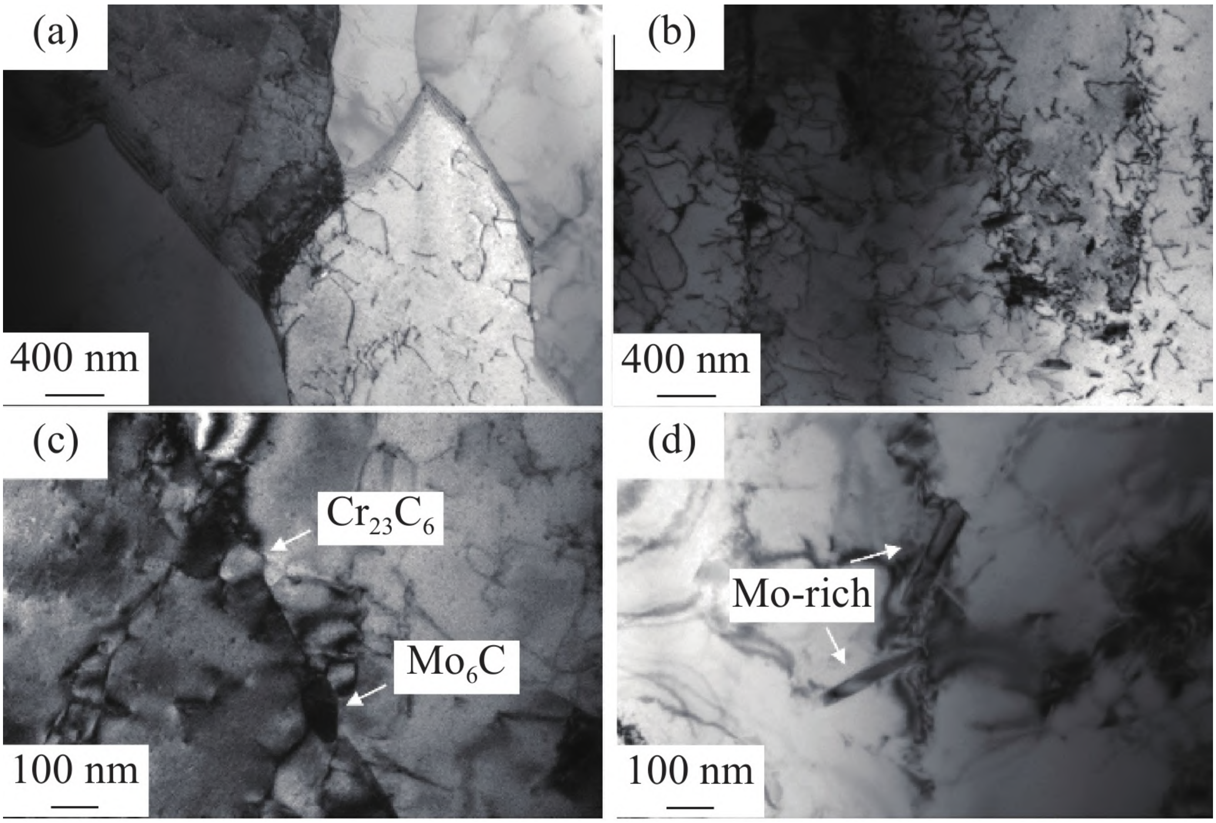

Figure 2.11: TThe micrograph shows the variation in the ratio of high angle grain boundaries(HAGB) and low angle grain boundaries(LAGB) for a)as built, b)HT1, and c)HT2 conditions. (Zhang et al., 2022)

Grain morphology and crystallographic texture

Most virtual testing frameworks use microstructure as input data, hence it is critical to define microstructural characteristics such as grain size, shape, twinning, orientation, and so on beforehand.

The grain shape and texture of polycrystalline materials are often represented using the electron backscatter diffraction(EBSD) technique. The colours on the EBSD map represent the orientation of the building direction in relation to the crystal reference frame, which follows the IPF triangle. The size and shape of individual grains, the overall texture of alloys, the presence and orientation of specific crystal structures, and crystallographic interactions between phases can all be measured with EBSD. Figure 2.12a, b depicts the EBSD maps of the longitudinal and transverse sections of as-built nickel-based superalloy (Divya et al., 2016). The EBSD maps show epitaxial grain growth in the build direction (Z), with grains that are heavily orientated in the <001> direction. Furthermore, in longitudinal section, the grain shapes exhibit strongly columnar structure, whereas in transverse section, the grain shapes exhibit bimodal(Divya et al., 2016) or equiaxed(Sanchez et al., 2021; Cheng et al., 2022b) structure. The grain morphologies measured in terms of ferret length in the longitudinal and transverse sections ranged from 100-200 μm and 40-50 μm, respectively(Divya et al., 2016). Importantly, this highlights the source of anisotropic mechanical response in AM specimen.

The Grain boundary misorientation information obtained from EBSD plots is defined as the difference in the crystallographic orientation (Euler, Rodriguez, etc.) of neighboring grains in the polycrystal. The wider the distribution of misorientation angles, the less likely that no preferential growth direction leads to the production of equiaxed grain structure(Gribbin et al., 2016; Sanchez et al., 2021), and the skewer the misorientation angle histogram, the more likely that directional grain growth leads to columnar grain structure(Divya et al., 2016; Zhang et al., 2022). Figure 2.12e, f depicts grain boundary misorientation histograms with lognormal distribution peak frequencies of 0.90 and 0.81 for longitudinal and transverse sections, respectively.

A pole figure is a graphical representation of object(in this case, polycrystals) orientation in space that shows the orientation of a chosen plane normal (a pole) with respect to the sample reference frame. Pole figures are commonly used to investigate the anisotropy of a sample. Figure 2.12 depicts the <001> pole figure from EBSD data for longitudinal and transverse sections. The presence of high intensity at the centre of the pole(in this case, <001>) is very prevalent in SLM microstructures, emphasising the strong anisotropy.

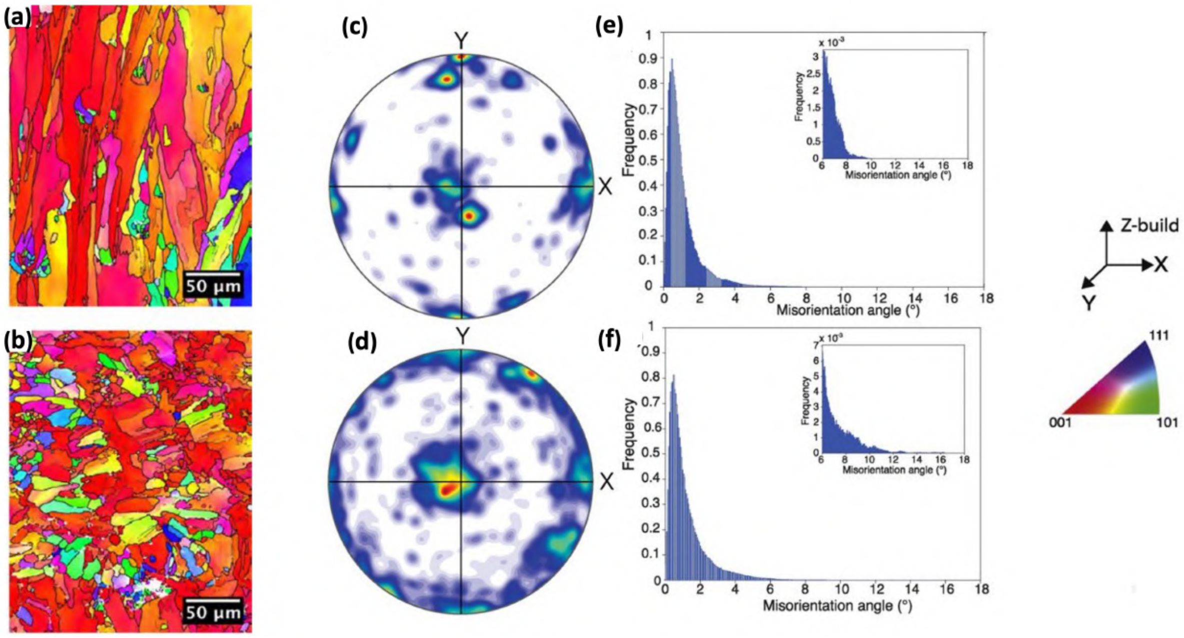

Figure 2.12: The EBSD maps(a,b), pole figures(c,d), and grain boundary misorientation histograms(e,f) for longitudinal (top) and transverse (bottom) sections of as-built samples. (Divya et al., 2016)

2.3 Mechanical performance of SLM Hastelloy-X

Before the industry can safely use the final part in specific applications, it is crucial to characterise and understand the performance of Hastelloy-X manufactured using SLM. Sanchez et al.(Sanchez et al., 2021) and Lwondaski et al. (Lewandowski and Seifi, 2016) provided a thorough evaluation of the mechanical properties of SLM-fabricated Ni-based superalloys. Understanding static and dynamic mechanical performance is essential from a design perspective for Hastelloy-X because it often functions in a moderate to high temperature range. Because research has advanced significantly in predicting the alloy's tensile and fatigue performance, this section reviews the quasi-static and fatigue performance of SLM manufactured Hastelloy-X while accounting for variable heat treatment(HT) conditions, process parameters, build orientation, and temperature.

2.3.1 Quasi-static performance of SLM Hastelloy-X

Tensile testing is the most frequent mechanical test, revealing the stress-strain relationship, elastic modulus, yield strength, ultimate tensile strength, toughness, and ductility of the material.

Strength and ductility

Ni et al. (Ni et al., 2019) investigated the effect of laser power and scan speed on the uniaxial tensile performance of SLMed as-built Hastelloy-X at room temperature. Furthermore, they examined the uniaxial tensile response of wrought and SLMed Hastelloy-X and determined that by selecting the suitable process parameters (see section 2.2), the SLM technique could create parts with higher yield stress than wrought samples. As illustrated in figure 2.13, Ni et al.(Ni et al., 2019) demonstrated that higher laser power and lower laser speed produce the maximum yield strength when compared to other processing parameters. Furthermore, the increased laser power and lower laser speed improved ultimate tensile stress (UTS) and ductility. The as-built Hastelloy-X has a high dislocation density and is less plastic (around 70 %) than its wrought counterpart. Zhonggang et al.(Zhonggang et al., 2020) also observed the increase of yield stress and loss off ductility of SLMed Hastelloy-X compared with the wrought alloy due to the higher dislocation density and finer grain sizes. Furthermore, Ni et al.(Ni et al., 2019) and Montero-Sistiaga et al.(Montero-Sistiaga et al., 2019b) shown that extremely high laser power results in lower cooling rates, resulting in larger grain size. Therefore, mechanical characteristics are degraded due to the coarsened microstructure.

In addition to the effect of dislocation densities and grain sizes in the yield and ductility, Zhonggang et al.(Zhonggang et al., 2020) discovered a considerable number of M_6C carbides, which aids in dispersion strengthening and yield strength. However, the metal carbides(MC) acts as a stress concentration site and is prone to cracking as a result of internal stresses, resulting in decreased sample ductility. Internal stresses are relieved as a result of HT, and few carbides are dissolved, increasing ductility but decreasing yield strength.

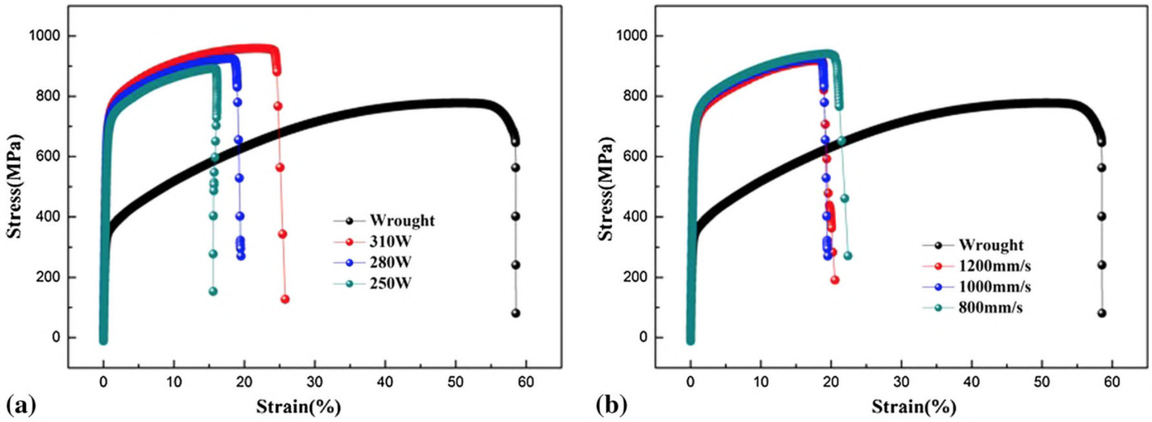

Figure 2.13: The stress-strain curve for the uniaxial tensile test was performed at room temperature for different heat treatment temperatures. Ni et al. (2019)

Thermal treatments, in addition to reduce the residual stresses, can be used to improve the ductility of SLM Hastelloy-X at the expense of the yield strength of the specimen. According to Zhonggang et al. (Zhonggang et al., 2020), for heat treatments over 1100°C, the MC progressively decomposes and the microstructure exhibits an increase in grain size. Furthermore, the grains precipitated formed grain boundaries. As a result, for treatments over 1200°C, the specimen exhibits decreased strength and more elongation. Cheng et al.(Cheng et al., 2022b) found a similar mechanical response; however, they claimed that the twin boundaries occurred due to grain recrystallization at higher temperatures, which enhances the ductility of the sample.

Strength anistropy

As stated before, anistropy is a characteristic of the SLMed Hastelloy-X parts. A factor that has a strong impact on anisotropy and mechanical performance is the build direction. Montero-Sistiga et al. (Montero-Sistiaga et al., 2019b) investigated the effect of built orientation on horizontal and vertically oriented samples at various HT conditions (1117 and 800°C) and test temperatures (RT, 650°C, 750°C, and 850°C). Figure 2.14 depicts the yield strength, ultimate tensile strength, and tensile elongation for quasi-static tests done at various HTs and temperatures. The horizontal sample had a higher yield stress and ultimate tensile stress than the vertical sample under all conditions. Mechanical anisotropy associated with build orientation is related to the number of grain boundaries perpendicular to the loading direction and the percentage of grain boundary carbides(Montero-Sistiaga et al., 2019b; Cheng et al., 2022a). In comparison to its vertical counterpart, the horizontal specimen exhibits less ductility. However, as testing temperatures increases, the anisotropy between vertical and horizontal samples decreases significantly.

Furthermore, Tomus et al.(Tomus et al., 2016) demonstrated that vertically oriented samples (30%) had higher ductility than horizontal samples (9 %). However, the anisotropy reduced when HT and hot isostatic pressing (HIP) were used. They justified the anisotropic response is due to porosity in horizontal (greater porosity) and vertical (lower porosity) oriented samples, as well as columnar grains oriented in the build direction.

Effect of temperature

Montero-Sistiaga et al.(Montero-Sistiaga et al., 2020) investigated the effect of temperature on the quasi-static response of SLM Hastelloy-X, as illustrated in figure 2.14.

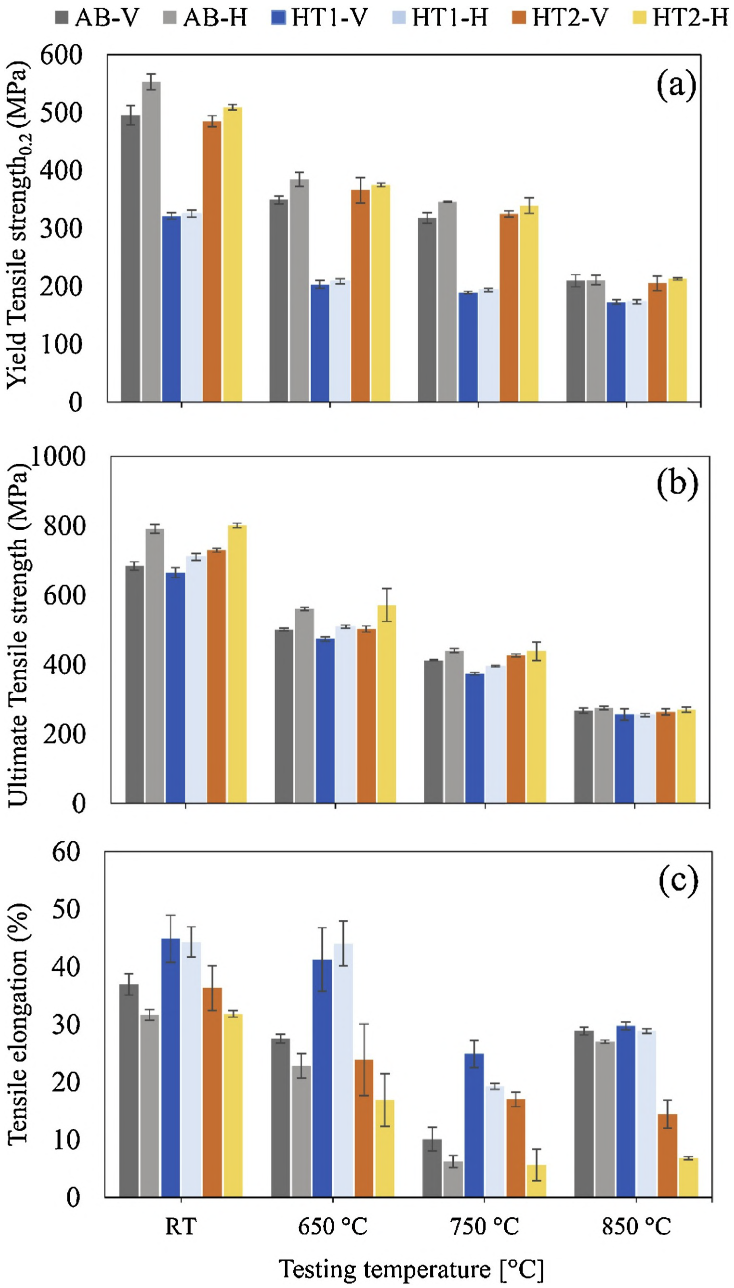

Figure 2.14: The comparative analysis of YTS, UTS, and elongation between horizontal and vertical built specimens for as-built, HT1, and HT2 conditions, was tested at different temperatures (RT, 650°C, 750°C, and 850°C). (Montero-Sistiaga et al., 2020)

Contrary to many precipitate based superalloys, in Hastelloy-X, the yield stress decreases monotonically as the test temperature rises. This decrease happens for temperatures below 850°C, temperature range in which no important microstructural changes are observed in terms of grain sizes and dislocation content.

Nevertheless, temperature enhance the presence of carbides. As a result, the elongation of SLMed Hastelloy-X specimens is gradually reduced to 750°C. Tomus et al.(Tomus et al., 2013), Zhang et al. (Zhang et al., 2022), and Montero-Sistiaga et al.(Montero-Sistiaga et al., 2019b, 2020) found carbide precipitates near grain boundaries. The formation of voids at grain boundaries has also been observed at 750°C, which explains why tensile elongation decreases at higher temperatures.

2.3.2 Fatigue performance of SLM Hastelloy-X

Fatigue is a progressive loss of material strength under repeated, cyclic loading. In general, the fatigue process is divided into crack initiation (crack nucleation) and crack propagation (growth of the crack to the final fracture). The fatigue performance of SLM-fabricated alloys is affected by porosity, process parameters, surface roughness, component orientation, and heat treatment conditions. The fatigue performance of SLM-fabricated alloys is poorer to that of forged alloys due to revved damage caused by process defects, as demonstrated in figure 2.15 for SLMed IN718.

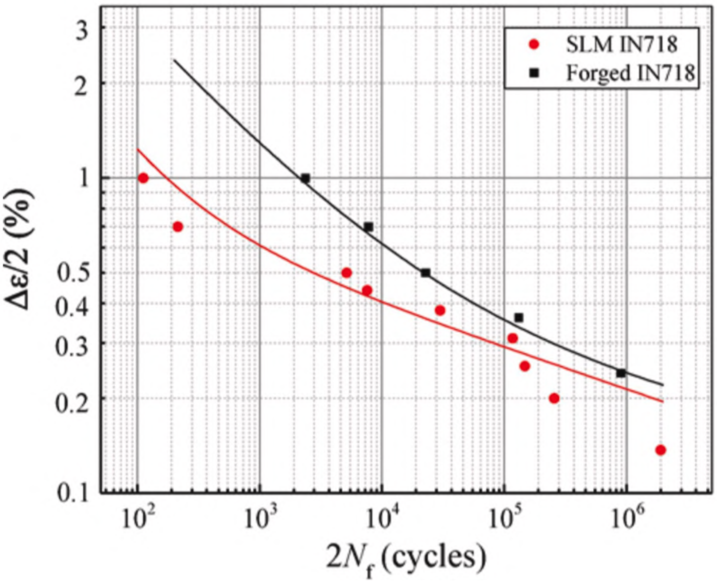

Figure 2.15: Comparison between strain controlled fatigue lives of conventional and SLM fabricated Inconel 718. Sanchez et al. (2021)

Esmaeilizadeh et al.(Esmaeilizadeh et al., 2021) recently investigated the impact of laser scan speed on the stress-controlled fatigue performance of SLM Hastelloy-X at room temperature. The hysteresis loops exhibited shakedown and ratcheting behaviour at both laser scan speeds (850mm/s (L-LSS) and 1150mm/s (H-LSS)). Figure 2.16 depicts S-N curves for two scan speeds. Lower laser scan speeds (L-LSS) provide better performance at higher cyclic stresses (LCF regime), whereas higher laser scan speeds (H-LSS) provide improved fatigue life at lower cyclic stresses (HCF regime). Although the materials have equal porosity at both laser scan speeds, L-LSS has lower surface valleys (Rv = 30.4μm) and coarse grain structure than H-LSS, which has larger surface valleys (Rv = 55.5μm) and fine grain structure.

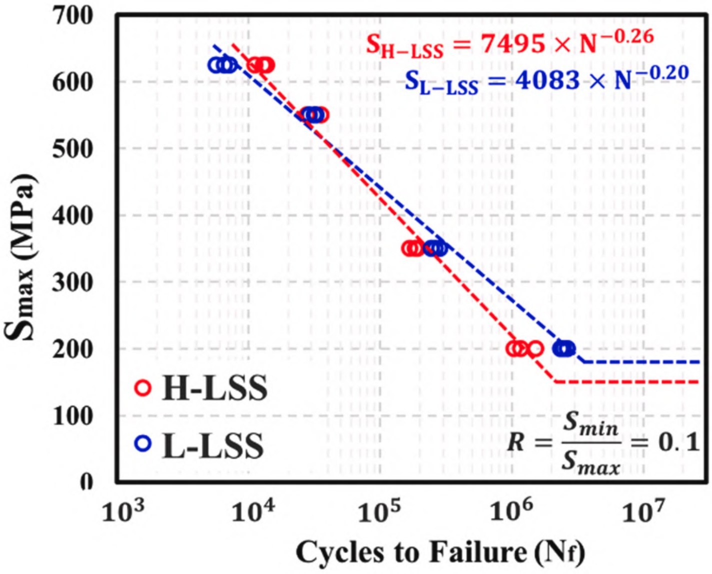

Figure 2.16: Effect of fatigue performance (as measured by S-N curves) at two distinct laser scan speeds, higher (in red) and lower (in blue). (Esmaeilizadeh et al., 2021)

As a result, in HCF, surface roughness effects dominate life, whereas in LCF, microstructure and grain sizes dominate life. Furthermore, process parameters can be tailored to provide superior fatigue performance in either the LCF or HCF regimes (Esmaeilizadeh et al., 2021; Keshavarzkermani et al., 2019; Shipley et al., 2018).

Wang et al. (Wang et al., 2011) emphasised the importance of part orientation in SLMed Hastelloy-X fatigue life under as-built and HIP conditions. They reported that the orientation of the part has no effect on fatigue life at low applied stress levels; nevertheless, at higher loads, the fatigue resistance of the vertically oriented specimen is lower to that of its horizontally oriented counterpart as illustrated in figure 2.17. In as-built conditions, Montero-Sistiga et al. (Montero-Sistiaga et al., 2019a) found that horizontally built samples outperformed vertical samples. Lindstrom et al. (Lindström et al., 2020) showed that the horizontally oriented specimen had greater plastic deformation than the vertically oriented specimen, which is advantageous for higher fatigue resistance.

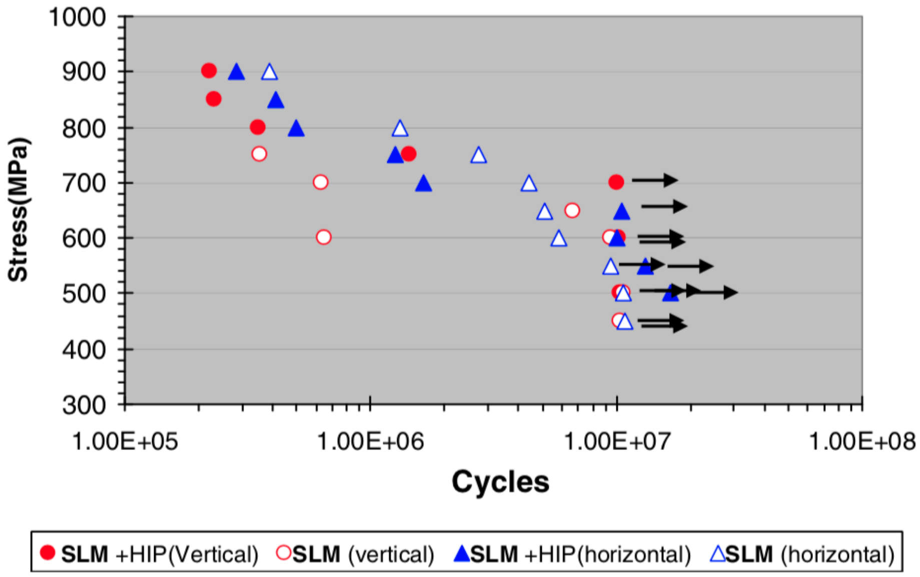

Figure 2.17: Effect of build orientation and heat treatment on the fatigue performance of SLM Hastelloy-X at room temperature (Wang et al., 2011)

2.3.3 Fractography analysis

Fractography is a technique for analysing the fracture surface in order to determine the cause of failure and the crack growth behaviour. Typically, digital microscopy and scanning electron microscopy (SEM) are used for fractography analysis.

Regarding monotonic failure, Cheng et al.(Cheng et al., 2022b) investigated the influence of heat treatment on the type of fracture observed in SLM Hastelloy-X at room temperature. The fracture surfaces under tensile loading observed in this work using SEM micrographs are represented in figure 2.18 for the as-built and heat treated(1050°C /1h) conditions. In both as-built and heat treated fracture samples, typical ductile necking and cup and cone failure were observed. Furthermore, Cheng et al.(Cheng et al., 2022b), Wang et al. (Wang et al., 2012) and Li et al. (Li et al., 2017), reported printing defects such as crack and porosity in as-built and heat treated samples. However, it should be noted that multiple authors have mitigated micro-cracks in SLM Hastelloy-X by reducing Si and Mn content in the alloy (Tomus et al., 2016), adding solid solution strengthening elements such as Co, W, and Mo (Harrison et al., 2015), or utilising a hot isostatic pressing process (Montero-Sistiaga et al., 2019b, 2020). Figure 2.18 depicts the dimple and tear characteristics that direct the normal ductile failure which leads to intergranular failure in SLM Hastelloy-X. Since the sizes of the dimples and subgrains are comparable, it can be concluded that, along with defects, subgrain boundaries also lead to crack initiation (Cheng et al., 2022b).

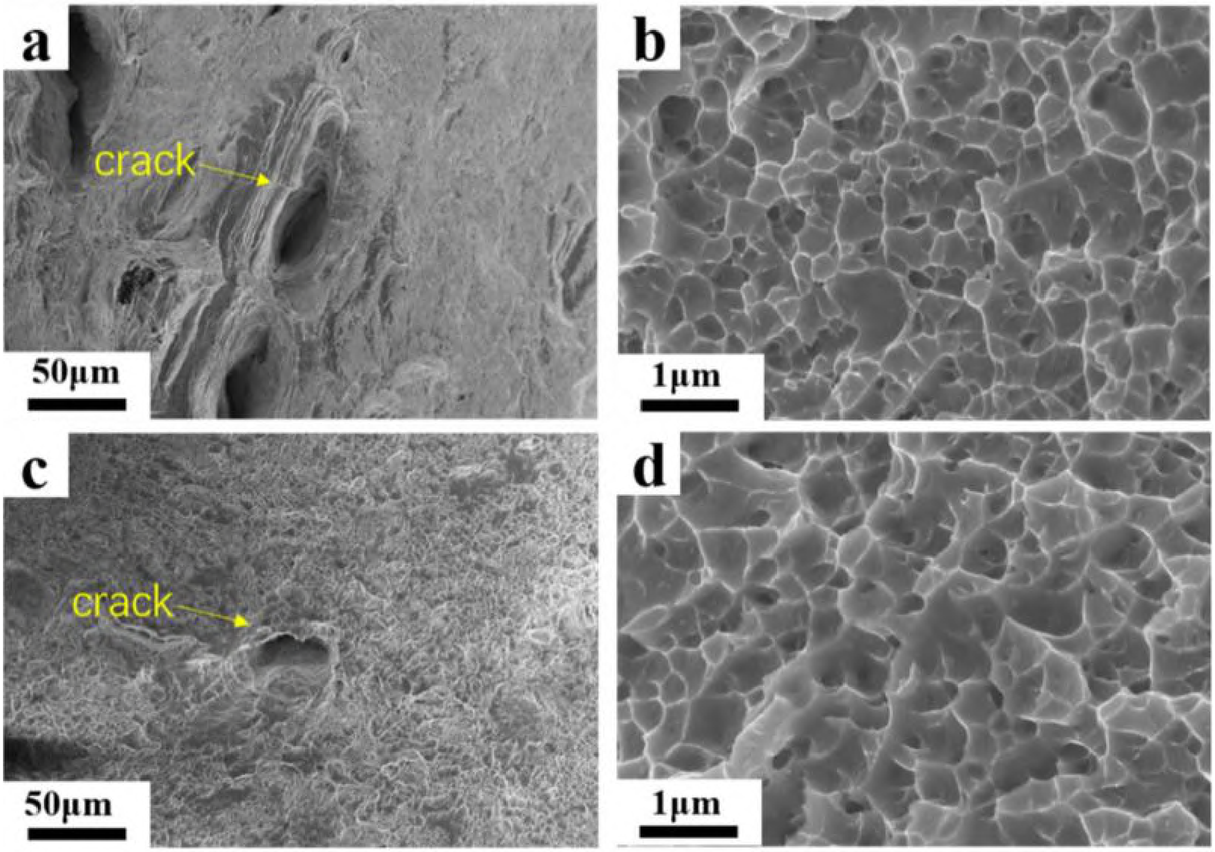

Figure 2.18: SEM images of SLM Hastelloy-X tensile fracture surfaces in a,b) as-built and c,d) heat treated conditions. (Cheng et al., 2022b)

The fatigue surface fractography reveals three distinct regimes: a) fatigue crack initiation, b) crack propagation, and c) final fracture. Multiple studies on the fractography analysis of SLM Hastelloy-X showed that cracks originated from microstructural defects such as unmelted or partially melted regions, surface roughness, and porosity (Wang et al., 2011; Montero-Sistiaga et al., 2019a; Esmaeilizadeh et al., 2021; Keshavarzkermani et al., 2019; Han et al., 2019). Esmaeilizadeh et al. (Esmaeilizadeh et al., 2021) investigated the influence of laser scan speed on the fracture surface under two stress-controlled loading conditions (200MPa and 350MPa). Figure 2.19 displays the fatigue crack process, highlighting the crack initiation, propagation, and final fracture regimes for lower (LSS) and higher (HSS) laser scan speeds. The fatigue cracks are initiated from micro-surface roughness induced by unmelted or partially melted powder and trapped porosities as shown by green arrow in figure 2.19a. When the laser scan speed is increased, the amount of porosity in the final part increases (see section 2.2), which act as dominant crack initiation site (Tammas-Williams et al., 2017).

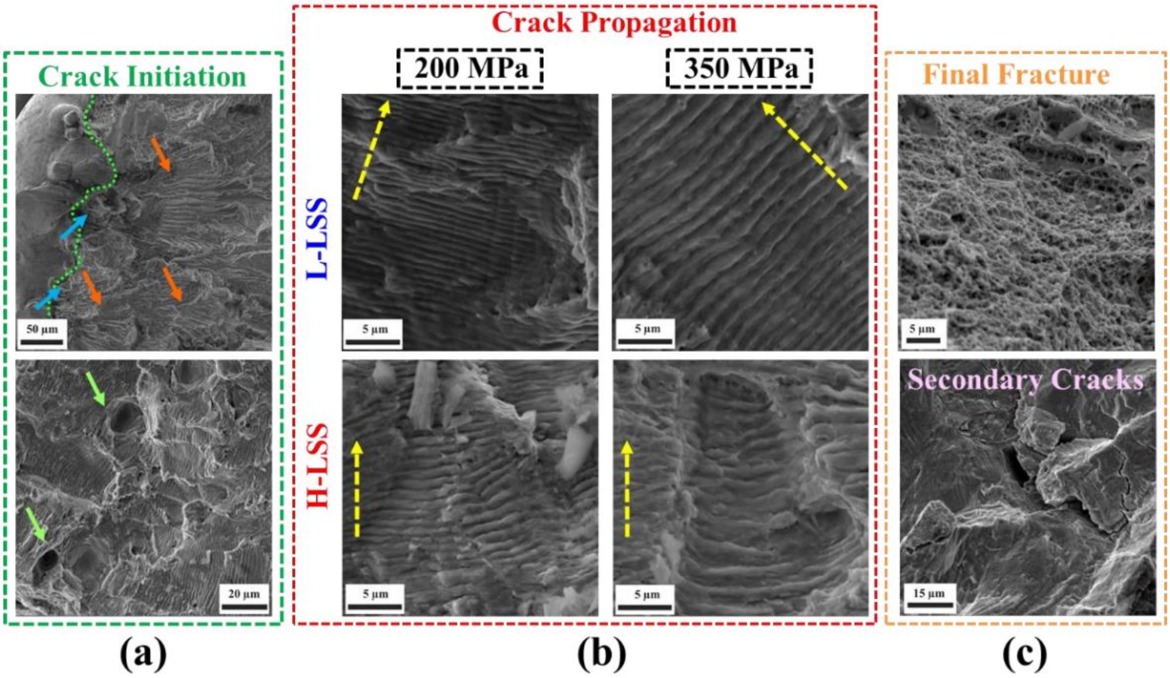

Figure 2.19: SEM images depict three fatigue fracture regimes: a) crack initiation b) crack propagation c) final fracture for lower laser scan speeds, L-LSS (top) and higher laser scan speeds-LSS (bottom) (Esmaeilizadeh et al., 2021)

Figure 2.19b depicts a crack propagation regime in which a fatigue fracture propagates in the form of beach waves (indicated in yellow) with striation spacing determined by the applied cyclic loading, with larger loads resulting in wider striations (Wang et al., 2011). Therefore, larger applied cyclic loads result in faster crack propagation (Esmaeilizadeh et al., 2021). It should be observed that for lower applied cyclic loads, the fatigue crack initiation regime consumes the majority of total life compared to higher cyclic loads.

Finally, SLM Hastelloy-X demonstrates typical intergranular fractures defined by the formation of dimples(see figure 2.19c), regardless of applied stresses or laser scan speeds.

To summarise this section, post-processing, process parameters, temperature, and build orientation all have a significant impact on the mechanical behaviour (quasi-static and fatigue) of SLM Hastelloy-X. The build orientation contributes significantly to anisotropy in the mechanical response. Simultaneously, process parameters can tailor the microstructure and defects, and hence change the mechanical properties of SLM Hastelloy-X depending on the application. The discussion shows that the as-built samples do not meet the required mechanical performance. Yet, post-processing conditions can increase the alloy's tensile and fatigue properties; however, the additional post-processing expense is a significant drawback. Therefore, when designing the component using the additive manufacturing method, all of these factors need to be properly taken into account.

2.4 Micromechanics based models for polycrystalline alloys

Macroscopic constitutive models aim at predicting the quasi-static and cyclic behaviour of metallic alloys using macroscopic material parameters measured from experiments. Even for the same alloy, changes in the microstructure, such as texture development, require new parameters to enter the model and therefore new full testing campaigns.

It is evident from section 2.3 that the microstructure has a significant impact on the mechanical characteristics of SLM Hastelloy-X. Having models able to predict the response of the alloy having as input the polycrystalline microstructure resulting from the SLM process will result in a strong reduction of experimental tests. Moreover, their integration with models able to predict microstructure from process parameters opens the door to optimal design of SLM parts with microstructure distribution engineered to achieve optimal response.

Micromechanics based models for polycrystals have developed as a crucial tool for understanding the effect of microstructure on the mechanical performance of metals and alloys (McDowell, 2007; Dunne, 2014; Roters et al., 2010; Cheng et al., 2022b; Ghorbanpour et al., 2022; Kapoor et al., 2018). These models incorporate grain size, shape, and orientation as actual representations of microstructure(Lucarini et al., 2021; Segurado et al., 2018; Shenoy et al., 2008). Using these techniques, virtual testing can be performed to estimate the mechanical response (quasi-static and fatigue) for different microstructure, without the need of performing new tests for each microstructure considered, making it perfect for designing metallic parts.

The crystal plasticity model as constitutive equation of the grains is the core of micromechanical approaches that is combined with some homogenization technique to consider the effect of the polycrystalline microstructure. The most accurate models are those in which the homogenization of the response is made using complex computational models which consider the spatial distribution of the grains. This techniques are usually referred as computational homogenization of polycrystals (Segurado et al., 2018).

Computational homogenization of polycrystals rely on replicating the actual microstructure in synthetic representative volume elements (RVE) and solve a boundary value mechanical problem on that RVE to find the macroscopic response as the average of the relevant microscopic fields. The RVE incorporates a statistical description of the size, shape, and orientations of the grains. The crystal plasticity (CP) framework is used to model the constitutive relationship for a single crystal. At the single-crystal level, the CP formulations account for isotropic hardening, kinematic hardening, and softening (Cruzado et al., 2017, 2018). In the last decade, full-field polycrystalline homogenization techniques (Segurado et al., 2018) have been widely used as a virtual testing framework to model the effect of the polycrystalline microstructure on the macroscopic response of superalloys. Several studies have been published that use computational homogenization to model various polycrystalne superalloys fabricated via standard routes, such as Inconel 718(Cruzado et al., 2017), René 88DT (Soare et al., 2020), MD2 and CMSX-4 (Bronkhorst et al., 2019), or generic FCC superalloys (Farooq et al., 2020).

Classically, most of these micromechanical studies use the finite element (FE) method to solve the mechanical problem. However, in the last two decades, Fast Fourier Transform (FFT) solvers have just been introduced as an alternative to FEM (Lebensohn et al., 2013; Eisenlohr et al., 2013; Lebensohn, 2001) for their excelent performance. The use of FFT-homogenization methods provides a precise prediction of the microfield response at a fraction of the cost of FE-based solvers, allowing for bigger RVE simulations and consideration of more accurate microstructural characteristics. According to Segurado et al. (Segurado et al., 2018), the accuracy of full-field homogenization is based on three factors: a) a digital representation of the microstructure, b) a crystal plasticity model providing a constitutive response of single-crystal behaviour, and c) a numerical approach solving the boundary value problem. Since computational homogenization of polycrystals will be the modeling framework of this thesis, this section will systematically discuss these three key factors.

2.4.1 Digital representation of microstructure

The most important step in microstructure-sensitive models is an accurate description of the actual microstructure. Microstructural characteristics such as grain size, shape, orientation, and defects can be accommodated digitally via representative volume elements (RVEs). As a result, they serve as a foundation for computational homogenization techniques. The RVE is the smallest microstructural volume subjected to computational homogenization resulting in effective properties that are representative of those of the macroscopic heterogeneous material(Lucarini and Segurado, 2020; Segurado et al., 2018; Cruzado et al., 2017).

Polycrystals are a conglomerate of single-crystalline grains. The generation of a polycrytalline microstructure is achieved synthetically by subdividing the volume of the RVE into a number of geometric entities. Each grain is identified by its well-defined size, shape, and crystallographic orientation. Additionally, other microstructural features like as porosity, defects, twin boundaries, metal carbides, second phases, and surface roughness can be explicitly included in the RVE.

The literature includes numerous ways for quantifying the 2D grain size and shape distribution. On the one hand, optical microscopy of polished and chemically etched samples can reveal grain boundaries, shape, and size distributions when coupled with image analysis tools. Some algorithms were developed to convert 2D microstructural data into 3D microstructure data. On the other hand, precise statistical descriptions of grain size and shapes can be obtained using sequential milling and 2D image techniques on the slides (Herrera-Solaz et al., 2020). Alternatively, direct 3D microstructures of polycrystals can be obtained using X-ray diffraction tomography (Poulsen et al., 2001)

Electron backscatter diffraction (EBSD) can provide an accurate description of grain orientation, grain and subgrain boundaries, 2D grain size, and the presence of twins within the microstructure. Furthermore, diffraction contrast can offer detailed grain size and orientations, and phase-contrast tomography can reveal second phases and porosity in the microstructure. As a result, precise 3D characterization of the microstructural data set is now possible. Similarly, grain sizes can be statistically characterised in some probability distribution function (usually log-normal) to avoid relaying on enormous 3D data sets in models.

Once the 3D description for individual crystals or some probability distribution function is known, a digital RVE is built to represent the actual microstructure. Geometric tessellation models were used to build the digital RVE with the necessary grain morphology and characteristics. Geometric tessellation is the subdivision of a three-dimensional domain into several convex polyhedrons that overlap only at the boundaries. Laguerre tessellation (LT), Voronoi tessellation (VT), and Johnson-Mehl tessellation are some common tessellation models (JMT). Out of these, Voronoi tessellation is the most popular model.

The first step in building the RVE is to spatially allocate the crystal centres ($\mathrm{x_i}$) according to the statistical distribution of grain size. The spatial allocation of crystal centres is random and is generally obtained using the Monte Carlo algorithm with the assumption that the grains are ellipsoidal (Lucarini and Segurado, 2018) . Once the crystal centres are fixed in the domain, the geometric polycrystals are defined by setting a random point (x) from RVE to the specific crystal C_i. The Voronoi tessellation measures the distance between a random point and the centre of each crystal and specifies the criteria under which the random point is located in each crystal as,

$$\mathbf{x} \in C_i \text{ if } \parallel \mathbf{x} - \mathbf{x_i} \parallel < \parallel \mathbf{x} - \mathbf{x_j} \parallel \forall j \neq i \tag{2.1}$$

The generated grain boundaries, on the other hand, are always equidistant from the crystal centre, limiting the grain pattern generation range and failing to account for actual grain size. To overcome this limitation weighted Voronoi algorithm and Laguerre tessellations are introduced which include a grain radius parameter, r_i as the weight associated with the point. The weighted Voronoi tessellation is defined as follows:

$$\mathbf{x} \in C_i \text{ if} \frac{\parallel \mathbf{x} - \mathbf{x_i} \parallel < \parallel \mathbf{x} - \mathbf{x_j} \parallel}{r_i} \forall j \neq i \tag{2.2}$$

and Laguerre tessellation is given by,

$$\mathbf{x} \in C_i \ \text{ if}(\parallel \mathbf{x} - \mathbf{x_i} \parallel^2 - {r_i}^2) < (\parallel \mathbf{x} - \mathbf{x_j} \parallel^2 - {r_j}^2) \, \forall j \neq i \tag{2.3}$$

Based on the tessellation data, the digital RVE can be built using two distinct discretization schemes. The first is the voxel-based model, in which the RVE is discretized into a regular grid of voxels and the grains are defined by a group of neighbouring voxels that follow the geometric tessellation criterion and have the same crystallographic orientation. Another Voronoi tessellation model representation is based on realistic polyhedron geometries such as vertex, surface, edge, and volume. Although the latter model accurately depicts the synthetic microstructure, adaptive remeshing and structuring of each realistic geometry necessitates additional computational cost. Voxel-based models, on the other hand, are built using the extracted 3D tessellation data. Furthermore, such models are exported as input to boundary value problem solvers such as the FFT (regular grid points) and FEM solver. Figure 2.20 (Segurado et al., 2018) shows examples of both representations of synthetic RVEs.

’

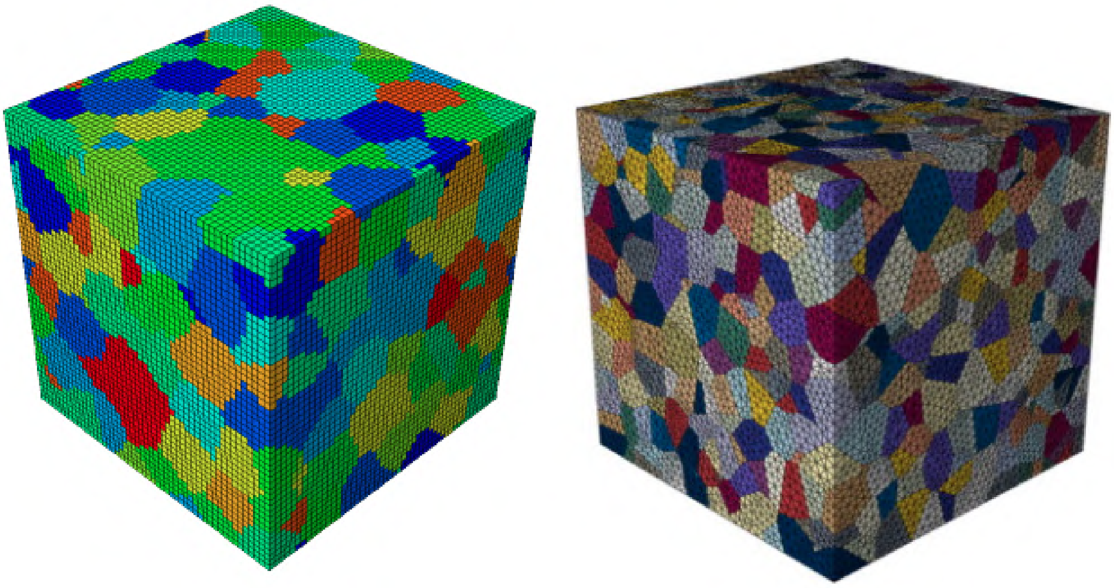

Figure 2.20: Representation of polycrystalline microstructures using synthetic RVEs: voxel-based RVE(left) and Voronoi-based RVE(right). (Segurado et al., 2018)

Once the RVE is generated based on the grain size distribution, the grain orientations are introduced using statistical distributions such as orientation distribution functions or one-to-one grain orientation as observed in EBSD. Furthermore, the RVE size should be large enough to accommodate the number of grains, ensuring the statistical grain size and orientation distribution's reproducibility and accuracy.

The digital representation of the microstructure is a difficult and time-consuming task. There are numerous open-source codes available, such as neper (Quey et al., 2011), Dream3D (Groeber and Jackson, 2014), and FFTMAD (Lucarini and Segurado, 2018), that can generate synthetic RVEs very efficiently and can be used directly for computational homogenization applications.

2.4.2 Crystal plasticity models

Crystal plasticity(CP) is the constitutive framework that describe the mechanical response of crystalline materials using the principles of dislocation slip and continuum mechanics on a mesoscopic scale(Roters et al., 2010). Plastic deformation in crystalline materials is primarily driven by dislocation movement on slip systems(Dieter and Bacon, 1988). The slip system is the combination of the slip plane and the slip directions with the containing closely packed atoms, i.e. highest number of atoms per unit area (Hull and Bacon, 2011). Taylor and Elam (Taylor and Elam, 1923, 1925) provided the first CP model to describe the plastic shear deformation of a single crystal of aluminium on 12 FCC slip systems. In their revolutionary work, they identified shear stresses in each slip system as the primary sources of plastic deformation. Since then, most crystal plasticity frameworks have been built on Taylor's approach that the material flows through the lattice along a well-defined slip system by dislocation motion while the lattice undergoes deformations and rotations (Roters et al., 2010; Segurado et al., 2018). The discrete distribution of dislocations within the crystal causes discontinuous displacement, which is challenging to map with a continuous deformation gradient field. Hill and Rice (Hill and Rice, 1972) proposed the CP finite-strain framework used now in most of modern models and based on the decomposition of the deformation gradient into elastic and plastic components.

Numerical methodologies for implementing CP models evolved significantly alongside the development of CP models. Some examples include effective numerical approaches for addressing non-linear viscoplastic formulations in finite-deformation frameworks. Furthermore, the improved computational capacity allows for the efficient simulation of large-scale deformations for complex 3D polycrystals using CP formulations. Segurado et al.(Segurado et al., 2018) and Roters et al.(Roters et al., 2010) provide a comprehensive review of the crystal plasticity models available to simulate metallic aggregates.

The review of phenomenological CP framework for predicting the quasi-static and fatigue behaviour of metallic alloys will be highlighted in this section.

The starting point of a CP model in finite strain is the multiplicative decomposition of the deformation gradient, $\mathbf{F}$ into elastic, $\mathbf{F}^e$ and plastic (inelastic), $\mathbf{F}^p$ components (Asaro and Needleman, 1985; Peirce et al., 1983).

$$\mathbf{F} = \mathbf{F}^e\mathbf{F}^p \tag{2.4}$$

where $\mathbf{F}^p$ is defined in the intermediate configuration on the assumption that the lattice remains undistorted and unrotated, while $\mathbf{F}^e$ is associated with lattice rotation and stretching. Figure 2.21 depicts the concept of multiplicative decomposition of a deformation gradient into elastic and plastic components, along with reference, intermediate, and current configurations.

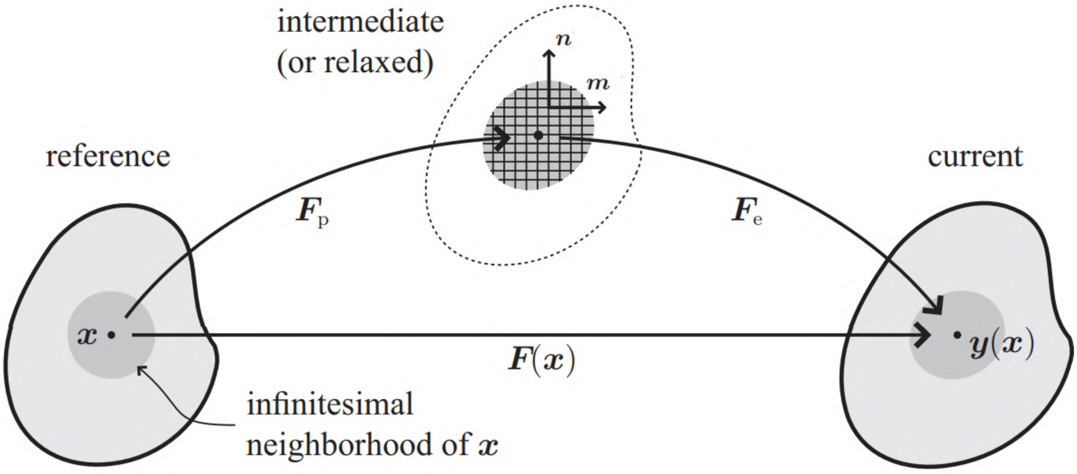

Figure 2.21: Multiplicative decomposition of deformation gradient into elastic and plastic components. (Roters et al., 2010)

The velocity gradient in current configuration can be calculated using the multiplicative decomposition of the deformation gradient as,

$$\mathbf{L} = \dot{\mathbf{F}}\mathbf{F}^{-1} = \dot{\mathbf{F}}^{e}\mathbf{F}^{e-1} + \mathbf{F}^{e}\dot{\mathbf{F}}^{p}\mathbf{F}^{p-1}\mathbf{F}^{e-1} \tag{2.5}$$

In the relaxed(intermediate) configuration, the plastic velocity gradient $\mathbf{L}^p$ is calculated as,

$$\mathbf{L}^{p} = \dot{\mathbf{F}}^{p}\mathbf{F}^{p-1} \tag{2.6}$$

The constitutive equations in the majority of CP formulations are derived from the energy density, Ψ in the intermediate configuration. The free energy density can be described as a function of internal variables, $\boldsymbol{\alpha}$ as,

$$\Psi = \Psi(\mathbf{F}, \boldsymbol{\alpha}) \tag{2.7}$$

According to Cuitio and Ortiz (Cuitiño and Ortiz, 1992), the free energy density Ψ can be separated into elastic, Ψ^e and plastic, Ψ^p energies. As a result, the total free-energy density is given as,

$$\Psi = \Psi^{e}(\mathbf{F}\mathbf{F}^{\mathbf{p}^{-1}}) + \Psi^{p}(\mathbf{F}^{\mathbf{P}}, \boldsymbol{\alpha}) \tag{2.8}$$

The second Piola-Kirchoff stress tensor can be obtained from the first derivative of elastic free energy density with the Green-Lagrange elastic strain tensor, $\mathbf{E}^e$ in the intermediate configuration as

$$\mathbf{S} = \frac{\partial\Psi^{e}(\mathbf{F}\mathbf{F}^{\mathbf{p}^{-1}})}{\partial\mathbf{E}^{e}} \tag{2.9}$$

The Green-Lagrange elastic strain tensor, $\mathbf{E}^e$ in the intermediate configuration, can be written as

$$\mathbf{E^e} = \frac{1}{2}(\mathbf{F^{e^T}F^e} - \mathbf{I}) \tag{2.10}$$

where $\mathbf{I}$ is the second-order identity tensor.

The Cauchy stress in the current(final) configuration is given by

$$\sigma = J\mathbf{F^eSF^{e^T}} \tag{2.11}$$

where J is the determinant of the deformation gradient, $\mathbf{F}$. Finally, assuming the quadratic free energy density, a linear map between the second-order Piola-Kiroff stress tensor, S and the Green-Lagrange strain tensor is given by

$$\mathbf{S} = \mathbb{C}\mathbf{E^e} \tag{2.12}$$

where $\mathbb{C}$ is the fourth-order elastic stiffness tensor of the single crystal. The elastic stiffness tensor for face-centered cubic metals(FCC) is represented by three independent constants, C_{11}, C_{12}, and C_{44}.

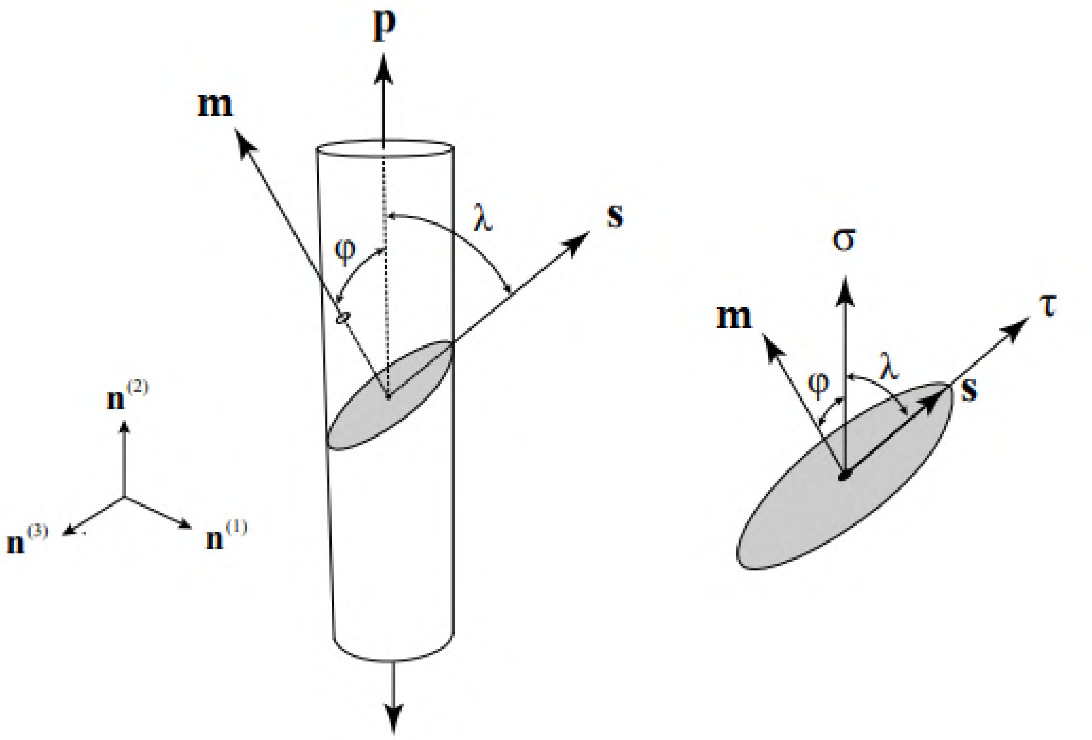

Figure 2.22: An illustration of deformation along an arbitrary slip system under uniaxial loading condition. (Roters et al., 2010)

Before delving into the continuum mechanics-based crystal plasticity models, it is critical to comprehend the concepts of slip system and critical resolved shear stress. According to Dieter and Bacon (Dieter and Bacon, 1988), slip occurs in single crystals along particular crystallographic planes (planes with the maximum atomic density). These planes are referred to as slip planes, and the direction normal to slip planes is referred to as slip normal, which also has the closest packed direction within the slip plane. The slip plane and slip normal are referred to as the slip system. In FCC materials, the $\{111\}$ octahedral slip plane and <100> slip direction have densely packed atomic structures.

Shear stresses, structure geometry, and slip plane orientation with respect to shear stresses all influence slip deformation on an arbitrary slip system. A slip system's resolved shear stress (RSS), τ_β is calculated as a projection of the imposed macroscopic load in the slip plane. The concept of resolved shear stress is depicted in figure 2.22. λ is the angle created by the applied load and the slip plane normal, whereas ϕ is the angle formed by the applied load and the slip plane normal(Dieter and Bacon, 1988; Hull and Bacon, 2011). As a result, RSS can be written as follows:

$$\tau^\beta = \frac{F}{A} \cos\phi \cos\lambda \tag{2.13}$$

The term $\cos\phi\cos\lambda$ refers to the Schmid factor, which is basically a measure of optimum orientation for a certain slip system, β.

The RSS in a system β characterized by its slip and normal directions $\mathbf{s}^\beta, \mathbf{m}^\beta$, in the context of finite-strain formulations with the assumption of small elastic strain can be written as

$$\tau^\beta = \mathbf{S} : \mathbf{s}^\beta \otimes \mathbf{m}^\beta \tag{2.14}$$

The geometrical description of slip planes and directions formed the basis for the initial explanation of the conventional flow rule for the single crystal given by Rice. They state that the plastic slip $\dot{\gamma}^\beta$ accumulated in all systems($\beta = 12$), which is represented by the plastic velocity gradient (Rice, 1971), is

$$\mathbf{L}^p = \sum_\beta \dot{\gamma}^\beta \mathbf{s}^\beta \otimes \mathbf{m}^\beta \tag{2.15}$$

where, the dyadic product $\mathbf{s}^\beta \otimes \mathbf{m}^\beta$ represents the non-symmetric Schmidt tensor in the slip system β.

In crystal plasticity, it is presumable that the resolved shear stress(τ), and internal state variables ($\boldsymbol{\alpha}$) will affect the evolution of plastic slip γ^β in the slip system β, which is given as,

$$\dot{\gamma}^{\beta} = \dot{\gamma}^{\beta}(\tau^{\beta}, \boldsymbol{\alpha}) \tag{2.16}$$

2.4.3 Flow rule

Various forms of flow rules have been studied in the literature. The most popular are 1) phenomeological power-law given by Pirece et al. (Peirce et al., 1983) 2) activation energy based Arrhenius model given by Kocks et. al. (Kocks, 1976) and 3) linear model given by Kocks et al. (Kocks et al., 1975).

Power-law model

The phenomenological CP model is built to compute the slip rate and is based on an accurate geometric representation of slip systems, with the evolution of internal variables representing the current state of the crystal. The independent CP model was pioneered by Rice and Hill(Hill and Rice, 1972), whereas the commonly used viscoplastic model was introduced in 1983 by Pierce et al (Peirce et al., 1983). According to Pierce et al.(Peirce et al., 1983), the plastic slip rate on any β slip system is power law proportional to the resolved shear stress and the critical resolved shear stress (CRSS).

$$\dot{\gamma}^{\beta} = \dot{\gamma}_0 \left(\frac{|\tau^{\beta}|}{g^{\beta}} \right)^{\frac{1}{m}} \text{sign}(\tau^{\beta}) \tag{2.17}$$

where m represents the strain rate sensitivity coefficient and $\dot{\gamma}_0$ represents the reference share slip rate

Arrhenius type model

The Arrhenius type flow rule explicitly takes temperature into consideration through thermally activated phenomena that aid in dislocation glides(Kocks, 1976; Shahba and Ghosh, 2016; Keshavarz and Ghosh, 2013).The Arrhenius type model can be expressed mathematically as:

$$\dot{\gamma}^{\beta} = \dot{\gamma}_0 \exp\left\{ \{ -\frac{Q^{\beta}}{k_B T} \left[1 - \left(\frac{|\tau^{\beta} - T^{\beta}_{ath}|}{T^{\beta}_{o}} \right)^{p} \right]^{q} \} \right\} sign(\tau^{\beta} - T^{\beta}_{ath}) \tag{2.18}$$

where p and q are constant factors whose values depend on local dislocation motion impediments, and k_B is Boltzmann constant. Q is the thermally activated energy, T^{β}_{o} is the thermal component of shear stress, and T^{β}_{ath} are the athermal components required to overcome the hindrance to dislocation.

Linear model

According to Kocks et al.(Kocks et al., 1975), at very high strain rates, viscous drag dominates dislocation motion, and so a linear flow rule is given as,

$$\dot{\gamma}^{\beta} = \dot{\gamma}_0 \frac{|\tau^{\beta} - T^{\beta}_{ath}|b^{\beta}}{B(T)} \tag{2.19}$$

where, b is Burgers vector and B is the drag coefficient which is the function of temperature.

2.4.4 Hardening models

The evolution of CRSS on a certain slip system is crucial to determine since it accounts for work hardening. Pierce et al.(Peirce et al., 1983) proposed the first isotropic hardening model, in which they calculated CRSS on each slip system by establishing a matrix that gives its activity in the same slip system (self hardening) and in other slip systems (latent hardening). The evolution of CRSS derived from the contribution of shear strain rate in all slip systems and the latent hardening matrix, which is given by,

$$\dot{g}^{\beta} = \sum_{\alpha} h_{\beta\alpha}|\dot{\gamma}_{\beta}| \tag{2.20}$$

where, $h_{\beta\alpha}$ is the latent and self hardening coefficients matrix and which is given as,

$$h_{\beta\alpha} = q_{\beta\alpha}h \tag{2.21}$$

where $\beta = \beta$ represents the self hardening coefficients and $\beta \neq \alpha$ represents the latent hardening coefficients. According to the Asaro-Needleman isotropic hardening model (Asaro and Needleman, 1985), the function determining the strain hardening modulus function, $h_{\beta\alpha}$ for FCC single crystals is given by,

$$h(\gamma_a) = h_0 sech^2 \left| \frac{h_0\gamma_a}{\tau_s - \tau_0} \right| \tag{2.22}$$

In Eq. (2.22), three parameters τ_0, τ_s, and h_0, which stand for initial CRSS, saturation CRSS, and initial hardening modulus, respectively, were to be fitted based on experimental data and γ_a is the accumulated shear strain from all slip systems $(\beta = 1 - 12)$, which is formulated as,

$$\gamma_a = \sum_{\beta} \int_0^t |\dot{\gamma^{\beta}}|dt \tag{2.23}$$

There are several variants of Eq. (2.22) in the literature. In Eq.2.22 , some researchers used a power-law function rather than a hyperbolic function (Becker, 1991), and others used modified hardening laws such as a generalized Voce equation (Voce, 1948; Kocks, 1976) instead of Eq.2.22

Voce (Voce, 1948) provided a generalized formulation of the self-hardening modulus using an exponential function with one additional parameter than the Asaro-Needleman model, which is the saturation hardening modulus, h_s. The Voce hardening modulus is given as

$$h(\gamma_a) = h_s + \left[h_0 - h_s + \frac{h_0 h_s \gamma_a}{\tau_s - \tau_0}\right] \exp\left\{\left(\frac{-h_0\gamma_a}{\tau_s - \tau_0}\right)\right\} \tag{2.24}$$

The phenomenological crystal plasticity models were modified to account for the effect of cyclic deformation by including a back stress term in Eq. (2.25). At the crystal level, the back stress term will incorporate the effect of kinematic hardening into the CP model. Several publications(Cruzado et al., 2017, 2018; Lucarini and Segurado, 2020; McDowell and Dunne, 2010) have adopted this formulation to mimic the fatigue behavior of polycrystalline materials. In a power-law type flow rule, the back stress term is introduced in the resolved shear stress term, which is defined as

$$\dot{\gamma}^\beta = \dot{\gamma}_0 \left(\frac{|\tau^\beta - \chi^\beta|}{g^\beta}\right)^{\frac{1}{m}} \text{sign}(\tau^\beta - \chi^\beta) \tag{2.25}$$

where χ^β is the back stress corresponding to the β slip system. Cailletaud (Cailletaud, 1992) presented the evolution of back stress term for FCC metals. The Armstrong-Fredrick(Cruzado et al., 2017) model is the most commonly used evolution law for backstress in the CP framework, providing non-linear kinematic hardening. The AF model is written as a first order differential equation, which is denoted as,

$$\dot{\chi}^\beta = c\dot{\gamma}^\beta - d|\dot{\gamma}^\beta| \tag{2.26}$$

In Eq. (2.26), the constants c and d describe the kinematic hardening and should be fitted using experimental data or an inverse fitting approach. Although the AF model accurately predicts the cyclic response under fully reversed cyclic loading, it fails to estimate the mean stress effects under non-symmetric cyclic loading. Later, Ohno-Wang model (OWM)(Ohno and Wang, 1993), which is a modified version of the AF model that provides correct modelling of mean stress effects and ratcheting in the CP framework. Cruzado et al. (Cruzado et al., 2017, 2018) recently used a simplified version of OWM for the cyclic deformation of IN 718 alloy, which is given as,

$$\dot{\chi}^\beta = c\dot{\gamma}^\beta - d|\dot{\gamma}^\beta| \left(\frac{|\chi^\beta|}{c/d}\right)^{k_o} \tag{2.27}$$

where k is an additional factor that governs the mean stress relaxation velocity.

Physically based constitutive models, as contrast to phenomenological constitutive models, rely on internal variables. Because dislocations induce plastic deformation, dislocation density is unquestionably the most important microstructural state variable in the case of plasticity. Several authors have proposed models that deal with the evolution of dislocation density and use it to predict flow stress. While dislocations are the most essential measure of internal variables, other factors such as grain size and shape, second phase fractions, precipitate morphology, and so on are necessary for a thorough characterisation of the microstructure. However, only a few of these parameters have been included in dislocation-based crystal plasticity models thus far. Due to the large number of variables and fitting parameters, physical-based model formulations are complex and computationally expensive. Phenomenological models, on the other hand, are much simpler, with just 5-6 fitting parameters required. This makes phenomenological models attractive in terms of computational cost and simplicity(Roters et al., 2010). As a result, in this work, phenomenological models are preferred over physical-based models.

2.4.5 FFT based computational homogenization

Homogenization theory is a mathematical framework aiming to obtain the macroscopic response of a heterogeneous material from the constitutive equations of the phases and some microstructural descriptors.

The most simple homogenization technique are the mean-field approaches, in which each phase (or crystal) is considered as an ellipsoid with a homogeneous stress state and which solution is derived from the Eshelby work (Eshelby and Peierls, 1957). Although mean-field homogenization techniques such as elastic self-consistent and viscoplastic self-consistent(VPSC) (Molinari et al., 1987; Tome et al., 1984; Lebensohn and Tomé, 1993) provide reliable estimates of effective material properties for linear and non-linear polycrystalline response(Lebensohn et al., 2013; Lucarini et al., 2021), Segurado et al.(Segurado et al., 2018) in their detailed review point out two key limitations. The first is that these approaches are based on the assumption of constant micromechanical fields within the grain or phase, which are not always true, especially in the event of plastic deformation, fatigue, and damage development, and large mechanical contrasts(Segurado and Llorca, 2002; González and LLorca, 2007). The second drawback is that, while mean-field techniques consider average values of grain size, shape, and orientation, they do not include local microstructural properties, such as heterogeneities or grain clustering, which are critical for fatigue and damage design(Molinari et al., 1987).

Full-field homogenization solutions address the limitations of mean-field techniques by obtaining the effective response of the non-homogeneous material as a function of microstructure (Becker, 1991; Delaire et al., 2000; Cruzado et al., 2017; Lebensohn et al., 2013; Lebensohn and Cazacu, 2012). Full-field homogenization solutions are obtained by solving the boundary value problem of the RVE subjected to some mechanical loads under prescribed homogeneous boundary conditions. As a result, the success of full-field homogenization will be determined by an accurate description of the RVE, the constitutive relationship of the single crystal, and the numerical technique to solve the BV problem (Segurado et al., 2018). FEM is typically used to solve the micromechanical governing partial differential equations in full field homogenization because of its effective implicit integration method for non-linear problems and adaptive remeshing algorithm that makes representation of complex geometric accuracy(Eisenlohr et al., 2013).

In the last decade, Fast Fourier transform (FFT) has evolved as an efficient alternative to FEM. This technique which was initially proposed by Moulinec and Suquet (Moulinec and Suquet, 1994). The very first approach presented for solving strong-form equilibrium equations was based on the application of Green's function in the reference medium and solved in Fourier space, providing the solution of the Lippmann-Schwinger equation.

Since then, many different techniques have been developed aiming at improve the convergence of the original method or extend its applicabilty to different materials and physical problems. A deep review of FFT approaches is out of the scope of this PhD work, but interested readers can consult a very complete review of the method and its applications recently published by Lucarini et al.(Lucarini et al., 2021). The FFT approach used in this work is the Fourier-Galerkian scheme because it has a good performance and its formulation close to FE and its formulation will be described in detail in this section.

2.4.6 Fourier-Galerkin method

Vondrejc et al.(Vondřejc et al., 2014) and Zeman et al.(Zeman et al., 2017) presented the Fourier-Galerkin methodology, also known as the variational approach, in which FFT homogenization was performed on the weak form of equilibrium equations following a Galerkin approximation. The studies illustrate that the solution of the periodic Lippman-Schwinger problem given by Moulinec and Suquet (Moulinec and

Suquet, 1994) is equivalent to a Galerkin approximation of weak formulations, using trigonometric polynomials as interpolating functions and solving the resulting linear system of equations with an efficient Krylov solver. The main advantage of this approach is that it does not require any definition of the reference medium, and because it is based on the Galerkin approximation, it is similar to FE approaches allowing to easily adapt constitutive equation implementations. Next section present the method for a fully prescribed deformation gradient, as it was originally proposed in (Vondřejc et al., 2014; Zeman et al., 2017). Its extension to any general macroscopic loading history as mixed loading was proposed by Lucarini and Segurado (Lucarini and Segurado, 2019) and is not fully recalled here for brevity.

Problem statement

The objective is to solve the full-field homogenization problem by computing the stress and strain micro-fields in any heterogeneous material using periodic boundary conditions and finite-strain. Consider a periodic domain Ω in its reference configuration. This domain is a rectangular parallelepiped, with dimensions L_1, L_2, and L_3 for 3D. The domain contains multiple phases, each with a non-linear behavior. As a result, the domain, Ω is divided into a number of sub-domains $(\Omega_1, \Omega_2, ...\Omega_n)$, each with a set of material properties. Figure 2.23 depicts a simplified two-phase situation, with each point(x) belonging to one of those phases.

In this non-linear setup, the method is used to obtain the strain and stress micro-fields, as well as the deformation gradient at equilibrium in the periodic domain, Ω, for a given macroscopic deformation history $\overline{\mathbf{F}}(t)$.

The starting point step is the linear momentum balance in the domain,

$$\textbf{Div P(x)} = 0 \tag{2.28}$$

where 'Div' is the divergence operator, **P(x)** is the first Piola Kirchoff stress tensor, which is given at each point of the domain by a non-linear constitutive law as follows:

$$\textbf{P(x)} = (\textbf{PF(x)}, \alpha(\mathbf{x})) \tag{2.29}$$

where $\alpha(\mathbf{x})$ represent the history variables present in the constitutive model. **F** is the field of the deformation gradient, which is broken down into the average (macroscopic, spatial average over volume), $\overline{\mathbf{F}}$ and fluctuating, $\widetilde{\mathbf{F}}$ fields.

$$\textbf{F(x)} = \overline{\mathbf{F}} + \widetilde{\mathbf{F}}(\mathbf{x}) \tag{2.30}$$

hence, the overall boundary value problem to be solved is as follows:

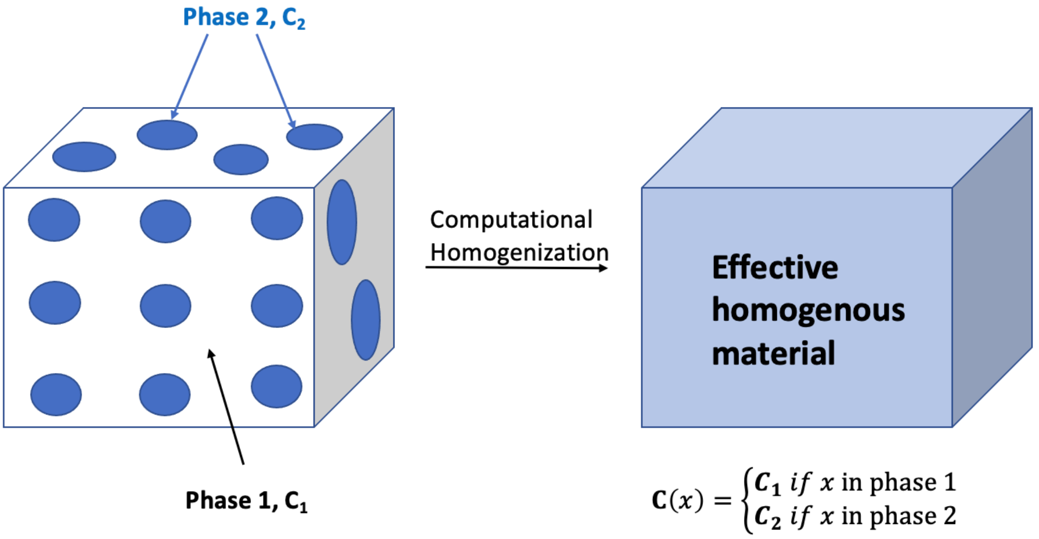

Figure 2.23: A 3D periodic RVE showing heterogeneous, two phase material (left) and the effective homogenized material after computational homogenization(right).

$$\begin{cases} \textbf{Div } \mathbf{P}(\mathbf{x}) = 0 \\ \mathbf{F}(\mathbf{x}) = \overline{\mathbf{F}} + \widetilde{\mathbf{F}}(\mathbf{x}) \\ \text{for} < \mathbf{F}(\mathbf{x}) >_{\Omega} = \overline{\mathbf{F}} \\ \text{ and } \widetilde{\mathbf{F}}(\mathbf{x}) \text{ is periodic} \end{cases} \tag{2.31}$$

Fourier-Galerkin solution

The first step in the Fourier-Galerkin scheme is to use the virtual work principle to recast the strong form of the BV problem into a weak form. The weak form of Eq. (2.31) is rewritten as follows:

$$\int_{\Omega} \delta\mathbf{F}(\mathbf{x}) : \mathbf{P}(\mathbf{F}(\mathbf{x}) + \widetilde{\mathbf{F}}(\mathbf{x}))\mathrm{d}\Omega \tag{2.32}$$

where $\delta\mathbf{F}(\mathbf{x})$ represents the test function, which can take the shape of any deformation gradient field and must satisfy the compatibility, periodicity, and symmetry criteria. The test function or virtual field, $\delta\mathbf{F}(\mathbf{x})$ is written as follows

$$\delta\mathbf{F}(\mathbf{x}) = (\mathbb{G} * \zeta)(\mathbf{x}) \tag{2.33}$$

being $\mathbb{G}$ a projection operator, which is a fourth-order tensor field that imposes the compatibility of any second-order tensor field, ζ, through the convolution operation, *. The projection operator, $\mathbb{G}$, for finite strains have a closed form expression on Fourier space which can be found in (Zeman et al., 2017).

Exploiting the major and minor symmetries of $\mathbb{G}$, using the null and Nyquist frequencies and substituting Eq.2.33 into the weak formulation equilibrium (Eq.2.32) provides the following integral equation,

$$\int_{\Omega} \zeta(x) : [(\mathbb{G}) : \mathbf{P(x)}]\, \mathrm{d}\Omega = 0 \tag{2.34}$$

Every test function ζ in the space of all square integrable tensor fields satisfies the equation. 2.34.

Following Galerkin, to solve the Eq.2.34, the unknown field and test functions are approximated by functions defined in a finite dimension subspace, $\mathbf{F}^h(\mathbf{x})$ and $\xi^h(\mathbf{x})$. To this aim, the domain Ω is discretized into a voxelised regular grid of n_x, n_y, and n_z voxels in the x, y, and z directions, respectively. Under this discretization, the tensorial fields are approximated using trigonometric interpolation, in which the weight of the each trigonometrical polynomial is the Fourier transform of the correspond field. Using the approximated fields the weak form, Eq.(2.34) can be written as,

$$\int_{\Omega_0} \zeta^h(\mathbf{x}) : [(\mathbb{G} * \mathbf{P}(\mathbf{F}^h(\mathbf{x}), \alpha^h(x))] \mathrm{d}\Omega = 0 \tag{2.35}$$

The trapezoidal rule is used to solve the above integral, and the interpolating trigonometric function is substituted by Fourier coefficients at the center of each voxel. Therefore, the integral can be calculated using the sum over voxels given by,

$$\sum_{x,y,z=1}^{n_x,n_y,n_z} \zeta_{xyz} : [\mathbb{G} * \mathbf{P}(\mathbf{F}_{xyz}, \alpha_{xyz})]_{xyz} = 0 \tag{2.36}$$

From the properties of the Fourier transform; a convolution operation in real space can be written as a multiplication operator in the Fourier space. Therefore in Fourier space, the convolution operation in Eq. (2.36) can be written as,

$$\mathbb{G} * \mathbf{P} = \mathcal{F}(\mathbb{G} : \mathbf{P}) = \hat{\mathbb{G}} : \mathcal{F}(\mathbf{P}_{xyz}) \tag{2.37}$$

Substituting Eq.2.37 in Eq. (2.36); Eq.2.36 can be rewritten as,

$$\sum_{x,y,z=1}^{n_x,n_y,n_z} \zeta_{xyz} : \mathcal{F}^{-1}[\hat{\mathbb{G}} : \mathcal{F}(\mathbf{P}(\mathbf{F}_{xyz}, \alpha_{xyz}))]_{xyz} = 0 \tag{2.38}$$

The preceding equation is applicable to any tensorial discrete field, and the right-hand side of Eq.2.38 must be zero, implying that

$$\mathcal{F}^{-1}[\hat{\mathbb{G}} : \mathcal{F}(\mathbf{P}(\mathbf{F}_{xyz}, \alpha_{xyz}))]_{xyz} = 0 \tag{2.39}$$

where $\mathcal{F}$ and $\mathcal{F}^{-1}$ are the Fourier and the inverse Fourier operators, respectively, and $\hat{\mathbb{G}}$ is the projection operator in Fourier space. Eq.2.39 is a non-linear system of $9 \times n_x \times n_y \times n_z$ algebraic equations, in which $\mathbf{F}_{xyz}$ is the unknown quantity that corresponds to the value for the deformation gradient at each voxel. Eq.2.39 can be written as:

$$\mathcal{G}(\mathbf{P}(\mathbf{F}_{xyz}, \alpha_{xyz})) = 0 \tag{2.40}$$

where $\mathcal{G}$ is the linear map of the vector space that acts on the discrete tensor field to create a new tensor field in the same space. The non-linear system of equations for each time step in Eq. 2.40 can be solved numerically. The prescribed condition of the original formulation is the deformation gradient history $\overline{\mathbf{F}}(t)$. For mixed loading cases, where only some components of the deformation gradient are prescribed, the extension of the Galerkin method proposed by Lucarini and Segurado (Lucarini and Segurado, 2019) can be used.

For the numerical solution, the time t is discretized into increments n, and the non-linear system of equations is solved iteratively for each time increment $t = t_m$ using the Newton-Raphson method. To this aim, the stress field is linearized for each Newton-Raphson iteration i, around the last iteration of the deformation gradient $\mathbf{F}^{i-1}_{xyz}$

$$\mathbf{P}^{i}_{xyz} = \mathbf{P}^{i-1}_{xyz} + \delta\mathbf{P}_{xyz} \tag{2.41}$$

with

$$\delta\mathbf{P}_{xyz} = \frac{\delta\mathbf{P}}{\delta\mathbf{F}} : \delta\mathbf{F}_{xyz} = \mathbb{K}^{i-1}_{xyz} : \delta\mathbf{F}_{xyz} \tag{2.42}$$

where $\mathbb{K}$ is a non-symmetric material tangent.

The combination of Eqs. 2.40, 2.44 and 2.42 leads to thee linear problem to be solved for each Newton iteration

$$\mathcal{G}_{\mathbb{K}^{i-1}}(\delta\mathbf{F}_{xyz}) = -\mathcal{G}(\mathbf{P}(\mathbf{F}^{i-1}_{xyz})) \tag{2.43}$$

and the result provides the new deformation gradient iteration as

$$\mathbf{F}^{i}_{xyz} = \mathbf{F}^{i-1}_{xyz} + \delta\mathbf{F}_{xyz} \tag{2.44}$$

similarly iterative equation for stress-field is given as, The coefficient matrix of Eq. 2.43 is dense and has very large dimensions. Nevertheless, the assembly of the coefficient matrix is not necessary if a Krylov iterative solver is used that just need the action of the linear operator $\mathbb{G}$ on discrete vector fields. Due to its superior numerical performance, the conjugate gradient method is commonly used to solve such equations(Schneider, 2021; Lucarini et al., 2021).

Numerical noise and mitigation methodologies

The results produced by FFT solvers are widely known to exhibit the Gibbs oscillation phenomenon, which occurs because to high contrast between the different phases in the microstructure. In the case of polycrystals, the high contrast is due to variances in the elasto-plastic response of the grains, which vary in orientation and size, as well as porosity and the presence of second phases such as carbides (Lucarini and Segurado, 2018). The spurious oscillations are caused by a variety of factors. According to Doitrand et al. (Doitrand et al., 2015), a non-smooth zig-zag surface between two interfaces causes oscillations in the voxel-based FE model (Kabel et al., 2014). These oscillations have also been recorded in stacked and embedded fibre reinforced composite meshes. Second, the Hourglass effect, which is typical in FE models, has been found in FFT models, causing oscillations (Leuschner and Fritzen, 2017). The FFT methods may also fail to meet Shannon's sampling theorem for heterogeneous polycrystals. According to Shannon's theorem, the cutoff frequency (the frequency above which the Fourier transform of the local microfield becomes zero) should be less than half the sampling frequency. However, in mechanics, the heterogeneous field, in this case polycrystal, has no cut-off frequency (Moulinec and Suquet, 1998). It should be noted that these local variations in the microscopic fields have no substantial effect on the homogenised polycrystalline response, at least from a quasi-static standpoint; nevertheless, because fatigue crack initiation modelling is dependent on localised extreme microfields, mitigation of Gibbs oscillations is critical from a fatigue standpoint. The detailed review of the occurrence of Gibbs oscillations in the FFT method and its mitigating methodologies is extensively described in (Ma et al., 2021; Lucarini et al., 2021; Gierden et al., 2022; Schneider, 2021).

Among the different mitigating strategies proposed in the literature, the most simple are based on dampening the high frequency terms through the use of linear spline functions (Kaßbohm et al., 2006) and low pass filtering of solutions (Shanthraj et al., 2015). Other alternative is the application of composite voxels or neighbouring voxel average, proposed by Kabel et al.(Kabel et al., 2015) and Ma et el.(Ma et al., 2021) respectively. More sophisticated approaches rely on the use of discrete Green operators (DGO) to mitigate inaccuracy caused by the discretization of the Fourier transform

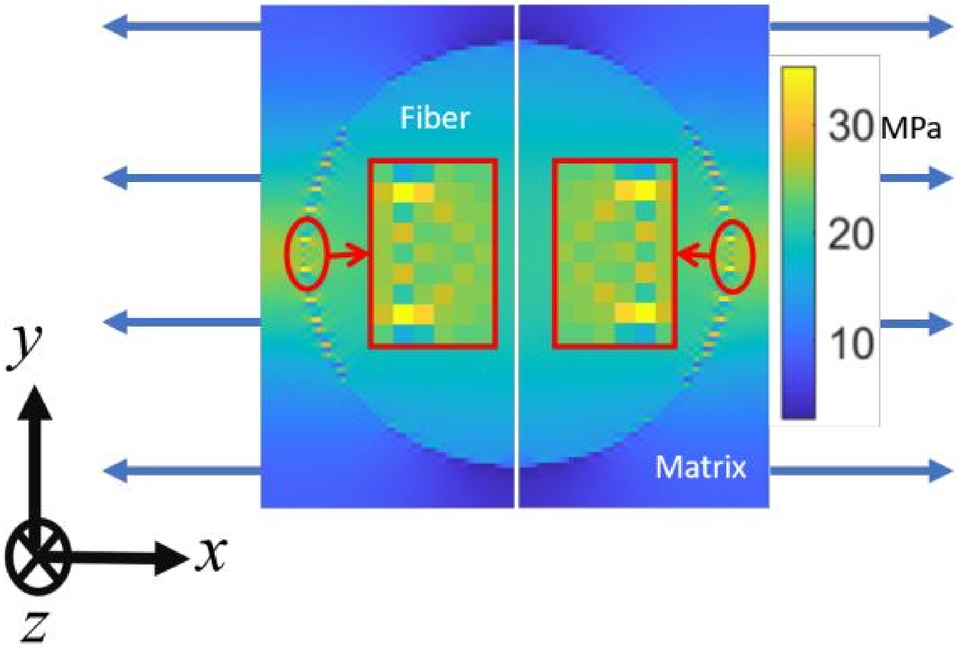

Figure 2.24: The portrayal of the Gibbs oscillation phenomena in local stress fields (σ_{xx}) in FFT(left) and FEM (right) models arose as a result of the strong contrast between the elastic modulus of the fiber and matrix. (Ma et al., 2021)

(Brisard and Dormieux, 2010, 2012; Shanthraj et al., 2015; Eloh et al., 2019). Brisard et al.(Brisard and Dormieux, 2012) proposed a rigorous expression of the DGO and integrated it into the Hashin-Striktman energy-based framework, but its exact computation becomes too expensive. Eloh et al.(Eloh et al., 2019) also proposed a DGO by assuming piecewise linear interpolation between voxels, and include it into Lippman-Schwinger equation. A simple way to derive a DGO is the use of some discretization technique, replacing partial differential with a finite difference scheme in real space. Breyer (Dreyer et al., 1999) and Brown (Brown et al., 2002) initially employed the centre finite difference (C-FD) method, but Willot et al.(Willot et al., 2014) later used backward and forward FD schemes. Willot et al.(Willot, 2015), suggested a rotated technique, in which the DGO is calculated using the C-FD scheme on a rotated grid. In this method, the grid is rotated by 45 degrees and the forward difference is computed diagonally (for the 2D instance), as illustrated in figure 2.25. Finally, Schneider et al.(Schneider et al., 2016) presented discretization based on linear hexahedral elements for basic and conjugate gradient solvers used for reduced integration and full integration to alleviate the hourglassing problem.

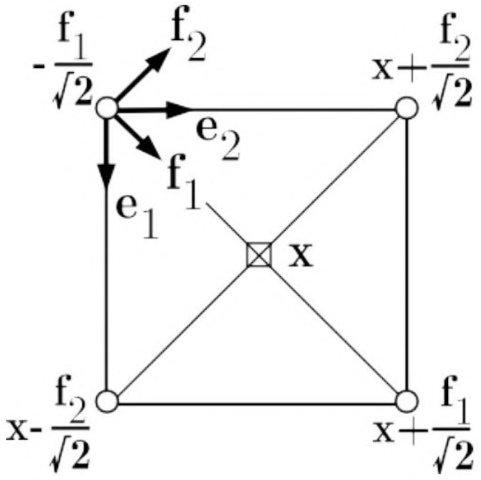

Figure 2.25: The original field is represented by circles around the corners, whereas DGO is calculated at the centre(x) of the square pixel. The caertesian axes (e_1, e_2) and 45 degree rotated axes are depicted on a regular grid (f_1, f_2) (Willot, 2015)

2.5 Fatigue life prediction models

In this section, a review of different models for predicting fatigue life will be presented. The focus is paid on crack initiation, a stage that includes the incubation of a crack from a persistent slip band to its growth until sizes around grain diameter (McDowell, 2007; McDowell and Dunne, 2010). This regime is the one in which microstructure effect is more influential and, in many cases, can take 90% of fatigue life. Propagation stage, profusely studied using fracture mechanics and models based on Paris' law is more adequate for macroscopic cracks and out of the scope of this thesis. Two type of models will be presented, macroscopic approaches such as S-N curves which indeed consider the whole fatigue life, and micromechanics models which are based on the computational homogenization approaches described above.

2.5.1 Macroscopic empirical models

Classical fatigue models are empirical models that estimate the overall fatigue life of a specimen from the characteristics of the applied load (triaxiality, stress amplitude, $\Delta\sigma$, or strain amplitude $\Delta\varepsilon$, etc) and some material parameters measured from experiments. Wohler (Wohler, 1860) established the first relationship between applied cyclic load and fatigue life by plotting applied stress versus total fatigue life, commonly known as the S-N curve.

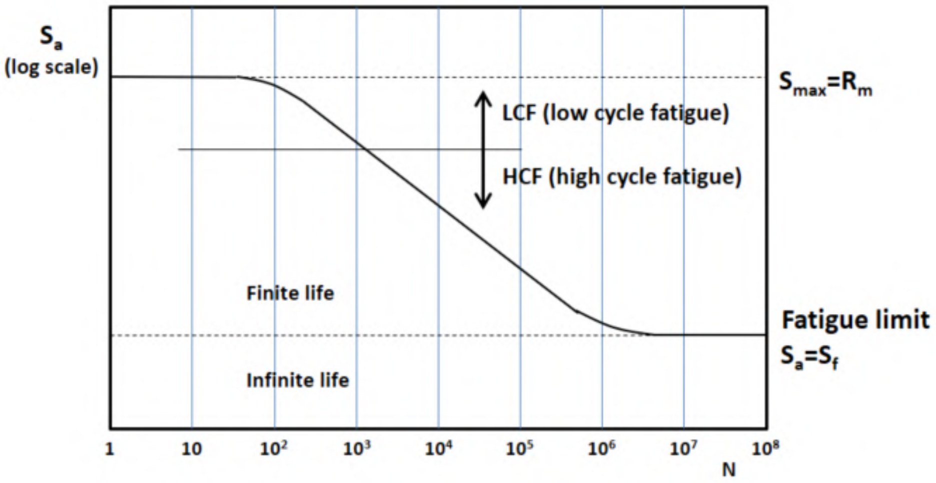

Figure 2.26: Typical depiction of Woehler's S-N curve

The S-N curve is used for uniaxial fatigue and is divided into two parts: low cycle fatigue (LCF) and high cycle fatigue (HCF). At higher applied stress, the LCF regime is observed, in which plasticity distributes homogeneously within the microstructure, resulting in a homogeneous distribution of micro-plastic strain within the microstructure. In the HCF regime, on the other hand, because the applied stress is lower, only a few grains (also known as hotspots) undergo cyclic plastic deformation, while the rest of the microstructure remains elastic(Cruzado et al., 2017, 2015). Figure 2.26 shows an example of a typical S-N curve with LCF and HCF regions. Fatemi and Yang (Fatemi and Socie, 1988) provide a comprehensive assessment of fatigue damage models.

Basquin (Basquin, 1910) established the first empirical relationship between stress amplitude and total fatigue life in 1910. He plotted stress amplitude and fatigue life on the log-log scale, which makes it possible for both quantities to be related linearly by using some material constants. Basquin's law is expressed in its most basic mathematical form as:

$$\Delta\sigma = C_b.2{N_f}^{m_b} \tag{2.45}$$

where N_f is the number of cycles before fracture for a given stress amplitude $\Delta\sigma$ and C_b and m_b are material constants that have been fitted using at least two experiments. Presently, strain controlled loading is used in the most of LCF experiments. Therefore, the Basquin's law has been modified to account for strain amplitude.

$$\frac{\Delta\varepsilon_e}{2} = \frac{\sigma_f}{E}(2N_f)^c \tag{2.46}$$

where E is the Youngs modulus, c is the slope of the log-log fitting curve, $\Delta\varepsilon_e$ is the elastic strain amplitude, and σ_f is the material constant that increases with fatigue yield strength.

Coffin and Manson (Coffin, 1954; Manson, 1954) presented a more sophisticated approach for uniaxial strain controlled loading using change in elastic locus due to Bauschinger effect(Bauschinger, 1880). The Coffin-Mansion model is given as,

$${N_f}^{m_3}\Delta\varepsilon_p = C_3 \tag{2.47}$$

where now the prediction is based on the plastic strain amplitude, $\Delta\varepsilon_p$, and m_3 and C_3 are material constants that have been fitted from at least two experiments.

Basquin-Coffin-Mansion(BCM) (Manson and Hirschberg, 1964; Norman, 2013) is a popular model that combines the Basquin and Coffin-Mansion models to estimate the strain-life relationship for metals and alloys. The elastic strain amplitude $(\Delta{\varepsilon_a}^e)$ and plastic strain amplitude $(\Delta{\varepsilon_a}^p)$ of the model are related to the Basquin and Coffin-Mansion models, respectively. The BCM model is given as,

$$\Delta\varepsilon_a = \Delta{\varepsilon_a}^e + \Delta{\varepsilon_a}^p = \frac{\sigma_f}{E}(2N_f)^c + \varepsilon_f(2N_f)^{c_1} \tag{2.48}$$

where c and σ_f are the fatigue strength exponent and coefficient, respectively, and ε_f and c_1 are the fatigue ductility coefficient and exponent, respectively.

The Smith-Watson-Topper(SWT)(Smith et al., 1969) model is an extension of the BCM model that accounts for mean stress effects by assuming that the product of peak

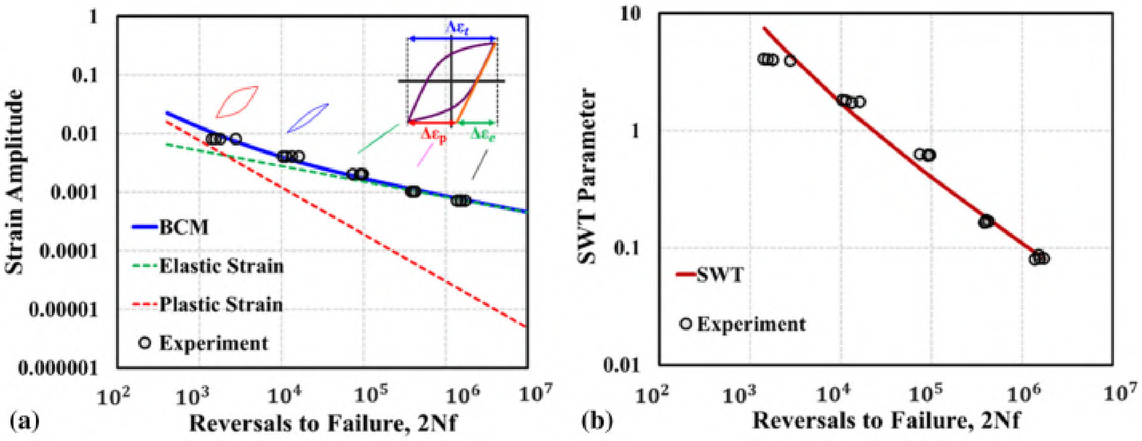

Figure 2.27: Empirical methods for fatigue life prediction a) Basquin-Coffin-Mansion (BCM) b) Smith-Watson-Topper (SWT) for SLM Hastelloy-X at room temperature Esmaeilizadeh et al. (2022)

stress at half life (σ_{max}) cycle and strain amplitude is constant. This is known as the SWT parameter, and it is dependent on four variables, similar to the BCM model. The SWT model is formulated as,

$$\sigma_{max}\varepsilon_a = \frac{{\sigma_f}^2}{E}(2N_f)^{2c} + \sigma_f \varepsilon_f (2N_f)^{c+c_1} \tag{2.49}$$

The models presented above are the most simple and common ones and only applicable for uniaxial loading. Many other more complex models can be found for uniaxial cases, but its analysis is out of the scope of this thesis. For multiaxial cases, most phenomenologial models are based on the critical plane approach (Deguang, 1998; Fatemi and Yang, 1998).

The application of phenomenological fatigue models to study fatigue life of Hastelloy-X has been covered done by (Branco et al., 2018b) and (Esmaeilizadeh et al., 2022). In the second work, the authors established a link between fatigue life and strain amplitude using the BCM model for SLM manufactured Hatselloy-X. Figure 2.27a depicts the $\varepsilon - N$ curve for the BCM model, elastic model, and plastic model, as well as the comparison with experimental data. The model is very accurate across the range from LCF to HCF regimes, however it does not account for mean stress effects. Esmaeilizadeh et al. (Esmaeilizadeh et al., 2022) used the SWT model to fit the experimental data, and the resulting SWT-N curve is presented in figure 2.27b. Esmaeilizadeh et al. (Esmaeilizadeh et al., 2022) employed the Jahed-Varvani (JV) model(Jahed et al., 2007) to predict the fatigue life for SLM Hastelloy-X under strain-controlled loading. The JV model is predicated on the idea that dissipated energy density has the highest impact on fatigue damage.

In a different study, Branco et al.(Branco et al., 2018b) employed the Ellyins model to predict fatigue lives and came to the conclusion that accurate fatigue lives could be predicted by taking into consideration total strain energy density.

2.5.2 Micromechanics based fatigue life prediction

In metallic alloys, fatigue crack initiation involves many length scales, resulting in plastic deformation localisation in slip bands. The location of a crack is determined by local microstructural characteristics such as grain size, shape, and orientation. Furthermore, AM is prone to defects such as porosity, lack of fusion, and surface roughness, and their influence on crack nucleation is dependent on local microstructural features. It should be highlighted that in the quasi-static analysis, average microstructural parameters are sufficient to predict yield strength and strain hardening behaviour; however, for fatigue, comprehending damage localization and their statistical distribution is critical from a modelling standpoint (Segurado et al., 2018).

The fatigue life is classified in low cycle fatigue (LCF) or high cycle fatigue (HCF). The plastic deformation happens in numerous grains in the LCF regime, but it is heterogeneous and localised. In contrast, the plastic deformation in HCF is highly dependent on the defects through which the plasticity deformation localises (Cruzado et al., 2017). Therefore, microstructure sensitive models are advantageous because they can establish a correlation between SLM alloy microstructure and fatigue performance taking into account the heterogeneous plastic deformation within the grains(Manonukul and Dunne, 2004; Sweeney et al., 2013; McDowell and Dunne, 2010). Based on these models, local microstructural characteristics such as grain size, shape, and orientation influence the local microfields and internal variables that evolve every cycle in the RVE under cyclic loading. According to Manonukul et al. (Manonukul and Dunne, 2004), these microsfields act as a driving force for crack formation, and various fatigue indicator parameters (FIP) are established which correlate with fatigue life (McDowell and Dunne, 2010). It should be emphasised that FIP values are determined by solving the BV problem and vary across the RVE based on local microstructural features.

Various definitions of FIP are available in the literature, including accumulated plastic slip per cycle $\mathbf{P}(\mathbf{x})$ (Manonukul and Dunne, 2004; McDowell et al., 2003; Sweeney et al., 2012, 2014), Fatemi Socie parameter $\mathbf{FS}(\mathbf{x})$ (Bennett and McDowell, 2003; Castelluccio and McDowell, 2014; Zhang et al., 2015; McDowell, 2007) , energy dissipated per cycle $W(\mathbf{x})$ (Dunne, 2014), plastic accumulated work per cycle (Sweeney et al., 2012, 2015), and many more (Ozturk et al., 2016; Sangid, 2013). The FIP based on plastic slip per cycle is defined as follows:

$$\mathbf{P}(\mathbf{x}) = \int_{cyc} \sqrt{\frac{2}{3}\mathbf{L}_p(\mathbf{x}) : \mathbf{L}_p(\mathbf{x})dt} \tag{2.50}$$

where, $\mathbf{L}_p$ is the plastic velocity gradient.

Secondly, the Fatemi-Socie parameter $\mathbf{FS}(\mathbf{x})$ is defined using of the maximum plastic amplitude of shear strain $\Delta\gamma^k$ on specific plane k, normal stress, σ_n perpendicular to plane k, and yield stress sigma σ_Y.

$$\mathbf{FS}(\mathbf{x}) = \frac{\Delta\gamma^k}{2}\left(1 + K\frac{\sigma_n{}^k}{\sigma_Y}\right)_{max} \tag{2.51}$$

Finally, the local value of energy dissipated per cycle W_{cyc}^{β} is defined using resolved shear stress τ_β and shear strain rate $\dot{\gamma}^\beta$ on slip system β as,

$$W(\mathbf{x})_{cyc}^{\beta} = \int_{cyc} \tau^\beta \dot{\gamma}^\beta dt \tag{2.52}$$

There is no obvious rule for choosing one FIP over the others. For comparable materials and processes, multiple authors rely on distinct definitions of FIP. An interesting approach for choosing the most appropiate FIP for a material was presented by (Rovinelli et al., 2015b) combining tomography experiments, CP-FFT simulations and machine learning, but it relies on a singular experimental framework and cannot be replicated in standard laboratories.

FIPs are the local values determined at a point x in an RVE in the preceding Eqs. 2.50,2.51, 2.52. As a result, the discretization of an RVE plays a significant role in the prediction of localised FIPs at a point $\mathbf{x}$ (Sweeney et al., 2013). To eliminate mesh dependence, FIP should be averaged over a well-defined integration volume representing the crack initiation zone. In the literature, two separate volume averaging approaches, grain (Shenoy et al., 2007) and slip band (Shenoy et al., 2007; Cruzado et al., 2018), are utilised to achieve this goal . The maximum non-local FIP in the integration volume is recognized the indicative parameter for fatigue damage accumulation over the cycle in the RVE and used to predict the fatigue crack initiation life. Castellucio et al.(Castelluccio and McDowell, 2015), Cruzado et al. (Cruzado et al., 2018) and Lucarini et al.(Lucarini and Segurado, 2019) have recently adopted the band averaged integration volume, in which FIPs are averaged on a slip band of constant thickness t parallel to the slip plane at point x. When an RVE is subjected to cyclic loading, the maximum FIP, W_{cyc}^b is obtained by employing the band averaging approach, which is formulated as,

$$W_{cyc}^b = \max_{i=1,nb}\left\{\max_{\beta_i} \frac{1}{V_i}\int_{V_i} W_{cyc}^{\beta_i}(x)dV_i\right\} \tag{2.53}$$

where β_i represents three distinct slip systems included in a slip plane parallel to the band i, V_i denotes band volume, while nb denotes the total number of bands in an RVE (Cruzado et al., 2018).

Once the non-local definition of FIP has been established, the final step is to connect the FIP to the fatigue life. Some micromechanics based models distinguish between incubation, small crack propagation (driven by the FIPs) and growth (McDowell et al., 2003). Nevertheless, the most common approach is assuming that, because the fatigue crack initiation process accounts for the majority of the total life, crack propagation can be ignored and the total fatigue life can be predicted by a single expression (Tanaka and Mura, 1981; Manonukul and Dunne, 2004; Cruzado et al., 2017, 2018; Lucarini and Segurado, 2019; Shenoy et al., 2007). The latter approach is used for fatigue life prediction in this work, so it is discussed here.

Tanaka and Mura (Tanaka and Mura, 1981) first developed a power law type relationship between FIP and fatigue crack nucleation life based on a single material constant FIP_{TM} and grain diameter d_g.

$$N_i(FIP)^2 = \frac{FIP_{TM}}{d_g} \tag{2.54}$$

Later, Manonukul et al. (Manonukul and Dunne, 2004) proposed a linear model, in which they hypothesised the existence of a critial value of FIP and whenever the local FIP at a point exceeds the critical FIP, it was assumed that crack has initiated, based on the assumption that initiation phases are orders of magnitude higher than crack propagation.

$$FIP.N_i = FIP_{crit} \tag{2.55}$$

This method, which is based on the accumulated plastic strain per cycle, can predict the fatigue life for the LCF and HCF regimes for C263 alloy with only one fitting parameter. Cruzado et al.(Cruzado et al., 2017) extended the above mentioned model in Eq. (2.55) to predict the bi-linear coffin mansion regime. They used the strain energy dissipation per cycle as FIP and a power law type model with two fitting parameters to predict the fatigue crack initiation life.

3 Fabrication, microstructure characterization and synthetic microstructure generation

As previously discussed in the literature, microstructure has an important influence on the mechanical performance of SLM-fabricated alloys. The first stage of this *Experiment-Modeling-Validation* approach is to fabricate using SLM Hastelloy-X specimens in various geometries for their microstructure and mechanical characterization. The second stage is to gather microstructural details from the EBSD analysis, such as grain shape, size, and orientations, which will be the initial input to the RVE. Finally, models will be constructed using microstructural data and the modeling and experimental results will be compared in order to validate them.

In this chapter, first the SLM process followed by ITP-Aero for the fabrication of SLMed specimens in various thicknesses will be described. Then the microstructure characterization and the production of synthetic microstructure, or RVE, will be discussed in detail, since they serve as the foundation for microstructure-sensitive virtual testing modeling.

This chapter is partially based on the paper *'Effect of printing direction and thickness on the mechanical behavior of SLM fabricated Hastelloy-X '* which was published in the

Table 3.1: Hastelloy-X nominal chemical composition (Jordan et al., 1993)

Element	Ni	C	Cr	Co	Mo	W	Fe	Mn	Si	P	S
Weight %	Bal	0.10	22.0	1.5	9	0.6	18.5	1	1	0.04	0.03

International Journal of Plasticity in June 2022.

3.1 Material and specimen fabrication

The Hastelloy-X specimens considered in this work have been fabricated using a Selective Laser Melting technique by ITP-Aero. The nominal material composition is shown in Table 3.1.

A Renishaw RenAM 500Q machine was used to build the sample. The SLM parameters such as energy density, hatch spacing and scan speed were optimized, and the layer thickness, t used was $60\mu m$. A 67° rotation in the laser scanning direction was performed between successive layers. Figure 3.1 shows a graphical representation of the SLM process, including layer thickness, coordinate axes, build direction, and laser scan rotation of each layer. The powder was produced using the Ar gas atomization and the powder size ranges from $15\mu m$ to $53\mu m$. Different specimens were prepared in ITP-Aero using SLM in the form of bulk blocks and flat sheets of different thicknesses were used for tensile and fatigue tests. The building direction was the same for both bulk and flat samples, Z direction.

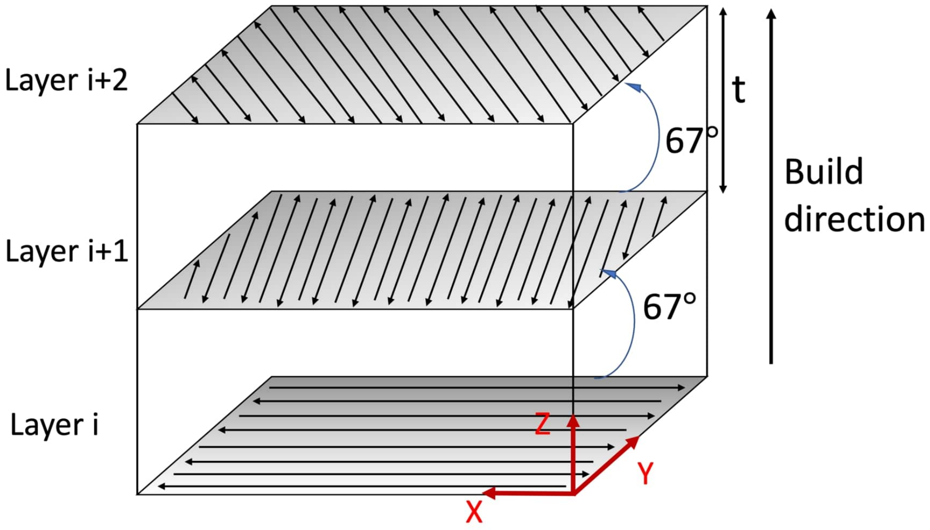

Figure 3.1: The graphical representation of the SLM process shows Build Direction(BD), layer thickness, coordinate axes and rotation of laser scan direction.

The bulk samples were additively manufactured with orientations parallel to the building direction, direction Z (Bulk Z), and perpendicular to the building direction (Bulk X). The bulk Z sample was cylindrical with a diameter of 15mm and length 100 mm. Coupons were machined to the common tensile cylindrical dog-bone shape having a gauge length of 25.4 mm. The bulk X specimen was fabricated in a rectangular shape with dimensions 15mm×15mm×100mm and was machined to a cylindrical dog-bone shape with the same gauge-length.

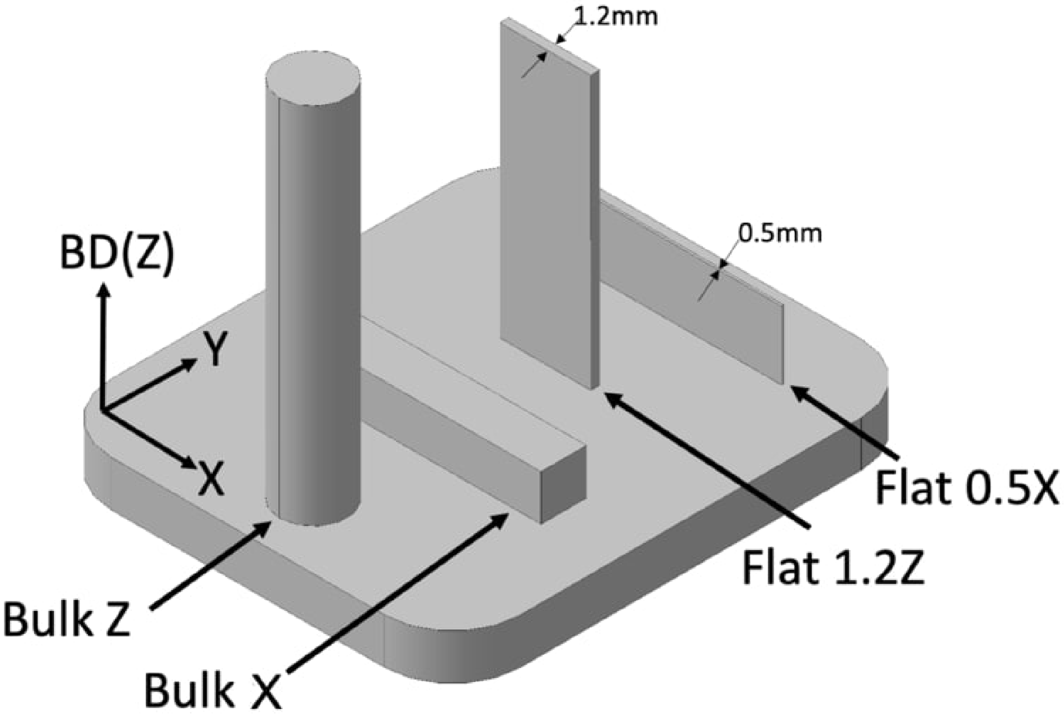

Figure 3.2: Bulk and flat specimens on the fabrication platform showing building direction and orientation.

Two different flat samples were fabricated, Flat 1.2Z and Flat 0.5X, with dimensions 1.2 mm×15 mm×70 mm and 0.5 mm×15 mm×70 mm, respectively (figure 3.2). The 1.2 mm thick sample (Flat 1.2Z) was oriented in the building direction (Z), while the 0.5 mm thick specimen (Flat 0.5X) orientation was direction X (figure 3.2). Coupons were machined to a tensile flat dog-bone shape having a gauge length of approximate 15.8 mm. Only the lateral surfaces were machined and the rest of the surfaces were preserved as a built surface condition.

All samples were heat treated at 1170°C for 30 minutes followed by gas fan quench and were tested in annealed conditions. The SLM thermal history was removed by this treatment and the SLM process dendrites were dissolved. This annealing also significantly minimises the residual stresses of Hastelloy-X, as observed in Karapuzha et al.

(Karapuzha et al., 2022). It is also interesting to note that precipitates were found in significant quantities in the Ni-based as-build samples, but after the heat treatment the presence of precipitates in the alloy was strongly reduced or even suppressed. Finally, the resulting porosity was obtained using a microCT analysis and was below 1% in all the samples.

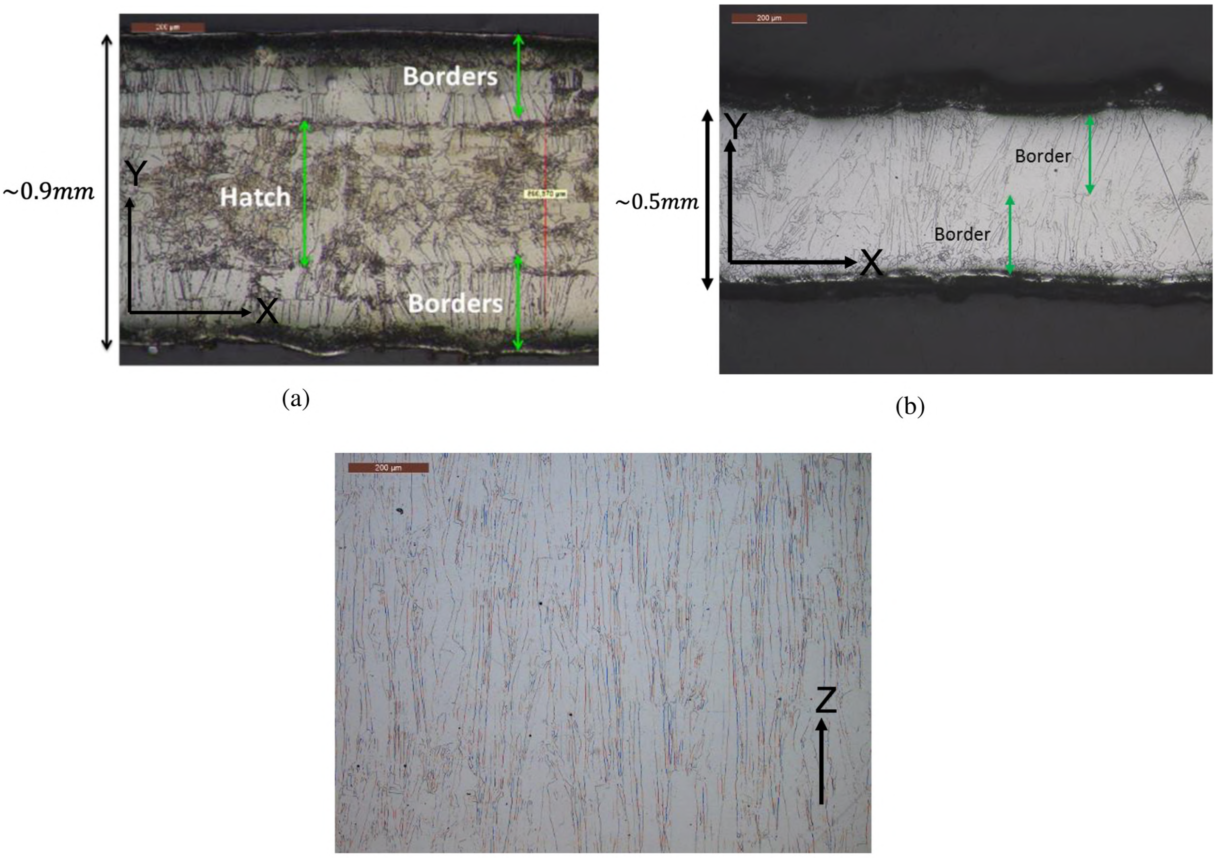

(a)

(b)

(c)

Figure 3.3: XY section of flat specimens showing different microstructure in the border and in the hatch area, as function of thickness a) 0.9mm b)0.5mm, and c) shows XZ section of 0.5mm thick sample with very strong columnar grains (Courtesy: ITP Aero)

3.1.1 Microstructure of SLM Hastelloy-X

The melting strategy and the parameters of the building process generate different microstructures in the material. Both the bulk and flat specimens show a different grain structure in the BD than in the XY plane, with elongated grains in the building direction, with a grain aspect ratio higher for the thinner samples. The direction of these columnar grains depends on the heat flow during the process, which is higher in all cases in the building direction (Tomus et al., 2016; Keshavarzkermani et al., 2019)

In addition to the elongation along the building direction, planar specimens also show grain elongation in the XY plane, which can be attributed to the heat extraction being higher within the thin-sample plane than the sideways toward the lower-conductivity powder bed.

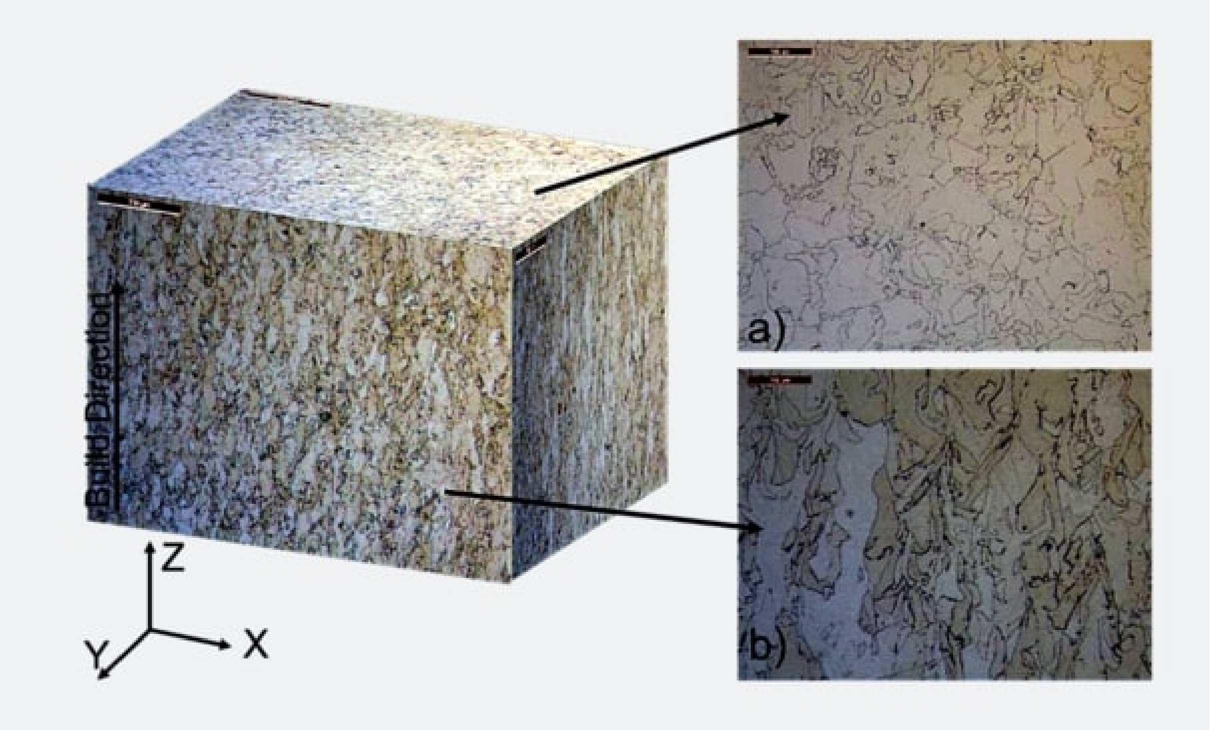

Figure 3.4: Microstructure of SLM manufactured bulk Hastelloy-X (a) Equiaxed grain structure in transverse direction (b) Elongated grain structure in building direction (Courtesy: ITP Aero)

Optical microscopy and Electron Backscatter Diffraction (EBSD) imaging were used to characterize the grain structure and obtain grain size, shape, and orientation distributions.

3.1.2 Grain shape and size distribution

In the case of flat samples, the solidification thermal gradient in the XY plane is constrained and the solidification near the free surface led to a special microstructure consisting of columnar grains with an elongated axis in direction Y, figure 3.3(a,b). This area is called *border*, it has a width of approximately 0.2mm for each free surface, which corresponds to 1-2 grains.

The portion of the transverse section of the specimen affected by these layers depends on the sample thickness. In the thinnest samples (0.5mm), the external layers occupy all the section (figure 3.3*b*), while in the larger samples (0.9 and 1.2mm) two regions can be differentiated, the *border*, and a central region, the *hatch*, with more isotropic grain size (figure 3.3a). In the building direction of flat samples, the grains were elongated with an average aspect ratio of 10:1 for 1.2mm and 20:1 for 0.5mm.

The flat sample with 1.2mm has around 4-5 grains along Y direction, compared to flat sample with 0.5mm thickness which has only 1-2 grains along thickness. This uneven distribution of grains per section, together with their preferential orientation, gives rise to a highly anisotropic material response.

Surface roughness is present in all specimens because of the unmelted and semi-melted powder left on the surface. The relative thickness of the rough surface area scales with the diameter of the laser. In flat samples, the surface roughness plays an important role as the effective cross sectional area changes with the roughness and impacts the effective load carrying capacity during uniaxial tensile tests. The relative area of the specimen transverse section affected by the roughness increases when decreasing the specimen section (figure 3.3c), leading to a strong mechanical effect in the case of the smallest samples (0.5mm).

The microstructure of the bulk Z specimen shows elongated grains in the building direction and a nearly equiaxed grain structure in XY section (see figure 3.4). The average aspect ratio of the elongated grains in BD was 2:1, and the average grain size was 35μm. In the XY plane, the equiaxed grains follow a log-normal distribution with average $17.69\mu m$ and standard deviation 0.94. The bulk X sample shows almost equiaxed grain structure in both sections. The grains follow a log-normal distribution with average $20.13\mu m$ and standard deviation 0.76.

3.1.3 Texture analysis

EBSD measurements were made in both bulk and plain samples prior to mechanical testing. For this analysis, a Scanning Electron Microscope (SEM) equipped with an EBSD detector was used. The step size used for all EBSD scans was $1.5\mu m$. The associated Euler angles were computed for all pixels with a confidence index greater than 0.02. The OIM analysis software was used to calculate the pole figures and texture.

The resulting EBSD orientation maps are represented in figure 3.5 for XY and XZ sections of Hastelloy-X. The colors in the map indicate the orientation of the building direction with respect to the crystal reference frame, which follows the IPF triangle.

To further analyze the texture of each specimen and the direction, pole figures were generated from the EBSD files using M-TEX software (Bachmann et al., 2011) and are represented in the left part of figure 3.6. The pole figures were generated in Z direction. In the case of bulk samples, it can be observed that the texture was almost random. In

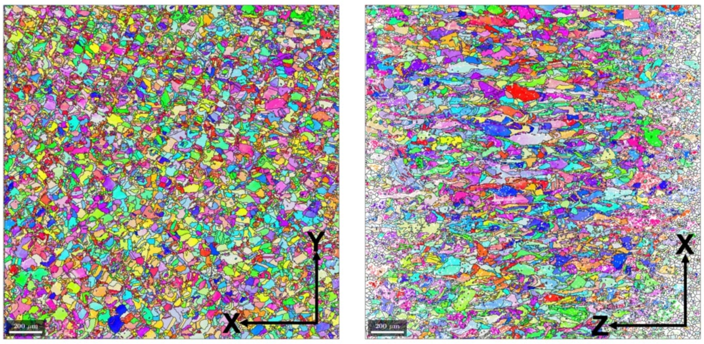

Bulk Z

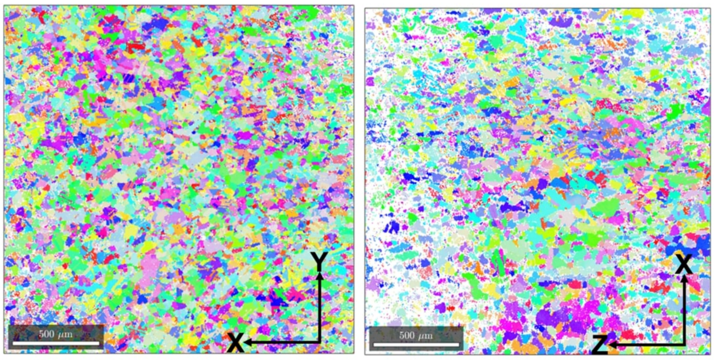

Bulk X

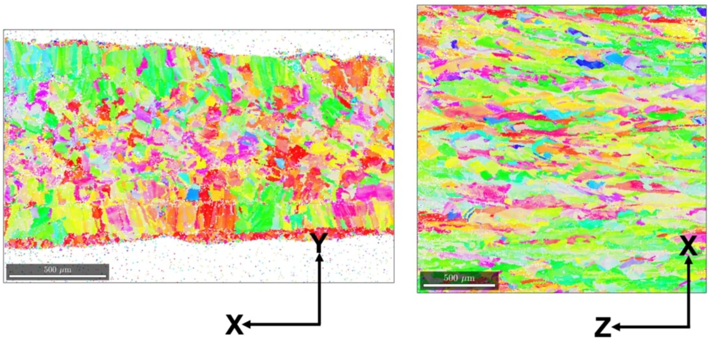

Flat 1.2mm

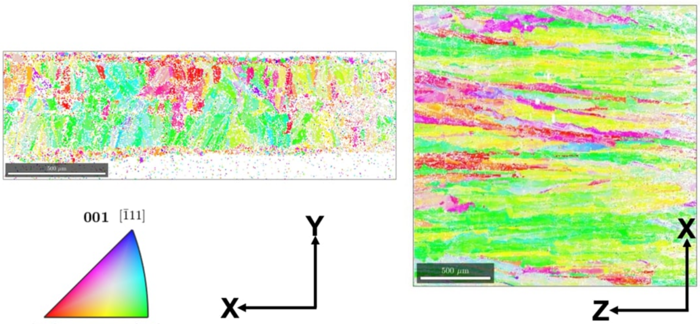

Flat 0.5 mm

Figure 3.5: EBSD maps of bulk Z (top), bulk X (second), flat 1.2 mm thick (third) and flat 0.5mm thick (bottom) specimens in XY and XZ sections. The colours in the map indicates the orientation of build direction with respect to crystal reference frame follows IPF triangle.(Courtesy: ITP Aero)

the case of flat specimens, the orientation of the boundary layers affects the overall texture and the non-homogeneous distribution of the crystallographic planes is observed (figure 3.6).

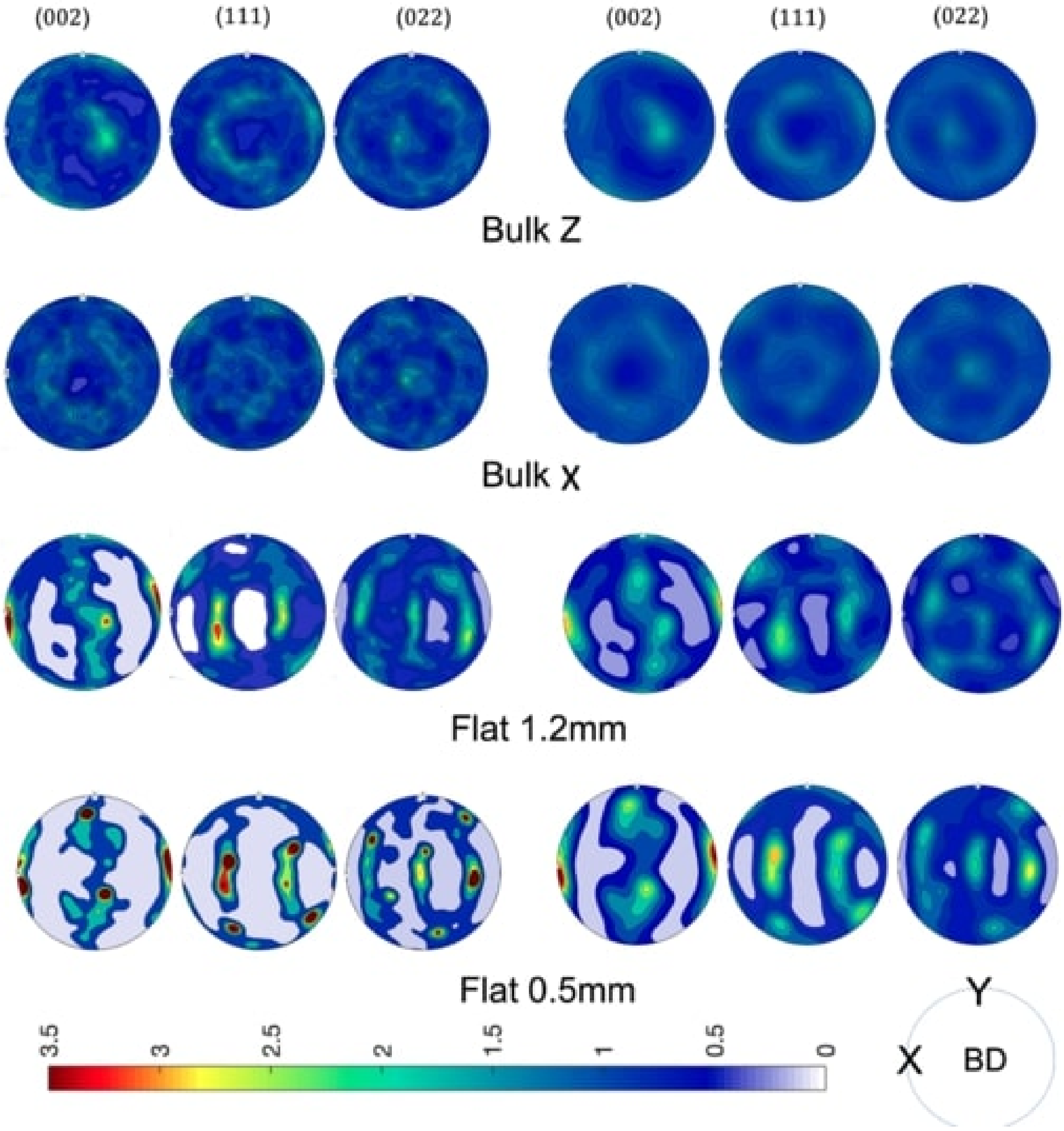

Figure 3.6: Pole figures using all orientations in the microstructure (left) and obtained sampling the ODF using Monte-Carlo method (right) for different bulk and plain specimens.

3.2 RVE Generation

The RVEs corresponding to the microstructures of each specimen are generated synthetically to statistically represent the grain size, shape, and orientation distributions obtained by EBSD.

The 2D grain size distribution was obtained from the EBSD maps shown in figure 3.5 using the texture analysis software *MTEX* (Bachmann et al., 2011). The software assumes an equiaxed grain microstructure, and the equivalent diameter of grain (assuming a circular shape) in 2D can be calculated as follows:

$$D_{eq_{2D}} = \sqrt{\frac{4A_g}{\pi}} \tag{3.1}$$

where, A_g is the diameter of 2D grain. The 2D grain diameters are fitted to the typical log-normal distribution.

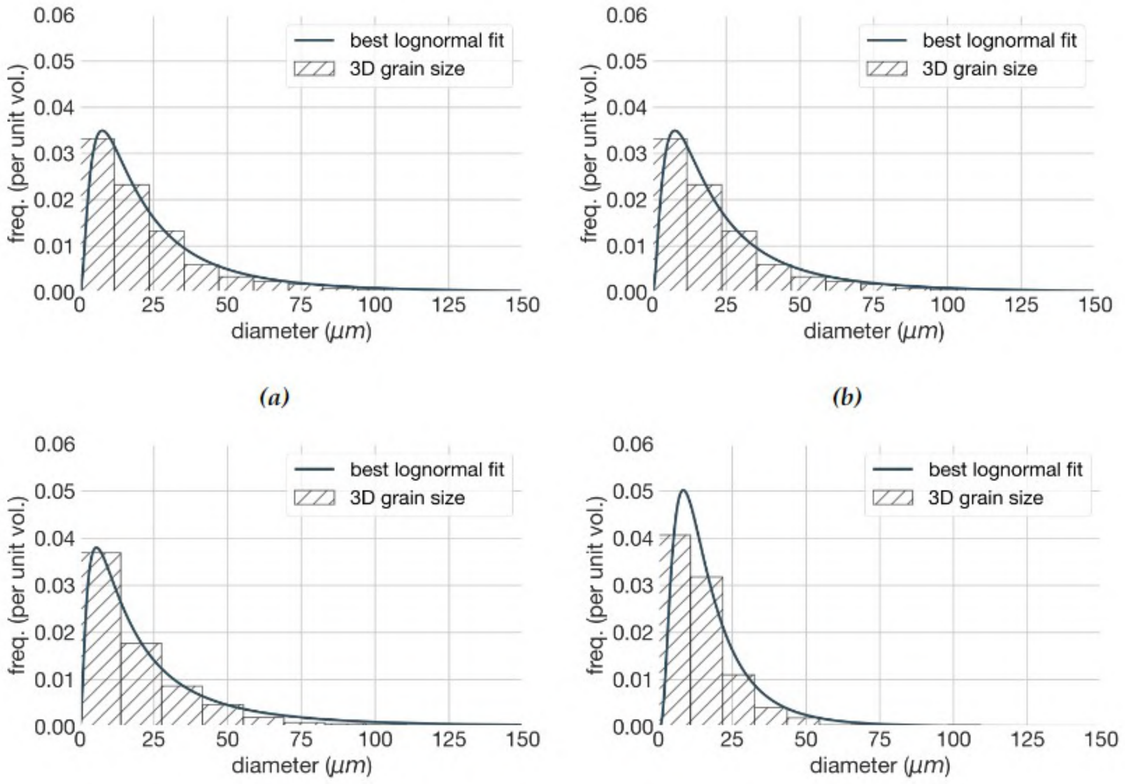

(a) *(b)*

(c) *(d)*

Figure 3.7: The histograms and lognormal distribution of 3D apparent diameters for a) Bulk Z b) Bulk X c) flat 1.2 mm d) flat 0.5 mm samples generated from 2D grain diameters using *GrainSizeTools* tool.

This 2D grain size distrbution was then converted into a 3D distribution assuming spherical grains using the open source tool *GrainSizeTools* (Lopez-Sanchez, 2018). The 3D grain size data is approximated by a lognormal distribution function. In both distributions, equiaxed grains are assumed, and the aspect ratio will be considered in a further step. Figure 3.7 depicts the histogram and lognormal distribution of 3D apparent diameters for all samples generated by open source tool *GrainSizeTools* (Lopez-Sanchez,

Table 3.2: Approximate aspect ratios in terms of length of grains included in the RVE

Sample	Bulk Z	Bulk X	Flat 1.2	Flat 0.5
X	1	1	1	1
Y	1	1	2	4
Z	2	1.5	10	20

2018). The lognormal distribution was used as input to generate a synthetic equiaxed polycrystalline microstructure using a weighted Voronoi tessellation in which the points defining the grain centers and the corresponding weights are defined to fulfil the target grain size distribution (Lucarini and Segurado, 2019). Finally, the RVEs are deformed in each direction proportionally to the aspect ratios (Table 3.2) measured in order to obtain the actual grain shape.

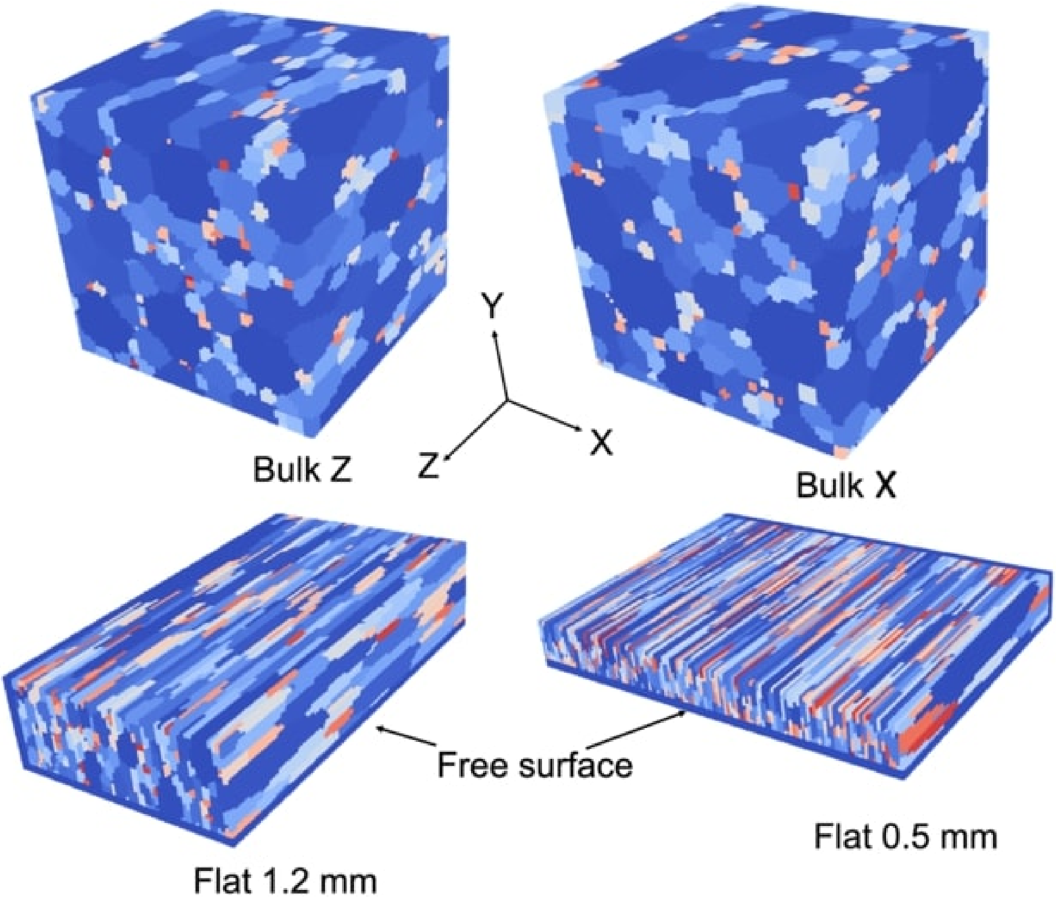

Figure 3.8: 3D images RVEs of polycrystalline Hastelloy-X for bulk Z(top left), bulk X(top right), flat 1.2mm (bottom left), 0.5mm(bottom right). Colours indicate the grain numbers

In the case of bulk samples (figure 3.5) the grain aspect ratios were chosen as $1:1:2$ for bulk Z and $1:1:1.5$ for bulk X sample. The real specimen cross sections are much larger than the average grain size, so the final RVE is taken as a cube with periodic boundary conditions in the three directions to represent an infinite arrangement of grains. These models contain 800-1000 grains on average.

In the case of flat samples, a very strong columnar grain structure was observed in the BD (Z) direction (figure 3.5). Therefore, the approximate aspect ratios were determined in terms of grain length for both 1.2Z and 0.5XY. These aspect ratios are $1:2:10$ for 1.2Z and $1:4:20$ for 0.5XY. In these samples, the actual cross section is comparable to the grain size, and the synthetic RVEs can reproduce the full specimen in this plane including a similar number of grains. To this aim, non-cubic RVEs are generated with relative edge sizes equal to the aspect ratio of the grains. Moreover, in these cases, stress-free boundary conditions are set on the surfaces of the cross section, to mimic the effect of the ratio between the actual specimen thickness and grain size. The prescription of Neumann free boundary conditions is approximated including very compliant layers at each of the RVE edges, while periodicity was preserved in the loading direction. The approximated number of crystals was 850 for the 1.2mm samples and 800 for the 0.5mm. The resulting RVEs are represented in figure 3.8. The discretization of the RVEs for the FFT simulations was done by rastering the Voronoi geometries in 64^3 voxels. This level of discretization was sufficient to obtain a macroscopic response of the voxelized RVE almost invariant under further discretization (Cruzado et al., 2017).

Once the geometries of the RVEs are generated, the orientation of each grain is set to have a statistically representative sampling of the texture measured for the specimen under consideration in the RVE. A Monte Carlo algorithm was used to randomly generate a set of points from the orientation distribution function (ODF) of the EBSD maps. In this study, the points were randomly generated from the actual EBSD maps. The number of random points was the same as the grains in an RVE, where each point carries information on a grain orientation for each grain. The pole figures resulting from the Monte Carlo algorithm are represented in the right column of figure 3.6. It can be seen that the sampled pole figures preserve the main characteristics of the original textures.

To further validate the representation of the microstructure, the sections of synthetic RVEs for the bulk and flat samples are shown in figure 3.9. The colors in the synthetic RVE correspond to the IPF using the same color scheme as that of experimental EBSD maps (see figure 3.5), so this figure represents an EBSD image of the synthetic RVEs. It can be concluded that qualitatively and quantitatively the EBSDs of the real material (Fig.3.5) and the synthetic microstructures (figure 3.9) are very similar.

To summarise, the digital representation of the microstructure is critical for polycrystal homogenization approaches. An RVE is constructed that takes into account

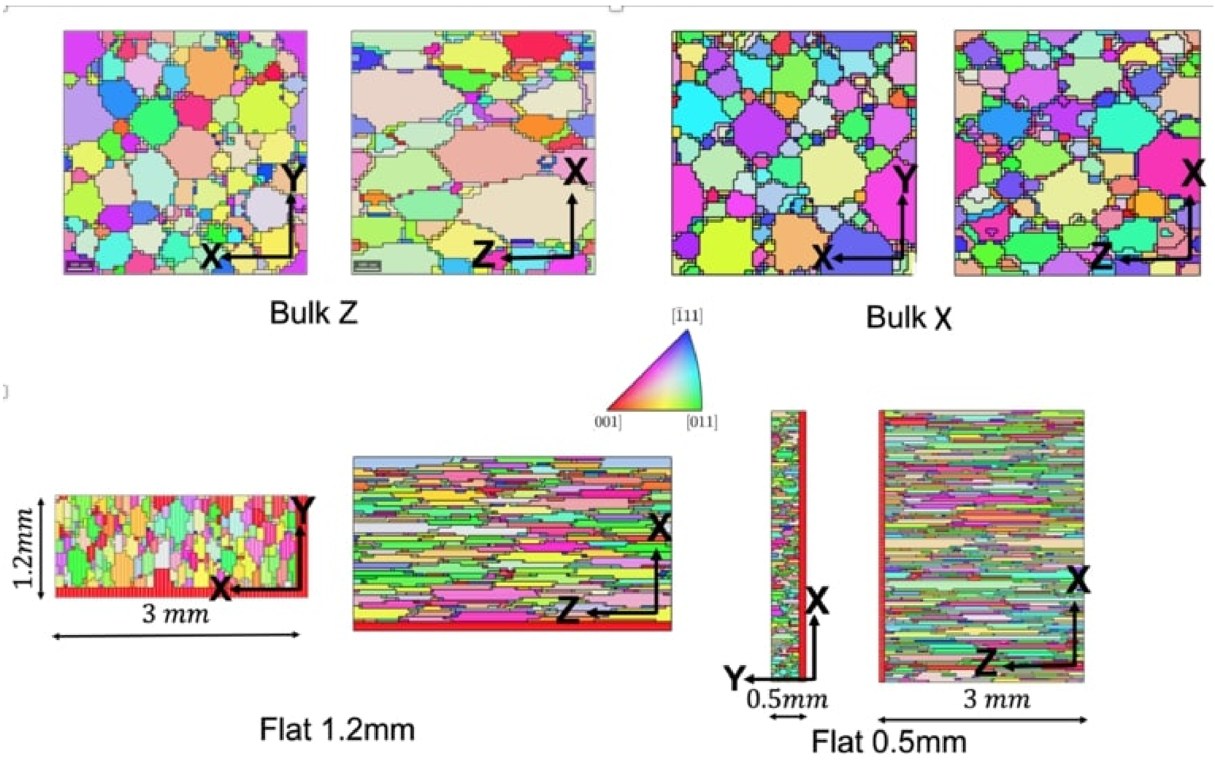

Figure 3.9: Cross sections of RVEs of polycrystalline Hastelloy-X for bulk Z(top left), bulk X(top right), flat 1.2mm (bottom left), 0.5mm(bottom right). The colors in the map indicates the orientation of build direction with respect to crystal reference frame following IPF triangle. The red lines in flat samples indicate the free surfaces.

various microstructural features such as grain size, shape, orientation, as well as geometric features such as final sample thickness in the case of flat samples. It should be noted, that all of these features are extracted from real microstructure or EBSD. As a result, these RVEs precisely represent the actual microstructure and anisotropy.

4 Microstructure sensitive quasi-static response of Hastelloy-X manufactured with SLM

In this section, the CP-FFT framework presented will be applied to predict the mechanical response of AM fabricated Hastelloy-X specimens with different shapes and printing directions. The objective is to validate the Hastelloy-X polycrystalline model and to elucidate whether the changes experimentally observed in the mechanical response for different AM samples can be directly correlated with their changes in the polycrystalline microstructure. The model predictions of the elastic modulus and the monotonic elastic-viscoplastic response for different temperatures and for different specimens will be analyzed in the next sections. Note that all curves in the section are normalized by a reference stress τ_0 and a reference strain ϵ_{max}, requirement of the confidentiality agreement signed with the industrial partner funding this study. τ_0 corresponds to the CRSS identified for Hastelloy-X grains at room temperature. ϵ_{max} is the strain corresponding to the ultimate tensile stress of specimen bulk Z, which is the most ductile specimen.

This chapter is based on the study *'Effect of printing direction and thickness on the mechanical behavior of SLM fabricated Hastelloy-X'* which was published in the International

Journal of Plasticity in June 2022.

4.1 Mechanical characterization

The tensile stress-strain behaviour of SLM manufactured Hast-X was determined using an Universal Testing Machine. The tests were carried out by Westmoreland Mechanical Testing & Research, Inc. laboratory according to ASTM E8M for tests at room temperature and according to the ASTM E21 for tests at high temperature. All the tests were conducted at a constant strain rate of $\dot{\epsilon} = 5 \times 10^{-5} s^{-1}$ until reaching the yield point and at $\dot{\epsilon} = 1.67 \times 10^{-3} s^{-1}$ thereon. The bulk sample with a cylindrical shape (bulk Z), is subjected to uniaxial tensile loading in building direction (z), while the sample with a rectangular shape (bulk X) is subjected to uniaxial tensile loading in X direction. The flat samples with 1.2 and $0.5mm$ thickness were subjected to uniaxial tensile loading in Z and X directions, respectively.

4.2 Crystal plasticity model

A phenomenological crystal plasticity model (Cruzado et al., 2017) has been adapted to model the mechanical response of Hastelloy-X grains as a function of temperature. The model is based on the multiplicative decomposition of the deformation gradient **F** into elastic ($\mathbf{F}^e$) and plastic ($\mathbf{F}^p$) components as

$$\mathbf{F} = \mathbf{F}^e \mathbf{F}^p \tag{4.1}$$

where, $\mathbf{F}^p$ is the plastic deformation gradient in the intermediate configuration.

The plastic velocity gradient L^p is defined in the intermediate configuration as the sum of shear rates $\dot{\gamma}^\alpha$ on all slip systems α,

$$\mathbf{L}^p = \dot{\mathbf{F}}^p {\mathbf{F}^p}^{-1} = \sum_\alpha \dot{\gamma}^\alpha \mathbf{s}^\alpha \otimes \mathbf{m}^\alpha \tag{4.2}$$

where, $\mathbf{s}^\alpha$ and $\mathbf{m}^\alpha$ are unit vectors in the slip direction and normal to the slip direction, respectively, in the reference configuration.

The symmetric second Piola-Kirchoff stress tensor **S** is linearly related to the Green-Lagrange strain $\mathbf{E}^e$ by, the fourth order elastic stiffness tensor $\mathbb{C}$.

$$\mathbf{S} = \mathbb{C}\mathbf{E}^e \tag{4.3}$$

The resolved shear stress τ^α on the slip plane α is taken as,

$$\tau^\alpha = \mathbf{S} : (\mathbf{s}^\alpha \otimes \mathbf{m}^\alpha), \tag{4.4}$$

and the Cauchy stress tensor can be recovered by,

$$\sigma = \frac{1}{J^e} \mathbf{F}^e \mathbf{S} \mathbf{F}^{e^T} \tag{4.5}$$

where J^e is the determinant of $\mathbf{F}^e$.

The plastic slip rate in a given slip system is given by a power law function as

$$\dot{\gamma}^\alpha = \dot{\gamma}_0 \left(\frac{|\tau^\alpha|}{g^\alpha} \right)^{\frac{1}{m}} \text{sign}(\tau^\alpha) \tag{4.6}$$

where, $\dot{\gamma}_0$ and m stand for reference strain rate and strain rate sensitivity parameter respectively. The function g^α represents the critical resolved shear stress on the α slip system.

The evolution of the CRSS for a given system, g^α, is obtained by the contribution of a shear strain $\dot{\gamma}^\beta$ in all slip systems β as,

$$\dot{g}^\alpha = \sum_\beta q_{\alpha\beta} h(\gamma_a) |\dot{\gamma}^\beta|. \tag{4.7}$$

where $q_{\alpha\beta}$ are the latent hardening coefficients, $(\alpha \neq \beta)$ with, $q_{\alpha\alpha} = 1$ and h is the self hardening modulus, The evolution of self-hardening follows Voce hardening model proposed in (Tome et al., 1984)

$$h(\gamma_a) = h_s + \left[h_0 - h_s + \frac{h_0 h_s \gamma_a}{\tau_s - \tau_0} \right] exp^{\left(\frac{-h_0 \gamma_a}{\tau_s - \tau_0} \right)} \tag{4.8}$$

being τ_0, τ_s, h_0 and h_s the hardening parameters and γ_a the accumulated plastic shear, defined as

$$\gamma_a = \sum_\alpha \int_0^t |\dot{\gamma}^\alpha| \mathrm{d}t. \tag{4.9}$$

4.3 Inverse parameter identification

First, the CP model parameters at room temperature of Hastelloy-X after annealing will be identified. The elastic constants for the single crystal are taken from Canistraro et al. (Canistraro et al., 1998). The parameters defining the critical resolved shear stress and hardening evolution are obtained by inverse fitting. The experimental data used for this purpose is the stress-strain response obtained in a uniaxial tensile test of the bulk sample Z, loaded in the building direction. The model used to predict that the response is the full FFT homogenization model with a synthetic RVE representing the microstructure of the bulk Z specimen(figure 3.8). Finally, since the strain rate does not play any role here, the strain-rate sensitivity parameters (reference strain rate, $\dot{\gamma}_0$ and strain rate sensitivity exponent, m), are taken from (Cruzado et al., 2017) for a similar alloy.

The RVE used for inverse parameter identification has a similar texture to the actual microstructure which accommodates approximately 1000 grains and 64^3 voxels. A Levenberg-Marquardt least squares algorithm is used, adapting the framework proposed by V. Herrera et.al. (Herrera-Solaz et al., 2014) to CP-FFT. The values identified using this procedure are the Voce hardening law parameters, τ_0, τ_s, h_0, and h_s, and the resulting values are given in Table 4.1 together with the rest of the CP model parameters. The experimental stress-strain curve is represented in figure 4.2 together with the polycrystalline model response after adjusting the CP parameters. The figure shows an almost superposed response between the model and experiments, confirming the accuracy of the CP model parameters fitting.

Table 4.1: *Crystal plasticity parameters of a AM Hastelloy-X at room temperature*

Elastic (GPa)	C_{11}	C_{12}	C_{44}	
	230.4	156.12	121.77	
Viscoplastic	m	$\dot{\gamma}_0(s^{-1})$		
	0.017	2.42×10^{-3}		
Isotropic hardening(MPa)	τ_0	τ_s	h_0	h_s
	τ_0	$1.228\tau_0$	$3.326\tau_0$	$1.078\tau_0$

4.4 Elastic response

Several models have been used to estimate the Young's modulus of each SLM specimen as a function of its microstructure. The most simple approaches considered are the Voigt (Voigt, 1889) and Reuss (Reuss, 1929) models, in which the only microstructure input is the texture given as the volume fraction of each crystal orientation included in the model. Both Voigt and Reuss are mean-field approaches which assume a constant value of the microfields in each crystal orientation. Voigt's model considers a constant deformation gradient (iso-strain) in all grains while Reuss assumes a constant stress tensor (iso-stress). The results of both approaches define two physical bounds for the polycrystal Young's modulus (Hill, 1952). The third model considered is the Elastic Self Consistent (ESC) approach, proposed by Tome et al. (Tome et al., 1984), in which

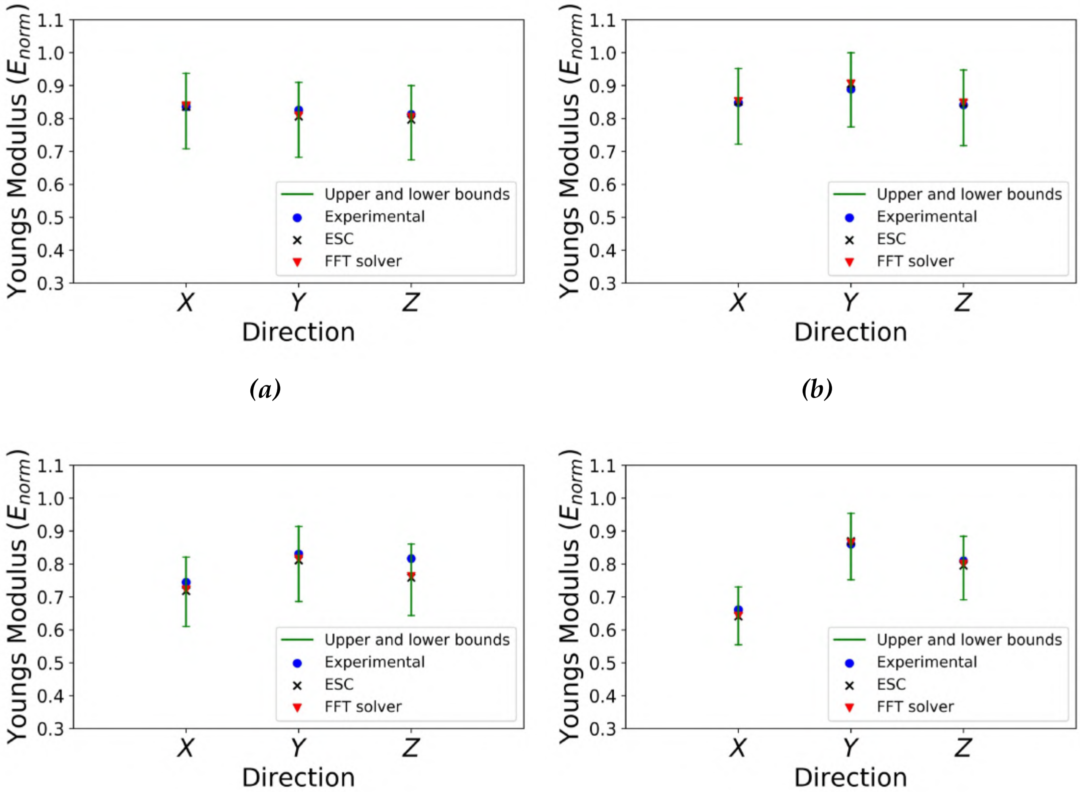

(a) *(b)*

(c) *(d)*

Figure 4.1: Young's modulus obtained by Voigt-Ruess bounds, Elastic self consistent approach (ESC), FFTMAD and experiments in X, Y and, Z directions for $a)$ bulk sample Z, $b)$ bulk sample X, $c)$ flat sample 1.2 mm thick and, $d)$ flat sample 0.5mm thick. Note that, elastic modulii are normalized by a constant factor, E_{max}

the elastic strain on each grain depends on its aspect ratio and orientation and is based on an Eshelby's inclusion framework. Its result lies always in between the Voigt-Reuss bounds. Finally, full field simulations have been performed using the polycrystalline FFT framework presented above to estimate the Young's modulii in all loading directions.

The parameters C_{11}, C_{12} and C_{44} at room temperature, given in Table 4.1, are used as input of the four models to describe the crystal elastic response. Four different samples are studied, the bulk sample with orientation parallel to BD (Bulk Z), perpendicular to BD (Bulk X), and flat samples with 1.2mm thickness and 0.5 mm thickness. In the case of the mean-field models, each orientation of the EBSD map (including around 40000 orientations) is included. In the ESC model, in addition to the orientation distribution, the average aspect ratio of the grains in each sample is also included as input (Table 3.2). The polycrystals used for the FFT simulations of each sample are described in section 3 including the number of grains (around 1000), aspect ratio, and discretization.

The Young's modulii obtained by each of the four models are represented in figure 4.1, together with its experimental value at room temperature. Note that all Young's modulii are normalized by a constant factor E_{max}, which is the maximum Young's modulus within the four samples. With respect to the experimental results, it can be observed in figure 4.1 that all samples show a certain degree of anisotropy as a result of the SLM process, being this anisotropy maximum for the flat sample with 0.5mm thickness. It is interesting to note that changes in printing direction and specimen thickness can lead to differences in Young's modulus of parts fabricated by SLM up to 25% (e.g. flat 0.5mm in X respect Bulk X in X.

The analysis of the model results shows that the Young's modulus predicted by both ESC and FFT models for all specimens fulfils the Voigt-Ruess bounds and lie in between them. Moreover, the Young's modulus obtained by the FFT solver and ESC approach are very similar, having a relative difference smaller than 1%. ESC and FFT models capture very accurately the experimental stiffness in all cases, with errors $< 1\%$ for bulk and $< 5\%$ for flat samples.

The conclusion of this comparison is that the differences found in the elastic behavior for different SLM specimens are only due to the changes in the microstructure (no effect of crystal response or porosity). The FFT and ESC models, which consider multiple microstructural features —texture and grain aspect ratios— accurately predict the experimental results. On the contrary, the Voigt and Reuss bounds, based on very simplistic approximations and without considering the aspect ratio, follow the experimental trend but fail to quantitatively predict the polycrystalline elastic response.

4.5 Elasto-viscoplastic response

The CP-FFT polycrystalline model was used to predict the elasto-viscoplastic response of the different Hastelloy-X specimens. Each RVE was deformed up to a normalized uniaxial strain, $\epsilon = 0.32\epsilon_{max}$, before damage started in the most brittle specimens. The CP parameters used are given in Table 4.1, and were obtained from the literature or fitted the results of the bulk sample Z loaded in the Z direction (section 4.3). Periodic boundary conditions in three directions are used for the bulk sample models, the most reliable solution considering the very high number of grains in the transverse sections of these specimens. The average stress- strain response of 10 RVEs and its comparison with experiments are shown in figure 4.2. The standard deviation in the stress-strain curves of the 10 different realizations was below 5% and is represented in figure 4.2 using error bars. It can be observed that the model was able to accurately capture the significant variation in the stress-strain behavior of the bulk samples, depending on the printing direction, which can therefore be attributed to their different polycrystalline microstructures.

The flat samples with thickness 1.2mm and 0.5mm show a columnar grain structure in BD (figure 3.3). Opposite to bulk samples, the ratio of the thickness of the surface affected by the roughness with respect to the total thickness of the specimens is not negligible. This roughness, consequence of the SLM process, plays a big role on the macroscopic behavior, leading to more noisy stress-strain curves. The origin of the surface roughness in flat specimens is the small number of grains through the thickness (figure 3.3 b)). This microstructure induces different through-thickness mechanical properties along X direction, which result in thickness variations due to the differentiated retraction during melting and cooling. The consequence of this roughness is a nonuniform deviation along "X" axis from the area defined in the design of the specimen (*nominal* cross section). To obtain a realistic stress from the force register of the tensile machine, the thickness is corrected to consider the smallest section measured along X which is slightly below the nominal value. The effective thickness for the 1.2mm sample and for 0.5mm were the nominal thickness divided by 1.05 and 1.15 respectively, and these values are obtained to compute the stress-strain curves.

The small thicknesses of the plain samples, together with the elongated grain shape allows to include in the RVE cross sections the actual number of grains observed in the EBSD images. Moreover, RVEs can include free boundary conditions allowing to model the full specimen size in the two cross-sectional directions. This stress-free boundary conditions in the cross section are imposed introducing boundary layers with negligible stiffness. On the other hand, in the loading direction, in which the specimen length is much larger than the average grain size, a periodic microstructure is introduced together with periodic boundary conditions (figure 3.8). The average number of grains in the RVE was kept approximately 1000 ± 100, achieved by changing the length of the RVE in the loading direction. A set with 10 realizations of each RVE per sample were simulated, and the discretization of each RVE was 64^3 voxels.

The introduction of the full microstructure in the cross section of plain specimens allows to account for the statistical size effect (Geers et al., 2006), which consists in the dependency of the macroscopic response with the ratio between the macroscopic size (specimen) and some characteristic length of the microstructure (grain size). In the present case, when the cross section is very small, only a few grains are contained and the weakest section controls the response of the specimen. This effect would be restricted imposing periodicity and can only be captured properly allowing every point of the cross sectional surface to move freely.

The 1.2mm sample was loaded in BD(Z) and the 0.5mm thickness sample in X direction. The results of these simulations, together with the corresponding experimental results are represented in figure 4.3. The agreement between the numerical results and experimental stress-strain curves is excellent, with errors in yield point lower than 3% for the 1.2mm thick sample and less than 4% for the 0.5mm thick sample, and an almost superimposed hardening evolution. Moreover, the experimental result lied inside the standard deviation of the 10 different realizations, which was always below 5%. Note that the introduction of free boundaries was fundamental to obtain this level of accuracy.

These results show that the CP-FFT model is able, using the same CP model parameters, to reproduce very accurately the differences in the elasto-plastic response consequence of the printing direction and specimen thickness provided the model includes a precise reproduction of the actual microstructure. These synthetic microstructures have to include the ODF, grain aspect ratio, and actual thickness if this length is comparable to the grain size. The conclusion is the same than in the case of elasticity, the effect of SLM process on the mechanical response is mainly due to changes in the polycrystalline microstructure, and other potential factors such as porosity or lack of fusion or changes in subgrain microstructure such as the development of GNDs (Witzen et al., 2020; Wang et al., 2019), do not play any significant role. This result is consequence, on one hand, of the optimal SLM process parameters used that result in a highly dense part with minimal number of defects. On the other hand, the invariant response of Hastelloy-X crystals with respect orientation and thickness are a consequence of the absence of precipitates in this alloy. In a precipitation hardened alloy, SLM processing parameters could alter the crystal response by inducing changes in size and volume fraction of precipitates, however, these changes are disabled in this solution-hardening

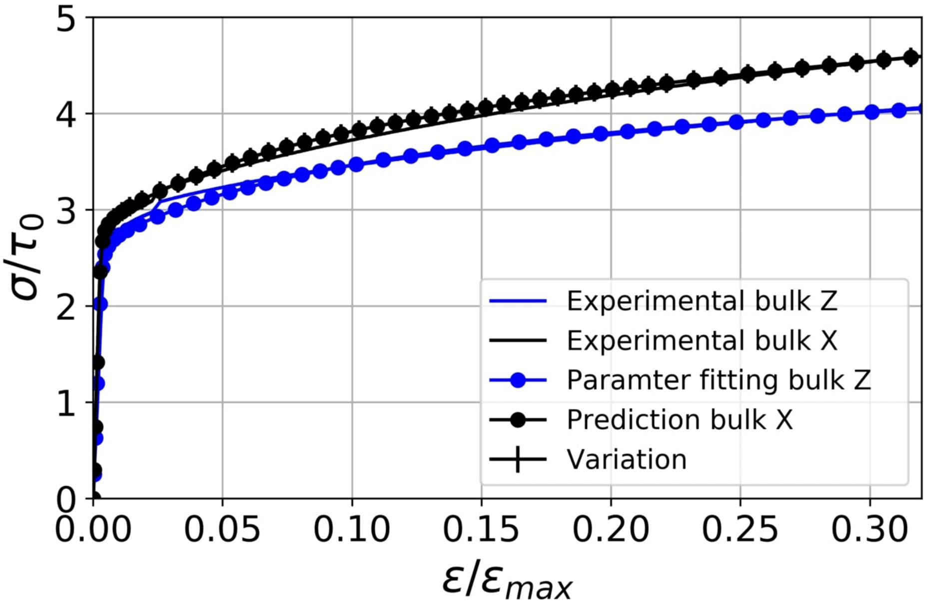

Figure 4.2: Prediction of stress-strain response for bulk samples in Z and X orientation. Stress is normalized by τ_0 and strain by a constant factor, ϵ_{max}

alloy. Moreover, the alloy is studied after annealing heat treatment, which homogenizes the distribution of the different species atoms in the FCC lattice, leading to a very similar subgrain microstructure independently to the SLM thermal history.

Plastic Anisotropy

The non-isotropic textures and grain aspect ratios of the specimens analyzed suggest a plastic anisotropic response, with different anisotropy levels depending on the particular specimen. To study the plastic anisotropy, CP-FFT simulations were performed for each sample, applying the load in three directions. Note that in the flat samples the stress-free boundary conditions were substituted with periodic boundary conditions when the load is applied in some of the directions of the cross section. A set of 10 realizations were simulated for each loading case and the averaged response is shown in figure 4.4. As expected, both bulk samples show limited plastic anisotropy, a consequence of the weak textures in these specimens (figure 3.6) and the nearly equiaxed grains forming the microstructure. Since both bulk samples present similar levels of texture (figure 3.6), the presence of elongated grains along BD is responsible for the slightly more anisotropic response of bulk Z respect Bulk X specimens. The flat specimen with 0.5mm thickness, which presents the strongest texture and the largest grain elongation, shows the highest plastic anisotropy.

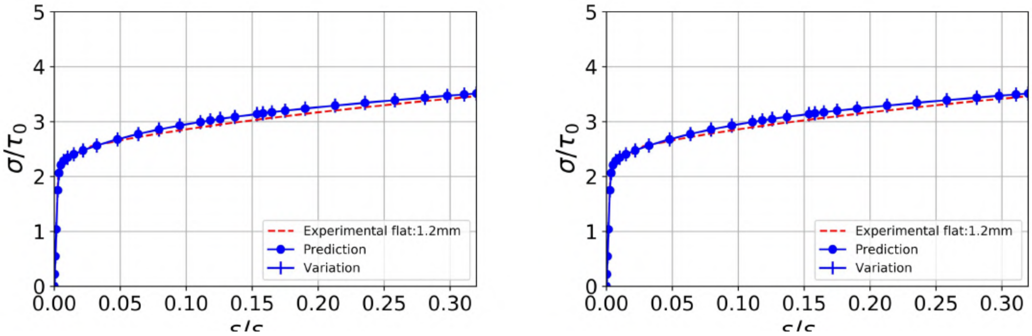

(a) *(b)*

Figure 4.3: Prediction of stress-strain response for flat samples, 1.2mm and 0.5mm, under uniaxial tensile loading in Z and X direction respectively. Stress is normalized by τ_0 and strain by a constant factor, ϵ_{max}

The plastic anisotropies here predicted are consistent with the elastic anisotropy as well as with literature results, both in experimental studies (Attallah et al., 2016; Murr, 2018; Niendorf et al., 2013) and using different modelling strategies (Liu et al., 2017; Rodgers et al., 2020) for AM metal samples.

4.6 Effect of Temperature

The specimen response at different temperatures and the ability of the CP-FFT model to capture the effect of temperature on the elasto-plastic response are analyzed. The study is focused on predicting the macroscopic response at the most general operating temperature regime of Hastelloy-X, which is $298K - 1023K(0.15T_m - 0.6T_m)$.

The temperature dependency of the elasto-viscoplastic response of Hastelloy-X alloy is accounted for in the crystal plasticity model. In the elastic regime, the temperature softening is considered using a phenomenological expression for the elastic constants, adjusted by experiments. The elastic tensor **C** of Hastelloy-X follows cubic symmetry and its elastic response is fully described by three constants, C_{11}, C_{12}, and C_{44}, which are made temperature dependent. In (Canistraro et al., 1998) the elastic constants of Hastelloy-X single crystals were measured using an acoustic time of flight technique. These experimental values are then used to adjust a quadratic empirical equation for each elastic constant as a function of the temperature T (in °C) . The

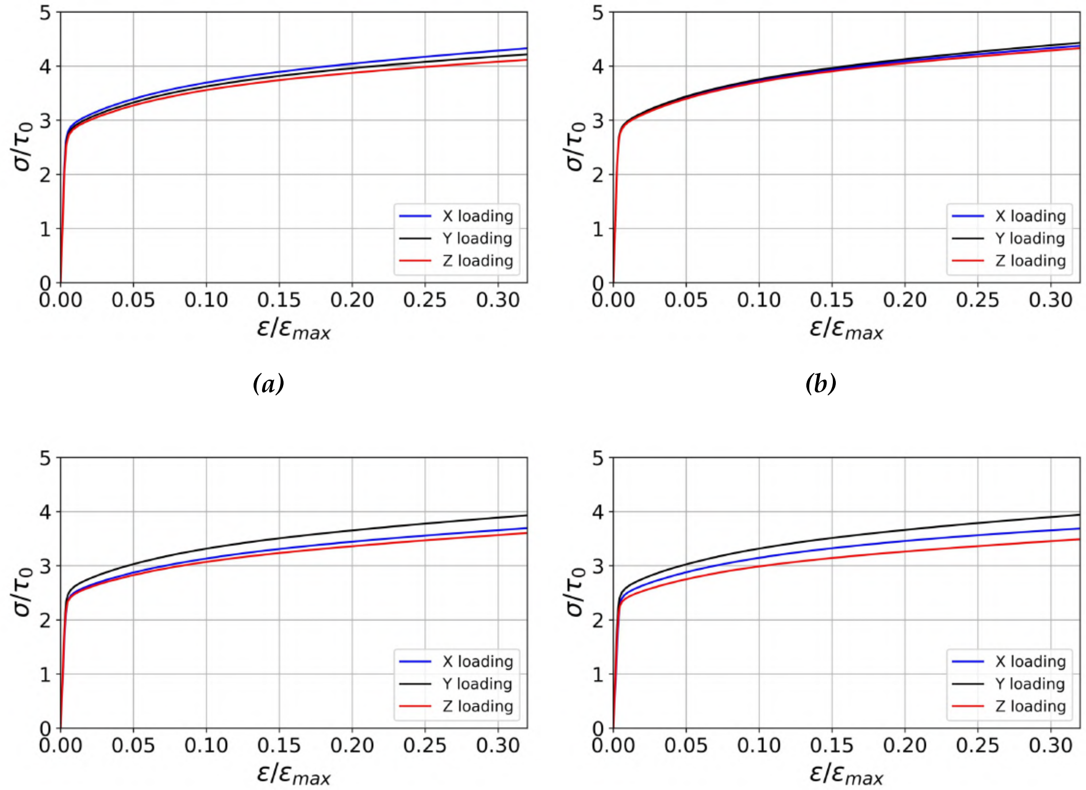

(a) *(b)* *(c)* *(d)*

Figure 4.4: Predicted stress-strain curves of RVEs in X, Y and Z directions for $a)$ bulk sample Z, $b)$ bulk sample X, $c)$ flat sample 1.2 mm thick and $d)$ flat sample 0.5mm thick. Each line represents the average response of 10 realisations of RVE. Stress is normalised by τ_0 and strain by a constant factor, ϵ_{max}

resulting expressions, given in Eq. (4.10), are included in the crystal plasticity model.

$$
\begin{aligned}
C_{11} &= 2.3039 \times 10^{2} - 3.9223 \times 10^{-2} T - 1.0980 \times 10^{-5} T^{2} \\
C_{12} &= 1.5612 \times 10^{2} - 1.7405 \times 10^{-2} T + 3.9772 \times 10^{-6} T^{2} \\
C_{44} &= 1.2177 \times 10^{2} - 3.9785 \times 10^{-2} T - 3.5194 \times 10^{-6} T^{2}
\end{aligned}
\tag{4.10}
$$

With respect to the viscoplastic regime, it is first assumed for simplicity that the effect of temperature on the strain rate sensitivity can be neglected. Therefore, the temperature effect is included in the CP model on the critical resolved shear stress (CRSS) and hardening evolution. In particular, the temperature dependence was introduced in the initial CRSS, τ_0 and its saturation value, τ_s, through a thermal softening function, $f(T)$,

$$
\begin{aligned}
\tau_{0(T)} &= \tau_{0(RT)} f(T) \\
\tau_{s(T)} &= \tau_{s(RT)} f(T)
\end{aligned}
. \tag{4.11}
$$

In equation (4.11) $\tau_{0(T)}$ and $\tau_{(s)_T}$ are the initial and saturation CRSSs at temperature T and $\tau_{0(RT)}$ and $\tau_{s(RT)}$ are the same quantities at room temperature. With respect to the thermal softening function, linear, exponential, or power law forms are considered in the literature (Rossiter et al., 2010; Klopp et al., 1985; Cyr et al., 2015). The different functions have been used to fit the experimental data of yield stress for different temperatures in the range 300K-1023K (figure 4.5). It was found that the power law expression with the room temperature as a reference temperature (Klopp et al., 1985; Clayton, 2005),

$$
f(T) = \left(\frac{T}{T_r} \right)^{p}, \tag{4.12}
$$

provides the most accurate prediction of the yield stress for AM Hastelloy-X within a working temperature range. In Eq. (4.12) T_r is the room temperature (298K) and p is a fitting parameter. The power law has been adopted separately for τ_0 and τ_s, and the corresponding values of the fitting parameter (p) are -0.3 and -0.32, respectively.

Temperature effect is introduced in the elastic and plastic CP model parameters as presented in section 4.6. To identify the parameters of the softening curves, the experimental values of the macroscopic yield stress σ_Y and ultimate strength σ_U for different temperatures are used as data. The macroscopic yield stress in the polycrystal for uniaxial loading σ_Y is a linear function of the initial critical resolved shear stress τ_0, being the Taylor factor the parameter relating both values . The nonlinear yield stress reduction with temperature can therefore be accounted for in the CP model through the temperature dependency of τ_0. In the power-law relation selected (section 4.6), the

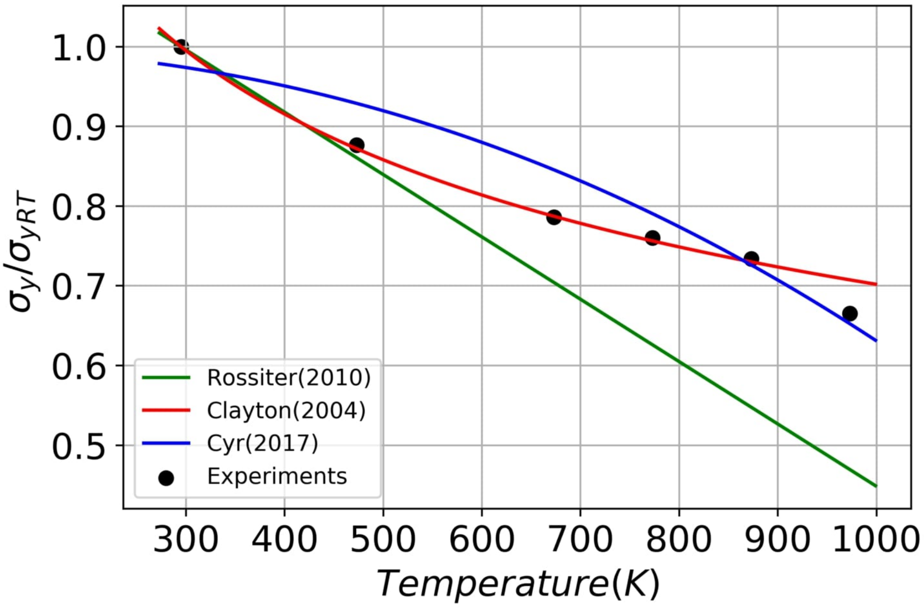

Figure 4.5: Comparison between different softening functions

reference temperature used was room temperature, therefore

$$\frac{\sigma_Y(T)}{\sigma_{Y(RT)}} = \frac{\tau_0(T)}{\tau_{0(RT)}} = \left(\frac{T}{T_{RT}}\right)^p \tag{4.13}$$

The logarithm of the experimental $\sigma_Y(T)/\sigma_{Y(RT)}$ versus the temperature ratio is represented in figure 4.6a, showing a linear relation. The parameter p in equation 4.13 is then identified as the slope of that curve, being equal to $p = -0.3$.

The second parameter that is made temperature dependent in the CP model is τ_s which is related to the saturation value of the resolved stress at a given strain. This parameter characterizes mostly the stage III hardening where the hardening rate decreases monotonically with flow stress and Rollett et al.(Rollett and U.F.Kocks, 1993) has shown that, indeed, is a temperature-dependent parameter. This parameter determines the ultimate tensile strength during uniaxial tensile testing, and the relation of this ultimate strength σ_U with τ_s is the same as Eq.4.13. To fit the exponent of the softening relation for the saturation stress, k, the log-log curve of the ultimate tensile stress as function of temperature T is represented (figure 4.6b) and the parameter k is then obtained as the slope of this linear relation, resulting in $k = -0.32$.

To validate the temperature-dependent CP-FFT model, uniaxial tensile simulations of the bulk and flat samples were performed at different temperatures with the same RVEs (figure 3.9) used throughout the study. The elasticity effects were also included

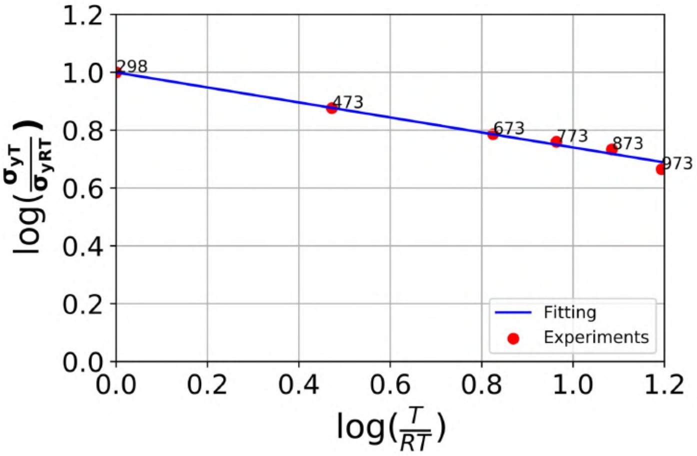

(a)

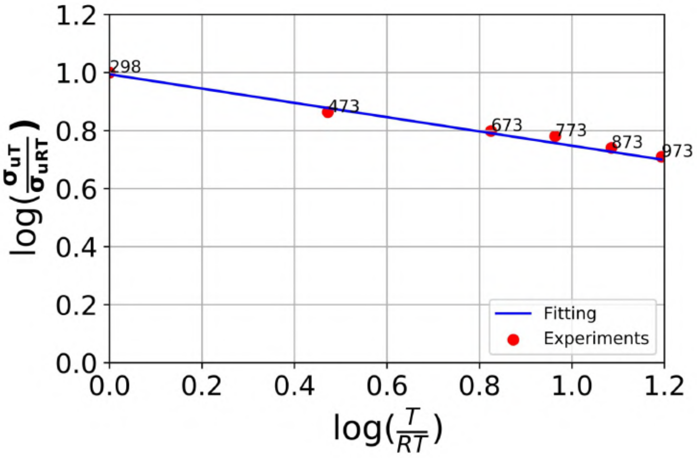

(b)

Figure 4.6: (a) Calculation of fitting parameter p for τ_0, (b) Calculation of fitting parameter k for τ_s.

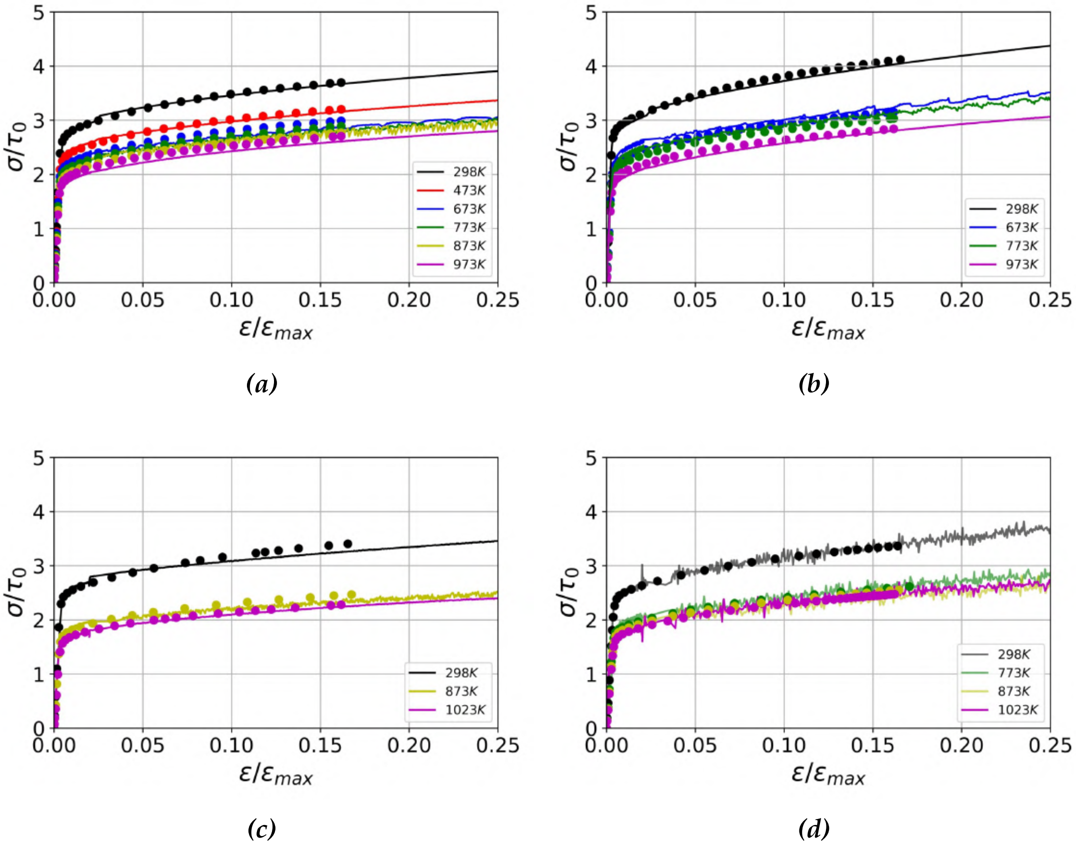

(a) *(b)*

(c) *(d)*

Figure 4.7: Predicted temperature dependent uni-axial stress-strain response (dotted lines) for a) bulk sample Z, b) bulk sample Y, c) flat sample 1.2 mm thick and, d) flat sample 0.5mm thick and their comparison with the experimental results(solid lines), Stress is normalised by τ_0 and strain by a constant factor, ϵ_{max}

in the model through the empirical relations in Eq.4.10. Again, the bulk and flat samples were uniaxially loaded in the respective directions. The predictions of the stress-strain curve obtained with the temperature-dependent model are shown in figure 4.7 together with the experimental stress-strain curves for a set of temperatures. The numerical results are the average of five different RVE realizations, with a standard deviation below 5%. Experimental results show a similar thermal softening for all specimens considered and, as in the case of room temperature, the different samples present different responses. The model predictions (dotted lines) are very accurate when compared with experimental data (solid lines). The reduction in the yield stress was accurately captured using the power law softening model for both bulk and flat samples. The slope of strain hardening is well captured without the need of introducing a temperature-dependent model for the initial hardening rate h_0.

The accurate model predictions for all specimens in a wide temperature range validate the phenomenological model used for temperature dependency, which includes only two adjustable parameters, fitted to a single type of specimen (Bulk Z). Moreover, the ability of the model to reproduce the response at any temperature confirms, once again, that the polycrystalline microstructure resulting from the printing process is the main responsible for the different specimen responses. Since the microstructures considered in the RVEs are the same for all temperatures (obtained at room temperature), it can also be concluded that temperature neither affects the polycrystalline microstructure (no recrystallization or grain coarsening) nor the deformation mechanisms at the crystal level.

5 Microstructure sensitive fatigue life prediction model for SLM fabricated Hastelloy-X

A computational polycrystalline homogenization framework based on the Crystal plasticity and FFT homogenization (CP-FFT) is used to simulate the cyclic response for SLM Hastelloy-X under strain and stress-controlled loading. The FFT-based homogenization code FFTMAD (Lucarini and Segurado, 2019) is used to simulate the cyclic response of Representative Volume Elements (RVE) of the microstructures considered.

The synthetic RVEs contain grain size distribution, grain aspect ratio, and orientations representative of the actual SLM microstructures experimentally characterized. This section will describe the RVE generation, crystal plasticity model that accounts for the cyclic deformation of grains, the FFT homogenization framework, and the quantification methodology to predict fatigue life based on the FIP.

This chapter is based on the study *'Microstructure sensitive fatigue life prediction model for SLM fabricated Hastelloy-X '* which is published in the International Journal of Fatigue in November 2022.

5.1 Introduction

The production of net-shape complex components of Hastelloy-X using a SLM process presents enormous potential for the industry, especially aerospace, which have already started to design and fabricate some jet engine parts using SLM fabricated Hastelloy-X. However, strong variability is found in the cyclic/fatigue behavior of SLM components depending on the process parameters and part geometry, and this indeed is the most critical design parameter for potential high-temperature applications.

This variability of properties is mainly attributed to the highly heterogeneous microstructures resulting from the complex thermal cycles followed during fabrication (Lewandowski and Seifi, 2016; Wilson-Heid et al., 2017; Pei et al., 2019; Kok et al., 2018) . Therefore, models able to predict the fatigue life for SLM components accounting for the effect the heterogeneous microstructure are fundamental for the progressive introduction of these components into industrial applications.

Multiple authors have studied the cyclic deformation and fatigue behavior of SLM components from an experimental viewpoint (Aydinöz et al., 2016; Kirka et al., 2017; Kanagarajah et al., 2013; Lewandowski and Seifi, 2016; Edwards and Ramulu, 2014a; Gribbin et al., 2016; Johnson et al., 2017). Most of these studies reported similar conclusions for a wide range of SLM alloys including IN718 or Ti-6Al-4V (Agius et al., 2017; Lewandowski and Seifi, 2016), namely an inferior fatigue performance of the SLM component compared to wrought and cast ones. In some cases, the reduction of fatigue life can be larger than one order of magnitude (Johnson et al., 2017; Agius et al., 2017; Pei et al., 2019). This worse fatigue performance of SLM components, particularly in as-built case, has been attributed to the porosity (Li et al., 2021), surface roughness (Konečná et al., 2016) or residual stresses (Yadollahi et al., 2017), and also to the resulting anisotropy of the part and its orientation with respect to the cyclic loading direction (Yadollahi et al., 2017; Agius et al., 2017). However, some studies reported the mitigation methodologies for porosity (Prithivirajan and Sangid, 2018), surface roughness (Esmaeilizadeh et al., 2022), and residual stresses (Leuders et al., 2013) effects on the fatigue lives by optimizing the processing parameters(Esmaeilizadeh et al., 2022), heat treatment(Leuders et al., 2013) and powder composition(Montero-Sistiaga et al., 2019b). With respect to the specimen orientation, the fatigue life of vertically built specimens has been found to be inferior to horizontally built parts when loaded under stress control (Edwards and Ramulu, 2014a; Lindström et al., 2020; Yadollahi et al., 2017). On the contrary, under strain-controlled loading, some studies (Kirka et al., 2017) show the opposite effect, vertically built samples having a superior fatigue performance than horizontally built samples. This fact is justified by the resulting elastic anisotropy, vertically built samples have lower elastic modulus and hence underwent lower stress amplitudes than horizontally built samples.

In the particular case of AM Hastelloy-X, a few recent studies can be found in the literature which cover its fatigue analysis. Han et al.(Han et al., 2019) studied the effect of hot isostatic pressing (HIP) on the fatigue life of AM Hastelloy-X and concluded that the fatigue life could be significantly improved by HIP due to closure of internal pores and relief of residual stresses. Esmaeilizadeh et al. (Esmaeilizadeh et al., 2021) studied the fatigue life of AM Hastelloy-X as a function of laser scanning speed at room temperature and concluded that fatigue lives could be improved by optimizing the processing parameters. Wang et al. (Wang et al., 2011) highlighted the importance of HIP on fatigue life improvement and reported that the part orientation does not play a significant role in the fatigue life for low applied stress level; however, at higher loads, observed that the fatigue resistance of vertically orientated specimen is inferior to its horizontally oriented counterpart. Lindstrom et al. (Lindström et al., 2020) reported that the fracture surface of the horizontally oriented specimen had shown more plastic deformation than the vertically oriented specimen.

From the modelling view point, empirical models such as Basquin, Coffin Manson, etc., have been used with experimental data to correlate the fatigue life of different additive manufactured alloys (Lee et al., 2020; Romano et al., 2018; Branco et al., 2018a), including the study of SLM Hastelloy-X by Esmaelizadeh et al.(Esmaeilizadeh et al., 2022). However, it is well known that there is a strong influence of the microstructure in the fatigue life of an alloy, and these models cannot account for it because they are empirical and calibrated with experimental data without considering any microstructural aspect.

The influence of the microstructure in the fatigue performance is mainly affecting the nucleation of a crack. The repeated deformation of the polycrystal induces the localization of plasticity at the grain level in persistent slip bands which degenerate finally in microscopic fatigue cracks (McDowell and Dunne, 2010). The regions of the microstructure in which these bands and subsequent cracks are more prone to appear correlate with the points in which some variable related with cyclic plastic deformation is localizing. In order to consider the effect of the microstructures resulting from SLM fabrication in the fatigue life prediction, micromechanical models which model this mechanisms have to be used.

In particular, the approaches relying on the use of polycrystalline computational homogenization (Segurado et al., 2018) to estimate the number of cycles for crack nucleation (McDowell and Dunne, 2010) allow to analyze crack nucleation as a function of the microstructure from a statistical viewpoint. Under the microstructure sensitive fatigue life approach, fatigue life is predicted by cyclic accumulation of plastic slip and localised stresses that act as a driving force for fatigue crack nucleation on persistent slip bands(Lucarini and Segurado, 2020). The driving force is quantified using Fatigue Indicator Parameters (FIP) that are based on accumulated plastic slip (Manonukul and Dunne, 2004; Sweeney et al., 2014), stored strain energy (Wan et al., 2014; Chen et al., 2018), dissipated energy (Cruzado et al., 2018) or in general any combination of stress, strain and plastic slip fields.

The FIP is evaluated at each material point by varying local micro-fields and internal variables, and fatigue life is calculated based on the maximum FIP (hot-spots) in the domain. These models include the relevant microstructural features of the polycrystal under study into Representative Volume Elements (RVE) of the microstructure. The mechanical response of the RVEs under a macroscopic cyclic history is then simulated using crystal plasticity and some computational homogenization approach to obtain some fatigue indicator parameter that is the driving force for crack nucleation. These micromechanics-based fatigue life prediction models have been successfully applied to a large number of alloys produced by standard fabrication routes, as wrought Ni-based superalloys (Manonukul and Dunne, 2004; Shenoy et al., 2008; Castelluccio and McDowell, 2014; Cruzado et al., 2018, 2017; Lucarini and Segurado, 2019). Most of the micromechanical studies of fatigue rely on finite element simulation and only recently Fast Fourier Transform (FFT) solvers have been introduced as an alternative to FEM (Rovinelli et al., 2015a; Lucarini and Segurado, 2018, 2019). The use of FFT-homogenization methods allow accurate prediction of the micro-field response over many cycles at a fraction of the cost of FE based solvers, making it possible to simulate larger RVEs and consider more accurate microstructural features (Lucarini and Segurado, 2018).

The application of crystal plasticity models to investigate the effect of the resulting microstructures of AM metals in their fatigue performance is a trending topic nowadays. These models have been applied to SLM fabricated aluminum (Cao et al., 2022), Ti-6AL-4V (Kapoor et al., 2018; Liu et al., 2021) and some superalloys (Prithivirajan and Sangid, 2018; Eghtesad and Knezevic, 2021; Cheng et al., 2022a; Ghorbanpour et al., 2022). In some cases the life prediction is focused on crack propagation (Cheng et al., 2022a) stage. Other studies consider crack nucleation but the life prediction model is directly linked with the macroscopic cyclic response (Esmaeilizadeh et al., 2021, 2022; Lee et al., 2020), without making use of the distribution of microscopic fields obtained. Only a few studies on AM alloys are available which rely on the use of micromechanical fields through fatigue indicator parameters (FIPs) to estimate the fatigue life assuming crack nucleation controlled fatigue. Among these studies, in some cases the real microstructures are not considered and simplified random textures are assumed (Cao et al., 2022; Ozturk and Rollett, 2017). In other cases, the actual microstructures obtained from EBSD data are included in the model (Ou et al., 2020; Eghtesad and Knezevic, 2021; Prithivirajan and Sangid, 2018; Ye et al., 2021) but the study is focused only on a particular fatigue regime, either LCF (Eghtesad and Knezevic, 2021; Ou et al., 2020; Ye et al., 2021) or HCF (Zhang et al., 2022; Han et al., 2020), and a particular loading control, either strain or stress control.

In this chapter, we present a micromechanics based fatigue life prediction approach valid for stress and strain control and a wide range of fatigue lives. From a numerical viewpoint, FFT based polycrystalline homogenization is used to simulate the cyclic response of the specimen. This framework is then applied to analyze the effect of the SLM resulting microstructures, including grain aspect ratios and orientation distributions. The model is applied to study the fatigue life of of Hastelloy-X specimens built in different directions 3 including its validation using experimental data under strain and stress control at 750 °C for a wide range of fatigue cycles from very low LCF to more than 10^5 cycles.

5.2 Crystal Plasticity Model

The crystal plasticity (CP) model developed by Cruzado et al.(Cruzado et al., 2017) for the cyclic response of Inconel 718 is used in this study to simulate the elasto-viscoplastic cyclic behavior of Hastelloy-X crystals. This model allows to reproduce the isotropic and kinematic hardening and mean stress relaxation effects which might appear under cyclic loading.

A multiplicative decomposition of the deformation gradient $\mathbf{F}$ into its elastic ($\mathbf{F}^e$) and plastic ($\mathbf{F}^p$) components is assumed,

$$\mathbf{F} = \mathbf{F}^e\mathbf{F}^p \tag{5.1}$$

The plastic velocity gradient $\mathbf{L}^p$ is computed in the intermediate (relaxed) configuration as function of the shear rates $\dot{\gamma}^\alpha$ on all the slip systems α,

$$\mathbf{L}^p = \dot{\mathbf{F}}^p{\mathbf{F}^p}^{-1} = \sum_\alpha \dot{\gamma}^\alpha \mathbf{s}^\alpha \otimes \mathbf{m}^\alpha \tag{5.2}$$

where, $\mathbf{s}^\alpha$ and $\mathbf{m}^\alpha$ are the slip and slip normal directions, respectively, in the initial configuration.

The second Piola-Kirchoff stress **S** depends linearly on the Green-Lagrange strain $\mathbf{E}^e$ through the elastic stiffness tensor $\mathbb{C}$, which is given by

$$\mathbf{S} = \mathbb{C}\mathbf{E}^e \tag{5.3}$$

and the Cauchy stress tensor is calculated as,

$$\sigma = \frac{1}{J^e}\mathbf{F}^e\mathbf{S}\mathbf{F}^{e^T} \tag{5.4}$$

, being J^e the determinant of $\mathbf{F}^e$.

A power-law is used to define the slip rate in each slip system as,

$$\dot{\gamma}^\alpha = \dot{\gamma}_0 \left(\frac{|\tau^\alpha - \chi^\alpha|}{g^\alpha}\right)^{\frac{1}{m}} \text{sign}(\tau^\alpha - \chi^\alpha) \tag{5.5}$$

where $\dot{\gamma}_0$ and m are, respectively, the reference strain rate and the strain rate sensitivity parameters. τ^α is the resolved shear stress, defined as,

$$\tau^\alpha = \mathbf{S} : (\mathbf{s}^\alpha \otimes \mathbf{m}^\alpha). \tag{5.6}$$

The functions g^α and χ^α are the critical resolved shear stress and backstress on the α slip system respectively.

The evolution of the backstress on each slip system defines the kinematic hardening. In the present model (Cruzado et al., 2017), a simplified version of the Ohno Wang Model (Ohno and Wang, 1993) limited to the first two terms is used,

$$\dot{\chi}^\alpha = c\dot{\gamma}^\alpha - d\chi^\alpha|\dot{\gamma}^\alpha| \left(\frac{|\chi^\alpha|}{c/d}\right)^k \tag{5.7}$$

where $c, d,$ and k are material parameter. k controls the mean stress relaxation, while c and d stand for direct hardening and dynamic recovery modulus, respectively.

The evolution of the Critical Resolved Shear Stress (CRSS) for a given slip system, g^α, defines the isotropic hardening and is given by

$$\dot{g}^\alpha = \sum_\beta q_{\alpha\beta} h(\gamma_a)|\dot{\gamma}^\beta| \tag{5.8}$$

where $q_{\alpha\beta}$ are the latent hardening coefficients and h is the self hardening modulus which follows the Voce hardening model (Tome et al., 1984), given by

$$h(\gamma_a) = h_s + \left[h_0 - h_s + \frac{h_0 h_s \gamma_a}{\tau_s - \tau_0}\right] exp^{\left(\frac{-h_0\gamma_a}{\tau_s-\tau_0}\right)} \tag{5.9}$$

where, τ_0, τ_s, h_0 and h_s are the hardening parameters and the accumulated plastic shear γ_a is computed as,

$$\gamma_a = \sum_{\alpha} \int_0^t |\dot{\gamma}^{\alpha}| \mathrm{d}t. \tag{5.10}$$

5.3 Fatigue Indicator Parameters and Life Prediction

The successive deformation of the polycrystal induces the localization of plasticity in persistent slip bands which degenerate finally in microscopic fatigue cracks (McDowell and Dunne, 2010). The areas of the microstructure in which these bands and subsequent cracks will appear correlate with regions where some Fatigue Indicator Parameter (FIP) is maximum. Moreover, quantifying the value of this FIP in that hot-spots allows to estimate the number of cycles to crack nucleation. In the current study, the Fatigue Indicator Parameter through the microstructure is obtained from computation homogenization of a full cycle. The FIP distribution within the RVE was computed from the variation of micro-fields and the state variables at every material point. This distribution defines the hot-spots in which fatigue cracks are more likely to appear and the fatigue life is predicted based on the most critical point. The most common FIPs found in the literature are, accumulated plastic strain per cycle (Manonukul and Dunne, 2004; McDowell and Dunne, 2010; Sweeney et al., 2014), the plastic stored energy per cycle (Sweeney et al., 2012, 2015), the maximum plastic shear strain (Fatemi and Socie, 1988; Fatemi and Yang, 1998) and some other parameters (Ozturk et al., 2016).

In this work, plastic work accumulated per cycle $W_{cyc}(\mathbf{x})$ is chosen as FIP due to the good predictive capacity shown on other superalloys as Inconel 718 (Cruzado et al., 2018). This FIP is defined as

$$W_{cyc}(\mathbf{x}) = \int_{cyc} \tau_{\alpha}(\mathbf{x}) \dot{\gamma}_{\alpha}(\mathbf{x}) dt \tag{5.11}$$

at each point $\mathbf{x}$ in the RVE being τ_{α} and $\dot{\gamma}_{\alpha}$ the resolved shear stress and shear strain rate respectively. Eq.5.11 is applied at the center of each voxel to obtain a local map of FIP values in the RVE.

However, the crack initiation on the persistent slip bands is a non-local phenomenon, as shown for example in Castelluccio et al. (Castelluccio and McDowell, 2014). For this reason, and considering also the strong mesh dependence of the local FIP maps, non-local FIP maps are defined as the volume averaged of local FIPs over the grains or bands within a grain parallel to the slip planes with a constant thickness (Castelluccio and McDowell, 2014; Cruzado et al., 2017). This type of non-local variable corresponds to an non-local integral type model. Alternative non-local FIP by means of gradient approaches can be derived, as proposed in (Xu et al., 2015).

The estimation of the number of cycles for crack nucleation is done based on the most critical point of an RVE. In this work, the maximum of the non-local FIPs defined at each band in the RVE is taken as driving force. More details on the geometrical definition in bands can be found in (Cruzado et al., 2017). Each grain is divided in four families of bands, being nb the total number of bands in the RVE. The FIP of the full RVE is then defined as

$$W^b_{cyc} = \max_{i=1,nb}\left\{\max_{\beta_i}\frac{1}{V_i}\int_{V_i} W^{\beta_i}_{cyc}(\mathbf{x})dV_i\right\} \tag{5.12}$$

where $1 \leq i \leq nb$ refers to each of the bands in the RVE, $\beta_i = 1, 2, 3$, corresponds to the three different slips systems contained in the slip plane parallel to that band and V_i is the volume of the band.

Normally, crack nucleation is directly related to the cyclic FIP obtained from Eq.5.12 using some empirical relations. However, in this work, a different methodology has been used to predict both fatigue life for stress- and strain-controlled loading, keeping a similar definition of FIP.

Strain Controlled Loading

The value of the FIP in a stable cycle can be used to estimate, based on extrapolation, the number of cycles for crack nucleation. The relation between this value and the number of cycles for nucleation can be based on a linear extrapolation (Manonukul and Dunne, 2004) or on other relation, as the power law in (Cruzado et al., 2017). In the latter case, the value of the FIP in a stable cycle, W_{cyc}, is linked to the number of cycles for nucleation N_i as

$$N_i = \frac{W_{crit}}{(W_{cyc})^m}, \tag{5.13}$$

where W_{crit} and m are two parameters of the material. This biparametric fatigue life prediction law requires the use of two independent fatigue experiments (Cruzado et al., 2018) to be calibrated.

The use of the previous approach implies direct simulation of the RVE deformation until a stable hysteresis cycle is reached. Under strain control, hysteresis evolves from cycle to cycle, and stabilization can be reached after a few cycles in some cases to thousands of cycles in other cases, depending on the material and loading conditions(Manonukul and Dunne, 2004). To limit the computational cost of these simulations, different strategies have been developed in the context of polycrystalline homogenization, such as the wavelet transformation-based multi-time scaling algorithm (WATMUS) (Joseph et al., 2010) or the linear extrapolation of internal variables or cycle jumps (Cruzado et al., 2018).

Stress Controlled Loading

Contrary to strain-controlled tests, under stress-control loading, the plastic flow is concentrated mainly in the first few cycles. From a computational point of view, this usually results in a relatively fast transition to an approximate elastic cyclic macroscopic response. Although microplasticity can still be observed after the shakedown regime, the associated FIPs are three to four orders of magnitude lower than the FIPs in plastic regimes, too small for an accurate prediction of crack nucleation based on the extrapolation approaches used for strain control. As an alternative, we consider that the total accumulated plastic deformation (also related to the stored energy) until the shakedown limit is the precursor to the nucleation of a crack. Therefore, in this work, the total accumulated plastic deformation, W_p^{acc}, is proposed as FIP to correlate the number of cycles for crack nucleation and the microplasticity effects after shaking are neglected in this correlation.

The approach proposed here first introduces a criterion to quantify, based on microscopic fields in an RVE simulation, the number of cycles $n = ns$ at which elastic shakedown occurs.

$$ns \text{ such that } W_{cyc}(n = ns) = 10^{-4} W_{cyc}(n = 1). \tag{5.14}$$

where $W_{cyc}(n)$ is the FIP value in the RVE (Eq. 5.12) on the n^{th} cycle. Then, the accumulated plastic deformation, W_p^{acc}, is given as

$$W^{acc} = \sum_{n=1}^{n=ns} W_{cyc}(n) \tag{5.15}$$

A power-law function is proposed (Eq. 5.16) which also includes two fitting parameters, W_σ^{crit}, and nk to link the accumulated plastic FIP, W_p^{acc}, and the fatigue crack initiation life N_i.

$$N_i = \frac{W_\sigma^{crit}}{(W_p^{acc})^{nk}} \tag{5.16}$$

5.4 Results

5.4.1 Experimental results

The uniaxial cyclic performance of SLM fabricated Hastelloy-X at 750° was experimentally determined by cyclic tests performed in a wide range of strain and stress amplitudes. The tests were carried out according to the standards PrEN3874-98 and ASTM E606. The results of the fatigue testing campaign will be presented in the this section.

Uniaxial tensile fatigue tests were performed using strain control in the case of Bulk X samples and under stress control for both Bulk X and Bulk Z. The cylindrical-shaped bulk sample (Bulk Z) was subjected to uniaxial tensile cyclic loading in the building direction (Z), while the rectangular-shaped sample (Bulk X) was subjected to uniaxial tensile cyclic loading in the X-direction. In the case of strain controlled tests, the hysteresis stress-strain cycle was registered cycle by cycle in order to obtain the cyclic plastic response. From now on, due to the confidentiality agreement signed with the industrial partner, all data are normalized by constant normalization factors. The normalization factor $\Delta\epsilon_{min}$ corresponds to the minimum applied strain range under strain loading conditions. For stress, the normalization factor is the critical resolved shear stress, τ_0, identified for Hastelloy-X grains at 750°C.

The cyclic uniaxial tests under strain control were carried out with strain amplitudes, $\frac{\Delta\epsilon}{\Delta\epsilon_{min}}$= 1, 1.1, 1.2, 1.3, 1.4, 1.5, 1.6, 1.7 and, 1.8 under strain ratio R_ϵ=0. The hysteresis cycles show a combination of isotropic and kinematic hardening and finally collapse in a stable cycle. An example of these experimental results is represented in figure 5.1, where the stress-strain cycle for the first and $N = 2000$ cycles (when the cycle became stable) is represented for two strain ranges, $\frac{\Delta\epsilon}{\Delta\epsilon_{min}}$= 1 (figure5.1(a) and $\frac{\Delta\epsilon}{\Delta\epsilon_{min}}$= 1.6 (figure5.1(b)). The rest of the results will be represented together with the model predictions in the next section.

In the case of stress-controlled tests, the applied uniaxial stress range considered was $\frac{\Delta\sigma}{\tau_0}$= 3.2, 3.57, 3.93, 4.29, 4.64, and 5 under stress ratio R_σ=0.03. These tests were performed with a trapezoidal (1s-1s-1s-1s) waveform with a frequency of 0.25Hz and a stress concentration factor($K_t = 1$).

The fatigue S-N curves obtained for strain control and stress control are represented in figure5.2(a) and figure 5.2(b), respectively. In these curves, the fatigue life N corresponds to the cycle in which the final fracture is reached on the specimen. The fatigue performance of the samples built in the X and Z directions 5.2(b) is different, especially for high stress levels where Bulk X samples present longer fatigue life. This result is

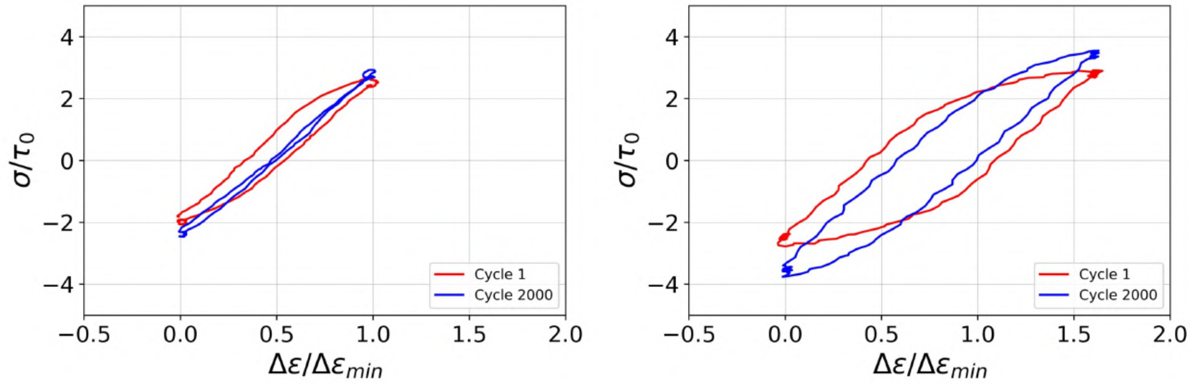

(a) *(b)*

Figure 5.1: Under strain controlled loading, the stress-strain cycle for the first(shown in red color), and $N = 2000$ cycles(shown in blue color) are represented for two strain ranges, (a) $\Delta\epsilon/\Delta\epsilon_{min}$= 1, and (b) $\Delta\epsilon/\Delta\epsilon_{min}$= 1.6

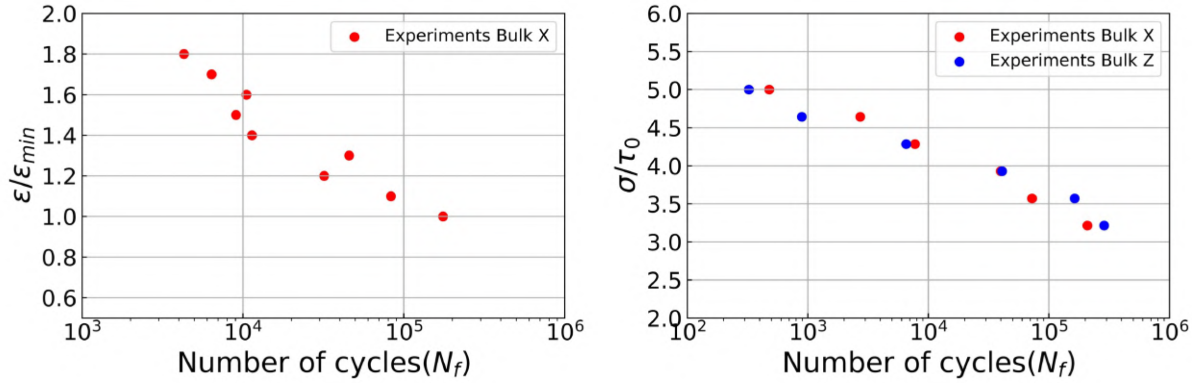

(a) *(b)*

Figure 5.2: The experimental fatigue (a)strain-life curve obtained using strain control loading for Bulk X and (b)stress-life curve obtained using stress control loading for Bulk X and Bulk Z samples.

in agreement with previous studies by Wang et al.(Wang et al., 2011) where the better performance of the samples built in the X direction is also observed for high stresses.

To observe the mechanism of fatigue failure, a fractography analysis was performed for the two samples loaded with cyclic strain amplitude $\Delta\epsilon/\Delta\epsilon_{min}$, 1 and 1.6 at 750°C. The fracture surfaces obtained are shown in figure5.3(a), and figure5.3(b) respectively, showing the crack initiation (flat areas origin of propagating cracks), propagation (beach marks), and final fracture regions (dimples). It is observed that the dominant crack initiation sites were subsurface areas that have some small defects (both un-melted particles or very small pores have been observed), as they act as stress concentration sites. For low strain amplitude $\Delta\epsilon/\Delta\epsilon_{min}$=1, multiple crack initiation sites were observed, while at higher applied strains,$\Delta\epsilon/\Delta\epsilon_{min}$=1.6, a single and well-defined crack initiation site was observed.

Multiple crack initiation sites for small strain amplitude ($\Delta\epsilon/\Delta\epsilon_{min}$=1) implies that very small heterogeneities near the surface are enough to nucleate a crack and therefore the expected scatter in these cases is greater.

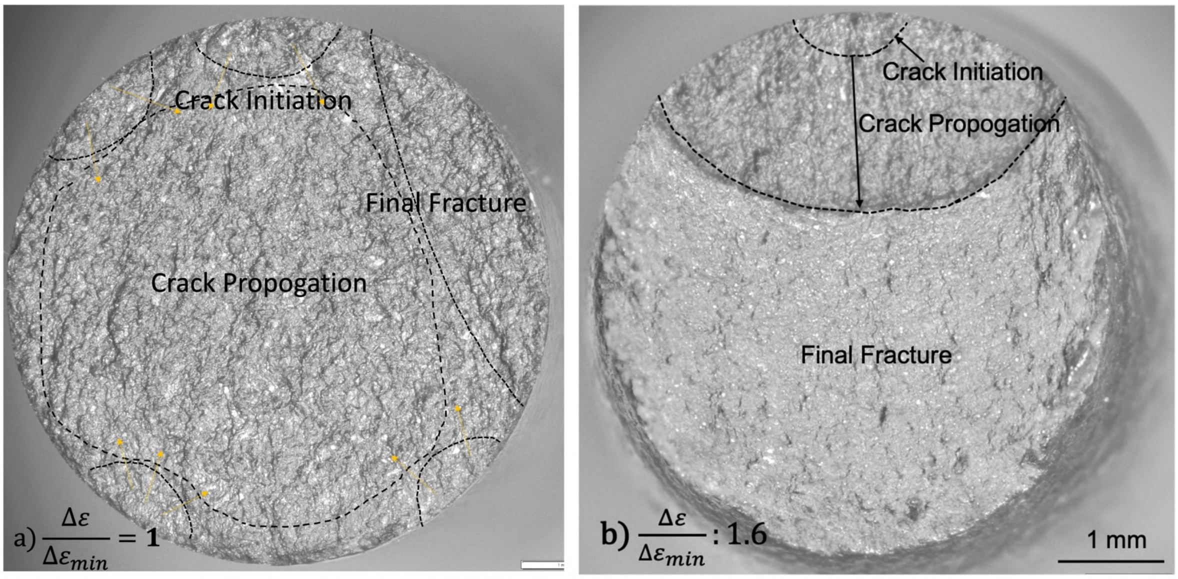

Figure 5.3: An overall view of the specimen subjected to cyclic strain amplitude, $\Delta\epsilon/\Delta\epsilon_{min}$= a) 1 and b) 1.6, $\%s$ showing crack initiation, propagation, and final fracture regions.

The number of cycles for propagation can be qualitatively estimated by the number of beach marks observed in the propagation area. The crack propagation area for both strain ranges is similar, but since the width of the beach marks is smaller for the lower strain amplitude, the propagation regime is slightly larger for the smaller strain range. A rough estimation of the number of propagation cycles is around $0.01N_f$ for $\Delta\epsilon/\Delta\epsilon_{min}$ = 1 and $0.1N_f$ for $\Delta\epsilon/\Delta\epsilon_{min}$=1.6, where N_f is the experimental fatigue life. In both cases, the ratio of propagation to total life is small and nucleation can be considered as the most dominant fatigue mechanism for both applied strains. This fact validates the modeling approach followed, in which fatigue life is estimated based on the number of cycles for nucleation.

The final fracture of the samples was reached when the crack reached the critical size, and the fracture surface area corresponding to this stage was easily observed as a typical ductile fracture surface with dimples (figure5.4).

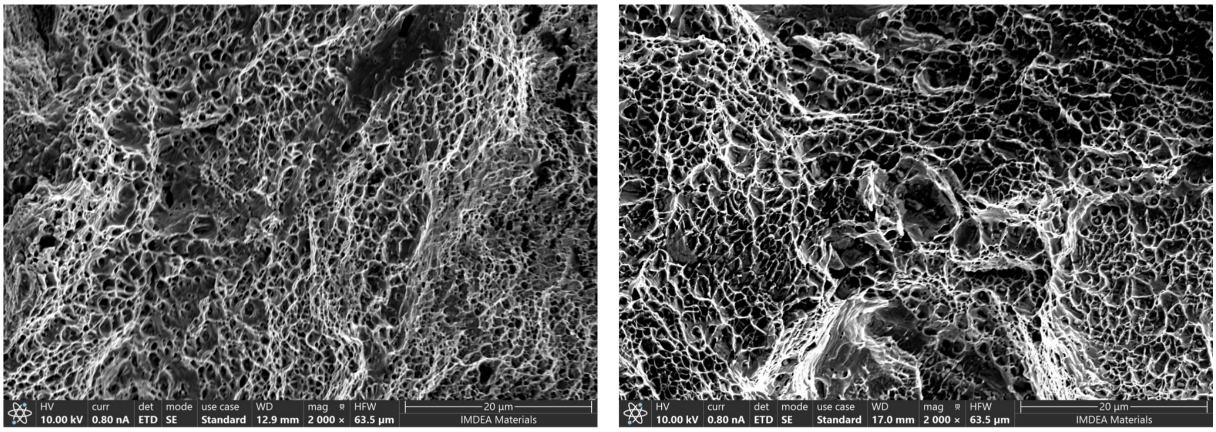

$(a)\ \frac{\Delta\varepsilon}{\Delta\varepsilon} = 1$ $(b)\ \frac{\Delta\varepsilon}{\Delta\varepsilon} = 1.6$

Figure 5.4: The final fracture surface of samples subjected to cyclic strain amplitude, $\Delta\epsilon/\Delta\epsilon_{min}$= a) 1 and b) 1.6, $\%s$ showing ductile failure with dimples.

5.4.2 Numerical results

The CP-FFT framework presented is applied to predict the cyclic response of bulk SLM Hastelloy-X built in different orientations, thus presenting different microstructural characteristics.

The first objective is to obtain the crystal plasticity parameters for an accurate prediction of the cyclic response for all of the specimens considered. Second, the fatigue life prediction model will be adjusted based on two fatigue tests under strain control. The resulting fatigue life prediction tool will be validated for the rest of the strain-controlled fatigue tests and also for the stress-controlled loading. Finally, the effect of the microstructures resulting from the different SLM processes on fatigue performance will be analyzed.

Crystal plasticity model parameters

The parameters of the CP model of SLM Hastelloy-X at $750°$C after annealing and thermal processing will be obtained. The elastic constants of Hastelloy-X single crystals are taken from Canistraro et al.(Canistraro et al., 1998). The strain rate sensitivity coefficient and exponent, $\dot{\varepsilon}_0$ and m, respectively, are taken from previous work in Hastelloy-X. The parameters defining the critical resolved shear stress and the evolution of the back stress, which are responsible for isotropic and kinematic hardening, respectively, are obtained by inverse fitting. The input data is the experimental uniaxial cyclic stress-strain response of the bulk sample X loaded in the X direction with strain control and $\Delta\epsilon/\Delta\epsilon_{min}$= 1.6, the one with the highest strain amplitude. The RVE used for the identification of CP parameters is generated to be statistically representative of the actual microstructure (same grain size, aspect ratio, and orientation distributions). The RVE accommodates approximately 1000 grains and is discretized in 64^3 voxels. The inverse optimization framework proposed by Herrrera-Solaz et al.(Herrera-Solaz et al., 2014), based on the Levenberg-Marqadt least squares algorithm, is used in this study.

Experimentally, it is observed that for SLM-Hastelloy-X, the cyclic stress-strain behavior stabilizes approximately after 2000 cycles for strain-controlled loading at 750°C. Numerically, simulating 2000 cycles makes the optimization process computationally too expensive. Some acceleration techniques have been proposed in the literature, such as the cycle jump approach (Cruzado et al., 2018). However, since the microstructure-sensitive fatigue crack initiation methodology is based on extrapolating the FIP distribution in the stable hysteresis loop (Manonukul and Dunne, 2004; McDowell and Dunne, 2010; Cruzado et al., 2017, 2018; Lucarini and Segurado, 2019), in this work we have opted for a simpler alternative. In our approach, the CP parameters controlling isotropic and kinematic hardening evolution have been fitted such that 15 numerical cycles of the RVE provide a stable hysteresis cycle equal to the experimental stable cycle, reached after 2000 cycles. The number of 15 cycles has been chosen large enough to ensure a progressive stabilization of the cyclic response and local history fields and FIPs.

The CP parameters correspond to the Voce isotropic hardening (τ_0, τ_s, h_0 and h_s), and the kinematic hardening of the Ohno-Wang model (c, d, k) are identified using the procedure mentioned above, and these values are tabulated in Table 5.1 along with the remaining CP parameters. The stable experimental cyclic stress-strain curve of the 2000th cycle is represented in Figure 5.5 together with the polycrystalline cyclic response of the 15th cycle after adjustment of the CP parameters. The figure shows an almost superimposed response between the model and the experiment, confirming the accuracy of fitting the parameters of the CP model.

Table 5.1: *Crystal plasticity parameters of a SLM Hastelloy-X at 750°C*

Elastic (GPa)	C_{11}	C_{12}	C_{44}	
	194.8	126.91	89.95	
Viscoplastic	m	$\dot{\gamma}_0(s^{-1})$		
	0.017	2.42×10^{-3}		
Isotropic Hardening (MPa)	τ_0	τ_s	h_0	h_s
	τ_0	$1.25\tau_0$	$78.7\tau_0$	$0.71\tau_0$
Kinematic Hardening	c(MPa)	d	k	
	$171.42\tau_0$	$2.57\tau_0$	0.1066	

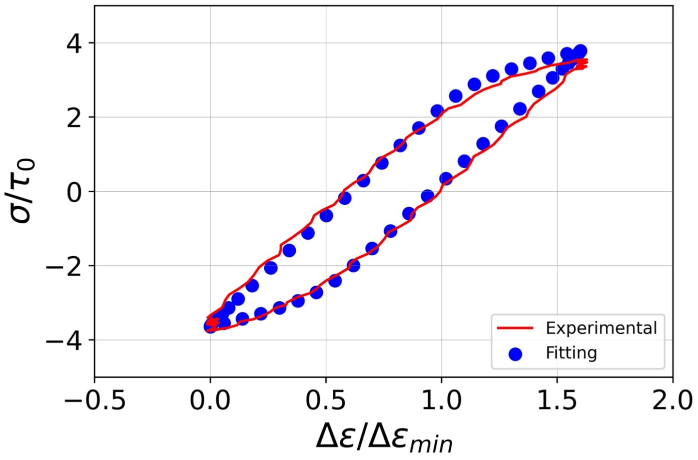

Figure 5.5: A stable cyclic experimental loop for applied strain range, $\Delta\epsilon/\Delta\epsilon_{min}$=1.6 and numerically fitted cyclic loop using LM algorithm.

5.4.3 Prediction of cyclic plastic response

The ability of the set of CP parameters fitted above to predict the cyclic deformation behavior for different applied strain amplitudes is presented in this section. In particular, the stress-strain curves and the evolution of minimum and maximum stress with the number of real cycles are predicted under the uniaxial cyclic strain amplitude $\frac{\Delta\epsilon}{\Delta\epsilon_{min}}$= 1, 1.1, 1.2, 1.4, 1.6, 1.8, with $R_\epsilon = 0$. All the cases considered correspond to bulk-X samples.

The stable experimental hysteresis curve, corresponding to the 2000th experimental cycle, is represented in figure 5.6 for six different strain amplitudes together with the computational homogenization results for the 15th cycle. The comparison shows that an accurate stabilized cyclic stress-strain loop can be predicted for all the applied strain amplitudes. These results validate the simulation strategy, based on accelerating the hardening evolution, to predict the stable cycle under a wide range of cyclic loading conditions.

The evolution of peak stresses until cycle stabilization is represented in figure5.7 for both the experimental results and the numerical predictions. It can be observed that the experimental results always stabilized before 2000 cycles and the numerical value for 15 cycles coincides with the stable value for all the strain range. The evolution of the stress peaks obtained by the model before stabilization also follows the experimental trend. The main differences can be found for large strains, where the fast evolution of the hysteresis curve is reproduced more gradually in the model.

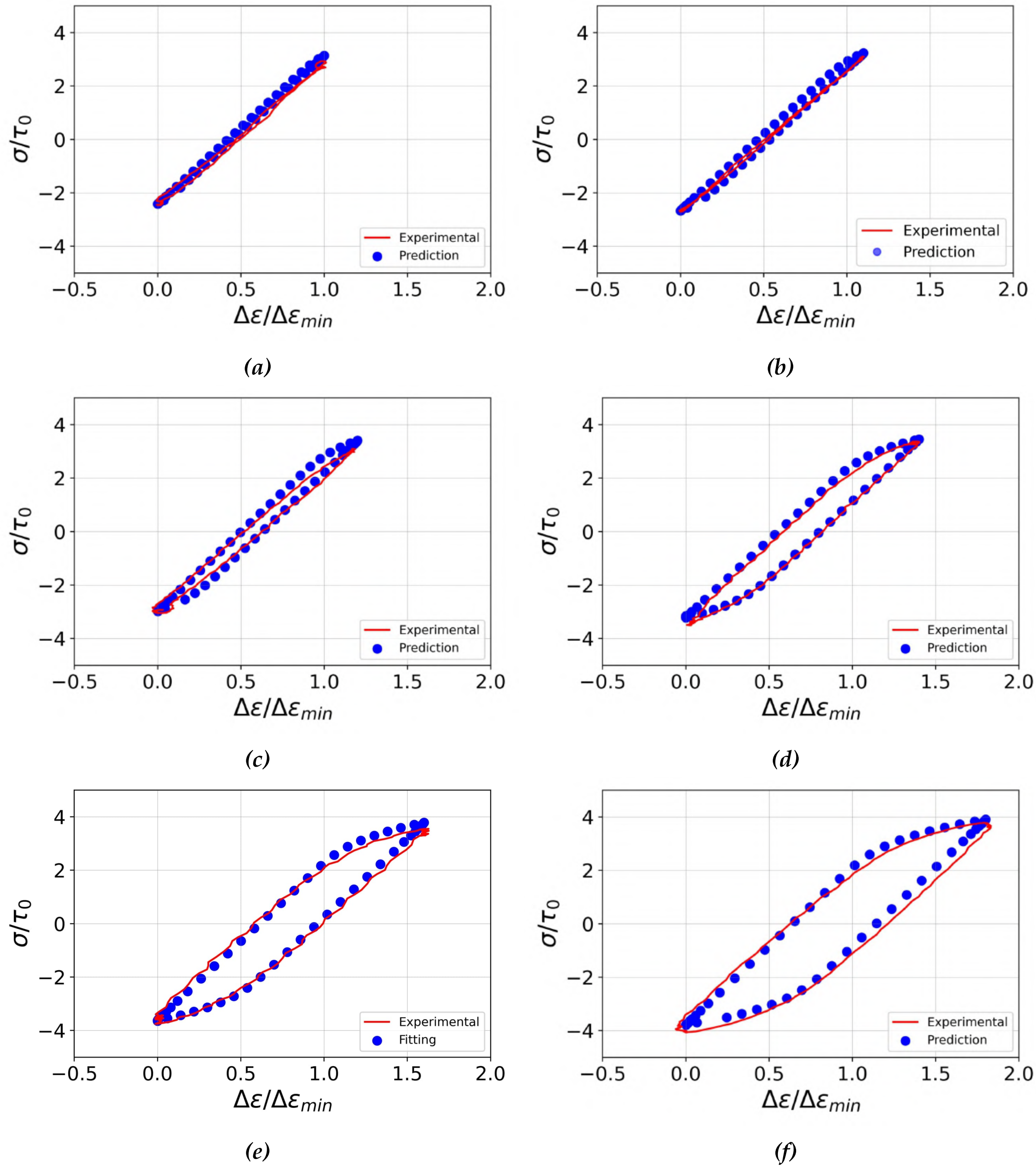

(a) *(b)* *(c)* *(d)* *(e)* *(f)*

Figure 5.6: Comparison between stable experimental 2000th cycle (solid red lines), and numerical cyclic 15th cycle (dotted blue lines) hysteresis loops for different applied strain ranges,($\Delta\epsilon/\Delta\epsilon_{min}$= a)1, b)1.1, c)1.2, d)1.4, e)1.6, and f)1.8. Note that τ_0 normalizes stresses.

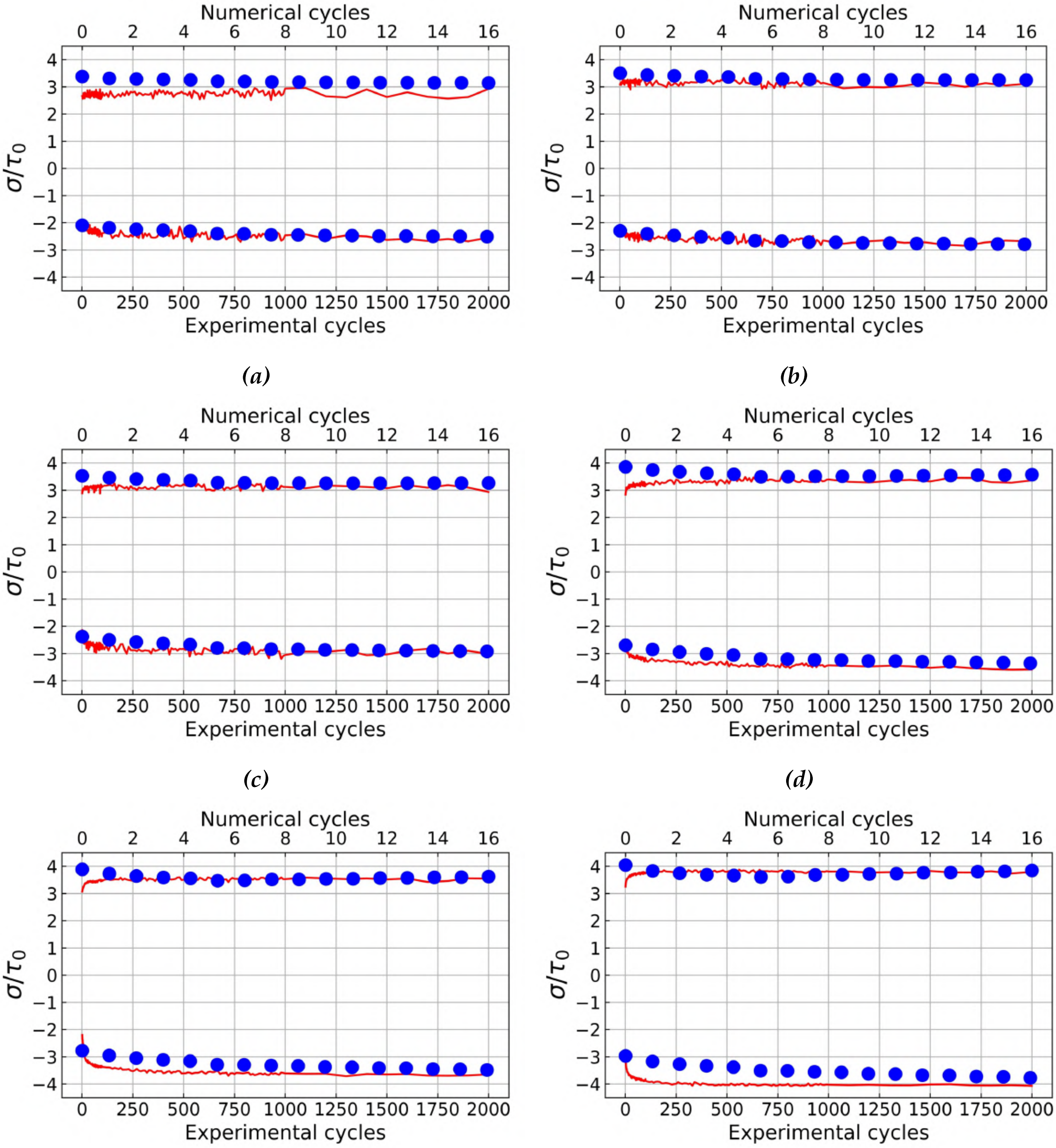

(a) *(b)*

(c) *(d)*

(e) *(f)*

Figure 5.7: Comparison between experimental(solid red lines) and numerical cyclic(dotted blue lines) response based on the evolution of maximum and minimum stresses with the number of cycles for different applied strain ranges,($\Delta\epsilon/\Delta\epsilon_{min}$= a)1, b)1.1, c)1.2, d)1.4, e)1.6, and f)1.8. Note that τ_0 normalizes stresses.

5.4.4 Fatigue Life Prediction

Life prediction model calibration

The parameters of the fatigue life models, W_{crit} and m in Eq.5.13 and W_{σ}^{crit} and n in Eq.5.15, respectively, for the strain- and stress-controlled loading, must be calibrated using some of the experimental data. In each case, two different experimental results and their corresponding cyclic behavior are necessary to predict the power law constants in Eqs.5.13 and 5.15. Furthermore, to consider the stochastic nature of fatigue, the average response of the simulation of 20 different RVE realizations (also known as Statistical Volume Element, SVE) was considered for each applied load. The use of an SVE is necessary to consider the differences between the results of different RVEs statistically. The fatigue model parameters obtained for the strain-controlled loading are $W_{crit} = 3.421 \times 10^{19}$ and $m = 2.62$ and for the stress-controlled loading are $W_{\sigma}^{crit} = 4.06 \times 10^{8}$ and $nk = -0.56$.

5.4.5 Fatigue Life Prediction: strain controlled tests

The cyclic stable FIPs and fatigue model Eq. 5.13 are used to predict fatigue life as a function of applied strain and microstructure. The experimental fatigue life for different strain amplitudes is plotted in figure 5.8. The two experiments $\frac{\Delta\epsilon}{\Delta\epsilon_{min}}= 1$ and 1.8, marked with black dots, and the average FIP of the simulation of 20 RVEs for these two applied strain ranges are used to calibrate the fatigue model parameters. Figure 5.8 plots the fatigue life predicted for the remaining strain amplitudes in the form of a life probability distribution, obtained from the results of the 20 RVEs. Very good agreement between the experiments and simulations is observed for all applied cyclic strain amplitudes. Furthermore, the results highlighted the predictive capacity of the model to consider the change in the FIP distribution between high and low strain amplitudes. The distribution of plastic deformation is heterogeneous at lower strain amplitudes, and very few grains undergo plastic deformation. However, at higher strain amplitudes, more homogeneous plastic deformation was observed. The effect of microstructure has a more pronounced effect at lower strain amplitudes than at higher strain amplitudes, since the localized continuous accumulation of plastic slip in very few grains leads to considerable experimental and numerical scatter in the fatigue life.

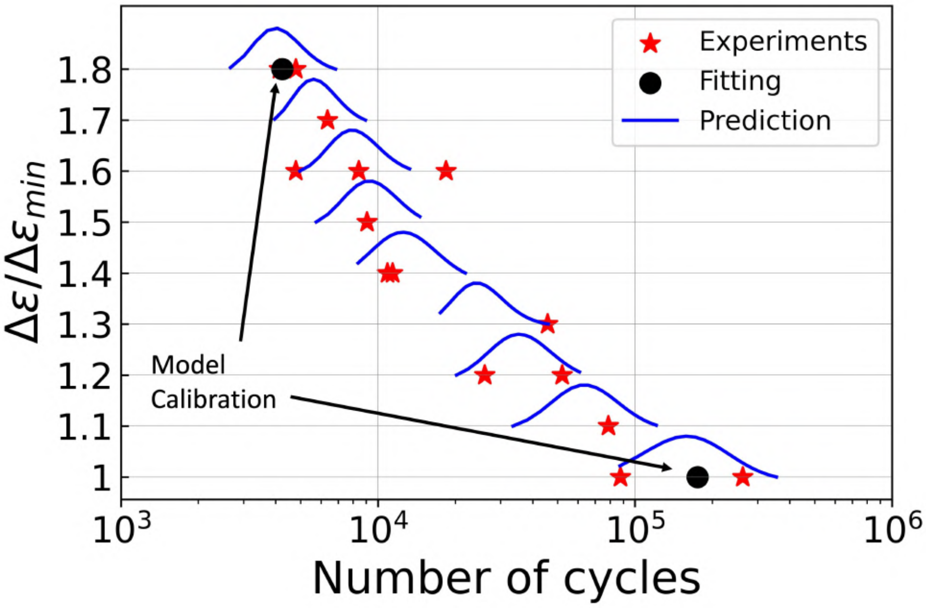

Figure 5.8: Experimental fatigue life and model predictions for bulk X under strain-controlled loading at 750°C . Note that the minimum cyclic strain amplitude $\Delta\epsilon_{min}$ normalizes strain.

.

5.4.6 Fatigue Life Prediction: Stress Controlled tests

The crystal plasticity model presented in section 5.2 is extended to predict fatigue life under stress-controlled loading. In this case, tests are available in two different building directions, Bulk X and Bulk Z, so the predictive capacity of the model for different microstructures will be assessed.

The methodology to predict fatigue life under stress-controlled loading is described in Section 5.3. Cumulative cyclic damage in the plastic regime (W_p^{acc}) is specified as the precursor to the onset of fatigue cracks, and fatigue live N is predicted using the modified criteria (Eq.5.15-5.16). Since under stress control, the scatter is usually larger, 50 RVEs were generated with an average grain size, aspect ratio, and grain orientations for Bulk X and Bulk Z samples. Virtual uniaxial cyclic tests were performed on RVEs under stress-controlled loading with $\Delta\sigma/\tau_0$= 3.2, 3.57, 3.93, 4.29, 4.64, and 5 and under a stress ratio R_σ = 0.03. Note that τ_0 corresponds to the critical resolved shear stress(CRSS). The adjustment parameters W_σ^{crit} and nk in Eq.5.16, which are necessary to predict the fatigue crack initiation under stress-controlled loading, were identified from the fatigue life obtained in two different tests ($\Delta\sigma/\tau_0 = 3.2, 5$) for a unique type of material, the one corresponding to fabrication in the X direction (Bulk X). The values of the fitting parameters are $W_\sigma^{crit} = 4.06 \times 10^8$ and $nk = -0.56$. The accumulated FIP, W_p^{acc} of these tests was obtained from the simulation of a SVE with 50 different RVEs.

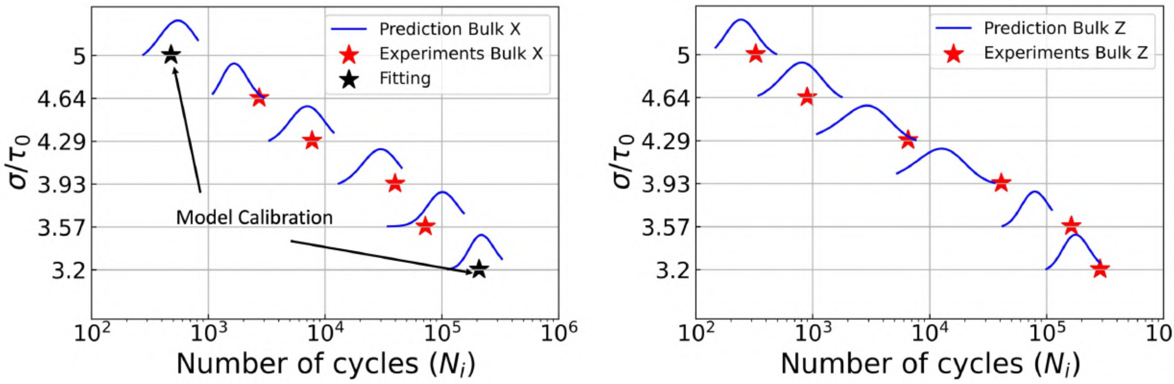

(a) *(b)*

Figure 5.9: Experimental results and numerical model predictions fatigue crack initiation life for SLM Hastelloy-X at 750°C as a function of cyclic applied stress,σ/τ_0. Note that the stress is normalized by τ_0. a) Bulk X b) Bulk Z. These results are for 50 RVE realizations for each applied stress, with a confidence level of 95%.

The large size of the SVE helps predict the stochastic nature of the fatigue life for a given microstructure and loading conditions.

Once the life prediction model is fitted, the SVE for Bulk-X samples is simulated and used to obtain the fatigue life prediction for the rest of the cases. In the case of Bulk-Z, a new SVE is generated containing 50 statistically representative RVEs of the microstructure of the material, which is different from the one of the Bulk-X samples. This SVE is then used to predict the fatigue life of these samples. It is important to note that no experimental results on Bulk-Z material have been used to calibrate the model, so the results are pure predictions and will assess the validity of the model to consider different microstructures for the same parameters.

The fatigue crack initiation predictions of the model for different applied cyclic stress ranges, $\Delta\sigma/\tau_0$ are represented in figure 5.9 for the orientation of the sample, (a) Bulk X and (b) Bulk Z, together with the respective experimental life.

The agreement between experimental and numerically predicted fatigue life is excellent for both building directions. The largest difference was found for the bulk Z sample in the stress ranges $\Delta\sigma/\tau_0$, 3.57 and 3.93, where fatigue life is slightly underestimated. These results highlight that the model can accurately predict the fatigue life that accounts for the effect of the microstructure. The agreement with the experimental results for the Bulk-Z direction is remarkable because the fatigue life law used for the predictions was calibrated only using two experiments of Bulk-X samples.

To analyze the effect of the building direction, the S-N curves for the two building directions together are represented in figure 5.10. In this figure, it can be observed that the direction of SLM fabrication significantly affects the fatigue life of Hastelloy-X. Experimentally, the horizontally built specimen (Bulk X) shows superior resistance to the initiation of fatigue cracks compared to the vertically built specimen (Bulk Z), with the exception of the two smallest stress ranges applied. These results are in agreement with the observations of Wang et. al. (Wang et al., 2011) for the same alloy, Hastelloy-X, and of Bayati et al.(Bayati et al., 2020) for SLM Ni-Ti. Furthermore, the better fatigue performance of the printed Bulk-X Hastelloy-X samples corresponds to a stronger quasistatic response, as shown in section(chapter 4).

The model can reproduce the better performance of Bulk X compared to Bulk Z for stresses greater than $3.9\tau_0$ observed in the experiments. Multiple factors could potentially contribute to this anisotropic fatigue performance, such as porosity, residual stresses, surface roughness, and orientation of the deposited layer with respect to the loading direction. However, the fabrication was designed to minimize most of them. For example, minimal porosity was observed in the samples as a result of an optimal selection of the SLM parameters, and a fine machining ensures that the sample has very minimal surface roughness. With respect to the level of residual stresses, it should be very small due to the annealing process and heat treatment. Therefore, the differences observed in the experiments should be mainly caused by the different microstructures (grain size, aspect ratio, and orientation) generated during SLM fabrication in different directions with respect to the loading axis. In the absence of porosity and defects, the slip band precursors of the nucleating cracks tend to appear in grains, whose shape, orientation with respect to macroscopic load, and surrounding area are specially suited for localizing plastic deformation and, therefore, the polycrystalline microstructure plays an essential role. Since the two materials have a very similar texture and average grain size, the main difference in their microstructures is their grain shape, having Bulk X grains a lower aspect ratio. The more equiaxed grain shape should then provide better resistance to fatigue, because the slip bands are larger and localize more plastic strain in the elongated grains.

Both the model and the experiments agree that the effect of anisotropy in fatigue life increases with the applied stress, being maximal for the highest stress amplitudes, where most of the grains show plastic deformation. At lower stresses, for long LCF lifes, the model shows a similar fatigue endurance for both samples. The prediction of a reduction in fatigue performance anisotropy has also been observed for SLM samples (Wang et al., 2011; Bayati et al., 2020). In contrast, the experimental results for the two smallest stress ranges show a different effect, a slightly longer life for Bulk-Z. The difference between these experimental results with the typical observations in the literature and the model could be due to the large dispersion of results at low stresses,

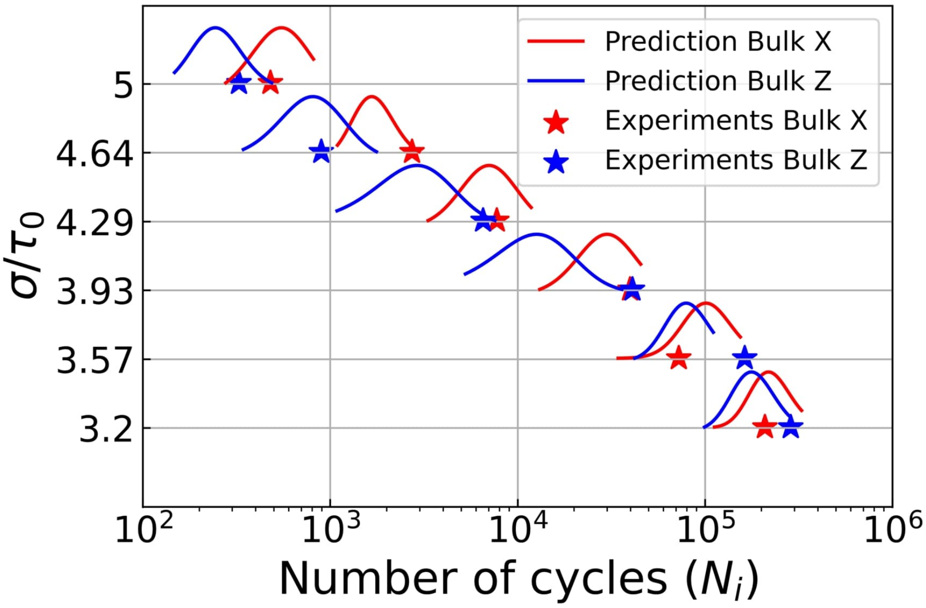

Figure 5.10: Comparison between predicted and experimental fatigue lives of Bulk X and Bulk Z, showing the effect of build orientation on fatigue lives.

being the result of a single experiment not enough to capture the actual statistical fatigue response. Furthermore, because tests are carried out at a higher temperature $750°\mathrm{C}$, fatigue-creep interaction may play a role when life extends for a very large number of cycles (greater than 10^5 here) for Hastelloy X(Esmaeilzadeh et al., 2017; Lee et al., 2020) and in our model, creep is not considered.

In summary, in addition to the effect of defects and porosity, the orientation of the building influences the lifetime of fatigue. The S-N curve shows a higher slope for horizontally oriented samples and lower slopes for vertically oriented samples. The reason behind the effect of the building direction on fatigue performance is the difference in the microstructures developed during the process. This influence is strong at higher applied stresses (LCF regime); however, such effects are minimal at lower applied stresses(in LCF regime). Therefore, to design the SLM of components against fatigue loading, microstructural aspects (grain aspect ratio, average size, and orientation result of the building orientation should be considered, as they significantly influence fatigue behavior. Furthermore, to capture this fatigue anisotropy, the use of microstructure-sensitive fatigue life nucleation approaches based on polycrystalline homogenization is essential.

6 Effect of surface roughness on the fatigue performance of flat samples

6.1 Introduction

As mentioned several times along this thesis, SLM-fabricated components might present some particular characteristics result of the processing such as porosity, residual stresses, surface roughness and anisotropy. These features lead to near net shaped AM components having lower fatigue performance than their wrought counterparts. The onset of fatigue cracks in SLM parts is reliant on the combination of all of the above-mentioned defects, however quantifying the effect of each defect on the fatigue life is a difficult task. Porosity is in general particularly prevalent in SLM components, and pores act as fatigue fracture initiation sites. Nevertheless, porosity can be minimised by optimising the process parameter selection. Addtionally, several authors (du Plessis and Macdonald, 2020; Han et al., 2018; Wang et al., 2012; Montero-Sistiaga et al., 2019b) used the hot isostatic pressing (HIP) technique to close the internal pores. Regarding residual stress, most SLM-fabricated aerospace components are subjected to stress-relieving treatment, which reduces the accumulated residual stresses in the part during SLM and therefore minimize their impact in the fatigue response (Karapuzha et al., 2022; Robinson et al., 2018).

The presence of free surface that are no longer entirely smooth, *surface roughness*, implies that tiny sized stress concentration sites exist which promote fatigue crack initiation. According to Stofferegen et al. (Stoffregen et al., 2014), surface roughness in SLM parts is produced by a) the stair case effect generated by process parameters, b) partly melted powder particles on the final part surface, and c) Plateau-Rayleigh instability. Several researchers have investigated the the effect of surface roughness of SLM parts in fatigue as well as possible mitigation procedures. Ferrar et al.(Ferrar et al., 2012) and Ali et al.(Ali et al., 2018) noted the low repeatability of fatigue tests due to surface roughness which result in randomly distributed flaws. Mumtaz et al. (Mumtaz and Hopkinson, 2009) found that decreasing laser scan speed can reduce top surface roughness while increasing side surface roughness of IN625. Esmaheldilah et al. (Esmaeilizadeh et al., 2022) also observed surface roughness reduction due to lowering the laser scan speed, in this case for Hastelloy-X. Abele et al. (Abele and Kniepkamp, 2015) shown that using a contour scan method reduces surface roughness significantly. Wang et al.(Wang et al., 2012) shown that re-melting surface layers can minimise the surface roughness of SLM Hastelloy-X. However, none of the approaches described above can completely eliminate surface roughness. Alternatively, surface roughness can be potentially eliminated by machining, polishing or with surface treatments such as chemical etching. Nevertheless, eradicating surface roughness for complex components and thin walled parts using these techniques is not always achievable, and if possible, the dimensions of the component might be affected forcing to consider this reduction in the design process. As a conclusion, surface roughness is probably the most critical factor influencing the fatigue life of metallic alloys fabricated by SLM due to its strong effect in the performance and the difficulties for its elimination.

Understanding the effect of the surface condition on the fatigue performance of thin samples in 'as-built condition' becomes a critical issue. In addition to the necessary experimental studies, is fundamental the development of fatigue model that considers surface roughness on top of the other microstructure features and allows to quantify its effect on fatigue life.

The first attempts to model the effect of surface roughness were based on linear elastic fracture mechanics (LEFM), with all micro-notches presumed to be micro-cracks and designs based on the material's fatigue crack propagation threshold ΔK_{th} (El Haddad et al., 1979; Smith and Miller, 1978). These methodologies are purely macroscopic, assume elastic fracture mechanics and might result too conservative. Few empirical models, such as the Murakami method (Murakami and Endo, 1986), were established by relating fatigue strength to defect size and micro-notches. Later, Pessard et al. (Pessard et al., 2013) and Lee et al. (Le et al., 2016) introduced stochastic models based on the LEFM and Dang Van criteria, in which fatigue life interplay between microplasticity and micro-notches drives fractures were modeled. Although these approaches are capable of quantifying the influence of surface roughness on fatigue life reduction, they are mostly empirical and macroscopic, with no incorporation of microstructural characteristics or surface roughness topology in the models.

The precise quantification of surface roughness profiles is crucial when modeling for the effects of surface roughness and, nowadays, highly accurate surface topography (down to the sub-micron level) can be produced using contact and non-contact profilometry. This topological description can be introduced explicitly in computational models. In this line, Campbell et al.(Campbell et al., 2002) used trigonometric equations to include surface roughness caused by the stair case effect in the CAD files. Perez et al.(Pérez et al., 2001) established a model based on sample and defect geometry that introduces the average surface roughness, R_a. These papers focus on empirical descriptions of surface roughness on bulk samples and do not directly consider its effect in the fatigue performance. Surface topography can be utilized as an input to the CPFEM models to account for surface roughness influence on the fatigue performance. As at al (AS et al., 2005) considered this approach using the average surface roughness R_a as roughness descriptor to predict fatigue un an aluminum alloy. These models were further improved by employing bezier spline interpolation formulas in the CPFE models to mimic surface roughness profiles (Ås et al., 2008). Their model, however, does not account for an accurate description of microstructure, which is critical for fatigue design. Yadollahi et al. (Yadollahi et al., 2018) accurately estimated the fatigue life of IN718 by constructing a surface roughness profile based on a semicircular locus whose dimensions are computed based on maximum valley depth. Belhadjamor et al.(Belhadjamor et al., 2019) recently proposed a theoretical CP-FE methodology with sinusoidal and random gaussian surface profiles and optimized them with skewness and kurtosis fitting based on the experimental observations, however their application in fatigue life prediction has not been investigated. Vayssette et al.(Vayssette et al., 2019) provided the most promising methodology up-to-daate that directly integrated experimental 3D profilometry measurements in the RVE to study fatigue performance using the CP-FE model.

All the studies reviewed focus on the effect of surface roughness of bulk samples. However, on thin flat samples the surface roughness effect is magnified because on top of the other effects, roughness introduces an non-negligible variation of the cross section that might lead to stress concentration on some specific regions. Furthermore, on flat samples the surface effect is superposed to higher anisotropy in the mechanical response due to the microstructures resulting from the high temperature gradients developed during fabrication, and the effect of surface roughness is different depending on the fabrication direction.

This chapter aims at covering some of the limitations of these previous models, extending the study of the surface roughness effects on fatigue life to flat samples. In particular, first the microstructure sensitive fatigue model for bulk samples will be extended to predict the fatigue life of flat samples while accounting for surface roughness effects. Second, the effect of building orientation on fatigue life of flat samples will be discussed.

6.2 Experimental Data

In this work, the Hastelloy-X specimens were fabricated using the Selective Laser Melting technique with same machine and process parameters specified in chapter 3.1. Different tensile specimens were prepared in ITP Aero in the form of bulk cylindrical samples (refer to section 3.1 and figure 3.2) and flat sheets with thickness 1.2mm.

The flat samples were manufactured using SLM with orientations parallel to build direction, direction Z (flat 1.2Z), and perpendicular to build direction (flat 1.2X) as shown in figure 6.1. Both flat specimens were fabricated in a flat sheet of dimensions 50mm×3mm×1.2mm and were machined to a rectangular dog-bone shape with the gauge-length of 15.68 μm. Finally, all samples were heat treated at 1170°C for 30 minutes followed by gas fan quench and were tested in annealed condition.

The surface roughness was always present in the SLM samples due to partially melted and unmelted powder left on the surface. Flat samples are machined along the thickness in the YZ section; however, due to geometrical constraints, the XZ section is difficult to machine and is consequently kept in as-built(unmachined) condition. The surface roughness of the plain specimens in the XZ surfaces is measured using a profilometer equipment "Mitutoyo SJ-210" with a stylus and the measurements were performed according to the ISO-4287. The surface roughness is represented by arithmetic mean surface roughness R_a, which is measured over a length as,

$$R_a = \frac{1}{L}\int_0^L |y| dz \tag{6.1}$$

where y represent the deviation form the average y-position of that surface. It must be noted that in Eq. 6.1, the surface roughness is in Y direction. The resulting mean surface roughness value obtained was $R_a \approx 10\mu m$.

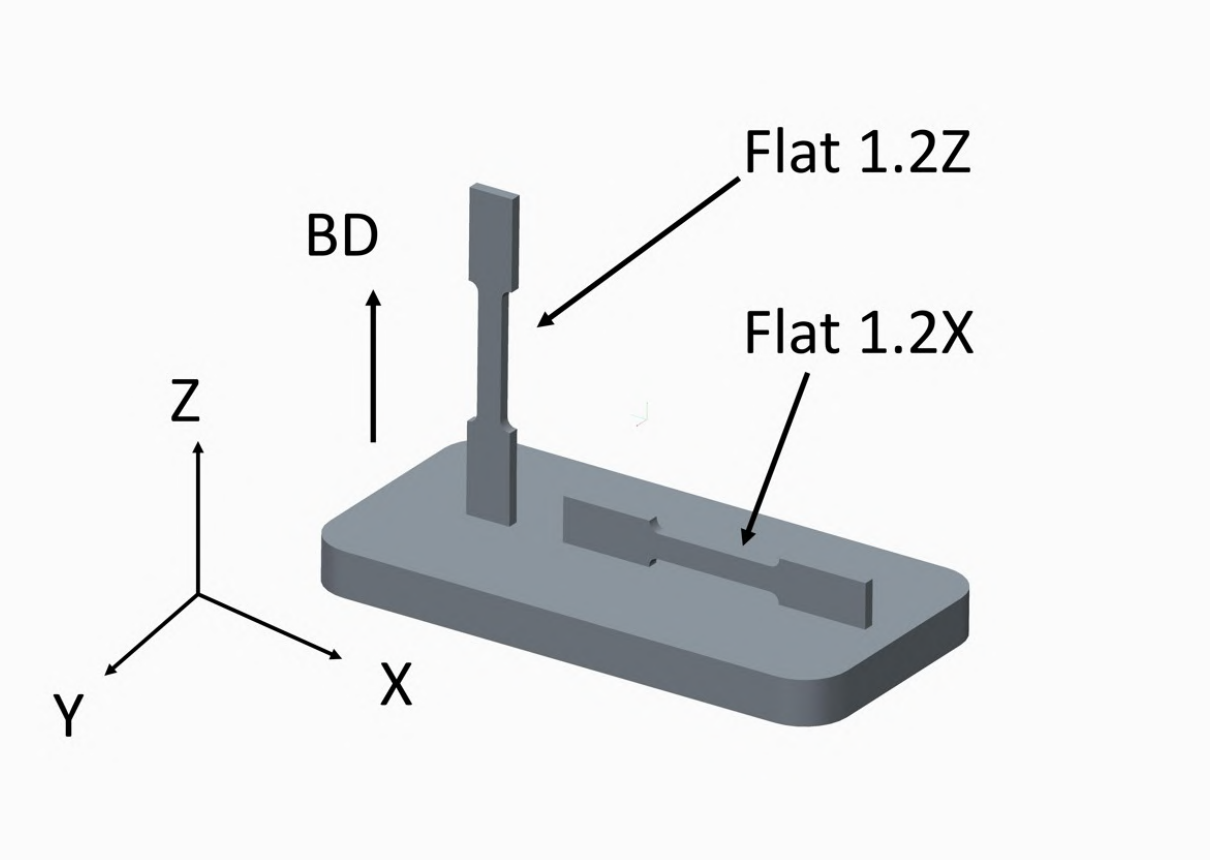

Figure 6.1: Description of coupon of flat sample with 1.2mm thickness built in Z and X direction

The uniaxial cyclic behavior of SLM fabricated Hastelloy-X at 750°C was experimentally determined by cyclic tests performed in a wide range of stress amplitudes. The experimental fatigue testing methodology is already addressed in section 5.4.1. The flat sample with a 1.2mm thickness oriented in Z direction (flat 1.2Z) is subjected to uniaxial tensile cyclic loading in building direction (Z), while the sample with 1.2 mm thickness oriented in X direction (flat 1.2X) is subjected to uniaxial tensile cyclic loading in the X-direction. The uniaxial cyclic tests for stress-controlled loading carried out with $\frac{\sigma}{\tau_0}$= 2.85,3.21,3.39,3.57 and $\frac{\sigma}{\tau_0}$= 2.85,3.21,3.57,4.29 for flat 1.2Z and flat 1.2X samples respectively with stress ratio R_σ=0.03. The normalization factor is the critical resolved shear stress, τ_0, identified for Hastelloy-X grains at 750°C.

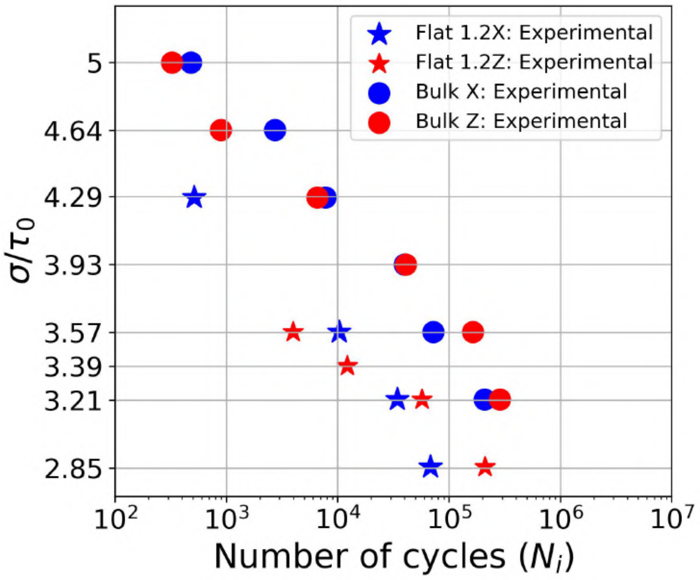

Figure 6.2: The experimental stress-life curve for flat 1.2X, 1.2Z sample along with bulk samples built in X and Z direction.

The fatigue S-N curve for stress control of flat samples are represented in figure 6.2. In these curves, the fatigue life N corresponds to the cycle in which the final fracture is reached on the specimen. The figure includes, for comparison purposes, the equivalent S-N results obtained for bulk samples (built in X and Z directions) with ultrafine surface polishing (with $R_a \leq 0.2\mu m$) under same testing conditions(refer section 5.4.1).

The first conclusion of the results represented in figure 6.2 is the clear reduction of life observed for the flat samples with respect to bulk ones. In addition, based on previous research findings (Shrestha et al., 2019; Wang et al., 2012) for similar alloys manufactured with SLM, it is expected that fatigue performance of the samples built in the X orientation should offer strong resistance to fatigue than in Z direction (see figure 6.2), similarly to what happens in the case of bulk samples(see section 5.4.1). However due to limited experimental data at higher stress levels, above mentioned fatigue anisotropy is not confirmed from experiment viewpoint. It should be emphasized that fatigue experiments are carried out at higher temperatures, i.e. 750°C, where fatigue-creep interaction is substantial at lower applied loads. The fatigue-creep interaction has the greatest influence in $\frac{\Delta\sigma}{\Delta\sigma_{min}}$= 2.85, 3.21, beyond which the fatigue mechanism dominates crack initiation.

6.3 Computational homogenization framework

6.3.1 RVE Generation

The microstructure of SLM Hastelloy-X is considered using cuboidal RVEs that, as in previous chapter 3, statistically represent the grain size, shape, and orientations obtained from the EBSD measurements. The detailed generation methodology of synthetic RVE, including grain size, aspect ratio, and orientation, is addressed in chapter 3.

The surface roughness of the actual specimens was located on YZ section of the flat samples and is the result of unmelted and semi-melted powder remaining on the surface. To introduce this roughness representing accurately the deformation of plain samples, the RVEs fulfilled these conditions:

- RVEs are right rectangular prisms with different edge lengths, being their relative edge lengths equal to the aspect ratio of the grains.
- RVE includes very compliant buffer layers to emulate stress-free boundary conditions in the planes perpendicular to the sample thickness (YZ plane). This free conditions are fundamental to consider the influence of the ratio between the actual specimen thickness and grain size.
- RVE is considered periodic in the other two directions, because sample size in those directions is much larger than grain size.
- Surface roughness is introduced in the YZ surfaces as the shape of the buffer region.

Regarding the shape of the rough surfaces, typical observation of the surface roughness profile is that it approximately resembles a sine curve shape (Pegues et al., 2019; Lorenz et al., 2021). Therefore, in this study, surface roughness is expressed by a simplified sinusoidal curve with amplitude R_a and wavelengths λ_x and λ_z in X and Z direction respectively, which is given as,

$$R_Y = R_a * \left(\sin \left(\frac{x}{\lambda_x} + \frac{z}{\lambda_z} \right) \right) \tag{6.2}$$

The average wavelength of surface roughness profiles in the X and Z directions is approximately the same($\lambda_x \approx \lambda_z$), and its measured value is 60 μm. The buffer layers of the compliant material (are placed on top and bottom of the cell in the Y direction and its surface has the sinusoidal shape provided by Eq. 6.2.

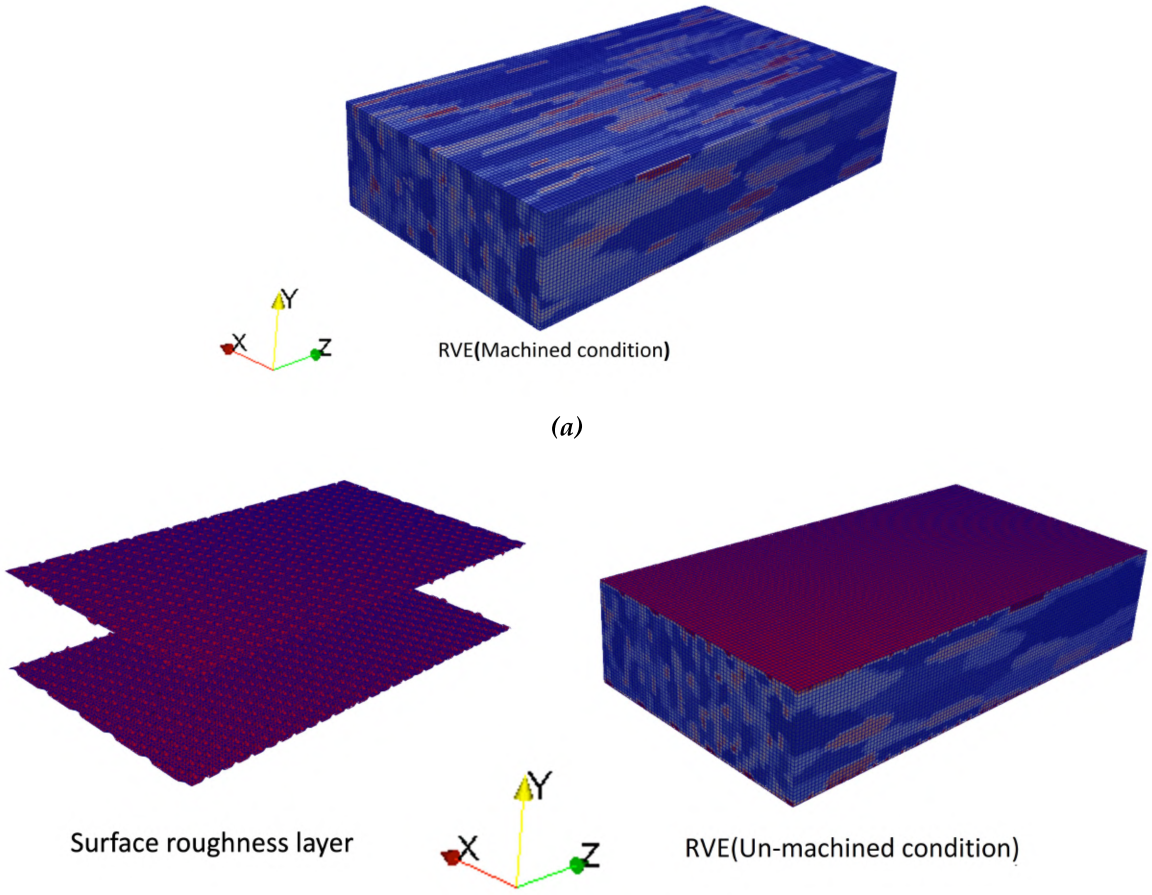

(a)

(b)

Figure 6.3: 3D non cubic RVEs of polycrystalline SLM Hastelloy-X for flat sample 1.2X in (a)machined and (b, right) as-built(with surface roughness) condition. (b, left) shows the layer of surface roughness. Note that colors indicate the grain numbers.

A resulting RVE is represented in figure 6.3. Figure 6.3(a) depicts the original periodic RVE that takes into account microstructural features such as grain size, shape, and orientation to represent machined samples. The shape of the buffer surfaces can be observed on figure 6.3(b), left part. Note that microstructure is periodic on X and Z directions and periodic boundary conditions are consider on that edges. The approximated number of crystals was 850 for the 1.2 mm samples. The resulting RVE with surface roughness is shown in the right part of figure 6.3(b).

6.4 Results

6.4.1 Simulation set-up

Following the digital representation of microstructure and geometry, the next stage is virtual testing using the CP-FFT full field homogenization framework.

The crystal plasticity model calibrated for cyclic behavior using Hastelloy-X bulk samples is discussed in section 5.3, and will be used without changes in this section. This election relies on the conclusions of chapters 4 and 5, where it is shown that microstructure changes are the only responsible of the different mechanical response obtained when varying building direction or specimen shape, and therefore crystal response of these samples should be identical to those. The CP-FFT computational homogenization framework used for the simulations is described in section2.4.5.

Finally, regarding the fatigue life prediction framework, FIP definition is the same as in section 5.3 and the approach for predicting fatigue life under stress-controlled loading described in section 5.4.6 is used here. Moreover, as in the case of the CP parameters, the constants of the fatigue life obtained for a bulk sample are kept, considered to be representative of the crystal. Therefore, no fitting parameters are necessary for the estimation of the fatigue life of the flat samples and the fatigue tests available in two different building directions, flat 1.2X and flat 1.2Z, can be used to validate the fatigue life predictions.

To quantify the effect of the free non-smooth surfaces with respect bulk smooth specimens, two set of simulations are considered. The first one, a statistically representative volume element (SVE) containing 20 random and statistically equivalent RVEs, represent a perfectly periodic microstructure which corresponds to flat specimens with no-surface effects (representing machined flat specimens). This fully periodic models reproduce the average grain size, aspect ratio, and grain orientations for flat 1.2X and flat 1.2Z samples (hereon called as machined).The second SVE, also with 20 different RVEs, correspond to the models depicted in figure 6.3b, where surface roughness is introduced on planes lateral planes perpendicular to the specimen thickness, being the other 2 directions fully periodic. These models reproduce the roughness, average grain size, aspect ratio, grain orientations of the plain 1.2mm samples and will be named as 'un-machined' samples.

SVEs were subjected to virtual uniaxial stress-controlled cyclic tests with $\frac{\sigma}{\tau_0}$= 2.85, 3.21, 3.39, 3.57 for flat 1.2Z and $\frac{\sigma}{\tau_0}$= 2.85, 3.21, 3.57, 4.29 for flat 1.2X with a stress ratio R_σ = 0.03 for both machined and as-built condition. τ_0 corresponds to the critical resolved shear stress (CRSS). The value of the parameters of the fatigue life prediction model, $W_{crit\sigma} = 5.06 \times 10^8$ and $nk = 0.56$, are taken from section 5.4.6 and were fitted using two experiments for Bulk X sample. The cumulative FIP, W_p^{acc} of these tests was calculated by simulating an SVE with 20 distinct RVEs. The large magnitude of the SVE aids in predicting the stochastic character of fatigue life for a given microstructure and loading conditions. It should be remarked that no experimental results on flat 1.2Z and flat 1.2X samples were utilised to calibrate the model, therefore the results are purely predictive and will evaluate the model's validity to consider alternative microstructures for the same parameters.

6.4.2 Effect of surface roughness

The prediction of fatigue crack initiation life for flat samples 1.2Z and 1.2X without surface roughness is represented by blue lines and in un-machined condition (with surface roughness) by red lines, together with the corresponding experimental life (black asterisks), is presented in figures 6.4a and 6.4b, respectively. Note that surface roughness is abbreviated as SR in the figure. For both building orientations, the agreement between experimental and numerically predicted fatigue life when surface roughness is taken into consideration is excellent. The largest difference was observed for the flat 1.2X sample in the stress ranges σ/τ_0, 2.85, and 3.21, where fatigue life is somewhat overestimated. If surface roughness is not taken into account in the model, the microstructure and sample geometry dominate fatigue crack initiation. In this scenario, the fatigue life prediction is represented by blue lines in figures 6.4a and 6.4b for samples 1.2Z and 1.2X, respectively. These figures show that in the absence of surface roughness, the predicted life is highly overestimated. As a result, in the case of flat samples with considerable surface roughness, merely microstructure is insufficient to predict fatigue life, and surface roughness addition is critical from a modelling standpoint.

These findings show that the model can adequately predict fatigue life while accounting for the effects of microstructure, surface roughness and geometry of samples. The consistency of predicted fatigue lives with the experimental results for both flat samples is noteworthy, given that the fatigue life law utilised for the predictions was calibrated using only two experiments of Bulk-X samples.

It is a well-known notion that as the applied cyclic stresses are reduced, the scatter in the fatigue lives increases. However, in the case of flat samples, this rule is not always followed due to a lack of fusion between consecutive layers, which is partly linked to surface roughness; this fact leads to variation in fatigue lives at all applied stresses(Shrestha et al., 2019). Furthermore, surface roughness in transverse section (normal to thickness, Y), where only 2-3 grains in the border area influence the fatigue resistance, will increase variability at higher stress levels.

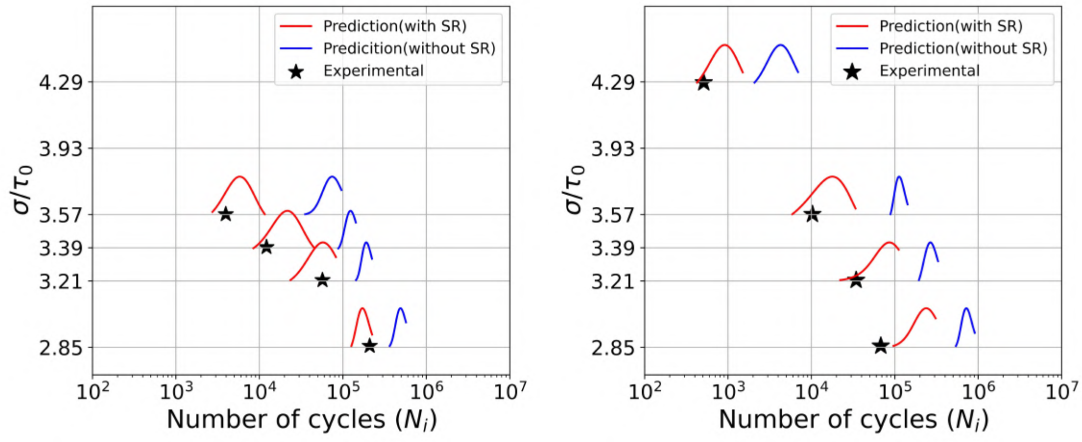

(a) *(b)*

Figure 6.4: Comparison between predicted and experimental fatigue life under machined(without surface roughness, SR) represented by blue lines and unmachined(with SR) conditions, shown by red lines for a) flat 1.2Z and b) flat 1.2X samples

6.4.3 Effect of build orientation

Figure 6.5 depicts the S-N curves for the two building directions(flat 1.2X an flat 1.2Z) that account for surface roughness in order to study the influence of the building direction on the fatigue life of flat samples. In experiments, it is expected that, horizontally built specimen (flat 1.2X) should exhibit higher resistance to fatigue crack initiation than the vertical counterpart (flat 1.2Z)(see section 5.4.1). However, experimental data for higher cyclic stress in flat samples is more limited, and the above-mentioned fatigue anisotropy cannot be substantiated based on the available experimental lives for the applied stress ranges. On the other hand, the proposed CP-FFT model suggest the above-mentioned fatigue anisotropy which is consistent with the research findings of Shreshta et al.(Shrestha et al., 2019) and Wang et al. (Wang et al., 2012). Therefore, further experimental fatigue campaign at higher stress levels is necessary to validate the predicted fatigue lives.

The model does not accurately predict the fatigue lives at two smallest stress ranges $\sigma/\tau_0 = 2.85, 3.21$. This effect is probably similar to one found in case of bulk, where horizontal samples(bulk X) are more resistant. At lower applied stresses, the difference in fatigue life diminishes because very small plasticity localizes at the microstructure. To accurately predict fatigue lives at lower stress levels, the fatigue-creep interaction mechanism must be accounted in the model.

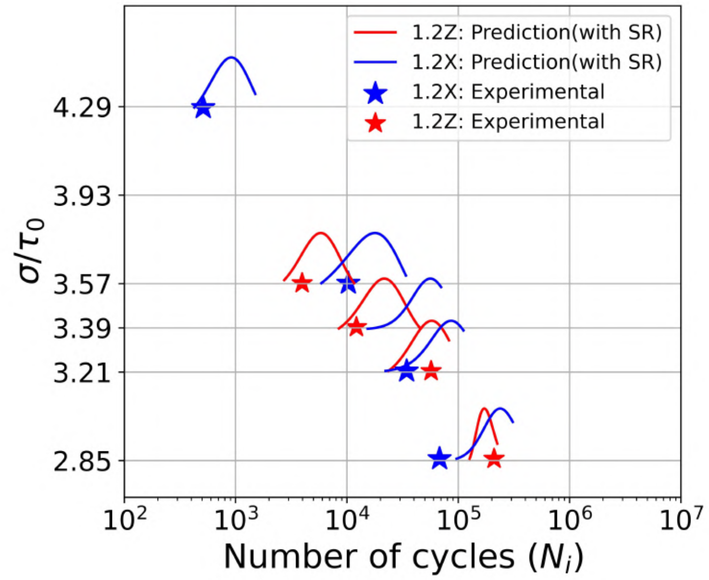

Figure 6.5: The comparison between experimental and predicted fatigue lives of flat 1.2X and flat 1.2Z, showing the effect of build orientation on fatigue performance of flat samples.

To summarize, the CP-FFT model predicts that the horizontally oriented samples perform better in terms of fatigue than vertically oriented samples regardless of geometry (i.e. bulk or flat). Furthermore, this anisotropy is caused by the microstructure, namely grain shape and orientation, and surface roughness has no effect on anisotropic fatigue response due to the building orientation. This conclusion is in line with the findings of Yadollahi et al.(Yadollahi et al., 2017), Sreshta et al.(Shrestha et al., 2019), and Edwards et al.(Edwards and Ramulu, 2014b). However, in this study, experimental fatigue tests at higher cyclic stress are rather limited, and further experimental campaigns are required to validate the model prediction, but it is believed that the experiment would confirm the numerical predictions.

7 Conclusions and future work

7.1 Conclusions

This thesis is focused on the development of a CP-FFT framework to predict the quasi-static and fatigue response of SLM-fabricated Hastelloy-X as function of its microstructure. Throughout the thesis, it was evident that microstructural factors does play an important role in anisotropic mechanical response in AM. The alloy microstructure for each specimen is represented by a Representative Volume Element (RVEs) of the microstructure, which comprises the experimentally observed grain size, shape (aspect ratio), and orientation distributions. Furthermore, for samples with thicknesses comparable to grain size, the actual specimen cross-section was taken into account. The CP model used for crystal response for quasi-static and fatigue cases was fitted with the Levenberg-Marquart algorithm utilizing one experiment in each case.

The first major contribution of the thesis is a calibrated numerical model able to predict the anisotropic quasi-static response of SLM Hastelloy-X as a function of its microstructure, temperature, and sample thickness. The model is validated against different build orientation and the study leads to the following conclusions:

- The proposed framework can accurately predict the Young's modulus and elastic anisotropy of various specimens over a wide temperature range.

- SLM built specimens after their corresponding heat treatment present the same crystal response. The large variations found of the mechanical response for different fabrication conditions are just the result of the changes in the polycrystalline microstructure.
- The CP-FFT model with precise reproduction of the actual microstructure can simulate very precisely the changes in elasto-plastic response caused by printing direction and specimen thickness using the same CP model parameters.
- The temperature dependence in the CP model is introduced using a power law formulation with two configurable parameters, and the resulting model can mimic the elasto-plastic response within a given temperature range of 298K-1023K for any initial microstructure.
- It is shown that if the key microstructural features (grain size, aspect ratio, and orientation) are considered, the same CP model can be used to accurately predict the response of any specimen, loading direction and temperature.

The second result of the work is the prediction of the fatigue life of SLM Hastelloy-X under strain and stress controlled loading as a function of build orientation and microstructure ; and the study leads to the following conclusions:

- A phenomenological crystal plasticity model with a back stress term can accurately reproduce the Hastelloy-X hysteresis curve under all loading conditions.
- Accelerating the evolution of internal variables so that the model's stable hysteresis cycle is reached prior to experimental stabilization significantly decreases computational cost and produces accurate results in fatigue prediction.
- A power-law life prediction model with two fitting parameters based on cyclic and accumulated plastic work FIP reliably predicts life for strain and stress controlled tests, respectively.
- The model can capture the effect of the fabrication direction on fatigue performance by using RVEs statistically representing the actual microstructure resulting from each fabrication direction.
- The direction of the SLM fabrication (along the loading axis or perpendicular to it) is found to influence the fatigue performance of Hastelloy-X, especially for high applied stress ranges.
- The model shows that grain elongation is the most relevant microstructural feature responsible for the better fatigue performance of Bulk-X samples.

Finally, the fatigue life prediction framework is extended to account for the effects of surface roughness, microstructure, and sample geometry for predicting the fatigue life of flat samples ; and the study leads to the following conclusions:

- The surface roughness profile that conforms to the analytical sinusoidal formulation is introduced to the RVE as an extra layer that serves as both a defect(surface roughness) and a free surface for the flat sample.
- The fatigue life of flat samples can be predicted using the same CP model as is used for bulk samples, without any adjustments.
- The model can predict the effect of surface roughness on SLM Hastelloy-X fatigue performance. The model demonstrates that the sample has a shorter fatigue life than the machined specimen in the presence of surface roughness.
- The model can capture the effect of build orientation on fatigue performance, demonstrating the combined effect of surface roughness and microstructure on the fatigue performance of flat samples.

7.2 Future work

Despite significant efforts to develop a microstructure sensitive virtual testing framework, the models presented can be enhanced in the following areas.

- The model developed in this study is phenomenological in nature, however physically based constitutive models could allow to further reduce the number of tests required and to include some physical measurable parameters in the model such as the dislocation density.
- For simplicity, the current model does not account for fatigue-creep interaction; however, at high temperatures, the current model will be adjusted to account for the mechanism of creep phenomena and fatigue-creep interaction.
- A fatigue life prediction model can be enhanced by adopting a more physical definition of FIP or FIPs obtained by in-situ experiments.
- The accuracy of the influence of surface roughness on the fatigue life prediction model will be improved by precisely representing the actual 3D surface roughness topology in the RVE.

- In some circumstances, the microstructure produced by the SLM method exhibits bi-modal grain distribution (Ma et al., 2020), with fine equiaxed grains in the hatch section and columnar grains in the border section. The anisotropic mechanical response will be obtained by including a bi-modal distribution of grains in the RVE.

Additionally, the present virtual testing framework can be combined with the virtual processing framework to build a complete virtual additive manufacturing framework in which the influence of different factors during part fabrication through SLM route on mechanical performance can be directly predicted. The combination of these two techniques would lead to a very powerful tool for the design of SLM components which include fabrication parameters to get optimal performance based on the microstructures developed.

A PERSONAL CONTRIBUTIONS

Publications

Chandrashekhar M.Pilgar, Ana M.Fernandez, Sergio Lucarini, Javier Segurado (June, 2022) Effect of printing direction and thickness on the mechanical behavior of SLM fabricated Hastelloy-X *International Journal of Plasticity 153:103250*

Chandrashekhar M.Pilgar, Ana M.Fernandez, Javier Segurado (March 2023) Microstructure sensitive fatigue life prediction model for SLM fabricated Hastelloy-X. *International Journal of Fatigue 168: 107372*

Chandrashekhar M.Pilgar, Ana M.Fernandez, Javier Segurado (2023) Effect of surface roughness and thickness on the fatigue performance of SLM fabricated Hastelloy-X *In preparation*

Bibliography

Terminology for additive manufacturing technologies,. URL `https://doi.org/10.1520/f2792-12`.

Additive manufacturing trend report 2021. HUBS survey report 2021, 2021.

E. Abele and M. Kniepkamp. Analysis and optimisation of vertical surface roughness in micro selective laser melting. *Surface Topography: Metrology and Properties*, 3(3): 034007, Sept. 2015. doi: 10.1088/2051-672x/3/3/034007. URL `https://doi.org/10.1088/2051-672x/3/3/034007`.

R. Acharya, J. A. Sharon, and A. Staroselsky. Prediction of microstructure in laser powder bed fusion process. *Acta Materialia*, 124:360–371, Feb. 2017. doi: 10.1016/j.actamat.2016.11.018. URL `https://doi.org/10.1016/j.actamat.2016.11.018`.

D. Agius, K. I. Kourousis, C. Wallbrink, and T. Song. Cyclic plasticity and microstructure of as-built SLM ti-6al-4v: The effect of build orientation. *Materials Science and Engineering: A*, 701:85–100, July 2017. doi: 10.1016/j.msea.2017.06.069. URL `https://DOI.org/10.1016/j.msea.2017.06.069`.

A. Ahmadi, R. Mirzaeifar, N. S. Moghaddam, A. S. Turabi, H. E. Karaca, and M. Elahinia. Effect of manufacturing parameters on mechanical properties of

316L stainless steel parts fabricated by selective laser melting: A computational framework. *Materials and Design*, 112:328–338, 2016. doi: https://10.1007/s11465-018-0505-y.

M. Akbari and R. Kovacevic. Closed loop control of melt pool width in robotized laser powder–directed energy deposition process. *The International Journal of Advanced Manufacturing Technology*, 104(5-8):2887–2898, July 2019. doi: 10.1007/s00170-019-04195-y. URL `https://doi.org/10.1007/s00170-019-04195-y`.

U. Ali, Y. Mahmoodkhani, S. I. Shahabad, R. Esmaeilizadeh, F. Liravi, E. Sheydaeian, K. Y. Huang, E. Marzbanrad, M. Vlasea, and E. Toyserkani. On the measurement of relative powder-bed compaction density in powder-bed additive manufacturing processes. *Materials and Design*, 155:495–501, Oct. 2018. doi: 10.1016/j.matdes.2018.06.030. URL `https://doi.org/10.1016/j.matdes.2018.06.030`.

M. A. Anam, D. Pal, and B. Stucker. Modeling and experimental validation of nickel-based super alloy (inconel 625) made using selective laser melting. 08 2013. doi: 10.13140/2.1.4009.1201.

M. T. Andani, M. R. Karamooz-Ravari, R. Mirzaeifar, and J. Ni. Micromechanics modeling of metallic alloys 3d printed by selective laser melting. *Materials &amp Design*, 137:204–213, Jan. 2018. doi: 10.1016/j.matdes.2017.10.026. URL `https://doi.org/10.1016/j.matdes.2017.10.026`.

S. AS, B. SKALLERUD, B. TVEITEN, and B. HOLME. Fatigue life prediction of machined components using finite element analysis of surface topography. *International Journal of Fatigue*, 27(10-12):1590–1596, Oct. 2005. doi: 10.1016/j.ijfatigue.2005.07.031. URL `https://doi.org/10.1016/j.ijfatigue.2005.07.031`.

S. K. Ås, B. Skallerud, and B. W. Tveiten. Surface roughness characterization for fatigue life predictions using finite element analysis. *International Journal of Fatigue*, 30(12):2200–2209, 2008.

R. Asaro and A. Needleman. Overview no. 42 texture development and strain hardening in rate dependent polycrystals. *Acta Metallurgica*, 33(6):923 – 953, 1985.

M. M. Attallah, R. Jennings, X. Wang, and L. N. Carter. Additive manufacturing of ni-based superalloys: The outstanding issues. *MRS Bulletin*, 41:758–764, 2016.

M. Aydinöz, F. Brenne, M. Schaper, C. Schaak, W. Tillmann, J. Nellesen, and T. Niendorf. On the microstructural and mechanical properties of post-treated additively manufactured inconel 718 superalloy under quasi-static and cyclic loading. *Materials Science and Engineering: A*, 669:246–258, 2016.

F. Azhari, C. Wallbrink, Z. Sterjovski, B. R. Crawford, A. Menzel, D. Agius, C. H. Wang, and G. Schaffer. Predicting the complete tensile properties of additively manufactured ti-6al-4v by integrating three-dimensional microstructure statistics with a crystal plasticity model. *International Journal of Plasticity*, 148:103127, 2022.

F. Bachmann, R. Hielscher, and H. Schaeben. Grain detection from 2d and 3d EBSD data—specification of the MTEX algorithm. *Ultramicroscopy*, (111):1637–1653, 2011. doi: doi:10.1016/j.ultramic.2011.08.002.

D. Barba Cancho, C. Alabort Martínez, T. Tang, M. Viscasillas, R. Reed, and E. Alabort. On the size and orientation effect in additive manufactured Ti-6Al-4V. *Materials and Design*, 186:108325, 2019.

O. Basquin. The exponential law of endurance tests. *American Society of Testing Materials*, 10:626–630, 1910.

J. Bauschinger. Ober das kristallinischwerden und die festigkeitsverminderung des eisens durch den gebrauch. *Dinglers J*, 13:1–115, 1880.

P. Bayati, A. Jahadakbar, M. Barati, M. Nematollahi, L. Saint-Sulpice, M. Haghshenas, S. A. Chirani, M. J. Mahtabi, and M. Elahinia. Toward low and high cycle fatigue behavior of slm-fabricated niti: Considering the effect of build orientation and employing a self-heating approach. *International Journal of Mechanical Sciences*, 185:105878, 2020.

R. Becker. Analysis of texture evolution in channel die compression—i. effects of grain interaction. *Acta Metallurgica et Materialia*, 39(6):1211 – 1230, 1991.

M. Belhadjamor, S. Belghith, S. Mezlini, and M. E. Mansori. Numerical study of normal contact stiffness: Non-gaussian roughness and elastic–plastic behavior. *Proceedings of the Institution of Mechanical Engineers, Part J: Journal of Engineering Tribology*, 234(9): 1368–1380, Dec. 2019. doi: 10.1177/1350650119893520. URL `https://doi.org/10.1177/1350650119893520`.

V. Bennett and D. McDowell. Polycrystal orientation distribution effects on microslip in high cycle fatigue. *International Journal of Fatigue*, 25(1):27 – 39, 2003.

A. Bhattacharyya, E. El-Danaf, S. R. Kalidindi, and R. D. Doherty. Evolution of grain-scale microstructure during large strain simple compression of polycrystalline aluminum with quasi-columnar grains: Oim measurements and numerical simulations. *International Journal of Plasticity*, 17(6):861 – 883, 2001.

C. M. Bhushan B. An overview of additive manufacturing (3d printing) for microfabrication. *Microsyst Technol*, 23:1117–1124, 2017.

G. Bi, C.-N. Sun, H. chi Chen, F. L. Ng, and C. C. K. Ma. Microstructure and tensile properties of superalloy IN100 fabricated by micro-laser aided additive manufacturing. *Materials & Design*, 60:401–408, Aug. 2014. doi: 10.1016/j.matdes.2014.04.020. URL `https://doi.org/10.1016/j.matdes.2014.04.020`.

R. Branco, J. Costa, F. Berto, S. Razavi, J. Ferreira, C. Capela, L. Santos, and F. Antunes. Low-cycle fatigue behaviour of AISI 18ni300 maraging steel produced by selective laser melting. *Metals*, 8(1):32, Jan. 2018a.

R. Branco, J. Costa, F. Berto, S. Razavi, J. Ferreira, C. Capela, L. Santos, and F. Antunes. Low-cycle fatigue behaviour of AISI 18ni300 maraging steel produced by selective laser melting. *Metals*, 8(1):32, jan 2018b. doi: 10.3390/met8010032.

S. Brisard and L. Dormieux. FFT-based methods for the mechanics of composites: A general variational framework. *Computational Materials Science*, 49(3):663–671, sep 2010. doi: 10.1016/j.commatsci.2010.06.009.

S. Brisard and L. Dormieux. Combining galerkin approximation techniques with the principle of hashin and shtrikman to derive a new FFT-based numerical method for the homogenization of composites. *Computer Methods in Applied Mechanics and Engineering*, 217-220:197–212, apr 2012. doi: 10.1016/j.cma.2012.01.003.

C. Bronkhorst, J. Mayeur, V. Livescu, R. Pokharel, D. Brown, and G. Gray. Structural representation of additively manufactured 316l austenitic stainless steel. *International Journal of Plasticity*, 118:70–86, 2019.

C. M. Brown, W. Dreyer, and W. H. Müller. Discrete fourier transforms and their application to stress—strain problems in composite mechanics: a convergence study. *Proceedings of the Royal Society of London. Series A: Mathematical, Physical and Engineering Sciences*, 458(2024):1967–1987, aug 2002. doi: 10.1098/rspa.2001.0955.

G. Cailletaud. A micromechanical approach to inelastic behaviour of metals. *International Journal of Plasticity*, 8(1):55 – 73, 1992.

R. Campbell, M. Martorelli, and H. Lee. Surface roughness visualisation for rapid prototyping models. *Computer-Aided Design*, 34(10):717–725, Sept. 2002. doi: 10.1016/s0010-4485(01)00201-9. URL `https://doi.org/10.1016/s0010-4485(01)00201-9`.

H. A. Canistraro, F. A. Reed, E. H. Jordan, and L. H. Favrow. Elastic constants of single crystal Hastelloy X at elevated temperatures. *Transactions of the ASME: Journal of engineering materials and technology*, 120(3):242–247, 1998. doi: https://doi.org/10.1115/1.2812350.

M. Cao, Y. Liu, and F. P. Dunne. A crystal plasticity approach to understand fatigue response with respect to pores in additive manufactured aluminium alloys. *International Journal of Fatigue*, page 106917, 2022.

Y. Cao and J. Choi. Solidification microstructure evolution model for laser cladding process. *Journal of Heat Transfer*, 129(7):852–863, Aug. 2006. doi: 10.1115/1.2712856. URL `https://doi.org/10.1115/1.2712856`.

L. N. Carter, X. Wang, N. Read, R. Khan, M. Aristizabal, K. Essa, and M. M. Attallah. Process optimisation of selective laser melting using energy density model for nickel based superalloys. *Materials Science and Technology*, 32(7):657–661, Feb. 2016. doi: 10.1179/1743284715y.0000000108. URL `https://doi.org/10.1179/1743284715y.0000000108`.

G. M. Castelluccio and D. L. McDowell. Mesoscale modeling of microstructurally small fatigue cracks in metallic polycrystals. *Materials Science and Engineering: A*, 598:34 – 55, 2014. ISSN 0921-5093.

G. M. Castelluccio and D. L. McDowell. Microstructure and mesh sensitivities of mesoscale surrogate driving force measures for transgranular fatigue cracks in polycrystals. *Materials Science and Engineering: A*, 639:626 – 639, 2015.

A. Charmi, R. Falkenberg, L. Ávila, G. Mohr, K. Sommer, A. Ulbricht, M. Sprengel, R. Saliwan Neumann, B. Skrotzki, and A. Evans. On the role of melt flow into the surface structure and porosity development during selective laser melting. *Materials Science and Engineering: A*, 799:140–154, 2021.

B. Chen, J. Jiang, and F. P. Dunne. Is stored energy density the primary meso-scale mechanistic driver for fatigue crack nucleation? *International Journal of Plasticity*, 101:213 – 229, 2018.

J. Cheng, P. Fernandez-Zelaia, X. Hu, and M. Kirka. Effect of microstructure on fatigue crack propagation in additive manufactured nickel-based superalloy haynes 282: an experiment and crystal plasticity study. *Journal of Materials Science*, 2022a.

X. Cheng, Z. Du, S. Chu, J. Wu, J. Dong, H. Wang, and Z. Ma. The effect of subsequent heating treatment on the microstructure and mechanical properties of additive manufactured hastelloy x alloy. *Materials Characterization*, 186:111799, Apr. 2022b. doi: 10.1016/j.matchar.2022.111799. URL `https://doi.org/10.1016/j.matchar.2022.111799`.

C. K. Chua and K. F. Leong. 3d printing and additive manufacturing: Principles and applications (with companion media pack) - fourth edition of rapid prototyping. 2014.

J. Clayton. Dynamic plasticity and fracture in high density polycrystals: constitutive modeling and numerical simulation. *Journal of the Mechanics and Physics of Solids*, 53 (2):261–301, 2005. doi: https://doi.org/10.1016/j.jmps.2004.06.009.

M. Cloots, P. J. Uggowitzer, and K. Wegener. Investigations on the microstructure and crack formation of IN738lc samples processed by selective laser melting using gaussian and doughnut profiles. *Materials & Design*, 89:770–784, Jan. 2016. doi: 10.1016/j.matdes.2015.10.027. URL `https://doi.org/10.1016/j.matdes.2015.10.027`.

L. Coffin. A study of the effects of cyclic thermal stresses on a ductile metal. *Transactions of the American Society of Mechanical Engineers*, 76:931–950, 1954.

A. Cruzado, B. Gan, M. Jiménez, D. Barba, K. Ostolaza, A. Linaza, J. Molina-Aldareguia, J. Llorca, and J. Segurado. Multiscale modeling of the mechanical behavior of in718 superalloy based on micropillar compression and computational homogenization. *Acta Materialia*, 98:242 – 253, 2015.

A. Cruzado, J. LLorca, and J. Segurado. Modeling cyclic deformation of inconel 718 superalloy by means of crystal plasticity and computational homogenization. *International Journal of Solids and Structures*, 122:148 – 161, 2017.

A. Cruzado, S. Lucarini, J. LLorca, and J. Segurado. Microstructure-based fatigue life model of metallic alloys with bilinear coffin-manson behavior. *International Journal of Fatigue*, 107:40–48, 2018.

A. Cuitiño and M. Ortiz. A material-independent method for extending stress update algorithms from small-strain pasticity to finite plasticity with multiplicative kinematics. *Engineering Computations*, 9:437 – 451, 1992.

E. D. Cyr, M. Mohammadi, R. K. Mishra, and K. Inal. A three dimensional (3d) thermo-elasto-viscoplastic constitutive model for fcc polycrystals. *International Journal of Plasticity*, 70:166–190, 2015. doi: https://doi.org/10.1016/j.ijplas.2015.04.001.

S. Deguang. A new multiaxial fatigue damage model based on the critical plane approach. *International Journal of Fatigue*, 20(3):241–245, 1998. doi: 10.1016/s0142-1123(97)00123-0. URL `https://doi.org/10.1016/s0142-1123(97)00123-0`.

F. Delaire, J. Raphanel, and C. Rey. Plastic heterogeneities of a copper multicrystal deformed in uniaxial tension: experimental study and finite element simulations. *Acta Materialia*, 48(5):1075 – 1087, 2000.

D. Deng. *Additively Manufactured Inconel 718 : Microstructures and Mechanical Properties*. Linköping University Electronic Press, Jan. 2018. doi: 10.3384/lic.diva-144491. URL `https://doi.org/10.3384/lic.diva-144491`.

G. E. Dieter and D. Bacon. *Mechanical Metallurgy*. 10 1988. ISBN 9780070841871.

V. Divya, R. Muñoz-Moreno, O. Messé, J. Barnard, S. Baker, T. Illston, and H. Stone. Microstructure of selective laser melted CM247lc nickel-based superalloy and its evolution through heat treatment. *Materials Characterization*, 114:62–74, Apr. 2016. doi: 10.1016/j.matchar.2016.02.004. URL `https://doi.org/10.1016/j.matchar.2016.02.004`.

A. Doitrand, C. Fagiano, F.-X. Irisarri, and M. Hirsekorn. Comparison between voxel and consistent meso-scale models of woven composites. *Composites Part A: Applied Science and Manufacturing*, 73:143–154, jun 2015. doi: 10.1016/j.compositesa.2015.02.022.

W. Dreyer, W. H. Mller, and J. Olschewski. An approximate analytical 2d-solution for the stresses and strains in eigenstrained cubic materials. *Acta Mechanica*, 136(3-4): 171–192, sep 1999. doi: 10.1007/bf01179256.

A. du Plessis and E. Macdonald. Hot isostatic pressing in metal additive manufacturing: X-ray tomography reveals details of pore closure. *Additive Manufacturing*, 34:101191, Aug. 2020. doi: 10.1016/j.addma.2020.101191. URL `https://doi.org/10.1016/j.addma.2020.101191`.

F. Dunne. Fatigue crack nucleation: Mechanistic modelling across the length scales. *Current Opinion in Solid State and Materials Science*, 18, 2014.

P. Edwards and M. Ramulu. Fatigue performance evaluation of selective laser melted ti–6al–4v. *Materials Science and Engineering: A*, 598:327–337, Mar. 2014a. doi: 10.1016/j.msea.2014.01.041. URL `https://DOI.org/10.1016/j.msea.2014.01.041`.

P. Edwards and M. Ramulu. Fatigue performance evaluation of selective laser melted ti–6al–4v. *Materials Science and Engineering: A*, 598:327–337, 2014b.

A. Eghtesad and M. Knezevic. A full-field crystal plasticity model including the effects of precipitates: Application to monotonic, load reversal, and low-cycle fatigue behavior of inconel 718. *Materials Science and Engineering: A*, 803:140478, 2021. ISSN 0921-5093.

P. Eisenlohr, M. Diehl, R. Lebensohn, and F. Roters. A spectral method solution to crystal elasto-viscoplasticity at finite strains. *International Journal of Plasticity*, 46:37 – 53, 2013.

M. El Haddad, T. Topper, and K. Smith. Prediction of non propagating cracks. *Engineering fracture mechanics*, 11(3):573–584, 1979.

S. Elahi, R. Tavakoli, A. Boukellal, T. Isensee, I. Romero, and D. Tourret. Multiscale simulation of powder-bed fusion processing of metallic alloys. *Computational Materials Science*, 209:111383, June 2022. doi: 10.1016/j.commatsci.2022.111383. URL `https://doi.org/10.1016/j.commatsci.2022.111383`.

S. Elahi, R. Tavakoli, I. Romero, and D. Tourret. Grain growth competition during melt pool solidification — comparing phase-field and cellular automaton models. *Computational Materials Science*, 216:111882, Jan. 2023. doi: 10.1016/j.commatsci.2022.111882. URL `https://doi.org/10.1016/j.commatsci.2022.111882`.

K. S. Eloh, A. Jacques, and S. Berbenni. Development of a new consistent discrete green operator for FFT-based methods to solve heterogeneous problems with eigenstrains. *International Journal of Plasticity*, 116:1–23, may 2019. doi: 10.1016/j.ijplas.2018.10.011. URL `https://doi.org/10.10162Fj.ijplas.2018.10.011`.

J. D. Eshelby and R. E. Peierls. The determination of the elastic field of an ellipsoidal inclusion, and related problems. *Proceedings of the Royal Society of London. Series A. Mathematical and Physical Sciences*, 241(1226):376–396, 1957.

R. Esmaeilizadeh, A. Keshavarzkermani, U. Ali, B. Behravesh, A. Bonakdar, H. Jahed, and E. Toyserkani. On the effect of laser powder-bed fusion process parameters on quasi-static and fatigue behaviour of hastelloy x: A microstructure/defect interaction study. *Additive Manufacturing*, 38:101805, Feb. 2021. doi: 10.1016/j.addma.2020.101805. URL `https://DOI.org/10.1016/j.addma.2020.101805`.

R. Esmaeilizadeh, A. Keshavarzkermani, S. Faghih, B. Behravesh, U. Ali, A. Bonakdar, H. Jahed, and E. Toyserkani. Fatigue characterization and modeling of additively manufactured hastelloy-x superalloy. *Journal of Materials Engineering and Performance*, 31(8):6234–6245, Feb. 2022. doi: 10.1007/s11665-022-06595-w. URL `https://doi.org/10.1007/s11665-022-06595-w`.

M. Esmaeilzadeh, F. Qods, H. Arabi, and B. Sadeghi. An investigation on crack growth rate of fatigue and induction heating thermo-mechanical fatigue (TMF) in hastelloy x superalloy via LEFM, EPFM and integration models. *International Journal of Fatigue*, 97:135–149, Apr. 2017.

T. Etter, K. Kunze, F. Geiger, and H. Meidani. Reduction in mechanical anisotropy through high temperature heat treatment of Hastelloy X processed by selective laser melting (SLM). *IOP Conference Series: Materials Science and Engineering*, 82:012097, 04 2015.

V. Fallah, M. Amoorezaei, N. Provatas, S. Corbin, and A. Khajepour. Phase-field simulation of solidification morphology in laser powder deposition of ti–nb alloys. *Acta Materialia*, 60(4):1633–1646, Feb. 2012. doi: 10.1016/j.actamat.2011.12.009. URL `https://doi.org/10.1016/j.actamat.2011.12.009`.

H. Farooq, G. Cailletaud, S. Forest, and D. Ryckelynck. Crystal plasticity modeling of the cyclic behavior of polycrystalline aggregates under non-symmetric uniaxial loading: Global and local analyses. *International Journal of Plasticity*, 126:102619, 2020.

A. Fatemi and D. F. Socie. A critical plane approach to multiaxial fatigue damage including out-of-phase loading. *Fatigue & Fracture of Engineering Materials & Structures*, 11(3):149–165, 1988.

A. Fatemi and L. Yang. Cumulative fatigue damage and life prediction theories: a survey of the state of the art for homogeneous materials. *International Journal of Fatigue*, 20(1):9–34, Jan. 1998. doi: 10.1016/s0142-1123(97)00081-9. URL `https://doi.org/10.1016/s0142-1123(97)00081-9`.

B. Ferrar, L. Mullen, E. Jones, R. Stamp, and C. Sutcliffe. Gas flow effects on selective laser melting (SLM) manufacturing performance. *Journal of Materials Processing*

Technology, 212(2):355–364, Feb. 2012. doi: 10.1016/j.jmatprotec.2011.09.020. URL `https://doi.org/10.1016/j.jmatprotec.2011.09.020`.

Z. GaoLe, J. Yun, H. XiaoAn, H. Jia, W. JinWu, and W. Yun. High-temperature mechanical properties of nickel-based superalloys manufactured by additive manufacturing. *Materials Science and Technology*, 36(14):1523–1533, 2020.

M. G. Geers, W. Brekelmans, and P. Janssen. Size effects in miniaturized polycrystalline fcc samples: Strengthening versus weakening. *International Journal of Solids and Structures*, 43(24):7304–7321, 2006.

F. Geiger, K. Kunze, and T. Etter. Tailoring the texture of IN738lc processed by selective laser melting (SLM) by specific scanning strategies. *Materials Science and Engineering: A*, 661:240–246, Apr. 2016. doi: 10.1016/j.msea.2016.03.036. URL `https://doi.org/10.1016/j.msea.2016.03.036`.

S. Ghorbanpour, M. Zecevic, A. Kumar, M. Jahedi, J. Bicknell, L. Jorgensen, I. J. Beyerlein, and M. Knezevic. A crystal plasticity model incorporating the effects of precipitates in superalloys: Application to tensile, compressive, and cyclic deformation of inconel 718. *International Journal of Plasticity*, 99:162–185, 2017.

S. Ghorbanpour, M. E. Alam, N. C. Ferreri, A. Kumar, B. A. McWilliams, S. C. Vogel, J. Bicknell, I. J. Beyerlein, and M. Knezevic. Experimental characterization and crystal plasticity modeling of anisotropy, tension-compression asymmetry, and texture evolution of additively manufactured inconel 718 at room and elevated temperatures. *International Journal of Plasticity*, 125:63–79, 2020.

S. Ghorbanpour, J. Bicknell, and M. Knezevic. Fatigue strength of additive manufactured mar-m-509 superalloy. *Materials Science and Engineering: A*, 840:142913, 2022. ISSN 0921-5093.

C. Gierden, J. Kochmann, J. Waimann, B. Svendsen, and S. Reese. A review of FE-FFT-based two-scale methods for computational modeling of microstructure evolution and macroscopic material behavior. *Archives of Computational Methods in Engineering*, 29(6):4115–4135, apr 2022. doi: 10.1007/s11831-022-09735-6.

I. Gitman, H. Askes, and L. Sluys. Representative volume: Existence and size determination. *Engineering Fracture Mechanics*, 74(16):2518 – 2534, 2007.

C. González and J. LLorca. Mechanical behavior of unidirectional fiber-reinforced polymers under transverse compression: Microscopic mechanisms and modeling. *Composites Science and Technology*, 67(13):2795–2806, Oct. 2007. doi: 10.1016/j.

compscitech.2007.02.001. URL https://doi.org/10.1016/j.compscitech.2007.02.001.

M. B. Gorji, T. Tancogne-Dejean, and D. Mohr. Heterogeneous random medium plasticity and fracture model of additively-manufactured Ti-6Al-4V. *Acta Materialia*, 148 (3):442–455, 2018. doi: https://doi.org/10.1016/j.actamat.2018.02.025.

S. Gribbin, J. Bicknell, L. Jorgensen, I. Tsukrov, and M. Knezevic. Low cycle fatigue behavior of direct metal laser sintered inconel alloy 718. *International Journal of Fatigue*, 93:156–167, 2016.

M. A. Groeber and M. A. Jackson. DREAM.3d: A digital representation environment for the analysis of microstructure in 3d. *Integrating Materials and Manufacturing Innovation*, 3(1):56–72, Apr. 2014. doi: 10.1186/2193-9772-3-5. URL https://doi.org/10.1186/2193-9772-3-5.

S. Gupta and C. A. Bronkhorst. Crystal plasticity model for single crystal ni-based superalloys: Capturing orientation and temperature dependence of flow stress. *International Journal of Plasticity*, 137:102896, 2021.

Q. Han, R. Mertens, M. L. Montero-Sistiaga, S. Yang, R. Setchi, K. Vanmeensel, B. V. Hooreweder, S. L. Evans, and H. Fan. Laser powder bed fusion of hastelloy x: Effects of hot isostatic pressing and the hot cracking mechanism. *Materials Science and Engineering: A*, 732:228–239, Aug. 2018. doi: 10.1016/j.msea.2018.07.008. URL https://doi.org/10.1016/j.msea.2018.07.008.

Q. Han, Y. Gu, R. Setchi, F. Lacan, R. Johnston, S. L. Evans, and S. Yang. Additive manufacturing of high-strength crack-free ni-based hastelloy x superalloy. *Additive Manufacturing*, 30:100919, Dec. 2019. doi: 10.1016/j.addma.2019.100919. URL https://doi.org/10.1016/j.addma.2019.100919.

S. Han, X. Yang, D. Shi, G. Miao, J. Huang, and R. Li. Microstructure-sensitive modeling of competing failure mode between surface and internal nucleation in high cycle fatigue. *International Journal of Plasticity*, 126:102622, Mar. 2020. doi: 10.1016/j.ijplas.2019.11.001. URL https://doi.org/10.1016/j.ijplas.2019.11.001.

N. J. Harrison, I. Todd, and K. Mumtaz. Reduction of micro-cracking in nickel superalloys processed by selective laser melting: A fundamental alloy design approach. *Acta Materialia*, 94:59–68, Aug. 2015. doi: 10.1016/j.actamat.2015.04.035. URL https://doi.org/10.1016/j.actamat.2015.04.035.

V. Herrera-Solaz, J. LLorca, E. Dogan, I. Karaman, and J. Segurado. An inverse optimization strategy to determine single crystal mechanical behavior from polycrystal tests: Application to AZ31 Mg alloy. *International Journal of Plasticity*, 57:1 – 15, 2014.

V. Herrera-Solaz, C. Cepeda-Jiménez, M. Pérez-Prado, J. Segurado, and M. Niffenegger. The influence of underlying microstructure on surface stress and strain fields calculated by crystal plasticity finite element method. *Materials Today Communications*, 24:101176, Sept. 2020. doi: 10.1016/j.mtcomm.2020.101176. URL `https://doi.org/10.1016/j.mtcomm.2020.101176`.

R. Hill. The elastic behaviour of a crystalline aggregate. *Proceedings of the Physical Society A*, 65(5):349–354, May 1952.

R. Hill and J. Rice. Constitutive analysis of elastic-plastic crystals at arbitrary strain. *Journal of the Mechanics and Physics of Solids*, 20(6):401 – 413, 1972.

D. Hull and D. Bacon. *Introduction to dislocations*. Butterworth-Heinemann, 5th edition, 2011.

J. Hunt. Steady state columnar and equiaxed growth of dendrites and eutectic. *Materials Science and Engineering*, 65(1):75–83, July 1984. doi: 10.1016/0025-5416(84)90201-5. URL `https://doi.org/10.1016/0025-5416(84)90201-5`.

H. Jahed, A. VARVANIFARAHANI, M. NOBAN, and I. KHALAJI. An energy-based fatigue life assessment model for various metallic materials under proportional and non-proportional loading conditions. *International Journal of Fatigue*, 29(4):647–655, apr 2007. doi: 10.1016/j.ijfatigue.2006.07.017.

A. S. Johnson, S. Shao, N. Shamsaei, S. M. Thompson, and L. Bian. Microstructure, fatigue behavior, and failure mechanisms of direct laser-deposited inconel 718. *Jom*, 69(3):597–603, 2017.

E. H. Jordan, S. Shi, and K. P. Walker. The viscoplastic behavior of Hastelloy-X single crystal. *International Journal of Plasticity*, 9(1):119–139, 1993.

D. S. Joseph, P. Chakraborty, and S. Ghosh. Wavelet transformation based multi-time scaling method for crystal plasticity fe simulations under cyclic loading. *Computer methods in applied mechanics and engineering*, 199(33-36):2177–2194, 2010.

M. Kabel, T. Böhlke, and M. Schneider. Efficient fixed point and newton-krylov solvers for FFT-based homogenization of elasticity at large deformations. *Computational Mechanics*, 54:1497–1514, 2014.

M. Kabel, D. Merkert, and M. Schneider. Use of composite voxels in fft-based homogenization. *Computer Methods in Applied Mechanics and Engineering*, 294:168 – 188, 2015.

P. Kanagarajah, F. Brenne, T. Niendorf, and H. Maier. Inconel 939 processed by selective laser melting: Effect of microstructure and temperature on the mechanical properties under static and cyclic loading. *Materials Science and Engineering: A*, 588:188–195, Dec. 2013. doi: 10.1016/j.msea.2013.09.025. URL `https://doi.org/10.1016/j.msea.2013.09.025`.

J. Kang. Effect of laser power and scanning speed on the microstructure and mechanical properties of SLM fabricated inconel 718 specimens. *Material Science & Engineering International Journal*, 3(3), 2019. doi: 10.15406/mseij.2019.03.00094. URL `https://doi.org/10.15406/mseij.2019.03.00094`.

K. Kapoor, Y. S. J. Yoo, T. A. Book, J. P. Kacher, and M. D. Sangid. Incorporating grain-level residual stresses and validating a crystal plasticity model of a two-phase ti-6al-4v alloy produced via additive manufacturing. *Journal of the Mechanics and Physics of Solids*, 121:447–462, 2018. doi: https://doi.org/10.1016/j.jmps.2018.07.025.

A. S. Karapuzha, T. Wegener, M. Krochmal, Y. Zhu, T. Niendorf, D. Fraser, X. Wu, and A. Huang. Fatigue crack growth in additively manufactured hastelloy x - influences of crack orientation and post-fabrication treatments. *Materials Science and Engineering: A*, 854:143773, Sept. 2022. doi: 10.1016/j.msea.2022.143773. URL `https://doi.org/10.1016/j.msea.2022.143773`.

G. Kasperovich, J. Haubrich, J. Gussone, and G. Requena. Correlation between porosity and processing parameters in TiAl6v4 produced by selective laser melting. *Materials & Design*, 105:160–170, Sept. 2016. doi: 10.1016/j.matdes.2016.05.070. URL `https://doi.org/10.1016/j.matdes.2016.05.070`.

S. Kaßbohm, W. H. Müller, and R. Feßler. Improved approximations of fourier coefficients for computing periodic structures with arbitrary stiffness distribution. *Computational Materials Science*, 37(1-2):90–93, aug 2006. doi: 10.1016/j.commatsci.2005.12.010.

N. Keller, F. Neugebauer, H. Xu, and V. Ploshikhin. Thermo-mechanical simulation of additive layer manufacturing of titanium aerospace structures. 09 2013.

S. Keshavarz and S. Ghosh. Multi-scale crystal plasticity finite element model approach to modeling nickel-based superalloys. *Acta Materialia*, 61:6549–6561, 2013.

A. Keshavarzkermani, E. Marzbanrad, R. Esmaeilizadeh, Y. Mahmoodkhani, U. Ali, P. D. Enrique, N. Y. Zhou, A. Bonakdar, and E. Toyserkani. An investigation into the effect of process parameters on melt pool geometry, cell spacing, and grain refinement during laser powder bed fusion. *Optics & Laser Technology*, 116:83–91, 2019. ISSN 0030-3992. doi: https://doi.org/10.1016/j.optlastec.2019.03.012. URL `https://www.sciencedirect.com/science/article/pii/S0030399218320760`.

D.-K. Kim, J.-H. Hwang, E.-Y. Kim, Y.-U. Heo, W. Woo, and S.-H. Choi. Evaluation of the stress-strain relationship of constituent phases in AlSi10mg alloy produced by selective laser melting using crystal plasticity FEM. *Journal of Alloys and Compounds*, 714:687–697, Aug. 2017. doi: 10.1016/j.jallcom.2017.04.264. URL `https://doi.org/10.1016/j.jallcom.2017.04.264`.

M. M. Kirka, D. A. Greeley, C. Hawkins, and R. R. Dehoff. Effect of anisotropy and texture on the low cycle fatigue behavior of inconel 718 processed via electron beam melting. *International Journal of Fatigue*, 105:235–243, 2017.

R. Klopp, R. Clifton, and T. Shawki. Pressure-shear impact and the dynamic viscoplastic response of metals. *Mechanics of Materials*, 4(3):375–385, 1985. doi: https://doi.org/10.1016/0167-6636(85)90033-X.

U. F. Kocks. Laws for work-hardening and low-temperature creep. *Journal of Engineering Materials and Technology*, 98(1):76–85, jan 1976. doi: 10.1115/1.3443340.

U. F. Kocks, K. UF, A. AS, and A. MF. Thermodynamics and kinetics of slip. 1975.

Y. Kok, X. Tan, P. Wang, M. Nai, N. Loh, E. Liu, and S. Tor. Anisotropy and heterogeneity of microstructure and mechanical properties in metal additive manufacturing: A critical review. *Materials and Design*, 139:565–586, Feb. 2018.

R. Konecna, L. Kunz, G. Nicoletto, and A. Baca. Fatigue crack growth behavior of inconel 718 produced by selective laser melting. *Frattura ed Integrità Strutturale*, (35): 31, 2016.

R. Konečná, G. Nicoletto, L. Kunz, and A. Bača. Microstructure and directional fatigue behavior of inconel 718 produced by selective laser melting. *Procedia Structural Integrity*, 2:2381–2388, 2016. doi: 10.1016/j.prostr.2016.06.298. URL `https://DOI.org/10.1016/j.prostr.2016.06.298`.

K. Kunze, T. Etter, J. Grässlin, and V. Shklover. Texture, anisotropy in microstructure and mechanical properties of IN738lc alloy processed by selective laser melting

(SLM). *Materials Science and Engineering: A*, 620:213–222, Jan. 2015. doi: 10.1016/j.msea.2014.10.003. URL `https://doi.org/10.1016/j.msea.2014.10.003`.

V.-D. Le, F. Morel, D. Bellett, N. Saintier, and P. Osmond. Simulation of the kitagawa-takahashi diagram using a probabilistic approach for cast al-si alloys under different multiaxial loads. *International Journal of Fatigue*, 93:109–121, 2016.

R. Lebensohn and C. Tomé. A self-consistent anisotropic approach for the simulation of plastic deformation and texture development of polycrystals: Application to zirconium alloys. *Acta Metallurgica et Materialia*, 41(9):2611 – 2624, 1993.

R. A. Lebensohn. N-site modeling of a 3d viscoplastic polycrystal using fast fourier transform. *Acta Materialia*, 49(14):2723 – 2737, 2001.

R. A. Lebensohn and O. Cazacu. Effect of single-crystal plastic deformation mechanisms on the dilatational plastic response of porous polycrystals. *International Journal of Solids and Structures*, 49(26):3838 – 3852, 2012.

R. A. Lebensohn, J. P. Escobedo, E. Cerreta, D. Dennis-Koller, C. A. Bronkhorst, and J. F. Bingert. Modeling void growth in polycrystalline materials. *Acta Materialia*, 61(18):6918 – 6932, 2013.

S. Lee, J. W. Pegues, and N. Shamsaei. Fatigue behavior and modeling for additive manufactured 304l stainless steel: The effect of surface roughness. *International Journal of Fatigue*, 141:105856, Dec. 2020.

S. Leuders, M. Thöne, A. Riemer, T. Niendorf, T. Tröster, H. Richard, and H. Maier. On the mechanical behaviour of titanium alloy TiAl6v4 manufactured by selective laser melting: Fatigue resistance and crack growth performance. *International Journal of Fatigue*, 48:300–307, Mar. 2013. doi: 10.1016/j.ijfatigue.2012.11.011. URL `https://DOI.org/10.1016/j.ijfatigue.2012.11.011`.

M. Leuschner and F. Fritzen. Fourier-accelerated nodal solvers (FANS) for homogenization problems. *Computational Mechanics*, 62(3):359–392, nov 2017. doi: 10.1007/s00466-017-1501-5.

J. J. Lewandowski and M. Seifi. Metal additive manufacturing: A review of mechanical properties. *Annual Review of Materials Research*, 46:151–186, 2016.

W. Li, R. Sun, T. Hu, X. Li, C. Li, Y. Zhang, X. Ding, and P. Wang. Effect of elevated temperature on high-cycle and very-high-cycle fatigue properties of ni-based superalloy manufactured by selective laser melting. *International Journal of Fatigue*, 148:

106250, July 2021. doi: 10.1016/j.ijfatigue.2021.106250. URL `https://DOI.org/10.1016/j.ijfatigue.2021.106250`.

Y. Li, H. Qi, H. Hou, and L. Lei. Effects of hot isostatic pressing on microstructure and mechanical properties of hastelloy x samples produced by selective laser melting. In *Proceedings of the Second International Conference on Mechanics, Materials and Structural Engineering (ICMMSE 2017)*. Atlantis Press, 2017. doi: 10.2991/icmmse-17.2017.6. URL `https://doi.org/10.2991/icmmse-17.2017.6`.

Z. Li, Z. Li, Z. Tan, D.-B. Xiong, and Q. Guo. Stress relaxation and the cellular structure-dependence of plastic deformation in additively manufactured alsi10mg alloys. *International Journal of Plasticity*, 127:102640, 2020.

T. Lindström, D. Ewest, K. Simonsson, R. Eriksson, J.-E. Lundgren, and D. Leidermark. Constitutive model of an additively manufactured ductile nickel-based superalloy undergoing cyclic plasticity. *International Journal of Plasticity*, 132:102752, Sept. 2020. doi: 10.1016/j.ijplas.2020.102752. URL `https://doi.org/10.1016/j.ijplas.2020.102752`.

T. Lindström, D. Ewest, K. Simonsson, R. Eriksson, J.-E. Lundgren, and D. Leidermark. Constitutive model of an additively manufactured ductile nickel-based superalloy undergoing cyclic plasticity. *International Journal of Plasticity*, 132:102752, 2020.

J. C. Lippold, S. D. Kiser, and J. N. DuPont. *Welding Metallurgy and Weldability of Nickel-Base Alloys*. 10 2009. ISBN 9780470087145.

J. Liu, W. Xiong, a. Behera, S. Thompson, and A. C. To. Mean-field polycrystal plasticity modeling with grain size and shape effects for laser additive manufactured FCC metals. *International Journal of Solids and Structures*, 112:35–42, 2017. doi: https://doi.org/10.1016/j.ijsolstr.2017.02.024.

W. Liu, J. Huang, J. Liu, X. Wu, K. Zhang, and A. Huang. Experimental and crystal plasticity modelling study on the crack initiation in micro-texture regions of ti-6al-4v during high cycle fatigue tests. *International Journal of Fatigue*, 148:106203, 2021. ISSN 0142-1123.

O. Lopez-Botello, U. Martinez-Hernandez, J. Ramírez, C. Pinna, and K. Mumtaz. Two-dimensional simulation of grain structure growth within selective laser melted AA-2024. *Materials and Design*, 113:369–376, Jan. 2017. doi: 10.1016/j.matdes.2016.10.031. URL `https://doi.org/10.1016/j.matdes.2016.10.031`.

M. A. Lopez-Sanchez. Grainsizetools: a python script for grain size analysis and paleopiezometry based on grain size. *Journal of Open Source Software*, (3):863, 2018. doi: https://doi.org/10.21105/joss.00863.

S. J. Lorenz, F. Sadeghi, H. K. Trivedi, L. Rosado, M. S. Kirsch, and C. Wang. A continuum damage mechanics finite element model for investigating effects of surface roughness on rolling contact fatigue. *International Journal of Fatigue*, 143:105986, Feb. 2021. doi: 10.1016/j.ijfatigue.2020.105986. URL `https://doi.org/10.1016/j.ijfatigue.2020.105986`.

S. Lucarini and J. Segurado. On the accuracy of spectral solvers for micromechanics based fatigue modeling. *Computational Mechanics*, 63(2):365–382, July 2018. doi: 10.1007/s00466-018-1598-1. URL `https://doi.org/10.1007/s00466-018-1598-1`.

S. Lucarini and J. Segurado. An upscaling approach for micromechanics based fatigue: from RVEs to specimens and component life prediction. *International Journal of Fracture*, 223(1-2):93–108, Dec. 2019. doi: 10.1007/s10704-019-00406-5. URL `https://doi.org/10.1007/s10704-019-00406-5`.

S. Lucarini and J. Segurado. An upscaling approach for micromechanics based fatigue: from rves to specimens and component life prediction. *International Journal of Fracture*, 223(1):93–108, 2020.

S. Lucarini, M. V. Upadhyay, and J. Segurado. FFT based approaches in micromechanics: fundamentals, methods and applications. *Modelling and Simulation in Materials Science and Engineering*, 30(2):023002, Dec. 2021. doi: 10.1088/1361-651x/ac34e1. URL `https://doi.org/10.1088/1361-651x/ac34e1`.

R. Ma, C. Peng, Z. Cai, R. Wang, Z. Zhou, X. Li, and X. Cao. Effect of bimodal microstructure on the tensile properties of selective laser melt al-mg-sc-zr alloy. *Journal of Alloys and Compounds*, 815:152422, Jan. 2020. doi: 10.1016/j.jallcom.2019.152422. URL `https://doi.org/10.1016/j.jallcom.2019.152422`.

X. Ma, M. Shakoor, D. Vasiukov, S. V. Lomov, and C. H. Park. Numerical artifacts of fast fourier transform solvers for elastic problems of multi-phase materials: their causes and reduction methods. *Computational Mechanics*, 67(6):1661–1683, apr 2021. doi: 10.1007/s00466-021-02013-5.

A. Manonukul and F. P. E. Dunne. High– and low–cycle fatigue crack initiation using polycrystal plasticity. *Proceedings of the Royal Society of London A: Mathematical, Physical and Engineering Sciences*, 460(2047):1881–1903, 2004.

S. Manson. Behavior of materials under conditions of thermal stress. *National Advisory Comission on Aeronautics*, Report 1170, 1954. cleveland: Lewis Flight Propulsion Laboratory.

S. S. Manson and M. H. Hirschberg. Fatigue behavior in strain cycling in the low and intermediate-cycle range. pages 13–16, 1964.

G. Marchese, G. Basile, E. Bassini, A. Aversa, M. Lombardi, D. Ugues, P. Fino, and S. Biamino. Study of the microstructure and cracking mechanisms of hastelloy x produced by laser powder bed fusion. *Materials*, 11(1):106, Jan. 2018. doi: 10.3390/ma11010106. URL `https://doi.org/10.3390/ma11010106`.

M.A.Rowley and E.A.Thornton. Constitutive modeling of the visco-plastic response of hastelloy-x and aluminum alloy 8009. *Journal of Engineering Materials and Technology*, 118(19–27), 1996.

D. McDowell and F. Dunne. Microstructure-sensitive computational modeling of fatigue crack formation. *International Journal of Fatigue*, 32(9):1521 – 1542, 2010.

D. McDowell, K. Gall, M. Horstemeyer, and J. Fan. Microstructure-based fatigue modeling of cast a356-T6 alloy. *Engineering Fracture Mechanics*, 70(1):49 – 80, 2003.

D. L. McDowell. Simulation-based strategies for microstructure-sensitive fatigue modeling. *Materials Science and Engineering: A*, 468-470:4 – 14, 2007.

P. Mercelis and J.-P. Kruth. Residual stresses in selective laser sintering and selective laser melting. *Rapid Prototyping Journal*, 12(5):254–265, Oct. 2006. doi: 10.1108/13552540610707013. URL `https://doi.org/10.1108/13552540610707013`.

A. Molinari, G. Canova, and S. Ahzi. A self consistent approach of the large deformation polycrystal viscoplasticity. *Acta Metallurgica*, 35(12):2983 – 2994, 1987.

M. Montero-Sistiaga, N. Dhansay, L. Bautmans, S. Nardone, T. Becker, J.-P. Kruth, and K. Vanmeensel. Fatigue performance of micro-crack free hastelloy x produced by selective laser melting (slm). 08 2019a.

M. L. Montero-Sistiaga, S. Pourbabak, J. Van Humbeeck, D. Schryvers, and K. Vanmeensel. Microstructure and mechanical properties of Hastelloy X produced by HP-SLM (high power selective laser melting). *Materials and Design*, 165:107598, 2019b.

M. L. Montero-Sistiaga, Z. Liu, L. Bautmans, S. Nardone, G. Ji, J.-P. Kruth, J. V. Humbeeck, and K. Vanmeensel. Effect of temperature on the microstructure and tensile properties of micro-crack free hastelloy x produced by selective laser melting. *Additive Manufacturing*, 31:100995, Jan. 2020. doi: 10.1016/j.addma.2019.100995. URL `https://doi.org/10.1016/j.addma.2019.100995`.

H. Moulinec and P. Suquet. Fast numerical method for computing the linear and nonlinear properties of composites. *Comptes Rendus de l'academie des Sciences. Série II*, 318: 1417–1423, 1994.

H. Moulinec and P. Suquet. A numerical method for computing the overall response of nonlinear composites with complex microstructure. *Computer Methods in Applied Mechanics and Engineering*, 157(1):69 – 94, 1998.

W. Muhammad, A. P. Brahme, O. Ibragimova, J. Kang, and K. Inal. A machine learning framework to predict local strain distribution and the evolution of plastic anisotropy and fracture in additively manufactured alloys. *International Journal of Plasticity*, 136: 102867, 2021.

K. Mumtaz and N. Hopkinson. Top surface and side roughness of inconel 625 parts processed using selective laser melting. *Rapid Prototyping Journal*, 2009.

R. Muñoz-Moreno, V. Divya, S. Driver, O. Messé, T. Illston, S. Baker, M. Carpenter, and H. Stone. Effect of heat treatment on the microstructure, texture and elastic anisotropy of the nickel-based superalloy CM247lc processed by selective laser melting. *Materials Science and Engineering: A*, 674:529–539, Sept. 2016. doi: 10.1016/j.msea.2016.06.075. URL `https://doi.org/10.1016/j.msea.2016.06.075`.

Y. Murakami and M. Endo. Effects of hardness and crack geometries on delta k sub th of small cracks emanating from small defects. *Mechanical Engineering Publications, The Behaviour of Short Fatigue Cracks,*, pages 275–293, 1986.

L. Murr, E. Martinez, X. Pan, S. Gaytan, J. Castro, C. Terrazas, F. Medina, R. Wicker, and D. Abbott. Microstructures of rene 142 nickel-based superalloy fabricated by electron beam melting. *Acta Materialia*, 61(11):4289–4296, June 2013. doi: 10.1016/j.actamat.2013.04.002. URL `https://doi.org/10.1016/j.actamat.2013.04.002`.

L. E. Murr. A metallographic review of 3d printing/additive manufacturing of metal and alloy products and components. *Metallography, Microstructure, and Analysis*, 7 (2):103–132, 2018.

X. Ni, D. Kong, L. Zhang, C. Dong, J. Song, and W. Wu. Effect of process parameters on the mechanical properties of hastelloy x alloy fabricated by selective laser melting. *Journal of Materials Engineering and Performance*, 28(9):5533–5540, Aug. 2019. doi: 10.1007/s11665-019-04275-w. URL https://doi.org/10.1007/s11665-019-04275-w.

T. Niendorf, S. Leuders, A. Riemer, H. A. Richard, T. Tröster, and D. Schwarze. Highly anisotropic steel processed by selective laser melting. *Metallurgical and Materials Transactions B*, 44(4):75–82, 2013. doi: https://10.1007/s11663-013-9875-z.

D. Norman. Mechanical behavior of materials-engineering methods for deformation, fracture, and fatigue. 2013.

N. Ohno and J.-D. Wang. Kinematic hardening rules with critical state of dynamic recovery, part ii: Application to experiments of ratchetting behavior. *International Journal of Plasticity*, 9(3):391 – 403, 1993.

J. Oliveira, A. LaLonde, and J. Ma. Processing parameters in laser powder bed fusion metal additive manufacturing. *Materials and Design*, 193:108762, Aug. 2020. doi: 10.1016/j.matdes.2020.108762. URL https://doi.org/10.1016/j.matdes.2020.108762.

C.-Y. Ou, R. Voothaluru, and C. R. Liu. Fatigue crack initiation of metals fabricated by additive manufacturing—a crystal plasticity energy-based approach to IN718 life prediction. *Crystals*, 10(10):905, Oct. 2020.

D. Ozturk, A. Shahba, and S. Ghosh. Crystal plasticity FE study of the effect of thermo-mechanical loading on fatigue crack nucleation in titanium alloys. *Fatigue & Fracture of Engineering Materials & Structures*, 39:752–769, 2016.

T. Ozturk and A. D. Rollett. Effect of microstructure on the elasto-viscoplastic deformation of dual phase titanium structures. *Computational Mechanics*, 61(1-2):55–70, Aug. 2017.

J. W. Pegues, N. Shamsaei, M. D. Roach, and R. S. Williamson. Fatigue life estimation of additive manufactured parts in the as-built surface condition. *Material Design &amp Processing Communications*, 1(3), Feb. 2019. doi: 10.1002/mdp2.36. URL https://doi.org/10.1002/mdp2.36.

C. Pei, D. Shi, H. Yuan, and H. Li. Assessment of mechanical properties and fatigue performance of a selective laser melted nickel-base superalloy inconel 718. *Materials Science and Engineering: A*, 759:278–287, June 2019. doi: 10.1016/j.msea.2019.05.007. URL https://DOI.org/10.1016/j.msea.2019.05.007.

D. Peirce, R. Asaro, and A. Needleman. Material rate dependence and localized deformation in crystalline solids. *Acta Metallurgica*, 31(12):1951 – 1976, 1983.

C. L. Pérez, J. V. Calvet, and M. S. Pérez. Geometric roughness analysis in solid free-form manufacturing processes. *Journal of Materials Processing Technology*, 119(1-3): 52–57, Dec. 2001. doi: 10.1016/s0924-0136(01)00897-4. URL `https://doi.org/10.1016/s0924-0136(01)00897-4`.

E. Pessard, D. Bellett, F. Morel, and I. Koutiri. A mechanistic approach to the kitagawa–takahashi diagram using a multiaxial probabilistic framework. *Engineering Fracture Mechanics*, 109:89–104, 2013.

H. F. Poulsen, S. F. Nielsen, E. M. Lauridsen, S. Schmidt, R. M. Suter, U. Lienert, L. Margulies, T. Lorentzen, and D. J. Jensen. Three-dimensional maps of grain boundaries and the stress state of individual grains in polycrystals and powders. *Journal of Applied Crystallography*, 34(6):751–756, Nov. 2001. doi: 10.1107/s0021889801014273. URL `https://doi.org/10.1107/s0021889801014273`.

V. Prithivirajan and M. D. Sangid. The role of defects and critical pore size analysis in the fatigue response of additively manufactured in718 via crystal plasticity. *Materials and Design*, 150:139–153, 2018.

C. Qiu, C. Panwisawas, M. Ward, H. C. Basoalto, J. W. Brooks, and M. M. Attallah. On the role of melt flow into the surface structure and porosity development during selective laser melting. *Acta Materialia*, 96:72–79, Sept. 2015. doi: 10.1016/j.actamat.2015.06.004. URL `https://doi.org/10.1016/j.actamat.2015.06.004`.

R. Quey, P. Dawson, and F. Barbe. Large-scale 3d random polycrystals for the finite element method: Generation, meshing and remeshing. *Computer Methods in Applied Mechanics and Engineering*, 200(17):1729 – 1745, 2011.

D. Raabe, M. Sachtleber, Z. Zhao, F. Roters, and S. Zaefferer. Micromechanical and macromechanical effects in grain scale polycrystal plasticity experimentation and simulation. *Acta Materialia*, 49(17):3433 – 3441, 2001.

A. Rai, M. Markl, and C. Körner. A coupled cellular automaton–lattice boltzmann model for grain structure simulation during additive manufacturing. *Computational Materials Science*, 124:37–48, Nov. 2016. doi: 10.1016/j.commatsci.2016.07.005. URL `https://doi.org/10.1016/j.commatsci.2016.07.005`.

R. C. Reed. *The Superalloys*. Cambridge University Press, Sept. 2006. doi: 10.1017/cbo9780511541285. URL `https://doi.org/10.1017/cbo9780511541285`.

A. Reuss. Berechnung der fließgrenze von mischkristallen auf grund der plastizitätsbedingung für einkristalle . *ZAMM - Journal of Applied Mathematics and Mechanics / Zeitschrift für Angewandte Mathematik und Mechanik*, 9(1):49–58, 1929.

J. Rice. Inelastic constitutive relations for solids: An internal-variable theory and its application to metal plasticity. *Journal of the Mechanics and Physics of Solids*, 19(6):433 – 455, 1971.

A. Riemer, S. Leuders, M. Thöne, H. Richard, T. Tröster, and T. Niendorf. On the fatigue crack growth behavior in 316L stainless steel manufactured by selective laser melting. *Engineering Fracture Mechanics*, 120:15–25, 2014.

J. Robinson, I. Ashton, P. Fox, E. Jones, and C. Sutcliffe. Determination of the effect of scan strategy on residual stress in laser powder bed fusion additive manufacturing. *Additive Manufacturing*, 23:13–24, Oct. 2018. doi: 10.1016/j.addma.2018.07.001. URL `https://doi.org/10.1016/j.addma.2018.07.001`.

T. M. Rodgers, J. D. Madison, and V. Tikare. Simulation of metal additive manufacturing microstructures using kinetic monte carlo. *Computational Materials Science*, 135:78–89, July 2017. doi: 10.1016/j.commatsci.2017.03.053. URL `https://doi.org/10.1016/j.commatsci.2017.03.053`.

T. M. Rodgers, H. Lim, and J. A. Brown. Three-dimensional additively manufactured microstructures and their mechanical properties. *JOM*, 72(1):75–82, 2020.

D. A. Rollett and U.F.Kocks. A review of the stages of work hardening. *Solid State Phenomena*, 35:1 – 18, 1993.

S. Romano, L. Patriarca, S. Foletti, and S. Beretta. Lcf behaviour and a comprehensive life prediction model for alsi10mg obtained by slm. *International Journal of fatigue*, 117:47–62, 2018.

J. Rossiter, A. Brahme, M. Simha, K. Inal, and R. Mishra. A new crystal plasticity scheme for explicit time integration codes to simulate deformation in 3d microstructures: Effects of strain path, strain rate and thermal softening on localized deformation in the aluminum alloy 5754 during simple shear. *International Journal of Plasticity*, 26(14):1702–1725, 2010. doi: 10.1016/j.ijplas.2010.02.007.

F. Roters, P. Eisenlohr, L. Hantcherli, D. Tjahjanto, T. Bieler, and D. Raabe. Overview of constitutive laws, kinematics, homogenization and multiscale methods in crystal plasticity finite-element modeling: Theory, experiments, applications. *Acta Materialia*, 58(4):1152 – 1211, 2010.

A. Rovinelli, R. A. Lebensohn, and M. D. Sangid. Influence of microstructure variability on short crack behavior through postulated micromechanical short crack driving force metrics. *Engineering Fracture Mechanics*, 138:265–288, Apr. 2015a.

A. Rovinelli, R. A. Lebensohn, and M. D. Sangid. Influence of microstructure variability on short crack behavior through postulated micromechanical short crack driving force metrics. *Engineering Fracture Mechanics*, 138:265 – 288, 2015b.

G. Sachs. Plasticity problems in metals. *Trans. Faraday Soc.*, 24:84–92, 1928.

T. Sakthivel, K. Laha, M. Nandagopal, K. Chandravathi, P. Parameswaran, S. Panneer Selvi, M. Mathew, and S. K. Mannan. Effect of temperature and strain rate on serrated flow behaviour of hastelloy x. *Materials Science and Engineering: A*, 534:580 – 587, 2012.

S. Sanchez, P. Smith, Z. Xu, G. Gaspard, C. J. Hyde, W. W. Wits, I. A. Ashcroft, H. Chen, and A. T. Clare. Powder bed fusion of nickel-based superalloys: A review. *International Journal of Machine Tools and Manufacture*, 165:103729, June 2021. doi: 10.1016/j.ijmachtools.2021.103729. URL `https://doi.org/10.1016/j.ijmachtools.2021.103729`.

M. D. Sangid. The physics of fatigue crack initiation. *International Journal of Fatigue*, 57: 58 – 72, 2013.

M. Schneider. A review of nonlinear FFT-based computational homogenization methods. *Acta Mechanica*, 232(6):2051–2100, mar 2021. doi: 10.1007/s00707-021-02962-1.

M. Schneider, F. Ospald, and M. Kabel. Computational homogenization of elasticity on a staggered grid. *International Journal for Numerical Methods in Engineering*, 105(9): 693–720, 2016.

J. Segurado and J. Llorca. A numerical approximation to the elastic properties of sphere-reinforced composites. *Journal of the Mechanics and Physics of Solids*, 50(10): 2107–2121, Oct. 2002. doi: 10.1016/s0022-5096(02)00021-2. URL `https://doi.org/10.1016/s0022-5096(02)00021-2`.

J. Segurado, R. A. Lebensohn, and J. LLorca. Chapter one - computational homogenization of polycrystals. In *Advances in Crystals and Elastic Metamaterials*, volume 51 of *Advances in Applied Mechanics*, pages 1 – 114. Elsevier, 2018.

A. Shahba and S. Ghosh. Crystal plasticity FE modeling of ti alloys for a range of strain-rates. part i: A unified constitutive model and flow rule. *International Journal of Plasticity*, 87:48–68, dec 2016. doi: 10.1016/j.ijplas.2016.09.002.

P. Shanthraj, P. Eisenlohr, M. Diehl, and F. Roters. Numerically robust spectral methods for crystal plasticity simulations of heterogeneous materials. *International Journal of Plasticity*, 66:31–45, mar 2015. doi: 10.1016/j.ijplas.2014.02.006. URL `https://doi.org/10.10162Fj.ijplas.2014.02.006`.

M. Shenoy, J. Zhang, and D. McDowell. Estimating fatigue sensitivity to polycrystalline Ni-base superalloy microstructures using a computational approach. *Fatigue and Fracture of Engineering Materials and Structures*, 30:889–904, 2007.

M. Shenoy, Y. Tjiptowidjojo, and D. McDowell. Microstructure-sensitive modeling of polycrystalline IN100. *International Journal of Plasticity*, 24:1694–1730, 2008.

H. Shipley, D. McDonnell, M. Culleton, R. Coull, R. Lupoi, G. O'Donnell, and D. Trimble. Optimisation of process parameters to address fundamental challenges during selective laser melting of ti-6al-4v: A review. *International Journal of Machine Tools and Manufacture*, 128:1–20, May 2018. doi: 10.1016/j.ijmachtools.2018.01.003. URL `https://doi.org/10.1016/j.ijmachtools.2018.01.003`.

R. Shrestha, J. Simsiriwong, and N. Shamsaei. Fatigue behavior of additive manufactured 316l stainless steel parts: Effects of layer orientation and surface roughness. *Additive Manufacturing*, 28:23–38, aug 2019. doi: 10.1016/j.addma.2019.04.011. URL `https://doi.org/10.1016%2Fj.addma.2019.04.011`.

Smith, Topper, and P. Watson. A stress-strain function for the fatigue of metals. 1969.

R. Smith and K. Miller. Prediction of fatigue regimes in notched components. *International Journal of Mechanical Sciences*, 20(4):201–206, 1978.

M. A. Soare, S. Huang, and M. Karadge. Crystal plasticity model for nickel-based superalloy rené 88dt at elevated temperature. In S. Tin, M. Hardy, J. Clews, J. Cormier, Q. Feng, J. Marcin, C. O’Brien, and A. Suzuki, editors, *Superalloys 2020*, pages 659–668, Cham, 2020. Springer International Publishing.

H. Stoffregen, K. Butterweck, and E. Abele. Fatigue analysis in selective laser melting: Review and investigation of thin-walled actuator housings. 2014.

A. T. Sutton, C. S. Kriewall, M. C. Leu, and J. W. Newkirk. Powder characterisation techniques and effects of powder characteristics on part properties in powder-bed fusion processes. *Virtual and Physical Prototyping*, 12(1):3–29, Dec. 2016. doi: 10.1080/17452759.2016.1250605. URL `https://doi.org/10.1080/17452759.2016.1250605`.

C. Sweeney, P. McHugh, J. McGarry, and S. Leen. Micromechanical methodology for fatigue in cardiovascular stents. *International Journal of Fatigue*, 44:202 – 216, 2012.

C. Sweeney, B. O'Brien, P. McHugh, and S. Leen. Experimental charactrisation for micromechanical modelling of CoCr stent fatigue. *Biomaterials*, 35:36–48, 2014.

C. Sweeney, B. O'Brien, F. Dunne, P. McHugh, and S. Leen. Micro-scale testing and micromechanical modelling for high cycle fatigue of CoCr stent material. *Journal of the Mechanical Behavior of Biomedical Materials*, 46:244 – 260, 2015.

C. A. Sweeney, W. Vorster, S. B. Leen, E. Sakurada, P. E. McHugh, and F. P. E. Dunne. The role of elastic anisotropy, length scale and crystallographic slip in fatigue crack nucleation. *Journal of the Mechanics and Physics of Solids*, 61:1224 – 1240, 2013.

M. Taheri Andani, M. R. Karamooz-Ravari, R. Mirzaeifar, and J. Ni. Micromechanics modeling of metallic alloys 3D printed by selective laser melting. *Materials and Design*, 137:204–213, 2018. doi: https://doi.org/10.1016/j.matdes.2017.10.026.

S. Tammas-Williams, P. J. Withers, I. Todd, and P. B. Prangnell. The influence of porosity on fatigue crack initiation in additively manufactured titanium components. *Scientific Reports*, 7(1), Aug. 2017. doi: 10.1038/s41598-017-06504-5. URL `https://doi.org/10.1038/s41598-017-06504-5`.

X. Tan, Y. Kok, Y. J. Tan, M. Descoins, D. Mangelinck, S. B. Tor, K. F. Leong, and C. K. Chua. Graded microstructure and mechanical properties of additive manufactured ti–6al–4v via electron beam melting. *Acta Materialia*, 97:1–16, Sept. 2015. doi: 10.1016/j.actamat.2015.06.036. URL `https://doi.org/10.1016/j.actamat.2015.06.036`.

K. Tanaka and T. Mura. A dislocation model for fatigue crack initiation. *Journal of Applied Mechanics*, 48:97 – 103, 1981.

H. Tang, H. Huang, C. Liu, Z. Liu, and W. Yan. Multi-scale modelling of structure-property relationship in additively manufactured metallic materials. *International Journal of Mechanical Sciences*, 194:106185, Mar. 2021. doi: 10.1016/j.ijmecsci.2020.106185. URL `https://doi.org/10.1016/j.ijmecsci.2020.106185`.

G. Taylor. Plastic strain in metals. *Journal of the Institute of Metals*, 62:307 – 324, 1938.

G. I. Taylor and C. F. Elam. Bakerian lecture: The distortion of an aluminium crystal during a tensile test. *Proceedings of the Royal Society of London. Series A, Containing Papers of a Mathematical and Physical Character*, 102(719):643–667, 1923.

G. I. Taylor and C. F. Elam. The plastic extension and fracture of aluminium crystals. *Proceedings of the Royal Society of London. Series A, Containing Papers of a Mathematical and Physical Character*, 108(745):28–51, 1925.

K. Terada, M. Hori, T. Kyoya, and N. Kikuchi. Simulation of the multi-scale convergence in computational homogenization approaches. *International Journal of Solids and Structures*, 37(16):2285 – 2311, 2000.

L. Thijs, K. Kempen, J.-P. Kruth, and J. V. Humbeeck. Fine-structured aluminium products with controllable texture by selective laser melting of pre-alloyed AlSi10mg powder. *Acta Materialia*, 61(5):1809–1819, Mar. 2013. doi: 10.1016/j.actamat.2012.11.052. URL `https://doi.org/10.1016/j.actamat.2012.11.052`.

C. Tome, G. Canova, U. Kocks, N. Christodoulou, and J. Jonas. The relation between macroscopic and microscopic strain hardening in f.c.c. polycrystals. *Acta Metallurgica*, 32(10):1637 – 1653, 1984.

D. Tomus, T. Jarvis, X. Wu, J. Mei, P. Rometsch, E. Herny, J.-F. Rideau, and S. Vaillant. Controlling the microstructure of hastelloy-x components manufactured by selective laser melting. *Physics Procedia*, 41:823–827, 2013. doi: 10.1016/j.phpro.2013.03.154. URL `https://doi.org/10.1016/j.phpro.2013.03.154`.

D. Tomus, Y. Tian, P. A. Rometsch, M. Heilmaier, and X. Wu. Influence of post heat treatments on anisotropy of mechanical behaviour and microstructure of hastelloy-x parts produced by selective laser melting. *Materials Science and Engineering: A*, 667:42–53, June 2016. doi: 10.1016/j.msea.2016.04.086. URL `https://doi.org/10.1016/j.msea.2016.04.086`.

B. Vayssette, N. Saintier, C. Brugger, M. E. May, and E. Pessard. Numerical modelling of surface roughness effect on the fatigue behavior of ti-6al-4v obtained by additive manufacturing. *International Journal of Fatigue*, 123:180–195, June 2019. doi: 10.1016/j.ijfatigue.2019.02.014. URL `https://doi.org/10.1016/j.ijfatigue.2019.02.014`.

T. Vilaro, C. Colin, J. Bartout, L. Nazé, and M. Sennour. Microstructural and mechanical approaches of the selective laser melting process applied to a nickel-base superalloy. *Materials Science and Engineering: A*, 534:446–451, Feb. 2012. doi: 10.1016/j.msea.2011.11.092. URL `https://doi.org/10.1016/j.msea.2011.11.092`.

E. Voce. The relationship between stress and strain for homogeneous deformations. 1948.

W. Voigt. Ueber die beziehung zwischen den beiden elasticitätsconstanten isotroper körper. *Annalen der Physik*, 274(12):573–587, 1889.

J. Vondřejc, J. Zeman, and I. Marek. An FFT-based galerkin method for homogenization of periodic media. *Computers and Mathematics with Applications*, 68(3):156 – 173, 2014.

V. V. C. Wan, D. W. MacLachlan, and F. P. E. Dunne. A stored energy criterion for fatigue crack nucleation in polycrystals. *International Journal of Fatigue*, 68:90 – 102, 2014.

F. Wang, X. H. Wu, and D. Clark. On direct laser deposited hastelloy x: dimension, surface finish, microstructure and mechanical properties. *Materials Science and Technology*, 27(1):344–356, Jan. 2011. doi: 10.1179/026708309x12578491814591. URL `https://doi.org/10.1179/026708309x12578491814591`.

H. Wang, A. Dhiman, H. E. Ostergaard, Y. Zhang, T. Siegmund, J. J. Kruzic, and V. Tomar. Nanoindentation based properties of inconel 718 at elevated temperatures: A comparison of conventional versus additively manufactured samples. *International Journal of Plasticity*, 120:380–394, 2019.

Z. Wang, K. Guan, M. Gao, X. Li, X. Chen, and X. Zeng. The microstructure and mechanical properties of deposited-IN718 by selective laser melting. *Journal of Alloys and Compounds*, 513:518–523, Feb. 2012. doi: 10.1016/j.jallcom.2011.10.107. URL `https://doi.org/10.1016/j.jallcom.2011.10.107`.

H. L. Wei, J. Mazumder, and T. DebRoy. Evolution of solidification texture during additive manufacturing. *Scientific Reports*, 5(1), Nov. 2015. doi: 10.1038/srep16446. URL `https://doi.org/10.1038/srep16446`.

F. Willot. Fourier-based schemes for computing the mechanical response of composites with accurate local fields. *Comptes Rendus Mecanique*, 343(3):232 – 245, 2015.

F. Willot, B. Abdalla, and Y. Pellegrini. Fourier-based schemes with modified green operator for computing the electrical response of heterogeneous media with accurate local fields. *International Journal for Numerical Methods in Engineering*, 98(7):518–533, 2014.

A. E. Wilson-Heid, Z. Wang, B. McCornac, and A. M. Beese. Quantitative relationship between anisotropic strain to failure and grain morphology in additively manufactured ti-6al-4v. *Materials Science and Engineering: A*, 706:287–294, 2017.

D. B. Witkin, P. Adams, and T. Albright. Microstructural evolution and mechanical behavior of nickel-based superalloy 625 made by selective laser melting. In H. Helvajian, A. Piqué, M. Wegener, and B. Gu, editors, *Laser 3D Manufacturing II*. SPIE, Mar. 2015. doi: 10.1117/12.2083699. URL `https://doi.org/10.1117/12.2083699`.

W. A. Witzen, A. T. Polonsky, T. M. Pollock, and I. J. Beyerlein. Three-dimensional maps of geometrically necessary dislocation densities in additively manufactured ni-based superalloy in718. *International Journal of Plasticity*, 131:102709, 2020.

A. Wohler. Versuche zur ermittlung der auf die eisenbahnwagenachsen einwirkenden krafte und die widerstandsfaihigkeit der wagen-achsen. *Zeitschrift fur Bauwesen*, pages 583–613, 1860.

W. Xu, M. Brandt, S. Sun, J. Elambasseril, Q. Liu, K. Latham, K. Xia, and M. Qian. Additive manufacturing of strong and ductile ti–6al–4v by selective laser melting via in situ martensite decomposition. *Acta Materialia*, 85:74–84, Feb. 2015. doi: 10.1016/j.actamat.2014.11.028. URL `https://doi.org/10.1016/j.actamat.2014.11.028`.

A. Yadollahi, N. Shamsaei, S. M. Thompson, A. Elwany, and L. Bian. Effects of building orientation and heat treatment on fatigue behavior of selective laser melted 17-4 PH stainless steel. *International Journal of Fatigue*, 94:218–235, Jan. 2017. doi: 10.1016/j.ijfatigue.2016.03.014. URL `https://DOI.org/10.1016/j.ijfatigue.2016.03.014`.

A. Yadollahi, M. Mahtabi, A. Khalili, H. Doude, and J. Newman. Fatigue life prediction of additively manufactured material: Effects of surface roughness, defect size, and shape. *Fatigue & Fracture of Engineering Materials and Structures*, 41(7):1602–1614, Mar. 2018. doi: 10.1111/ffe.12799. URL `https://doi.org/10.1111/ffe.12799`.

I. Yadroitsev, P. Bertrand, B. Laget, and I. Smurov. Application of laser assisted technologies for fabrication of functionally graded coatings and objects for the international thermonuclear experimental reactor components. *Journal of Nuclear Materials*, 362(2-3):189–196, May 2007. doi: 10.1016/j.jnucmat.2007.01.078. URL `https://doi.org/10.1016/j.jnucmat.2007.01.078`.

I. Yadroitsev, P. Krakhmalev, I. Yadroitsava, S. Johansson, and I. Smurov. Energy input effect on morphology and microstructure of selective laser melting single track from metallic powder. *Journal of Materials Processing Technology*, 213:606–613, 2013. doi: https://doi.org/10.1016/j.jmatprotec.2012.11.014.

W. Yan, S. Lin, O. L. Kafka, C. Yu, Z. Liu, Y. Lian, S. Wolff, J. Cao, G. J. Wagner, and W. K. Liu. Modeling process-structure-property relationships for additive manufacturing. *Frontiers of Mechanical Engineering*, 13(4):482–492, Feb. 2018. doi: 10.1007/s11465-018-0505-y. URL `https://doi.org/10.1007/s11465-018-0505-y`.

D. Yang, Y. Yin, X. Kan, Y. Zhao, Z. Zhao, and J. Sun. The mechanism of substructure formation and grain growth 316l stainless steel by selective laser melting. *Materials Research Express*, 8(9):096510, Sept. 2021. doi: 10.1088/2053-1591/ac21ea. URL `https://doi.org/10.1088/2053-1591/ac21ea`.

C. Y. Yap, C. K. Chua, Z. L. Dong, Z. H. Liu, D. Q. Zhang, L. E. Loh, and S. L. Sing. Review of selective laser melting: Materials and applications. *Applied Physics Reviews*, 2(4):041101, Dec. 2015. doi: 10.1063/1.4935926. URL `https://doi.org/10.1063/1.4935926`.

C. Y. Yap, H. K. Tan, Z. Du, C. K. Chua, and Z. Dong. Selective laser melting of nickel powder. *Rapid Prototyping Journal*, 23(4):750–757, June 2017. doi: 10.1108/rpj-01-2016-0006. URL `https://doi.org/10.1108/rpj-01-2016-0006`.

W. Ye, P. Kumar, and L. T. Mushongera. Understanding the low cycle fatigue of additive manufactured inconel 718: a crystal plasticity modelling approach. *International Journal of Theoretical and Applied Multiscale Mechanics*, 3(4):313, 2021.

Y. Yin, J. Zhang, S. Yang, T. Liu, Q. Han, Z. Zhang, and H. Yang. Effect of microstructure on the electrochemical dissolution behaviour of hastelloy® x superalloy processed by selective laser melting and heat treatments. *Materials & Design*, 206:109828, Aug. 2021. doi: 10.1016/j.matdes.2021.109828. URL `https://doi.org/10.1016/j.matdes.2021.109828`.

C.-H. Yu, R. L. Peng, V. Luzin, M. Sprengel, M. Calmunger, J.-E. Lundgren, H. Brodin, A. Kromm, and J. Moverare. Thin-wall effects and anisotropic deformation mechanisms of an additively manufactured ni-based superalloy. *Additive Manufacturing*, 36:101672, 2020a.

C.-H. Yu, R. L. Peng, V. Luzin, M. Sprengel, M. Calmunger, J.-R. Lundgren, H. Brodin, A. Kromm, and J. Moverare. Thin-wall effects and anisotropic deformation mechanisms of an additively manufactured ni-based superalloy. *Additive Manufacturing*, 36:101672, 2020b. doi: https://doi.org/10.1016/j.addma.2020.101672.

J. Zeman, T. W. J. de Geus, J. Vondřejc, R. H. J. Peerlings, and M. G. D. Geers. A finite element perspective on nonlinear FFT-based micromechanical simulations. *International Journal for Numerical Methods in Engineering*, 111:903–926, 2017.

M. Zhang, B. Zhang, Y. Wen, and X. Qu. Research progress on selective laser melting processing for nickel-based superalloy. *International Journal of Minerals, Metallurgy and Materials*, 29(3):369–388, Jan. 2022. doi: 10.1007/s12613-021-2331-1. URL `https://doi.org/10.1007/s12613-021-2331-1`.

T. Zhang, J. Jiang, B. A. Shollock, T. B. Britton, and F. Dunne. Slip localization and fatigue crack nucleation near a non-metallic inclusion in polycrystalline nickel-based superalloy. *Materials Science and Engineering: A*, 641:328 – 339, 2015.

X. Zhang, C. J. Yocom, B. Mao, and Y. Liao. Microstructure evolution during selective laser melting of metallic materials: A review. *Journal of Laser Applications*, 31(3): 031201, Aug. 2019. doi: 10.2351/1.5085206. URL `https://doi.org/10.2351/1.5085206`.

Z. Zhao, L. Li, W. Yang, Y. Zeng, Y. Lian, and Z. Yue. A comprehensive study of the anisotropic tensile properties of laser additive manufactured ni-based superalloy after heat treatment. *International Journal of Plasticity*, 148:103147, 2022.

S. Zhonggang, J. Shuwei, G. Yanhua, L. Yichen, C. Lili, and X. Fei. Microstructure evolution and mechanical properties of Hastelloy X alloy produced by selective laser melting. *High Temperature Materials and Processes*, 39:124–135, 05 2020. doi: 10.1515/htmp-2020-0032.